# Electron and hadronic recoil calibration for the first measurement of the mass of the $W$ boson by the ATLAS experiment at the Large Hadron Collider

Eleanor Davies

Linacre College, Oxford






Thesis submitted in partial fulfilment
of the requirements for the degree of
Doctor of Philosophy

University of Oxford, Hilary Term 2014

# Electron and hadronic recoil calibration for the first measurement of the mass of the $W$ boson by the ATLAS experiment at the Large Hadron Collider

Eleanor Davies
Linacre College, Oxford

Thesis submitted in partial fulfilment of the requirements
for the degree of Doctor of Philosophy

April 2014

## Abstract

This thesis presents work towards the first measurement of the mass of the W boson ($m_W$) at ATLAS at the Large Hadron Collider using $\sqrt{s} = 7$ TeV collision data taken in 2011. The electron energy calibration is presented, including a detailed study of the linearity of the ATLAS electromagnetic calorimeter. Separately, the measurement of the W boson recoil is calibrated using Z boson events. Recoil corrections for the underlying event, pileup, recoil magnitude resolution, recoil angular resolution and recoil response mismodelling are determined, with statistical uncertainties on these corrections corresponding to an estimated uncertainty on $m_W$ of 3.9 MeV. The corrections for calorimeter non-linearity and recoil modelling improve the description of the data, though systematic biases remain. To achieve a precision commensurate with the statistics of the data, these biases will need to be understood.

# Acknowledgements

I'd like to thank the STFC for funding my D.Phil and allowing me to spend 2 wonderful years on Long Term Attachment at CERN. I'd also like to thank Stephen Haywood, my RAL supervisor, who was always available for discussions and provided a lot of help and support and Chris Hays, my Oxford supervisor, who gave me detailed technical help and the benefit of his expertise from the CDF $m_W$ measurement. Maarten, Nenad and JB from the ATLAS W mass group also provided a lot of technical support. I also could not have completed my thesis without the help of the former residents of Rue de L'Athenee (and associates) who were much quicker than google in providing knowledge about ATLAS and programming. Geneva would also have been a lot less fun without them. Geneva would also have been a lot less fun without the LTA girls, especially Zoe, Clara, Ailsa and Lucy. I'd also like to thank the Reading girls (Mandy, Sam, Amy, Kirsty, Beks, Barney, Rochelle, George, Kate and Nicole) who always seemed to schedule a trip away just as I was reaching the end of my tether. Many members of Linacre college have helped me out and supported me over the years, but I'd especially like to thank Philippa, Frannie and Jen.

I would also like to thank my mum and dad, and Stewart who kept me sane during the writing up period.

# Contents


**1 Introduction** **1**
1.1 Overview of the $W$ boson mass measurement . . . . . 1
1.2 Contributions . . . . . 3

**2 Theoretical overview** **4**
2.1 The Standard Model . . . . . 4
2.2 Standard Model Lagrangian . . . . . 6
2.3 Electroweak theory . . . . . 6
2.4 Quantum Chromodynamics . . . . . 8
2.5 Electroweak Symmetry Breaking . . . . . 9
2.6 Problems with the Standard Model . . . . . 11
2.7 Proton collisions at the Large Hadron Collider . . . . . 13
2.8 $W$ production and decay at the Large Hadron Collider . . . . . 15
2.9 Radiative corrections . . . . . 17
2.10 Electroweak fits . . . . . 18
2.11 Recent measurements of $m_W$ . . . . . 19
2.12 Expectations for ATLAS measurement . . . . . 25

**3 The ATLAS Detector** **32**
3.1 Introduction . . . . . 32
3.1.1 The Large Hadron Collider . . . . . 32
3.2 Luminosity . . . . . 34
3.3 ATLAS detector requirements and specifications . . . . . 36
3.4 Magnets . . . . . 38
3.5 Inner Detector . . . . . 38
3.5.1 Pixel detector . . . . . 39
3.5.2 Semiconductor Tracker . . . . . 41
3.5.3 Transition Radiation Tracker . . . . . 41
3.6 Calorimetry . . . . . 42
3.6.1 Electromagnetic calorimeter . . . . . 42
3.6.2 Hadronic calorimeter . . . . . 44
3.7 Muon system . . . . . 45
3.8 Forward detectors . . . . . 48
3.9 Trigger . . . . . 48
3.9.1 The L1 trigger . . . . . 48
3.9.2 The High Level Trigger . . . . . 50

**4 Simulation and Reconstruction** **53**
4.1 ATLAS simulation framework . . . 53
4.2 Monte Carlo generation . . . 53
4.3 Detector simulation . . . 54
4.4 Data processing . . . 55
4.5 Particle identification . . . 56
4.6 Track reconstruction . . . 57
4.6.1 Inside-out tracking . . . 57
4.6.2 Outside-in tracking . . . 57
4.6.3 Vertex finding . . . 58
4.7 Calorimeter cluster reconstruction . . . 58
4.8 Jet reconstruction . . . 59
4.8.1 Theoretical requirements . . . 59
4.8.2 Jet algorithms . . . 59
4.8.3 ATLAS jet reconstruction . . . 60
4.9 Muon reconstruction . . . 60
4.9.1 Combined muon reconstruction . . . 62
4.9.2 Standalone muon reconstruction . . . 62
4.9.3 Segment tagged reconstruction . . . 63
4.10 Electron reconstruction . . . 63
4.10.1 Electron candidates . . . 63
4.10.2 Variables used for electron identification . . . 64
4.11 Triggers for the $W$ boson mass measurement . . . 69
4.11.1 Efficiency of medium electron selection . . . 70
4.11.2 Specialised $m_W$ trigger . . . 71
4.11.3 Rates . . . 76
4.11.4 Outcome . . . 78

**5 Electron energy calibration** **80**
5.1 Electron calibration overview . . . 80
5.2 Electron energy calculation . . . 80
5.3 Data-driven energy calibration . . . 82
5.4 Energy resolution . . . 83
5.5 Absolute energy scale . . . 84
5.6 $E/p$ fits . . . 86
5.7 Uniformity and linearity: $E/p$ template method . . . 88
5.7.1 Event selection . . . 89
5.7.2 Method . . . 89
5.7.3 Comparison with the convolution method . . . 96
5.7.4 Comparison with log likelihood method . . . 97

**6 Hadronic recoil for $W$ mass** **105**
6.1 Recoil overview . . . 105
6.2 Algorithm . . . 107
6.3 Recoil algorithm limitations . . . 110

6.4 Algorithm efficiency . . . 111
6.5 Performance . . . 117
6.6 Pileup and underlying event correction . . . 123
6.7 Jet energy resolution correction . . . 139
6.8 Jet angular resolution correction . . . 141
6.9 Iterating . . . 145
6.10 Response correction . . . 149
6.11 $\Sigma E_T$ reweighting . . . 153
6.12 Correlations between corrections . . . 157
6.13 Impact on the $m_W$ measurement . . . 163

**7 Conclusions** **167**

**References** **170**

# List of Figures


2.1 A proton-proton interaction at the Large Hadron Collider. . . . . 14
2.2 Feynman diagrams for W production. . . . . 16
2.3 One-loop corrections to the W mass. . . . . 18
2.4 $m_W$ indirect fit and experimental measurement. . . . . 19
2.5 68% and 95% confidence level contours in the $m_W$-$m_t$ plane. . . . . 20
2.6 Summary of the measurements of $W$ mass and their average (as of March 2012). 24

3.1 An Artist's view of the LHC and experiments. . . . . 33
3.2 Peak instantaneous luminosity delivered to ATLAS each day vs time in 2010, 2011 and 2012. . . . . 35
3.3 Cumulative luminosity delivered to and recorded by ATLAS in 2011 during stable beams. . . . . 36
3.4 Layout of the ATLAS detector. . . . . 37
3.5 The solenoid and the toroids of ATLAS. . . . . 38
3.6 The layout of the Inner Detector of ATLAS. . . . . 39
3.7 Cross-section of the ID, showing the coverage in $\eta$ of the Pixel detector, SCT and the TRT. . . . . 40
3.8 Layout of the ATLAS calorimetry. . . . . 42
3.9 Different samplings in the ATLAS Electromagnetic calorimeter. . . . . 43
3.10 Layout of the ATLAS muon chambers. . . . . 46
3.11 Schematic of the ATLAS trigger system. . . . . 49
3.12 Event Filter stream recording rates from 2011. . . . . 51
3.13 Event Filter stream recording rates from 2012. . . . . 52

4.1 A sketch showing how various particles interact with the detector. . . . . 56
4.2 A high-$p_T$ jet in the transverse plane of the ATLAS detector. . . . . 61
4.3 $R_\eta$ (the ratio of the cell energies in 3×7 and 7×7 windows) for data and Monte Carlo. . . . . 64
4.4 $R_{had}$ (the ratio of $E_T$ in all layers of the hadronic calorimeter to $E_T$ of the electron cluster) for data and Monte Carlo. . . . . 65
4.5 $\omega_{\eta 2}$ (Lateral width of the shower in $\eta$ weighted by the energy in the 2nd sampling) for data and Monte Carlo. . . . . 65
4.6 $E_{ratio}$ (ratio of the energy difference of the largest and second largest energy deposits in the first sampling of the calorimeter over the sum of those deposits) for data and Monte Carlo. . . . . 66
4.7 $\omega_{stot}$ (lateral width of the shower in strips in the 1st sampling) for data and Monte Carlo. . . . . 66

4.8 TRT High threshold hits ratio (Ratio of High Threshold hits in the TRT to the total number of hits in the TRT) for data and Monte Carlo. . . . . 67
4.9 $\Delta\eta$ (distance in $\eta$ between the extrapolated track and the cluster) for data and Monte Carlo. . . . . 67
4.10 Efficiency of the medium trigger used in 2011. . . . . 72
4.11 $R_\eta$ pre-data taking (G4.9.2) and after the simulation had been optimised (G4.9.4 new. geo.). . . . . 72
4.12 $\omega_{\eta 2}$ pre-data taking (G4.9.2) and after the simulation had been optimised (G4.9.4 new. geo.). . . . . 73
4.13 Efficiency of reconstruction of electrons as a function of $E_T$ with only the cut on $d_0$ applied. . . . . 74
4.14 Efficiency of reconstruction of electrons as a function of $E_T$ with only the cut on $E_{ratio}$ applied. . . . . 74
4.15 Efficiency of reconstruction of electrons as a function of $E_T$ with only the cut on $R_\eta$ applied. . . . . 75
4.16 Efficiency of reconstruction of electrons as a function of $E_T$ with only the cut on $\omega_{\eta 2}$ applied. . . . . 75
4.17 Efficiency of reconstruction of electrons as a function of $E_T$ with only the cut on $\omega_{stot}$ applied. . . . . 76
4.18 Efficiency of reconstruction of electrons of the medium trigger and the proposed mw trigger. . . . . 77
4.19 The statistical, systematic and total uncertainty on the scale factors as a function of $E_T$. . . . . 77
4.20 Efficiency of the Missing $E_T > 20$ GeV trigger as a function of $E_T$. . . . . 79

5.1 The ratio of reconstructed electron energy to the truth level electron energy in Monte Carlo. . . . . 87
5.2 The ratio of truth level electron momentum to the reconstructed electron momentum in Monte Carlo. . . . . 87
5.3 $E/p$ distribution showing data and Monte Carlo. . . . . 88
5.4 $E/p$ distribution showing data and Monte Carlo. Monte Carlo shown with nominal scaling, and with $\alpha$ of 0.97 and 1.03. . . . . 90
5.5 $\chi^2$ for each $\alpha$ for $0.1 < \eta < 0.2$ and 40 GeV $< E_T <$ 50 GeV. . . . . 91
5.6 Change in $\alpha$ with different upper bands on the fit range of the $E/p$ distribution for $0.1 < |\eta| < 0.2$. . . . . 92
5.7 Change in $\alpha$ with different lower bands on the fit range of the $E/p$ distribution for for $0.1 < |\eta| < 0.2$. . . . . 92
5.8 Change in $\alpha$ with change in range of $\alpha$ used in the polynomial fit to find the $\chi^2$ minimum for $0.1 < |\eta| < 0.2$. . . . . 93
5.9 $\chi^2$ for each $\alpha$ for $0.1 < \eta < 0.2$ and 40 GeV $< E_T <$ 50 GeV, with the momentum scale smearing applied to the $E/p$ distribution. Minimum of the fit shows the best fit $\alpha$ between data and MC. The range used to fit the parabola was 0.975-1.015. The fit is shown by the red line. . . . . 93
5.10 Smeared and nominal $E/p$ distribution for the optimal $\alpha$ correction found using the $\chi^2$ fits above for $0.1 < \eta < 0.2$ and 40 GeV $< E_T <$ 50 GeV. . . . 94

5.11 Change in $\alpha$ for nominal and smeared $E/p$ distributions for $0.1 < |\eta| < 0.2$. . 94
5.12 $\alpha$ for each $\eta$ and $E_T$ bin overlaid. . . . . 94
5.13 Uniformity of the calorimeter response modelling: Energy scale $\alpha$ for each $\eta$ bin for all electrons passing the selection. . . . . 96
5.14 Uniformity of the calorimeter response modelling: Energy scale $\alpha$ for each $\phi$ bin for all electrons passing the selection. . . . . 96
5.15 Linearity plots from the template method and the convolution method overlaid for $0 < |\eta| < 0.1$. . . . . 97
5.16 Linearity plots from the template method and the convolution method overlaid for $0.1 < |\eta| < 0.2$. . . . . 98
5.17 Linearity plots from the template method and the convolution method overlaid for $0.5 < |\eta| < 0.6$. . . . . 98
5.18 Linearity plots from the template method and the convolution method overlaid for $0.9 < |\eta| < 1$. . . . . 99
5.19 Linearity plots from the template method and the convolution method overlaid for $1.1 < |\eta| < 1.2$. . . . . 99
5.20 Linearity plots from the template method and the convolution method overlaid for $1.47 < |\eta| < 1.55$. . . . . 100
5.21 Linearity plots from the template method and the convolution method overlaid for $1.55 < |\eta| < 1.63$. . . . . 100
5.22 Linearity plots from the template method and the convolution method overlaid for $2 < |\eta| < 2.1$. . . . . 101
5.23 Linearity plots from the template method, the convolution method and the log likelihood method overlaid for $0 < |\eta| < 0.6$. . . . . 102
5.24 Linearity plots from the template method, the convolution method and the log likelihood method overlaid for $0.6 < |\eta| < 1$. . . . . 102
5.25 Linearity plots from the template method, the convolution method and the log likelihood method overlaid for $1 < |\eta| < 1.37$. . . . . 103
5.26 Linearity plots from the template method, the convolution method and the log likelihood method overlaid for $1.37 < |\eta| < 1.82$. . . . . 103
5.27 Linearity plots from the template method, the convolution method and the log likelihood method overlaid for $1.82 < |\eta| < 2.4$. . . . . 104

6.1 Diagram showing electron, neutrino and recoil in $W$ events . . . . . 106
6.2 Recoil from $Z \to ee$ events for data and POWHEG Monte Carlo. . . . . 109
6.3 $M_Z$ from $Z \to ee$ events for data and POWHEG Monte Carlo. . . . . 109
6.4 $M_Z$ from $Z \to \mu\mu$ events for data and POWHEG Monte Carlo. . . . . 110
6.5 $u_{parallel}$ distribution for all electrons (including those that only pass the probe selection) and only electrons that pass the tag selection for $Z \to ee$ events. . 112
6.6 $u_{parallel}$ distribution for electrons passing the background estimate selection and electrons passing the probe selection for $Z \to ee$ events. . . . . 113
6.7 Efficiency vs $u_{parallel}$ for data and Monte Carlo for $Z \to ee$ events. . . . . 114
6.8 Data efficiency divided by Monte Carlo efficiency fitted with a parameterisation for $Z \to ee$ events. . . . . 114

6.9 Data efficiency divided by Monte Carlo efficiency after the reweighting for $Z \to ee$ events. . . . 115
6.10 Data and Monte Carlo efficiency vs $u_{parallel}$ for $Z \to \mu\mu$ events. . . . 116
6.11 Data efficiency divided by Monte Carlo efficiency vs $u_{parallel}$ for $Z \to \mu\mu$ events. 116
6.12 $Z$ boson $p_T$ distribution for $Z \to ee$ events for data and POWHEG Monte Carlo. 118
6.13 $Z$ boson $p_T$ distribution for $Z \to \mu\mu$ events for data and POWHEG Monte Carlo. 118
6.14 Component of recoil parallel to the $Z$ boson $p_T$ for $Z \to ee$ events for data and POWHEG Monte Carlo. . . . 119
6.15 Component of recoil perpendicular to the $Z$ boson $p_T$ for $Z \to ee$ events for data and POWHEG Monte Carlo. . . . 119
6.16 Component of recoil parallel to the $Z$ boson $p_T$ for $Z \to \mu\mu$ events for data and POWHEG Monte Carlo. . . . 120
6.17 Component of recoil perpendicular to the $Z$ boson $p_T$ for $Z \to \mu\mu$ events for data and POWHEG Monte Carlo. . . . 120
6.18 Recoil response ($Z$ $p_T$/ -component of recoil parallel to the $Z$ boson) in $Z \to ee$ events for data and POWHEG Monte Carlo. . . . 121
6.19 Recoil response ($Z$ $p_T$/ -component of recoil parallel to the $Z$ boson) in $Z \to \mu\mu$ events for data and POWHEG Monte Carlo. . . . 121
6.20 Balance distribution (the component of the recoil parallel to the $Z$ $p_T$ added to the $Z$ $p_T$ after scaling the $Z$ $p_T$ for imperfect calorimeter response) for $Z \to ee$ events for data and POWHEG Monte Carlo. . . . 122
6.21 Balance distribution (the component of the recoil parallel to the $Z$ $p_T$ added to the $Z$ $p_T$ after scaling the $Z$ $p_T$ for imperfect calorimeter response) for $Z \to \mu\mu$ events for data and POWHEG Monte Carlo. . . . 122
6.22 Resolution of $u_\alpha$ in bins of $Z$ $p_T$ for $Z \to ee$ events for data and POWHEG Monte Carlo. . . . 124
6.23 Resolution of $u_\epsilon$ in bins of $Z$ $p_T$ for $Z \to ee$ events for data and POWHEG Monte Carlo. . . . 125
6.24 Mean of $u_\alpha$ in bins of $Z$ $p_T$ for $Z \to ee$ events for data and POWHEG Monte Carlo. . . . 126
6.25 Mean of $u_\epsilon$ in bins of $Z$ $p_T$ for $Z \to ee$ events for data and POWHEG Monte Carlo. . . . 127
6.26 Resolution of $u_\alpha$ in bins of $Z$ $p_T$ for $Z \to \mu\mu$ events for data and POWHEG Monte Carlo. . . . 128
6.27 Resolution of $u_\epsilon$ in bins of $Z$ $p_T$ for $Z \to \mu\mu$ events for data and POWHEG Monte Carlo. . . . 129
6.28 Mean of $u_\alpha$ in bins of $Z$ $p_T$ for $Z \to \mu\mu$ events for data and POWHEG Monte Carlo. . . . 130
6.29 Mean of $u_\epsilon$ in bins of $Z$ $p_T$ for $Z \to \mu\mu$ events for data and POWHEG Monte Carlo. . . . 131
6.30 Mean $\Sigma E_T$ as a function of $\mu$ for data and POWHEG Monte Carlo for $Z \to ee$ and $Z \to \mu\mu$ events combined. . . . 132
6.31 Mean $\Sigma E_T$ as a function of the number of vertices for data and POWHEG Monte Carlo for $Z \to ee$ and $Z \to \mu\mu$ events combined. . . . 133

6.32 Difference between Mean $\Sigma E_T$ as a function of $\mu$ for data and POWHEG Monte Carlo divided by the Monte Carlo gradient for both $Z \to ee$ and $Z \to \mu\mu$ events combined. . . . 134
6.33 Mean $\Sigma E_T$ as a function of $\mu$ for data, shifted data (to which the Monte Carlo is reweighted) and Monte Carlo for $Z \to ee$ events. . . . 135
6.34 Mean $\Sigma E_T$ as a function of $\mu$ for data, shifted data (to which the Monte Carlo is reweighted) and Monte Carlo for $Z \to \mu\mu$ events. . . . 135
6.35 Resolution of $u_\alpha$ for data and Monte Carlo before and after the $\mu$ reweighting is applied for $Z \to ee$ events. . . . 136
6.36 Resolution of $u_\alpha$ for data and Monte Carlo before and after the $\mu$ reweighting is applied for $Z \to \mu\mu$ events. . . . 137
6.37 Resolution of $u_\epsilon$ for data and Monte Carlo before and after the $\mu$ reweighting is applied for $Z \to ee$ events. . . . 138
6.38 Resolution of $u_\epsilon$ for data and Monte Carlo before and after the $\mu$ reweighting is applied for $Z \to \mu\mu$ events. . . . 138
6.39 Sum of $\chi^2$ values from $Z \to ee$ and $Z \to \mu\mu$ $u_\alpha$ and $u_\epsilon$ plots vs the underlying event correction used. . . . 139
6.40 Quadrature difference of data and MC $u_\alpha$ resolution as a function of the square root of $Z$ $p_T$ for $Z \to ee$ events . . . 140
6.41 Quadrature difference of data and MC $u_\alpha$ resolution as a function of the square root of $Z$ $p_T$ for $Z \to \mu\mu$ events . . . 140
6.42 Sum of $\chi^2$ values from $Z \to ee$ and $Z \to \mu\mu$ $u_\alpha$ plots as a function of the recoil magnitude correction. . . . 142
6.43 $\Delta\phi$ between $-p_T^Z$ and the recoil vector for data and Monte Carlo for $Z \to ee$ events. . . . 143
6.44 $\Delta\phi$ between $-p_T^Z$ and the recoil vector for data and Monte Carlo for $Z \to \mu\mu$ events. . . . 144
6.45 Sum of $\chi^2$ values from $Z \to ee$ and $Z \to \mu\mu$ $u_\epsilon$ plots as a function of the recoil phi correction used. . . . 144
6.46 Sum of $\chi^2$ values from $Z \to ee$ and $Z \to \mu\mu$ $u_\alpha$ and $u_\epsilon$ plots vs the underlying event correction used. . . . 146
6.47 Sum of $\chi^2$ values from $Z \to ee$ and $Z \to \mu\mu$ $u_\alpha$ plots vs the recoil magnitude correction used. . . . 147
6.48 Sum of $\chi^2$ values from $Z \to ee$ and $Z \to \mu\mu$ $u_\epsilon$ plots vs the recoil phi correction used. . . . 148
6.49 Resolution of $u_\alpha$ in $Z \to ee$ events as a function of $Z$ $p_T$ after the corrections for pileup and underlying event, recoil magnitude smearing and recoil $\phi$ smearing .149
6.50 Resolution of $u_\epsilon$ in $Z \to ee$ events as a function of $Z$ $p_T$ after the corrections for pileup and underlying event, recoil magnitude smearing and recoil $\phi$ smearing corrections. . . . 150
6.51 Resolution of $u_\alpha$ in $Z \to \mu\mu$ events as a function of $Z$ $p_T$ after the corrections for pileup and underlying event, recoil magnitude smearing and recoil $\phi$ smearing . . . 150

6.52 Resolution of $u_\epsilon$ in $Z \to \mu\mu$ events as a function of $Z$ $p_T$ after the corrections for pileup and underlying event, recoil magnitude smearing and recoil $\phi$ smearing corrections. . . . . 151
6.53 Recoil response ($Z$ $p_T$/ -component of recoil parallel to the $Z$ boson) in $Z \to \mu\mu$ events for data and POWHEG Monte Carlo. . . . . 152
6.54 Recoil response ($Z$ $p_T$/-component of recoil parallel to the $Z$ boson) in $Z \to ee$ events for data and POWHEG Monte Carlo. . . . . 152
6.55 Sum of the $\chi^2$ of plots of the mean of $u_\alpha$. . . . . 153
6.56 $u_\alpha$ distribution for data, uncorrected Monte Carlo (or no RW) and calibrated Monte Carlo (new RW) for $Z \to ee$ events. . . . . 154
6.57 $u_\epsilon$ distribution for data, uncorrected Monte Carlo (or no RW) and calibrated Monte Carlo (new RW) for $Z \to ee$ events. . . . . 154
6.58 $u_\alpha$ distribution for data, uncorrected Monte Carlo (or no RW) and calibrated Monte Carlo (new RW) for $Z \to \mu\mu$ events. . . . . 155
6.59 $u_\epsilon$ distribution for data, uncorrected Monte Carlo (or no RW) and calibrated Monte Carlo (new RW) for $Z \to \mu\mu$ events. . . . . 155
6.60 $\Sigma E_T$ for $Z \to ee$ events with $\mu < 6$ for data, Monte Carlo and Monte Carlo with the underlying event and pileup tune applied . . . . . 156
6.61 $\Sigma E_T$ for $Z \to \mu\mu$ events with $\mu < 6$ for data, Monte Carlo and Monte Carlo with the underlying event and pileup tune applied. . . . . 156
6.62 A profile of the reconstructed $\Sigma E_T$ as a function of the MC production level $\Sigma E_T$ for $Z \to ee$ and $Z \to \mu\mu$ Monte Carlo events. . . . . 157
6.63 $\Sigma E_T$ for $Z \to ee$ events with $\mu < 6$ for data, Monte Carlo and Monte Carlo with the $\Sigma E_T$ reweighting applied. . . . . 158
6.64 $\Sigma E_T$ for $Z \to \mu\mu$ events with $\mu < 6$ for data, Monte Carlo and Monte Carlo with the $\Sigma E_T$ reweighting applied. . . . . 158
6.65 $u_\alpha$ distribution for data, calibrated Monte Carlo and calibrated Monte Carlo with $\Sigma E_T$ reweighting for $Z \to ee$ events. . . . . 159
6.66 $u_\epsilon$ distribution for data, calibrated Monte Carlo and calibrated Monte Carlo with $\Sigma E_T$ reweighting for $Z \to ee$ events. . . . . 159
6.67 $u_\alpha$ distribution for data, calibrated Monte Carlo and calibrated Monte Carlo with $\Sigma E_T$ reweighting for $Z \to \mu\mu$ events. . . . . 160
6.68 $u_\epsilon$ distribution for data, calibrated Monte Carlo and calibrated Monte Carlo with $\Sigma E_T$ reweighting for $Z \to \mu\mu$ events. . . . . 160
6.69 $\chi^2$ as the constants used in the recoil magnitude smearing and the underlying event correction are varied. . . . . 161
6.70 $\chi^2$ as the constants used in the recoil $\phi$ smearing and the underlying event correction are varied. . . . . 162
6.71 $\chi^2$ as the constants used in the recoil $\phi$ smearing and the recoil magnitude smearing correction are varied. . . . . 162
6.72 $u_{parallel}$ for uncorrected MC, corrected MC with the nominal UE correction and with the correction $\pm 1$ standard deviation and data for $W \to e\nu$ events. 165
6.73 $u_{perpendicular}$ for uncorrected MC, corrected MC with the nominal UE correction and with the correction $\pm 1$ standard deviation and data for $W \to e\nu$ events. . . . . 165

6.74 $u_{parallel}$ for uncorrected MC, corrected MC with the nominal UE correction and with the correction $\pm 1$ standard deviation and data for $W \to \mu\nu$ events. 166
6.75 $u_{perpendicular}$ for uncorrected MC, corrected MC with the nominal UE correction and with the correction $\pm 1$ standard deviation and data for $W \to \mu\nu$ events. . . . . 166

# List of Tables


2.1 Particles of the Standard Model. . . . . 5
2.2 Combined total cross-section multiplied by branching ratio for $W^+$, $W^-$ and $W^\pm$ production. . . . . 15
2.3 Branching ratios for the $W$ boson. . . . . 16
2.4 Uncertainties on the combined result of $m_W$ from CDF using 2.2 fb$^{-1}$ of Run II data. . . . . 22
2.5 Uncertainties on the D0 measurement of $m_W$ using 4.3 fb$^{-1}$ of Run II data. . 23
2.6 Breakdown of systematic uncertainties affecting the ATLAS $m_W$ measurement, when using the $p_T^l$ distribution. . . . . 30
2.7 Breakdown of systematic uncertainties affecting the ATLAS $m_W$ measurement, when using the $m_T^W$ distribution. . . . . 31

4.1 Definition of variables used in electron identification . . . . . 68
4.2 Typical cuts on each variable for the loose, medium and tight selections for electrons with $25 < E_T < 32$ GeV and $0.1 < |\eta| < 0.6$. . . . . 69
4.3 Tag and probe selection for trigger studies. . . . . 71
4.4 Typical cuts on each variable for the loose, medium, tight and W mass selections for electrons with $25 < E_T < 32$ GeV and $0.1 < |\eta| < 0.6$. . . . . 78

5.1 $Z \to ee$ event selection for $E/p$ studies. . . . . 89
5.2 $W \to e\nu$ event selection for $E/p$ studies. . . . . 89
5.3 $\alpha$ for each $E_T$ (in GeV) and $|\eta|$ bin. . . . . 95

6.1 $Z \to ee$ event selection for recoil studies. . . . . 108
6.2 $Z \to \mu\mu$ event selection for recoil studies. . . . . 108
6.3 Best-fit values for the intercept tune constant with no other corrections applied. 136
6.4 Best-fit values for the recoil magnitude constant with only the initial intercept tune applied. . . . . 141
6.5 Best-fit values for the recoil $\phi$ smearing constant with the first tunes for the intercept and recoil magnitude smearing constant applied. . . . . 142
6.6 Best-fit values for the intercept tune constant with the best-fit values for the recoil magnitude and recoil $\phi$ smearing applied. . . . . 145
6.7 Best-fit values for the recoil magnitude smearing constant with the best-fit values for the intercept and recoil $\phi$ smearing applied. . . . . 145
6.8 Best-fit values for the recoil $\phi$ smearing constant with the best-fit values for the intercept tune and recoil magnitude smearing applied. . . . . 145
6.9 Best-fit values for the recoil response tune. . . . . 151

# Chapter 1

# Introduction

## 1.1 Overview of the $W$ boson mass measurement

When the Large Hadron Collider (LHC) began operation, the Higgs boson was the final piece of the Standard Model left undiscovered. Previous searches for the Higgs boson by the Tevatron and LEP experiments had failed to discover the particle, although they did succeed in excluding the boson having a mass below 114 GeV (LEP) [1] or a mass between 147 GeV and 180 GeV (Tevatron) [2]. Without the discovery of the Higgs boson, the Standard Model would be incomplete and have no explanation of the masses of the vector bosons in the context of gauge theories. Hence, discovering the Higgs boson was a principal aim of the two general purpose detectors at the LHC: ATLAS and CMS.

The LHC began colliding protons with a centre-of-mass energy of 7 TeV in March 2010. By the end of 2011, ATLAS and CMS had each collected 5 $\text{fb}^{-1}$ of data, yet neither had found an excess with the five sigma confidence level necessary to claim a discovery of the Higgs boson. With these data, ATLAS was able to exclude the mass regions of 112.9-115.5 GeV, 131-238 GeV and 251-466 GeV [3], whereas CMS excluded the region of 127-600 GeV [4]. In 2012, the centre-of-mass energy of the collisions at the LHC was increased to 8 TeV. On the 4th July 2012, ATLAS and CMS both announced the discovery of a previously un-

observed particle with a significance of over 5.9 standard deviations (ATLAS) [5] and 5.0 standard deviations (CMS) [6]. ATLAS measured the mass to be 126.0 ± 0.4 (stat.) ± 0.4 (syst.) GeV [5]. CMS measured it to be 125.3 GeV ± 0.4 ± 0.5 GeV [6]. The cross-section, couplings and spin of the boson are consistent with it being the Higgs boson [7].

Along with the Higgs boson, the $W$ boson, $Z$ boson and top quark are the most massive particles in the Standard Model. Interactions with the Higgs field allow elementary particles to gain mass. The direct measurement of the mass of the Higgs boson at the Large Hadron Collider has provided the final input parameter of the Standard Model, allowing a full assessment of the consistency of the Standard Model. The mass of the $Z$ boson is already known to sufficient precision, but reduction of the uncertainties on the masses of the Higgs, top and $W$ particles is necessary to further test the Standard Model, and to provide constraints on radiative corrections from unknown particles arising from extensions to the Standard Model, such as Supersymmetry [8] [9].

The world average measurement for the mass of the $W$ boson is $m_W = 80.385 \pm 0.015$ GeV [10]. This is a combination of measurements from LEP experiments (ALEPH, DELPHI, OPAL and L3) and from Tevatron experiments (CDF and D0). The CDF measurement has the lowest error of all the measurements by a single experiment with $m_W = 80.387 \pm 0.019$ GeV [11]. The largest uncertainties on the CDF and D0 experiments arose from lepton scale calibration, recoil calibration and parton density functions. As the Tevatron is also a hadron collider, I anticipate that the largest sources of error in the ATLAS measurement will also be from these sources. ATLAS aims for a final sensitivity of 7 MeV in each decay channel [12].

## 1.2 Contributions

Within this thesis, I discuss my contributions towards the first $W$ boson mass measurement by ATLAS at the Large Hadron Collider. This measurement will be performed using data from the 2011 run of the Large Hadron Collider only. Prospects for an $m_W$ measurement by ATLAS are also discussed here. Chapter 2 provides an overview of the Standard Model, and a discussion of the phenomenology of $W$ boson production at the Large Hadron Collider. A description of the Large Hadron Collider and the ATLAS detector is given in Chapter 3. Chapter 4 discusses the simulation, identification and reconstruction of events at the Large Hadron Collider and shows how the real-time data selection, or trigger, can bias the $W$ mass measurement. I propose a new trigger to minimise these biases.

Within Chapter 5, I discuss the electron calibration methods used by ATLAS and show my contributions to this effort. I also estimate the impact of my work on the $m_W$ uncertainty. Recoil calibration is discussed within Chapter 6, including my work on a new method of calibrating the recoil. I propose several corrections to the recoil measurement and evaluate the resulting uncertainties on $m_W$.

# Chapter 2

# Theoretical overview

## 2.1 The Standard Model

The Standard Model consists of fermions, with half-integer spin, and bosons, with integer spin [10]. In the fermion sector there are six leptons and six quarks. Each six are arranged into three generations, each with progressively higher mass but identical quantum numbers (other than flavour). Quarks can form baryons, which consist of three quarks (or antiquarks), or mesons which consist of one quark and one antiquark. Quarks and leptons show no evidence of internal structure at our current limit of resolution, which is approximately $10^{-18}$m [13]. Each quark and lepton (aside from neutrinos) has an antiparticle partner, with opposite charge and identical mass. It is not yet resolved whether neutrinos have antiparticle partners.

Each quark generation consists of one 'up-type' quark with a positive charge of $\frac{2}{3}$ (taking the proton as the unit of charge) and a 'down-type' quark with a negative charge of $\frac{1}{3}$. The up-type quarks in order of increasing mass are *up*, *charm* and *top*. The down-type, again in order of increasing mass, are *down*, *strange* and *bottom*. Protons consist of two up-quarks and one down-quark. Beyond distances of 1 fm, free quarks cannot exist. Instead, they are bound in 'colourless' singlet states.

| Particles | Symbols | Mass | Charge |
|---|---|---|---|
| **Quarks** | | | |
| up | $u$ | $2.3^{+0.7}_{-0.5}$ MeV | $+\frac{2}{3}$ |
| down | $d$ | $4.8^{+0.5}_{-0.3}$ MeV | $-\frac{1}{3}$ |
| charm | $c$ | $1.275 \pm 0.025$ GeV | $+\frac{2}{3}$ |
| strange | $s$ | $95 \pm 5$ MeV | $-\frac{1}{3}$ |
| top | $t$ | $173.07 \pm 0.52 \pm 0.72$ GeV | $+\frac{2}{3}$ |
| bottom | $b$ | $4.18 \pm 0.03$ GeV | $-\frac{1}{3}$ |
| **Leptons** | | | |
| electron | $e^-$ | 0.511 MeV | -1 |
| muon | $\mu^-$ | 106 MeV | -1 |
| tau | $\tau^-$ | $1776 \pm 0.2$ MeV | -1 |
| electron neutrino | $\nu_e$ | $< 2$ eV | 0 |
| muon neutrino | $\nu_\mu$ | $< 2$ eV | 0 |
| tau neutrino | $\nu_\tau$ | $< 2$ eV | 0 |
| **Gauge Bosons** | | | |
| photon | $\gamma$ | 0 | 0 |
| $W^\pm$ | $W^\pm$ | $80.385 \pm 0.015$ GeV | $\pm 1$ |
| $Z$ | $Z$ | $91.187 \pm 0.0021$ GeV | 0 |
| gluon | $g$ | 0 | 0 |
| Higgs | $H$ | $125.9 \pm 0.4$ GeV | 0 |

Table 2.1: Particles of the Standard Model. Mass and charges taken from [10]. Masses of the lighter quarks are not well determined. The top quark mass quoted is from direct measurements. Neutrino masses were measured indirectly from their oscillations.

Lepton generations consist of an electrically charged lepton and a neutrino. The pairs in increasing mass order are as follows: electron and electron neutrino, muon and muon neutrino, and tau and tau neutrino.

The boson sector consists of 4 types of gauge bosons, and the Higgs boson. The electromagnetic force is mediated by the photon, the weak force by the $W^+$, $W^-$ and $Z$ bosons and the strong force by 8 gluons. At the beginning of LHC operation, all of the above particles had been discovered and only the elusive Higgs boson remained. A principal aim of the LHC was therefore to find the Higgs boson and to measure its mass, spin, charge and coupling to decay products [14]. Gravity is not explained by the Standard Model, and is significantly weaker at the microscopic scale. Hence, the Standard Model describes only three of the four fundamental forces.

## 2.2 Standard Model Lagrangian

The Standard Model is a quantum gauge field theory and is renormalisable and mathematically self-consistent. The Lagrangian of the SM can be split into several terms, as follows in Equation 2.1:

$$\mathcal{L}_{SM} = \mathcal{L}_{EW} + \mathcal{L}_{QCD} + \mathcal{L}_{H} \tag{2.1}$$

## 2.3 Electroweak theory

Electroweak theory is a single relativistic quantum field theory that unites electromagnetism with the weak force [13]. It is an $SU(2) \times U(1)$ theory, where $SU(2)$ represents the weak isospin symmetry, and $U(1)$ represents the weak hypercharge symmetry. The electroweak Lagrangian can itself be split into two terms: a gauge term and a fermion term as shown in equation 2.2.

$$\mathcal{L}_{EW} = \mathcal{L}_{gauge} + \mathcal{L}_{fermion} \tag{2.2}$$

The gauge term is as follows in Equation 2.3 [15].

$$\mathcal{L}_{gauge} = -\frac{1}{4}\sum_{i=1}^{3} W^{i}_{\mu\nu} W^{i,\mu\nu} - \frac{1}{4} B_{\mu\nu} B^{\mu\nu}, \tag{2.3}$$

where

$$W^{i}_{\mu\nu} = \partial_\mu W^{i}_{\nu} - \partial_\nu W^{i}_{\mu} - g\epsilon^{ijk} W^{j}_{\mu} W^{k}_{\nu} \quad (\text{summation} \quad \text{over} \quad j,k = 1-3) \tag{2.4}$$

$$B_{\mu\nu} = \partial_\mu B_\nu - \partial_\nu B\mu \tag{2.5}$$

$W^{i}_{\mu}$ corresponds to the gauge field required to maintain the $SU(2)$ symmetry associated with weak isospin I, and $B^{i}_{\mu}$ represents the gauge field $U(1)$ of weak hypercharge $Y_W$. $g$ and $g'$ are the gauge couplings for weak isospin and weak hypercharge, respectively, and $\epsilon^{ijk}$ is the

Levi-Civita tensor [14].

The second term, $\mathcal{L}_{fermion}$, concerns the interactions of the fermions with the gauge bosons, which is described by the following equation (2.6).

$$\mathcal{L}_{Ferm} = i\bar{\psi}_L \not{D} \psi_L + i\bar{\psi}_{l_R} \not{D} \psi_{l_R} + i\bar{\psi}_Q \not{D} \psi_Q + i\bar{\psi}_{u_R} \not{D} \psi_{u_R} + i\bar{\psi}_{d_R} \not{D} \psi_{d_R} \tag{2.6}$$

Electroweak theory is a chiral theory, with left-handed and right-handed particles behaving differently under the same gauge group. All right-handed particles are isospin singlets, whereas all left-handed particles form doublets. $L$ represents the left-handed isospin doublets of charged leptons and neutrinos, and $Q$ represents the left-handed doublets of quarks. $l_R$, $u_R$ and $d_R$ represent the right handed singlets for charged leptons, up-type quarks $(u, c, t)$ and down-type quarks $(d, s, b)$. $\not{D}$ includes the actual interaction with the gauge fields and is denoted as follows:

$$\not{D} = \gamma^\mu (\partial_\mu + igI^i W_\mu^i + \frac{ig' Y B_\mu}{2}) \tag{2.7}$$

$I^i$ and $Y$ are the generators of the gauge groups in the representation of the fermions they act on. One can associate the $W^+$ and the $W^-$ with raising and lowering operations in the $SU(2)$ isospin group. The left-handed up-type (down-type) fermions are each a component of a doublet with isospin = $1/2$ $(-1/2)$, whereas the right-handed fermions have an isospin of 0 [16]. The weak hypercharge is related to the electric charge $Q$ by the Gell-Mann-Nishijima relation $Q = I^3 + \frac{Y}{2}$ [17] [18] [19]. $\not{D} = \gamma^\mu D_\mu$ where $\gamma^\mu$ are the Dirac matrices and $D_\mu$ is the covariant derivative. The Dirac matrices are a set of $4 \times 4$ conventional matrices with specific anticommutation relations [20].

The observed photon and $Z$ fields are derived from the orthogonal combination of the $W_\mu^3$ and $B_\mu$ fields, with the $W_\mu^3$ left over from the $SU(2)$ group, and the $B_\mu$ coming from the $U(1)$.

$$\begin{pmatrix} Z_\mu \\ A_\mu \end{pmatrix} = \begin{pmatrix} c_W & -s_W \\ s_W & c_W \end{pmatrix} \begin{pmatrix} W_\mu^3 \\ B_\mu \end{pmatrix} \tag{2.8}$$

This fixes the weak mixing angle $\theta_W$ and the electric charge $e$ as follows.

$$\cos(\theta_W) \equiv c_W = \sqrt{1 - s_W^2} = \frac{g}{\sqrt{g^2 + (g')^2}}, e = \frac{gg'}{\sqrt{g^2 + (g')^2}} \tag{2.9}$$

## 2.4 Quantum Chromodynamics

Quantum Chromodynamics or QCD is the theory of the strong nuclear force [15]. QCD is a non-abelian theory, resulting in interactions between the gluons. It is a renormalizable gauge theory based on the group $SU(3)$, which is associated with three 'coloured charges': *red*, *blue* and *green*. Its Lagrangian is as follows in Equation 2.10.

$$\mathcal{L}_{QCD} = -\frac{1}{4}\sum_{A=1}^{8} F^{A,\mu\nu} F^A_{\mu\nu} + \sum_{j=1}^{n_f} \bar{q_j}(i\not{D})q_j \tag{2.10}$$

The first sum is over the 8 gluon fields, whereas the second sum is over the quark fields, with $n_f$ different flavours.

$$F^A_{\mu\nu} = \partial_\mu G^A_\nu - \partial_\nu G^A_\mu - g_s C_{ABC} G^B_\mu G^C_\nu \quad (\text{summation} \quad \text{over} \quad B, C = 1 - 9) \tag{2.11}$$

$C_{ABC}$ represents the structure constants for $SU(3)$ and $g_s$ is the gauge coupling. $\alpha_s$ is the strong coupling constant, defined as 2.12:

$$\alpha_s = \frac{g_s^2}{4\pi} \tag{2.12}$$

The complete Standard Model combines the second term of the following equation with the terms in Equation 2.7.

$$D_\mu = \partial_\mu - ig_s \sum_A t^A g^A_\mu \tag{2.13}$$

$t^A$ are the $SU(3)$ group generators in the triplet representation of quarks, which obey the commutation relation $[t^A, t^B] = iC_{ABC}t^C$. As the $SU(3)$ group is non-Abelian with non-zero structure constants (like $SU(2)$), three-gluon couplings and four-gluon couplings can occur,

with orders $g_s$ and $g_s^2$ respectively.

The QCD Lagrangian leads to two important properties: confinement and asymptotic freedom. These occur since $\alpha_s$ is a running coupling and is a function of $Q^2$, the four momentum transferred in each interaction. Within a hadron, the colour charges of the quarks compensate for each other, resulting in a tightly-bound colourless state. Confinement refers to the impossibility of separating colour charges beyond $\approx 1$ fm. When coloured states are separated, the interaction potential increases until there is sufficient energy to produce a new quark-antiquark pair to form new colourless states.

## 2.5 Electroweak Symmetry Breaking

Everything described so far contains no mass terms. The introduction of mass terms involves an extension to the theory, if the theory is to remain gauge invariant. A Dirac mass term cannot be introduced as this would break gauge invariance as follows:

$$-m\bar{\psi}\psi = -m\psi^\dagger\lambda^0\psi = -m(\bar{\psi_L}\psi_R + \psi_R\psi_L) \tag{2.14}$$

The problem occurs as $\psi_L$ is an $SU(2)$ doublet, whereas $\psi_R$ is an $SU(2)$ singlet so their product is a doublet and therefore not $SU(2)$ invariant.

The Higgs term in the Lagrangian can be broken into two parts: the Higgs term itself and the fermion coupling to the Higgs. The Higgs term adds a longitudinal polarization state for the $W^0$, $W^-$ and $W^+$, which can be seen as follows.

$$\mathcal{L}_H = (D_\mu\Phi)^\dagger(D^\mu\Phi) - V(\Phi) \tag{2.15}$$

This equation extends the particle content of the Standard Model by a complex scalar $SU(2)_I$ doublet, $\Phi \equiv (\Phi^+, \Phi^0)^T$. It has weak hypercharge $Y_{W,\Phi}$ and four degrees of freedom in total.

Its self interaction can be described by

$$V(\Phi) = -\mu^2(\Phi^\dagger\Phi) + \frac{\lambda}{4}(\Phi^\dagger\Phi)^2 \tag{2.16}$$

The form of this equation is constrained by the necessity of it being gauge invariant and that the model be renormalizable. Renormalizability is guaranteed by having polynomial structure of degree $\leq 4$ in the field components. Gauge invariance is ensured by the $\Phi^\dagger\Phi$ form of the equation. This leaves only two real free parameters $\mu$ and $\lambda$ [14]. When $\mu^2 > 0$, the potential forms the shape of a Mexican hat and the minimum energy is not at $|\Phi| = 0$ but is instead at:

$$|\Phi| = \frac{v}{2}, v = 2\sqrt{\frac{\mu^2}{\lambda}} \tag{2.17}$$

Choosing the SU(2) basis such that the charged field and the imaginary part of the field have zero vacuum expection value, one can reparameterise $\Phi$ by splitting it into the field for the Higgs boson and the fields for three Goldstone bosons [21] [22] [23]. The non-vanishing vacuum expectation value, $v$, generates mass for the $W^+$, $W^-$ and $Z$ bosons. Due to the mixing of the electrically neutral fields, $W^3_\mu$ and $B_\mu$, eigenstates can be identified corresponding to the observed $Z$ boson and photon. With a suitable choice of gauge, the Goldstone boson fields are absorbed and become the longitudinal polarisation states of the $W^+$, $W^-$ and $Z$ bosons.

The Standard Model theory can be used to make several phenomenological predictions. A physical neutral spinless particle is postulated, i.e. the Higgs boson. It must be CP even, as it is a quantum excitation of the vacuum and therefore carries the vacuum quantum numbers. The ratio $\rho = \frac{M_W^2}{c_W^2 M_Z^2}$ must be equal to 1 at lowest order. The model predicts Higgs boson couplings to massive vector bosons proportional to $\frac{M_v^2}{v}$ because the Higgs couplings originate from the factor $(1 + \frac{H}{v})^2$ which multiplies the gauge boson mass term. Quartic couplings of two Higgs bosons and two gauge bosons are also predicted, as there is a square in the factor. Both triple and quartic Higgs self-couplings are predicted, proportional to $M_H$

and $M_H^2$ respectively [14].

All fermions can have Yukawa couplings to the Higgs doublet, the most general form of which is shown below in Equation 2.18.

$$\mathcal{L}_{Yuk.} = -\overline{\Psi}_L G_l \Psi_{l_R} \Phi - \overline{\Psi}_Q G_u \Psi_{u_r} \tilde{\Phi} - \overline{\Psi}_L G_d \Psi_{d_R} \Phi + h.c. \tag{2.18}$$

where $h.c.$ stands for hermitian conjugate and $\tilde{\Phi} = ((\Phi^0)^*, -\Phi^-)^T$, which has the opposite quantum numbers to the Higgs doublet. $G$ are 3×3 matrices, filled with complex numbers. At first glance, this implies that $\mathcal{L}_{Yuk}$ has lots of free parameters; however, most of these can be eliminated or do not have physical values [14].

$$\mathcal{L}_{Yuk.} = -\sum_f m_f (\bar{\Psi}_{f_L} \Psi_{f_R})(1 + \frac{H}{v}) + h.c \tag{2.19}$$

The non-diagonal elements of $G$ mix the left and right-handed components of the different $l$, $u$ and $d$ generations, i.e. a fermion would mix into a fermion of a different generation when propagating through space. This oscillation can be removed by transforming the current flavour basis, into a 'mass basis', using a unitary matrix. The overall result of this is that the $G_f$ matrices become diagonal in form, all fermion fields are replaced by fields in the mass basis, and the unitary matrix used for the transform appears in the Cabbibo-Koboyashi-Maskawa matrix [24] [25]. The coupling of the Higgs boson to fermions is equal to $\frac{m_f}{v}$. The Yukawa coupling strength to fermions should therefore be directly proportional to their mass [14].

## 2.6 Problems with the Standard Model

The Standard Model is not very satisfying as a complete theory, as it has such a large number of free parameters. These free parameters are the three gauge couplings ($g$, $g'$ and $g_s$), the strong CP-violating phase, six quark and three charged lepton masses, three CKM mixing angles, one CKM mixing phase and the mass of the Higgs boson and a weak gauge boson [26].

In addition to these 19 parameters, the discovery of neutrino oscillations adds extra parameters. A deficit of electron neutrinos arriving from the sun, called the 'solar neutrino problem', was first discovered at the Homestake experiment in the 1960's [27]. Sudbury Neutrino Observatory proved that this deficit arose from solar neutrino oscillations by measuring electron and muon neutrino fluxes at different times of day and night [28]. Atmospheric neutrino oscillations have were first measured by the Super Kamiokande experiment in 1998 [29]. This adds 7 extra parameters: three neutrino masses, three mixing angles and one CP-violating phase.

It is not expected to have such a large number of fundamental free parameters in the Standard Model. One way to reduce the number of parameters is to unify the electroweak and strong forces into one force [30]. These theories are known as Grand Unified Theories (GUT) [31]. The strong coupling constant decreases as energy increases, whereas the electroweak coupling constant increases. GUTs invoke mechanisms to make the coupling constants unify at a high scale ($10^{15} - 10^{16}$ GeV). The difference in strength at lower energy that we observe is explained by radiative corrections. All GUTs postulated so far introduce additional fields, interactions or extra dimensions of space.

The final remaining fundamental force, gravity, is not included in the Standard Model. The most successful theory of gravity, General Relativity, cannot be easily reconciled with quantum mechanics. Theories which attempt to incorporate gravity into the Standard Model are known as 'Theories of Everything'. String theories are perhaps the best candidates for such a theory, but they are not yet well enough understood to make experimental predictions.

Gravity affects elementary particle physics at the Planck scale ($\approx 10^{19}$ GeV) [32]. The Standard Model could be valid up to this cut-off. However, the Higgs boson receieves radiative corrections from all Standard Model particles and the scale of these corrections

is proportional to the cut-off of the model. If the Standard Model is valid up to the Planck scale, corrections can be many orders of magnitude larger than the Higgs mass itself and must be cancelled by the tree-level mass of the Higgs to obtain the 126 GeV we observe. Using two large numbers that cancel each other to fix a quantity to the observed value is known as 'fine tuning', and is considered undesirable. Supersymmetry is a theory that proposes that each Standard Model particle has a 'superpartner' with spin differing by a half-integer. It has been proposed as a solution to this problem, as the radiative correction of each supersymmetric particle can cancel the correponding Standard Model particle radiative corrections, removing the need for fine tuning [8] [9].

## 2.7 Proton collisions at the Large Hadron Collider

A diagram of a typical proton-proton interaction at the Large Hadron Collider can be seen in Figure 2.1 [33]. Protons consist of partons which can be quarks or gluons. The processes involved can be split into two types: hard and soft. Hard processes can be calculated with perturbation theory, whereas soft processes are sensitive to non-perturbative QCD effects and are less well understood [34]. The Figure shows a hard collision of two incoming partons, which can radiate on their incoming or their outgoing legs. Particles radiated from incoming legs are known as initial state radiation or ISR, whereas outgoing leg radiation is known as final state radiation or FSR. The remaining partons in the proton not involved in the collision undergo softer interactions, which form what is known as the 'underlying event'.

In order to calculate cross-sections at the Large Hadron Collider, factorisation is used to separate the parton-parton collision from the proton-proton collision. In a hard scattering process, a quark or a gluon from one proton scatters from a quark or a gluon in another proton. Hence, to calculate the cross-section one must know the fraction of momentum of the proton each quark or gluon has [35]. Experiments have measured these distributions and universal parton distribution functions, or PDFs, have been produced. One must also know

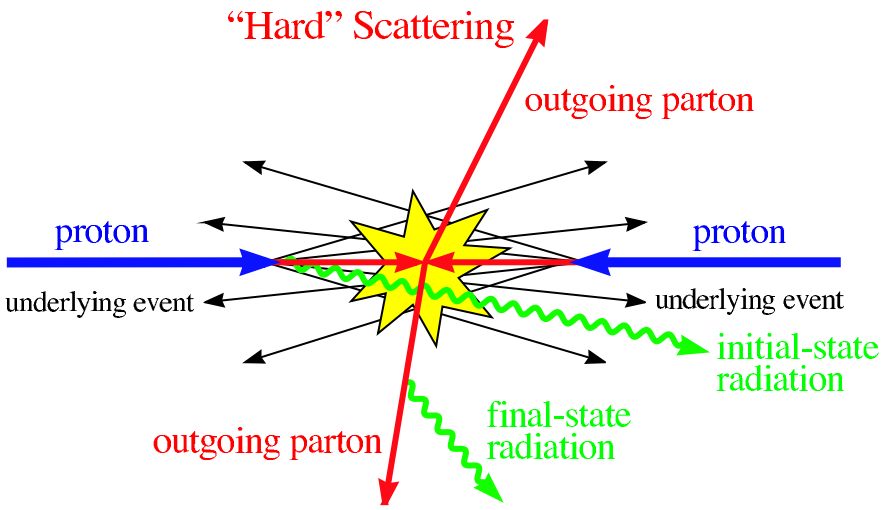



Figure 2.1: A proton-proton interaction at the Large Hadron Collider [33].

the hard scattering cross-section, which can be calculated at leading order (LO), next-to-leading order (NLO) or next-to-next-to-leading order (NNLO) in $\alpha_s$.

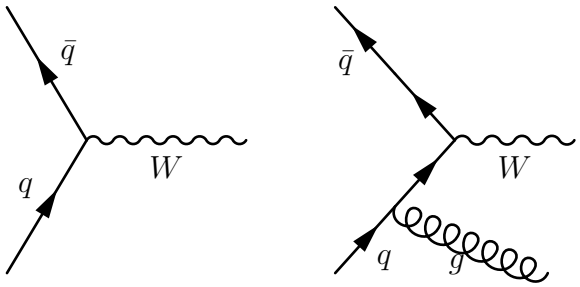
PDFs are calculated from a variety of data from hadron-hadron and lepton-hadron collisions, as they cannot be calculated easily from first principles. For the LHC, the main PDF sets used are CTEQ [36], MSTW [37] and NNPDF [38]; each is produced by a different collaboration and uses a slightly different collection of datasets. PDF sets are calculated consistently to a particular order in $\alpha_s$, with PDF sets available at LO, NLO and NNLO. The difference between cross-sections calculated at different orders is known as the $k$-factor and is useful when calculating QCD corrections [14]. PDFs are calculated for each hadron and are different for valence and sea quarks. Valence quarks are those that give rise to the quantum numbers of the hadron, whereas sea quarks are the virtual quark-antiquark pairs that arise from gluon splitting. The virtual quarks and anti-quarks quickly annihilate another to form a gluon again. The constant flux of gluon creation and gluon splitting within a hadron is known as the 'sea'. PDF's cannot be calculated for collisions with low energy transfer, but the evolution of PDF's with respect to energy transfer can be calculated using QCD.

| $\sigma_W^{tot}$.BR( $W \to l\nu$ ) [nb] | | | | | |
|---|---|---|---|---|---|
| | | stat. | syst. | lum. | acc. |
| $W^+$ | 6.048 | $\pm$0.016 | $\pm$0.072 | $\pm$0.206 | $\pm$0.096 |
| $W^-$ | 4.160 | $\pm$0.014 | $\pm$0.057 | $\pm$0.141 | $\pm$0.083 |
| $W^\pm$ | 10.207 | $\pm$0.021 | $\pm$0.121 | $\pm$0.347 | $\pm$0.164 |

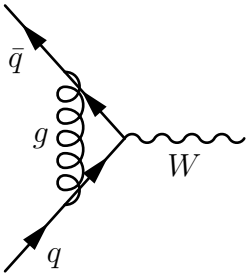
Table 2.2: Combined total cross-section multiplied by branching ratio for $W^+$, $W^-$ and $W^\pm$ production with statistical (stat.), systematic (syst.), luminosity (lum.) and extrapolation (acc.) uncertainties (from extrapolating to the full phase space), as measured by ATLAS from data collected in 2010 [40].

## 2.8 $W$ production and decay at the Large Hadron Collider

$W$'s can decay to hadrons ($W \to u\bar{d}$ and $W \to s\bar{c}$). They also decay in the following ways: $W \to e\nu$, $W \to \mu\nu$ and $W \to \tau\nu$. The hadronic decay mode dominates due to the fact that each quark can have three possible colours. The $W$ boson branching ratios can be seen in Table 2.3. The Large Hadron Collider is a proton-proton collider, and therefore $W$ boson production is dominated by valence-sea and sea-sea collisions of $u\bar{d}$ and $d\bar{u}$ [39]. Feynman diagrams showing $W$ production at the LHC at various orders in $\alpha_s$ can be seen in Figure 2.2. Collisions of $s\bar{c}$ and $c\bar{s}$ sea quarks are also possible, which provide the next largest contribution of 17% of the total cross-section for $W^+$ and 23% for $W^-$. Collisions of $u\bar{s}$ etc. are Cabibbo suppressed. The $W$ boson cross-section was measured by ATLAS in 2010 and can be seen in Table 2.2 [40]. The theoretical cross-sections used in this paper were generated at NNLO by the Monte Carlo generator MC@NLO [41] using the CTEQ6.6 PDF set. The calculated theoretical cross-section for $W^+$ is 6.16 $\pm$ 0.31 nb and for $W^-$ is 4.30 $\pm$ 0.21 nb. $Z$ production at the LHC is dominated by $u\bar{u}$ and $d\bar{d}$, with lesser contributions arising from $s\bar{s}$ and $c\bar{c}$ (the smallest contribution). The sea quark contributions are larger at the LHC than at the Tevatron. The $W/Z$ cross section ratio was measured to be 11.7 $\pm$ 0.9 (stat.) $\pm$ 0.4 (syst.) during early data taking [42].




(a) LO (b) NLO




(c) NNLO

Figure 2.2: Feynman diagrams for W production at Leading Order, Next to Leading Order and Next to Next to Leading Order at the LHC.

| Mode | Fraction |
|---|---|
| $e\nu$ | $10.75 \pm 0.13$ % |
| $\mu\nu$ | $10.57 \pm 0.15$ % |
| $\tau\nu$ | $11.25 \pm 0.20$ % |
| hadrons | $67.60 \pm 0.27$ % |

Table 2.3: Branching ratios for the $W$ boson [10].

## 2.9 Radiative corrections

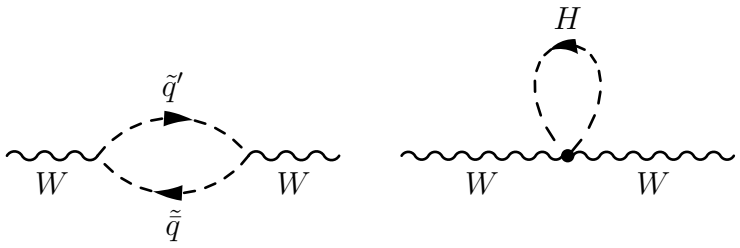
The Fermi weak coupling, $G_F$, can be expressed in terms of the $W$ boson mass ($m_W$), the $Z$ boson mass ($m_Z$) and the electromagnetic coupling ($\alpha_{EM}$) at the renormalisation energy scale ($Q = m_Z c^2$). $G_F$ can be derived from the muon lifetime formula. This can be inverted to determine $m_W$ in terms of the other parameters of the Standard Model (in the 'on-shell' scheme), as follows in Equation 2.20.

$$m_W^2 = \frac{\hbar^3}{c} \frac{\pi \alpha_{EM}}{\sqrt{2} G_F (1 - m_W^2/m_Z^2)(1 - \Delta R)} \tag{2.20}$$

$\Delta R$ includes all radiative corrections [43].

Within the Standard Model, two different types of loop corrections contribute to $m_W$: fermionic and boson loops. One-loop and two-loop and three-loop corrections have been evaluated, as well as four-loop fermionic corrections (which were found to be small) [44]. Fermionic loops increase $m_W$, with contributions proportional to $\ln(m_Z/m_f)$ for $m_f << m_Z$ [45]. Top and bottom quarks do not satisfy this condition and have a large mass spliting within their isospin doublet. As a result, $m_W$ has a quadratic dependence upon $m_t$. Higgs loops have a smaller contribution and decrease $m_W$ by terms proportional to $\ln(m_H)$.

In supersymmetric extensions to the Standard Model, squark loops contribute and tend to increase $m_W$. Slepton and additional Higgs loops also contribute. In the MSSM, the leading one-loop contribution arises from the stop-sbottom doublet [44]. The total radiative correction from supersymmetric loops can be as large as several hundred MeV, and therefore the $W$ boson mass can provide constraints on SUSY models. Existing $m_W$ measurements already provide a constraint on the SUSY mass scale of $M_{\tilde{f}} < 800$ GeV (assuming the current experimental central value for $m_t$) [44]. Higher precision measurements of $m_W$ can provide stringent upper limits on the mass of the stop and sbottom [46]. Figure 2.3 shows Feynman diagrams the one-loop corrections to the W mass from Supersymmetry and the Higgs boson.




(a) Supersymmetry (b) Higgs

Figure 2.3: One-loop corrections to the W mass from (a) Supersymmetry and (b) the Higgs boson.

## 2.10 Electroweak fits

Including the value of $m_H$ in a fit to electroweak measurements has allowed indirect determination of Standard Model parameters. The indirect measurement of $m_W$ now exceeds the experimental measurement in precision (Equation 2.21) [47].

$$\begin{aligned} m_W = (80.3593 \pm 0.0056_{m_t} \pm 0.0026_{M_Z} \pm 0.0018_{\Delta\alpha_{had}} \\ \pm 0.0017_{\alpha_S} \pm 0.0002_{m_H} \pm 0.0040_{theoretical})\,\text{GeV} \\ = (80.359 \pm 0.011_{tot})\,\text{GeV} \end{aligned} \tag{2.21}$$

The largest uncertainty arises from the error on the top mass, followed by the theoretical uncertainty (arising from the calculation of the hadronic radiative corrections). $m_H$ contributes a relatively small uncertainty (when compared to the current error on the mass of the Higgs boson) due to the weak logarithmic dependence of $m_W$ on this measurement.

The deviation between the value of $m_W$ obtained from the fit, and the direct measurements by experiments can be seen in Figure 2.4. This deviation is found to be $1.2\sigma$, not significant at the current level of precision. A more precise direct determination of the $W$ mass is therefore desirable in order to probe for new physics. Reduced errors on $m_t$ and improved theoretical uncertainties, arising from calculations with higher-order corrections,

will help reduce the error in the indirect result, allowing the validity of the Standard Model at the electroweak scale to be evaluated.

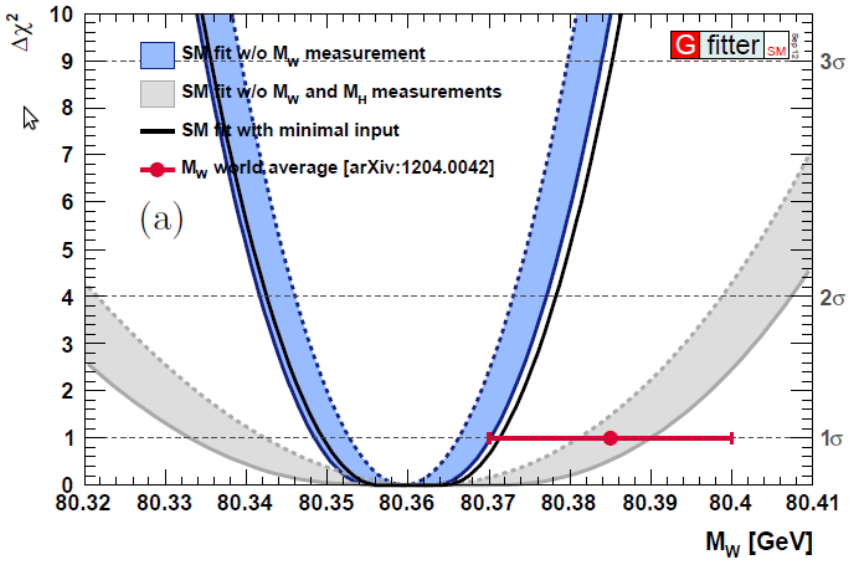



Figure 2.4: $m_W$ indirect fit and experimental measurement. The fit, including $m_H$ as an input parameter, is shown in blue (dark band), whereas the fit without is shown in grey (lighter band). The dotted lines show the fit with theoretical uncertainties set to 0. The black solid line shows the SM prediction using a minimal set of parameters. The red marker shows the current world average of the direct measurement of $m_W$ [47].

A simultaneous indirect fit of $m_W$ and $m_t$, both with and without $m_H$ included, is also performed. As can be seen in Figure 2.5, the direct measurements and indirect measurements show good agreement, providing confidence in the consistency of the Standard Model. The lack of a significant discrepancy means contributions from new physics are not apparent and limits can be placed on their parameters.

## 2.11 Recent measurements of $m_W$

In hadron colliders, $p_z(\nu)$ cannot be reconstructed. This is due to the fact that the energy of the incoming partons is unknown, and energy of the decay products in the $z$ direction is predominantly lost down the beampipe or in the uninstrumented highly forward region. The momentum of a neutrino can only be measured in the transverse plane, and is inferred from the momentum imbalance in the event, known as 'missing $E_T$' or $\not{E}_T$. Therefore,

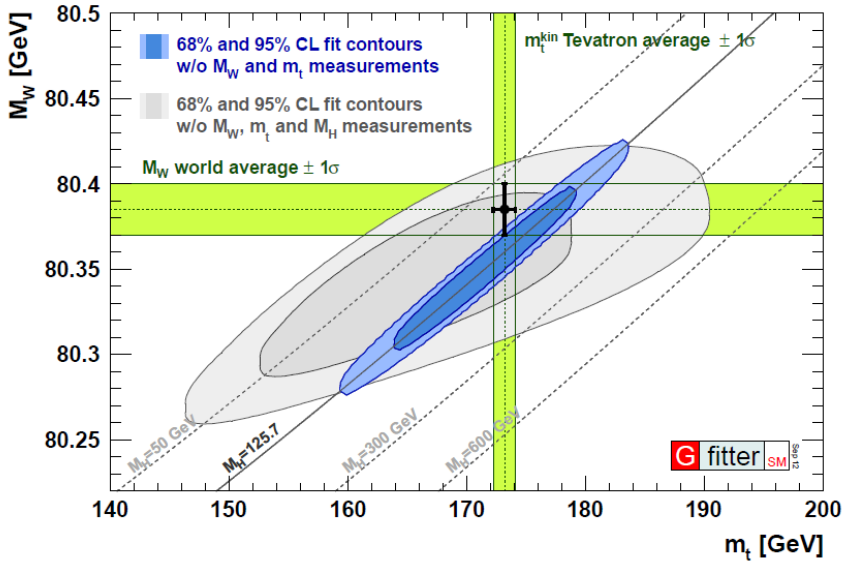



Figure 2.5: 68% and 95% confidence level contours in the $m_W$-$m_t$ plane. Direct measurements of $m_W$ and $m_t$ were excluded from the fit. Values of the direct measurements are shown with horizontal and vertical green bands showing one standard deviation. Dashed lines show predictions for different values of $m_H$ [47].

measurements of $m_W$ use the transverse mass, shown in Equation 2.22:

$$m_T^W = \sqrt{2p_T^l p_T^\nu (1 - cos(\phi^l - \phi^\nu))} \tag{2.22}$$

$m_T^W$ is relatively insensitive to the production dynamics of the boson but does depend on an accurate measurement of the recoil energy of the boson, which is used to calculate the neutrino transverse momentum. Lepton $p_T$ can also be used to measure the $W$ boson mass, as it reduces the dependence on the neutrino $p_T$ measurement, which generally has poor resolution. However, the shape of the lepton $p_T$ distribution is sensitive to the transverse motion of the $W$ boson, and therefore $W$ boson production dynamics must be fully understood. Generally, both measurements are made in order to cross-check each other and to reduce systematics.

The most recent measurements of $m_W$ were performed at the Tevatron by the CDF and D0 experiments [48] [11]. The Tevatron is a proton-antiproton collider based at the Fermi National Accelerator Laboratory, which operated between 1986 and 2011. This operation

period was split into three runs: Run 0, Run I and Run II. CDF's most recent measurement of $m_W$ is in both electron and muon channels and uses 2.2 fb$^{-1}$ of data collected between 2002 and 2007 [11]. D0's latest measurement was performed using only the electron channel and uses 4.3 fb$^{-1}$ of data collected between 2006 and 2009 [49].

The CDF result comes from a combination of 6 observables: $m_T^{\mu}$, $E_T^{\mu}$, $\not\!\!E_T{}^{\mu}$,$m_T^{e}$, $E_T^{e}$ and $\not\!\!E_T{}^{e}$ [11]. $Z$ bosons, and $J/\Psi$ and $\Upsilon$ mesons were used to set the absolute momentum scale of the tracker. The momentum measured in the tracker was compared with energy measured in the calorimeter to transfer this scale to the calorimeter, using $Z$ and $W$ boson events. The calorimeter energy was divided by the momentum measured in the tracker resulting in a variable called $E/p$. The simulated energy scale in the calorimeter was set such that the peak matched the data. The resolution of the calorimeter was measured using the widths of the $E/p$ peak and the $Z \to ee$ mass peak. Two $Z$ boson mass measurements were made as a consistency check using $Z \to \mu\mu$ events from tracker information alone and $Z \to ee$ events from calorimeter energy alone. Both of these measurements were consistent with the world average value of the $Z$ boson mass.

In general, when $W$ or $Z$ bosons are produced in a hadron collider, they have a non-zero transverse momentum caused by the recoil against ISR jets. The recoil is calculated using the vector sum of transverse energy over all calorimeter towers, with towers associated to the lepton removed. In $Z \to ll$ events, the recoil must be equal to the dilepton momentum, by conservation of momentum. Hence, $Z$ boson events are used to calibrate the mean and the resolution of the recoil distributions. The calibration is performed on two axes, along the measured boson $p_T$ and perpendicular to this axis. Understanding the recoil is necessary to accurately measure $p_T^{\nu}$ from W decays and to model the shape of the $m_T$ peak.

The CDF combined result from both electron and muon channels is $M_W = 80387 \pm 12(stat.) \pm 15(syst.)$ MeV. The uncertainties on this result can be seen in Table 2.4. The

| Source | Uncertainty (MeV) |
|---|---|
| **Experimental** | |
| Lepton energy scale and resolution | 7 |
| Hadronic recoil energy scale and resolution | 6 |
| Lepton removal | 2 |
| Backgrounds | 3 |
| **Production** | |
| Parton distributions | 10 |
| QED radiation | 4 |
| $p_T(W)$ model | 5 |
| **Statistical** | |
| $W$ boson statistics | 12 |

Table 2.4: Uncertainties on the combined result of $m_W$ from CDF using 2.2 fb$^{-1}$ of Run II data [11].

largest experimental uncertainties arise from lepton energy scale and resolution, and hadronic recoil energy scale and resolution.

The D0 result uses only the two most sensitive observables: $m_T^e$ and $p_T^e$ [49]. The absolute energy scale in the tracker was calibrated using only $Z \to ee$ events, correcting to the world average measurement for $M_Z$. $E/p$ was not used in this measurement as the electromagnetic calorimeter had a far superior resolution in comparison to the D0 tracking and muon systems. The amount of material in front of the electromagnetic calorimeter is determined by studying the longitudinal energy profile in the calorimeter. The electron energy is corrected for energy lost in this material. The recoil is tuned using $Z \to ee$ events, along the axes parallel and perpendicular to the dilepton momentum.

The D0 measurement is equivalent to a measurement of the ratio of the $Z$ and $W$ boson masses and the precision is limited by the size of the $Z$ boson dataset. D0 measures a $W$ boson mass of $m_W = 80367 \pm 13(stat.) \pm 22(syst.)$ MeV. The uncertainties on the D0 result can be seen in Table 2.5. The largest experimental uncertainty arises from electron energy calibration (due to the calibration being performed with $Z \to ee$ events only) and the second largest is hadronic recoil energy scale and resolution.

| Source | Uncertainty (MeV) |
|---|---|
| **Experimental** | |
| Electron energy calibration | 16 |
| Electron resolution model | 2 |
| Electron shower modelling | 4 |
| Hadronic recoil energy scale and resolution | 5 |
| Electron efficiencies | 1 |
| Backgrounds | 2 |
| **Production** | |
| Parton distributions | 11 |
| QED radiation | 7 |
| $p_T(W)$ model | 2 |
| **Statistical** | |
| $W$ boson statistics | 13 |

Table 2.5: Uncertainties on the D0 measurement of $m_W$ using 4.3 fb$^{-1}$ of Run II data [49].

Older measurements were also used in the world average. The measurements made in Run 0 and Run Ia were updated to use newer parton density function sets. However, as all PDF sets used are similar, uncertainties arising from PDF sets are assumed to be partially correlated [48]. The original measurements use differing values for the $W$ boson width. This has been corrected for and the uncertainties due to the $W$ boson width are therefore taken to be 100% correlated across all measurements. Uncertainties from QED radiative corrections from purely theoretical sources are considered to be correlated. The combined measurement from all Tevatron results is $m_W = 80387 \pm 16$ MeV.

LEP-II provides a $W$ boson mass measurement determined from $WW$ production [50]. It is assumed there are no correlations with Tevatron measurements. LEP-II performed two different measurements of the W boson mass : a threshold measurement and a direct reconstruction measurement. As LEP is an electron-positron collider, the cross-section for $e^+e^- \rightarrow W^+W^-$ can be measured as a function of centre-of-mass energy. When LEP was operating close to the threshold of $W^+W^-$ production, the cross-section was sensitive to the $W$ boson mass. The mass was measured by this method in two channels: $W \rightarrow qql\nu$ and $W \rightarrow qqqq$. At higher energies, as the energy of the colliding particles is known, the $W$ boson invariant mass can be reconstructed precisely from the observed jets and leptons.

The threshold result from LEP has a large statistical uncertainty, but small systematic uncertainty. The direct reconstruction result statistical uncertainty is slightly larger than the systematic uncertainty. The largest systematic errors arise from the jet energy scale, fragmentation and uncertainty on the energy of the electron-positron collisions. LEP provides a combined $W$ boson mass measurement of $m_W = 80.376 \pm 0.033$ GeV [50].

A combination of the results from all Tevatron runs and the LEP results, assuming no correlations between the Tevatron and LEP uncertainties, results in a world average $W$ boson mass measurement of $M_W = 80385 \pm 15$ MeV [48] [11]. A summary of the $W$ boson mass measurements and their average can be seen in Figure 2.6.

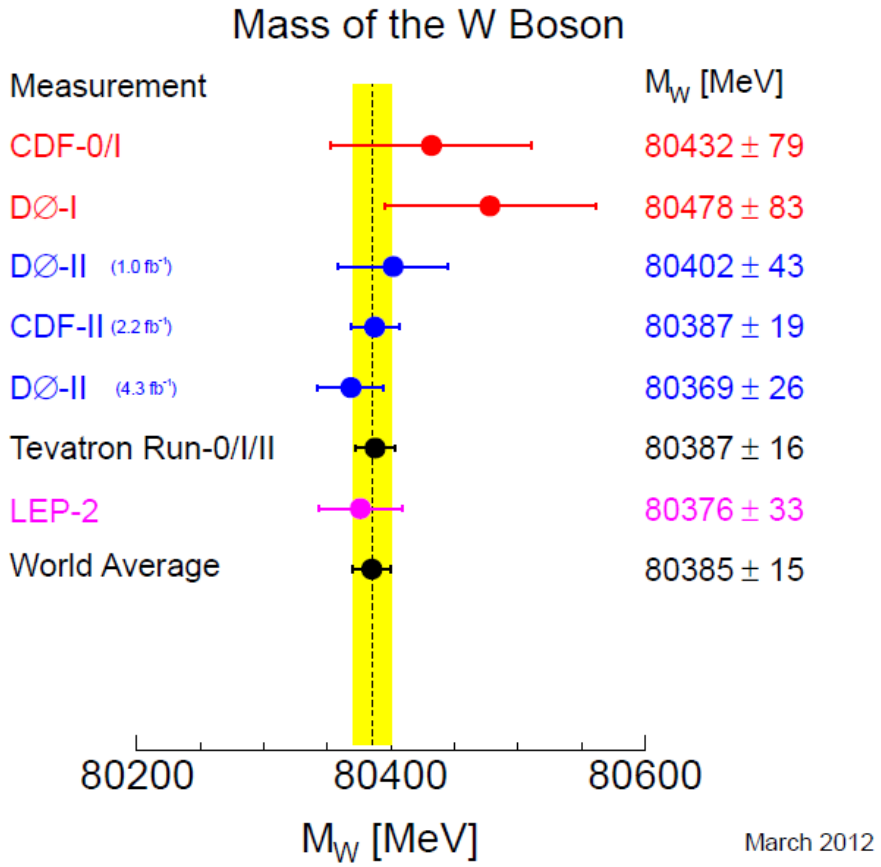



Figure 2.6: Summary of the measurements of $W$ mass and their average (as of March 2012). The world average is a combination of the Tevatron and LEP-II results, assuming no correlations between the Tevatron and LEP results [48].

## 2.12 Expectations for ATLAS measurement

The ATLAS measurement of the mass of the $W$ boson will use both electron and muon channels and will measure $p_T^l$, $\not{E}_T$ and $m_T^W$ [12]. Electrons will be measured using both the calorimeter and the inner detector of ATLAS, and the muon channel will use the inner detector. $m_W$ will be extracted by comparing the data to a series of 'template distributions' obtained from generating $W$ boson events with different boson mass parameters in the generation. $\chi^2$ tests will be used to compare the data to each template. The $\chi^2$ is defined as follows [12]:

$$\chi^2 = \Sigma_i \frac{(n_i^{obs} - n_i^{exp})^2}{\sigma_i^2} \tag{2.23}$$

Where $n_i^{exp}$ is the number of events in each bin of the template distribution, $n_i^{obs}$ is the number of events in the data in each bin $i$ of the fitting distribution, $\sigma_i$ is the uncertainty on $n_i^{exp}$ and the sum is over all bins in the fitting window. This is a Gaussian approximation and can be used as the $W$ boson mass analysis has such large statistics. The $\chi^2$ is plotted as a function of the value of $m_W$ and a parabola is fitted to the distribution. The minimum of the parabola provides the $W$ boson mass.

The ATLAS measurement will use $Z$ bosons to calibrate the energy scales of the leptons and the recoil. Template histograms will be produced from $Z$ boson events smeared and recalibrated with different energy-scale factors and resolutions. $\chi^2$ tests will be performed, forming a two-dimensional grid as a function of the scale and smearing parameters. The average resolution parameter $\sigma$ and the average mass scale $\alpha$ can be applied to all leptons via smearing and reweighting procedures. However, this method only provides an energy scale averaged over the $p_T^l$ distribution found in $Z$ boson events, which differs from that found in $W$ boson events. Hence, an energy-dependent scale must also be found, where the templates and data are classified as a function of lepton energy and the procedure is repeated.

$m_W$ has a strong dependence on the error on the average absolute energy scale, $\alpha_l$. A fractional uncertainty on $\alpha_l$ gives a fractional uncertainty on $m_W$. A series of toy measurements (simulations varying the value of $\alpha$) also found a strong dependence, as can be seen in Equation 2.24, where $\partial_{rel}\alpha_l$ is the fractional uncertainty [12].

$$\frac{\partial m_W}{\partial_{rel}\alpha_l} \approx 800 \text{ MeV}/\% \tag{2.24}$$

If the scale is energy dependent, the uncertainty on $m_W$ can be found by injecting random energy-dependent decalibrations in the pseudodata. The scale induced uncertainty on $m_W$ was found to be $\delta m_W(\alpha_l) = 4$ MeV [12]. $m_W$ also has a small dependence on the resolution, $\sigma_l$ as follows (Equation 2.25).

$$\frac{\partial m_W}{\partial_{rel}\sigma_l} = 0.8 \text{ MeV}/\% \tag{2.25}$$

There will also be energy-scale variations as a function of lepton pseudorapidity. However, as the rapidity distributions are expected to be similar (difference of $< 5$ %) for $W$ and $Z$ boson events within the detector acceptance, the absolute scale in each pseudorapidity bin can be found using $Z$ events and applied to the $W$ events.

An overconstrained measurement can also be performed. First, the inner detector (ID) scale is measured using $Z$ boson, $J/\psi$ and $\Upsilon$ meson events in muon final states. The ID scale can be transported to the calorimeters using the $E/p$ distribution with isolated electrons. The $Z$ boson and $J/\psi$ meson mass peaks in the electron final states are then used to cross-check the calorimeter energy scale. This method is similar to the CDF measurement.

The $p_T^l$ distributions will also reflect any energy dependence of the reconstruction efficiency. To measure this reconstruction efficiency in data, a method called 'tag and probe' will be used in $Z$ boson events. Two leptons are selected, one well identified and the other with a looser selection. To ensure they are $Z$ boson events, leptons with an invariant mass greater than 10 GeV from the $Z$ boson mass are rejected. The efficiency is calculated by

finding the fraction of events for which the second loosely identified lepton passes the final lepton selection. Events can be reweighted to account for any dependence of reconstruction efficiency on $p_T^l$ but it is also desirable to minimise this dependence to reduce systematic errors. The measurement of $m_W$ was most sensitive to any slope in the reconstruction efficiency as a function of $E_T$. The slope must be understood to a high level of precision, as defined by the following equation (where $\partial_{rel}b$ is the relative error on the slope) [12]. In this equation, the efficiency has been measured using tag and probe with $2 \times 10^5 Z$ boson decays, and scale factors have been applied to the $p_T$ distribution to compensate for the inefficiency. When calculating the error given below, it is assumed that with 10 $fb^{-1}$ of data, there has been a factor of 4 improvement in the efficiency determination. If templates are made assuming no $p_T$ dependence in the lepton reconstruction efficiency, the $m_W$ distribution is biased by 450 MeV.

$$\frac{\partial m_W}{\partial_{rel} b} = 4 \text{ MeV}/\% \tag{2.26}$$

The recoil calibration will be performed by comparing the measured recoil to the dilepton momentum in $Z$ boson events (as there should be no significant $\not\!\!E_T$ ), with the lepton calibration discussed in the previous paragraphs applied. As $W$ and $Z$ bosons are produced in similar partonic processes, the recoil is expected to behave similarly. Both the absolute scale, $\alpha_{rec}$ and the resolution, $\sigma_{rec}$ must be tuned. $E_T^{miss}$ is formed from the vector sum of the recoil and the lepton in the event. By using pseudodata samples with different recoil scales and fitting these samples to perfectly calibrated templates, the effect on $m_W$ is as follows in equations 2.27 and 2.28 (where $\partial_{rel}\alpha_{E_T^{miss}}$ and $\partial_{rel}\sigma_{E_T^{miss}}$ are the relative errors on the scale and resolution of the $E_T^{miss}$, which has been found by adding the leptons and recoil vectorially) [12]. The minus signs indicate that the change in recoil scale and resolution results in a fit to the $W$ mass that is less than the true value of $m_W$.

$$\frac{\partial m_W}{\partial_{rel}\alpha_{E_T^{miss}}} = -200 \text{ MeV}/\% \tag{2.27}$$

$$\frac{\partial m_W}{\partial_{rel}\sigma_{E_T^{miss}}} = -25 \text{ MeV}/\% \tag{2.28}$$

There are also several theoretical uncertainties that can affect the $W$ boson mass measurement. The shape of the peak will be affected if there is a change in the $W$ boson width $\Gamma_W$. The error due to the width will be calculated by producing templates with widths varying between 1.7 and 2.5 GeV , where the current world average at the time this estimation was made for the width is $\Gamma_W = 2.085 \pm 0.042$ GeV [51]. Measurements at the LHC will reduce the uncertainty on the $W$ width. An improvement of a factor of five has been assumed when calculating the systematic.

QED final-state radiation can also affect the lowest-order $p_T$ spectrum of leptons from $W$ boson decays. In the electron channel, the majority of the energy from FSR will be reconstructed in the same calorimeter energy cluster as the electron. However, the muon momentum will be measured independently of any photon radiation. A program called PHOTOS generates the radiative corrections in the decay of any resonances [52]. Within the program, it is possible to switch between several theoretical assumptions of photon emission, and therefore varying these assumptions allows an error on the FSR to be calculated.

Depending on the parton distribution function used, the $W$ rapidity distribution can vary, resulting in differences in acceptance. Measurements by ATLAS will also improve the PDF sets; these include the $W$ charge asymmetry [53] and $W + c$ quark production cross-section measurements [54]. An improvement of by a factor of 30 on the error on the Z rapidity distribution is assumed, following ATLAS measurements.

Another crucial input for the $W$ boson mass analysis is the $p_T^W$ distribution. The $p_T^{ll}$ distribution from $Z$ boson events can be used to predict the $p_T^W$ distribution, using a theoretical model of the ratio of $p_T^W$ to $p_T^Z$. ATLAS has also measured the $p_T^W$ distribution directly [55].

Errors arising from the $p_T^W$ distribution are calculated by applying scaling factors to $p_T^W$ distributions and modelling the corresponding mass fit distributions. The bias is estimated by fitting these distributions with undistorted templates.

The $W$ boson mass is measured in electron and muon channels as they benefit from low backgrounds. However, there is a small background from $W \to \tau(\to l\nu\nu)\nu$ events, $Z \to ll$ events (where one lepton is not reconstructed) and $Z \to \tau(\to l\nu\nu)\tau$ events. The $W \to \tau\nu$ background is irreducible. QCD dijet events will also contribute to the background, but the identification requirements on the leptons reduce the contribution from jets to a minimum. Systematic uncertainties on the background will be found by varying the background shapes within their uncertainties and refitting $m_W$.

Additional proton-proton collisions known as pileup can contribute extra soft hadronic activity to the event. This can result in additional calorimetric energy in the region of the electron signal which can affect the electron scale measurement. The muon scale should not be affected. However, as the additional hadronic activity can be measured in areas of the event away from high-$p_T$ objects in data with sufficient accuracy, this should result in a small impact on $p_T^l$. Small changes in the beam crossing angle may also result in a systematic shift in $p_x$ or $p_y$ of the particles produced. However, most of this effect is averaged out by rotational symmetry of the ATLAS detector.

There are systematic uncertainties arising from the backgrounds to the $W$ signal. The following backgrounds are considered : $W \to \tau\nu$, $Z \to ll$, $Z \to \tau\tau$ and jet production. The uncertainty on background due to jet production is assumed to be far smaller than at the Tevatron experiments due to the superior granularity and resolution of the ATLAS electromagnetic calorimeter.

Tables 2.6 and 2.7 show the breakdown of the expected systematic uncertainties affecting

| **Source** | **Effect** | $\partial m_W/\partial_{rel}\alpha$ (MeV/%) | $\delta_{rel}\alpha$ (%) | $\delta m_W$ (MeV) |
|---|---|---|---|---|
| Production Model | $W$ boson width | 1.2 | 0.4 | 0.5 |
| | $y^W$ distribution | - | - | 1 |
| | $p_T^W$ distribution | - | - | 3 |
| | QED radiation | - | - | $< 1$ |
| Lepton measurement | Scale & linearity | 800 | 0.005 | 4 |
| | Resolution | 1 | 1.0 | 1 |
| | Efficiency | - | - | 4.5($e$) , <1 ($\mu$) |
| Recoil measurement | Scale | - | - | - |
| | Resolution | - | - | - |
| Backgrounds | $W \to \tau\nu$ | 0.15 | 2.5 | 2.0 |
| | $Z \to l(l)$ | 0.08 | 2.8 | 0.3 |
| | $Z \to \tau\tau$ | 0.03 | 4.5 | 0.1 |
| | Jet events | 0.05 | 10 | 0.5 |
| Pile-up and U.E | | | | <1($e$), ≈0($\mu$) |
| Beam crossing angle | | | | <0.1 |
| Total($p_T^l$) | | | | ≈7($e$),6($\mu$) |

Table 2.6: Breakdown of systematic uncertainties affecting the ATLAS $m_W$ measurement, when using the $p_T^l$ distribution. Table taken from an evaluation of the LHC potential for $m_W$ performed pre-data taking [12]. If there is a cut on recoil in the event selection used for $p_T^l$, there will be a dependence on recoil and the associated uncertainty should be added to this table. The improved systematic uncertainties when compared to the CDF and D0 experiments arise from the large number of $Z$ bosons available for calibration, assumed improvements to the parton distribution functions and $W$ width from ATLAS measurements and the improved granularity and resolution of the ATLAS calorimeters. The errors arising from parton distribution functions are included in the estimate of the error from the $W$ rapidity distribution.

the measurement of $m_W$ using the $p_T^l$ distribution and using the $m_T^W$ distribution respectively. The resulting total systematic uncertainty on the final measurement is estimated to be between 6 and 8 MeV. The improved systematic uncertainties when compared to the CDF and D0 experiments arise from the large number of $Z$ bosons available for calibration, assumed improvements to the parton distribution functions and $W$ width from ATLAS measurements and the improved granularity and resolution of the ATLAS calorimeters.

| **Source** | **Effect** | $\partial m_W/\partial_{rel}\alpha$ (MeV/%) | $\delta_{rel}\alpha$ (%) | $\delta m_W$ (MeV) |
|---|---|---|---|---|
| Production Model | $W$ boson width | 3.2 | 0.4 | 1.3 |
| | $y^W$ distribution | - | - | 1 |
| | $p_T^W$ distribution | - | - | 1 |
| | QED radiation | - | - | $< 1$ |
| Lepton measurement | Scale & lin. | 800 | 0.005 | 4 |
| | Resolution | 1 | 1.0 | 1 |
| | Efficiency | - | - | 4.5($e$) , <1 ($\mu$) |
| Recoil measurement | Scale | -200 | - | - |
| | Resolution | -25 | - | - |
| | Combined | - | - | 5 |
| Backgrounds | $W \to \tau\nu$ | 0.11 | 2.5 | 1.5 |
| | $Z \to l(l)$ | -0.01 | 2.8 | 0.2 |
| | $Z \to \tau\tau$ | 0.01 | 4.5 | 0.1 |
| | Jet events | 0.04 | 10 | 0.4 |
| Pile-up and U.E | | | | <1($e$), ≈0($\mu$) |
| Beam Crossing Angle | | | | <0.1 |
| Total($p_T^l$) | | | | ≈8($e$),7($\mu$) |

Table 2.7: Breakdown of systematic uncertainties affecting the ATLAS $m_W$ measurement, when using the $m_T^W$ distribution. Table taken from an evaluation of LHC potential for $m_W$ performed pre-data taking [12]. The improved systematic uncertainties when compared to the CDF and D0 experiments arise from the large number of $Z$ bosons available for calibration, assumed improvements to the parton distribution functions and $W$ width from ATLAS measurements and the improved granularity and resolution of the ATLAS calorimeters. The errors arising from parton distribution functions are included in the estimate of the error from the $W$ rapidity distribution.

# Chapter 3

# The ATLAS Detector

## 3.1 Introduction

### 3.1.1 The Large Hadron Collider

The Large Hadron Collider was designed to collide proton beams with an unprecedented luminosity of $10^{34}$ cm$^{-2}$ s$^{-1}$ and energy of 14 TeV [56]. It is installed in a 26.7 km circular tunnel at CERN, near Geneva, Switzerland. It consists of two rings with counter rotating beams. As the tunnel was already built for LEP, there was a hard limit on space, hence a twin bore magnet design was adopted, which consists of two sets of coils and beam channels within the same mechanical structure and cryostat.

At nominal luminosity, there are 2808 bunches per proton beam collected into trains of bunches. In 2011, the number of colliding bunches varied between 1 and 1400. When trains collide, the bunch collisions occur every 50 ns in 2011. At nominal luminosity, the bunch collisions would occur every 25 ns. Crossing-angle orbit bumps separate the two beams upstream and downstream of the experimental regions to prevent parasitic collisions on either side of the nominal interaction points in the centre of the experiments. Four main experiments are situated around the ring: ATLAS, CMS, LHCb and ALICE. There are also two

smaller experiments, TOTEM and LHCf. A schematic showing the layout of the LHC can be seen in Figure 3.1.

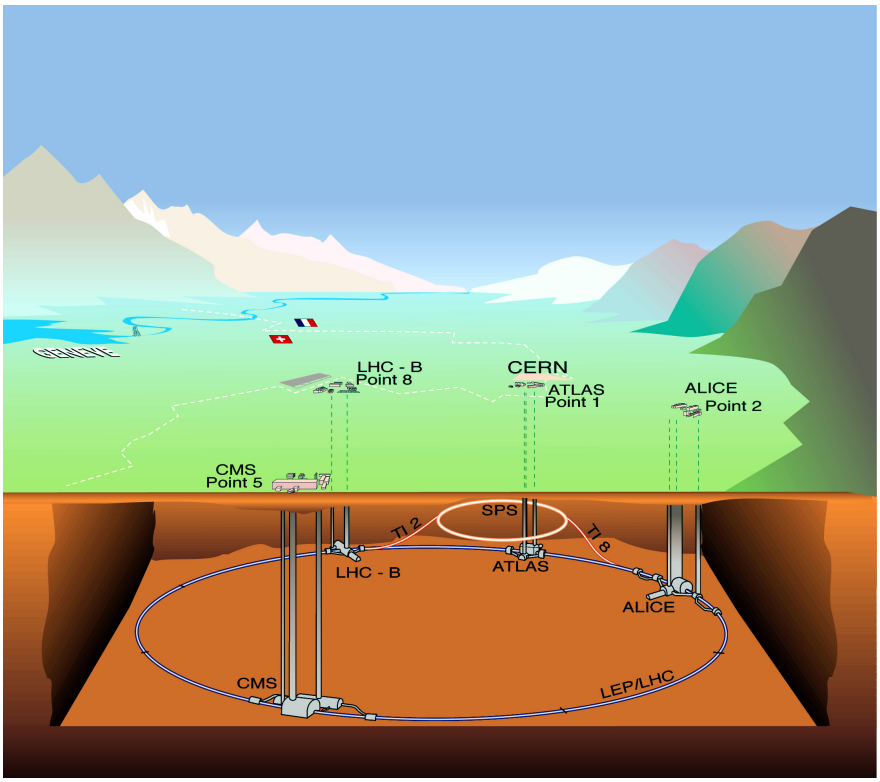



Figure 3.1: An Artist's view of the LHC and experiments [57].

The ring consists of 8 arcs and 8 straight sections, where the experiments and utilities are inserted [58]. ATLAS and CMS are located in straight sections opposite from each other on the ring. The beam injection takes place at the experimental points where LHCb and ALICE are located. The beams can only cross at these four straight sections. Two of the remaining four sections are used to collimate the beam. Another straight section contains the RF systems that are used to accelerate the beam. The final straight section is used to dump the beam. The arc sections contain dipoles, to bend the beam, and quadrupoles, which focus the beam. The magnets are cooled to 1.9 K by superfluid helium, and provide a maximum magnetic field of 8.3 T.

The proton bunches for the LHC are first accelerated in a linear accelerator before being injected into a synchrotron known as the proton synchrotron (PS) booster, which accelerates

them from 50 MeV to 1.4 GeV [59]. They pass from the PS booster into the PS where they are accelerated further to 26 GeV and adjusted to the required bunch spacing. The beams are injected into the super proton synchrotron (SPS), where they are accelerated to 450 GeV and the bunches are matched to the LHC buckets. Finally, the LHC receives the bunches and takes approximately 20 minutes to accelerate them from 450 GeV to a momentum of 7 TeV. For data taken in 2011, each beam was accelerated to 3.5 TeV.

## 3.2 Luminosity

Instantaneous luminosity is calculated using the following equation, where two bunches each with $n_1$ and $n_2$ particles collide with frequency $f$ [10]:

$$\mathcal{L}_{inst.} = f\frac{n_1 n_2}{4\pi\sigma_x\sigma_y} \tag{3.1}$$

$\sigma_x$ and $\sigma_y$ are the horizontal and transverse beam widths. In 2010, the peak luminosity delivered by the LHC was $\mathcal{L}_{peak} = 2.0 \times 10^{32}$ cm$^{-2}$ s$^{-1}$, which increased to $\mathcal{L}_{peak} = 3.6 \times 10^{33}$ cm$^{-2}$ s$^{-1}$ in 2011 [60]. An increase in the number of bunches crossing in the LHC and an increased instantaneous luminosity per bunch-crossing led to this rise. The increased instantaneous luminosity was achieved by increasing the typical number of protons in each bunch from $0.9\times10^{11}$ in 2010 to $1.2\times10^{11}$ in 2011 [60]. The peak instantaneous luminosity delivered to ATLAS each day can be seen in Figure 3.2. The average beam width in x and y in 2011 is approximately 0.025 mm and approximately 60mm in z.

The instantaneous luminosity at the LHC is measured in several different ways [60]. One is known as event counting, where bunch crossings are characterised according to whether an inelastic proton-proton collision has occured. This method is less useful when there is likely to be more than one inelastic collision per bunch crossing. In this instance, hit counting is used, where the number of detector channels with a readout higher than a defined threshold is counted. In finely segmented subdetectors, particle counting algorithms are also used,

when the number of particles entering that subdetector are counted.

Another way to determine the luminosity is known as a Van der Meer (vdM) scan, which is performed by sweeping beams transversely across each other to measure the beam widths, with the other beam parameters being fixed. The luminosity can be calculated directly from these beam parameters using the above equation. In ATLAS, the vdM scans are used to calibrate the event counting, hit counting and particle counting methods. 5 sets of vdM scans were performed in 2010 and 2 in 2011. Generally two scans are performed at the same time with the same beam parameters, one with the beams separated in $x$ and another with the beams separated in $y$. LUCID is a subdetector that also provides an independent measurement of the luminosity, as discussed later in this chapter.

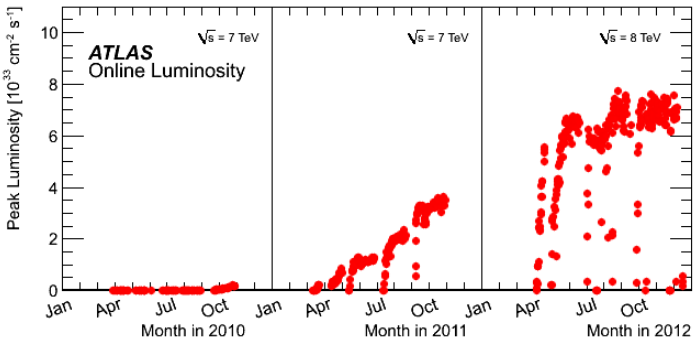



Figure 3.2: Peak instantaneous luminosity delivered to ATLAS each day vs time in 2010, 2011 and 2012 [61].

Integrated luminosity is defined as the instantaneous luminosity integrated over time, and can be used to predict the expected number of events at a particular cross-section, $\sigma_{exp}$, as shown in Equation 3.2 [10].

$$N_{exp} = \sigma_{exp} \int \mathcal{L}_{inst} dt \tag{3.2}$$

The LHC delivered 5.46 fb$^{-1}$ of data to ATLAS in 2011, of which 5.08 fb$^{-1}$ were successfully recorded. The cumulative luminosity delivered to ATLAS over time in 2011 can be seen in Figure 3.3. Half the total integrated luminosity of 2011 was recorded in the last two months

of the year.

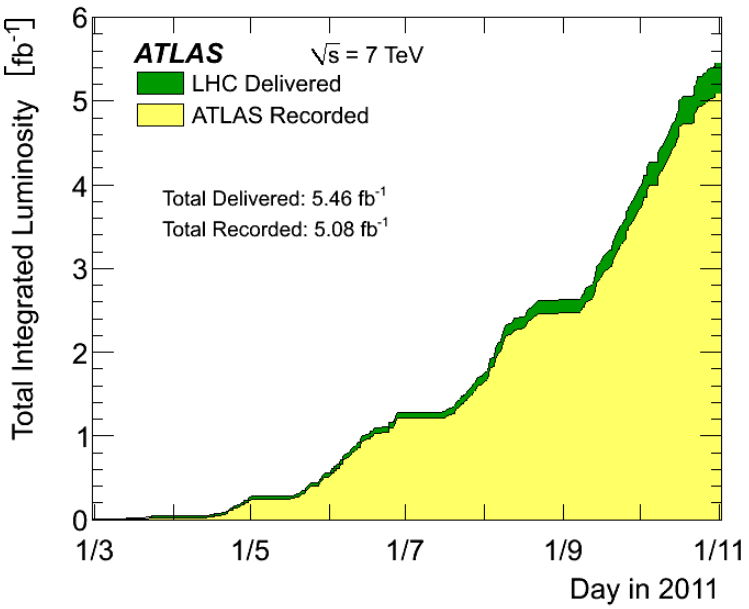



Figure 3.3: Cumulative luminosity delivered to and recorded by ATLAS in 2011 during stable beams [61].

## 3.3 ATLAS detector requirements and specifications

Firstly, we must define the coordinate systems used within the detector. The beam direction defines the $z$-axis [56]. The positive $x$-axis points from the interaction point to the centre of the LHC ring, and the positive $y$-axis is defined as pointing upwards. The polar angle $\theta$ is the angle from the $z$-axis. Pseudorapidity describes the angle of a particle relative to the beam axis and is given by the equation:

$$\eta = -\ln\left[\tan\left(\frac{\theta}{2}\right)\right] \tag{3.3}$$

Pseudorapidity is preferred to using $\theta$ itself as particle production is approximately constant as a function of rapidity. Changes in pseudorapidity are Lorentz invariant. The term 'forward' is used to describe particles with a large pseudorapidity, meaning they are close to the beam axis. The azimuthal angle is measured in the $x$-$y$ plane around the beam axis. A variable known as $\Delta R$ combines the $\eta$ and $\phi$ measurements as follows in Equation 3.4.

$$\Delta R = \sqrt{\Delta\eta^2 + \Delta\phi^2} \tag{3.4}$$

The ATLAS detector consists of 3 sets of detectors: the Inner Detector (ID), the calorimeters and the Muon Spectrometer (MS). The ID is further subdivided into three subdetectors: the Pixel detector, the Semiconductor Tracker (SCT), and the Transition Radiation Tracker (TRT). There are two calorimeters: the Electromagnetic Calorimeter(ECal) and the Hadronic Calorimeter (HadCal). The layout of the detector can be seen in figure 3.4.

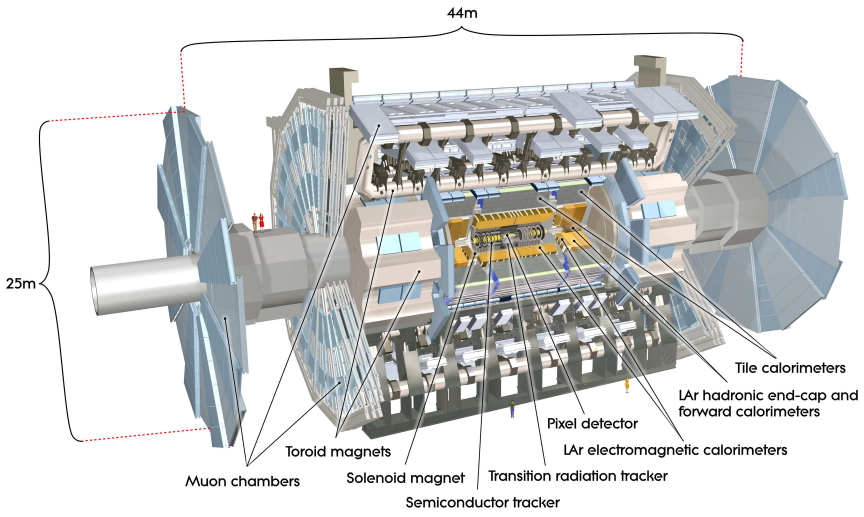



Figure 3.4: Layout of the ATLAS detector [56].

Detector components and electronics must be fast to handle the high data rate and be radiation-hard in order to survive the large integrated luminosities produced by the LHC. The ID must have good momentum resolution and include a vertex detector so that the secondary vertices of $b$-jets can be observed. The calorimetry must extend over the full azimuthal region and have a large acceptance in pseudorapidity to allow missing transverse-energy measurements to be made, with minimal losses in the forward regions. The electromagnetic calorimetry is designed to identify and measure electrons and photons and have excellent energy resolution. Likewise, the MS identifies muons and measures their momentum. Finally, a highly efficient trigger is necessary to select only events with potentially interesting final states and reduce the rate to a level that can be recorded offline.

## 3.4 Magnets

The ATLAS magnet system is split into two different types: a solenoid, surrounding the ID and the toroids, embedded in the MS. Both types of magnet are superconducting. The solenoid generates a 2 T field along the beam axis in the ID, causing charged particles to curve, allowing the measurement of momentum. It shares a cryostat with the ECal. A 0.5 T field is generated by the toroid in the central region of the muon detectors, and a 1 T field in the endcap region. This field circulates azimuthally around the beam axis, within the volume defined by the coils [56]. The layout of the magnets can be seen in Figure 3.5.

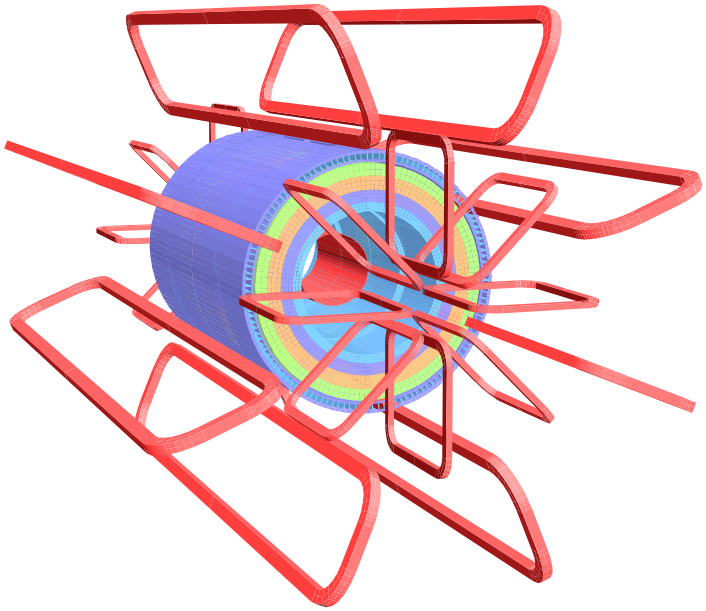


Figure 3.5: The solenoid (innermost central cylinder) and the toroids (outer red loops) of ATLAS. The outermost cylinders in the centre represent the tile calorimeter, which is depicted by four layers with differing magnetic properties [56].

## 3.5 Inner Detector

The ATLAS Inner Detector consists of three subdetectors, the innermost of which is the Pixel detector, followed by the SCT, then the TRT which is the outermost. The layout can be seen in Figure 3.6. For high momentum tracks, the ID has an impact parameter resolution of $22.1 \pm 0.9$ $\mu$m and a relative momentum resolution of $\frac{\sigma_p}{p} = (4.83 \pm 0.16) \times 10^{-4}$ GeV$^{-1}$ $\times$

$p_T$ [62]. The fitting of tracks in the Inner Detector is discussed in the following chapter. The excellent momentum resolution of the Inner Detector is used in the $m_W$ analysis to calibrate the Electromagnetic calorimeter, which measures electron $E_T$.

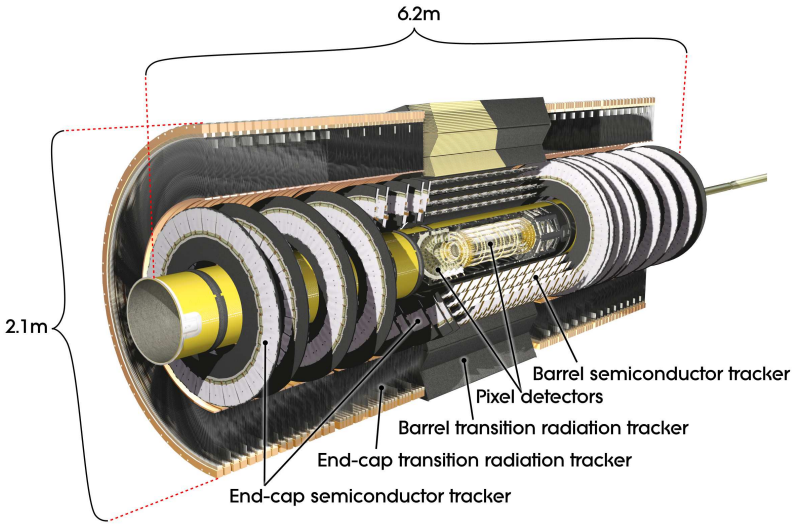



Figure 3.6: The layout of the Inner Detector of ATLAS [56].

### 3.5.1 Pixel detector

The Pixel detector consists of 1744 silicon pixel sensors, corresponding to a total of $8 \times 10^7$ pixels, which are arranged in three layers in the barrel and three layers in each of the endcaps [63]. The innermost pixel layer, also known as the *b*-layer or the vertexing layer, receives the highest radiation fluences and will need to be replaced sooner than the other pixel layers. It is situated close to the beam pipe at $R = 50.5$ mm. The lifetime of this layer at nominal luminosity is designed to be 3 years, whereas the other two layers are designed to last for 10 years (a lifetime dose of 50 MRad) [56]. The $\eta$ coverage of the Pixel detector (and the SCT and TRT) can be seen in figure 3.7. The intrinsic accuracy of a position measurement made by the pixels is 10 $\mu$m in $R$-$\phi$ and 115 $\mu$m in $z$. There are 80.4 million readout channels in total.

The sensors consist of oxygenated $n$-type wafers with readout pixels on the $n+$ implanted side of the detector and a $p$-$n$ junction on the back side. $n+$ denotes a $n$-type semiconductor that is very highly doped with atoms that donate additional free electrons. A bias voltage

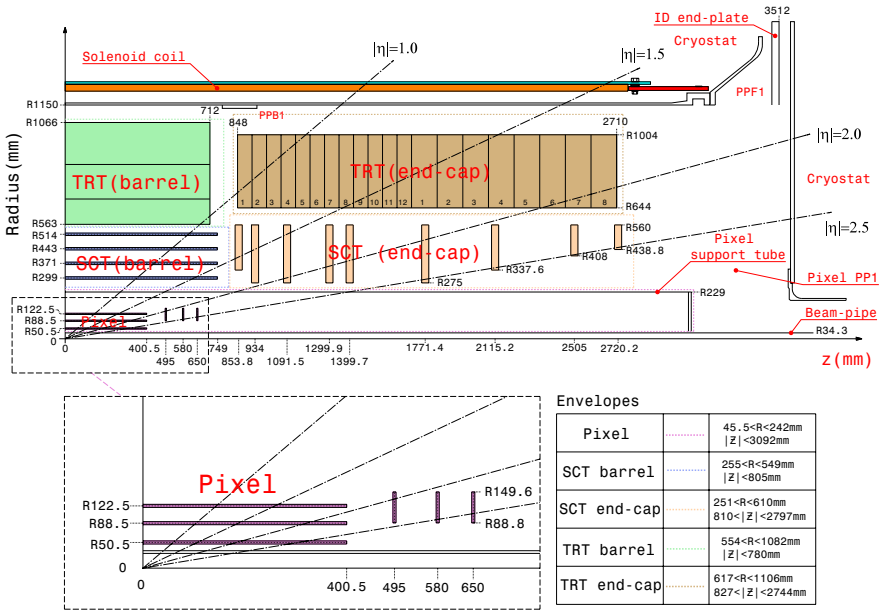



Figure 3.7: Cross-section of the ID, showing the coverage in $\eta$ of the Pixel detector, SCT and the TRT [56].

across the pixel creates a depletion region. Before irradiation, the depletion region starts at the $p$-side (the back). When particles pass through the depletion region, electron-hole pairs are created, which travel to the electrodes and deposit their charge creating a signal. As the sensor is irradiated, the effective doping of $n$-type silicon wafer decreases until the doping becomes effectively $p$ value after a fluence of $2 \times 10^{-13}$ cm$^{-2}$. This process is known as type inversion. The $n+$ implants allow the detector to operate with a good charge collection efficiency once inversion has occurred, with the depletion region growing from the readout side [64]. Each sensor is subdivided into 47628 pixels. Highly oxygenated material was chosen as it gives increased radiation tolerance to charged hadrons. The leakage current increases linearly with radiation dose [56].

The required operating voltage will change over the lifetime of the pixel sensors, as it depends on both the irradiation and the subsequent temperature-sensitive annealing. The sensors are operated at temperatures between $-5$°C and $-10$°C, to reduce the leakage current and contain the annealing. Nevertheless, the sensors will initially operate at 150 V bias voltage, but this will have to be increased to 600 V towards the end of their lifetime to maintain a good charge collection efficiency [56].

### 3.5.2 Semiconductor Tracker

The SCT consists of silicon microstrip sensors. It utilises $p$-in-$n$ semiconductor technology. There are 4088 modules, arranged in 4 layers in the barrel and 9 disks in the endcaps. A module consists of 2 pairs of sensors, daisy-chained to form a strip length of 12 cm [65]. One pair is aligned in the azimuthal direction, whereas the other pair is rotated by a stereo angle of 40 mrad. There are a total of 768 active readout strips per sensor. The SCT has a resolution of 17 $\mu$m in the $R-\phi$ plane and, thanks to the stereo measurement, a resolution of 580 $\mu$m in the $z$ plane [56].

The SCT sensors will initially operate at 150 V bias voltage. This operating voltage will be increased over time as the sensor is irradiated to maintain a good charge collection efficiency.

### 3.5.3 Transition Radiation Tracker

At larger radii (56 - 107 cm) from the beam-pipe is the TRT [66]. This consists of gaseous straw drift-tubes interleaved with transition radiation material. The TRT provides an average of 36 hits per track, improving the $p_T$ resolution of charged tracks by adding additional points for fitting, and the transition radiation material assists in electron identification. The TRT is designed to operate at room temperature. The gas mixture within the tubes is 70% Xe, 27% $CO_2$, and 3% $O_2$. The cathode consists of the polyimide tube, and the anode is a 31 $\mu$m diameter tungsten wire at the centre of the tube [56]. The TRT straws have an intrinsic resolution of 130 $\mu$m (the operational drift time accuracy).

Transition radiation is emitted when a particle crosses the interface of two media with different dielectric constants. The intensity of the x-ray radiation emitted is proportional to the Lorentz factor ($\gamma = E/mc^2$), and hence electrons traversing the material emit more transition radiation than hadrons with the same momentum. In addition, particles passing

through the drift tubes ionise the gas atoms, isolating charged particles that are collected at the anode and cathode. Two independent thresholds are used in the drift tubes. The lower threshold is passed by minimum ionising particles traversing the detector, whereas the higher threshold is sensitive to transition radiation.

## 3.6 Calorimetry

The ATLAS Calorimetry consists of electromagnetic and hadronic calorimeters. The layout can be seen in Figure 3.8. Both calorimeters are sampling calorimeters, which means they consist of absorbers interleaved with active material. The electron $E_T$ used in the $m_W$ analysis is measured in the electromagnetic calorimeter. Both calorimeters are used in measuring the recoil from the $W$ boson - another essential component of the $m_W$ analysis.

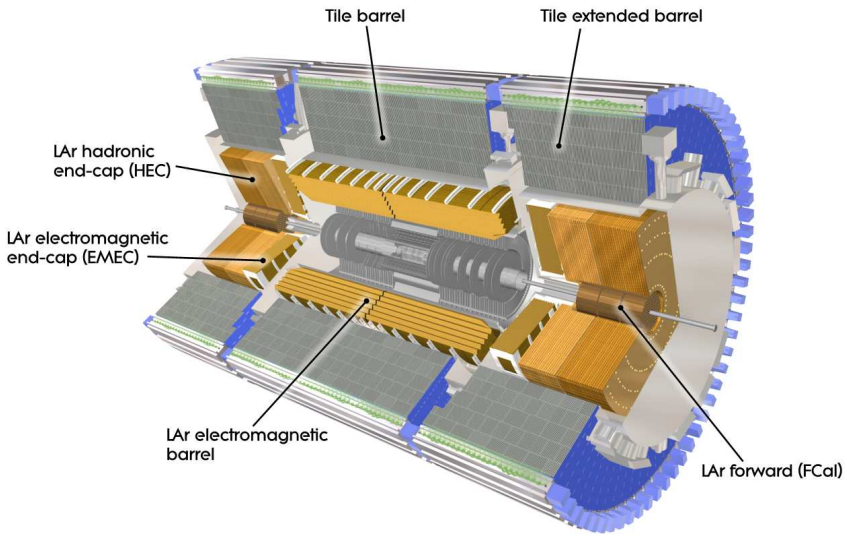



Figure 3.8: Layout of the ATLAS calorimetry [56].

### 3.6.1 Electromagnetic calorimeter

The ECal is finely grained so that precision measurements of electrons and photons can be made. The thickness of the ECal is $> 22$ radiation lengths in the barrel and $> 24$ radiation lengths in the endcaps. It consists of lead absorption plates with liquid argon filling the gaps

between them. The accordion geometry provides complete coverage in $\phi$ and enables the readout to be placed outside the sensitive volume ensuring complete hermicity [56]. Over the range of $|\eta| < 2.5$, i.e. the length of the ID and the range devoted to precision physics, the ECal is divided into three samplings in depth, each with a different granularity [56]. The different samplings can be seen in figure 3.9. The first sampling is finely segmented in $\eta$ to provide an accurate position measurement. Within the eta range of $2.5 < |\eta| < 3.2$, the ECal has two samplings.

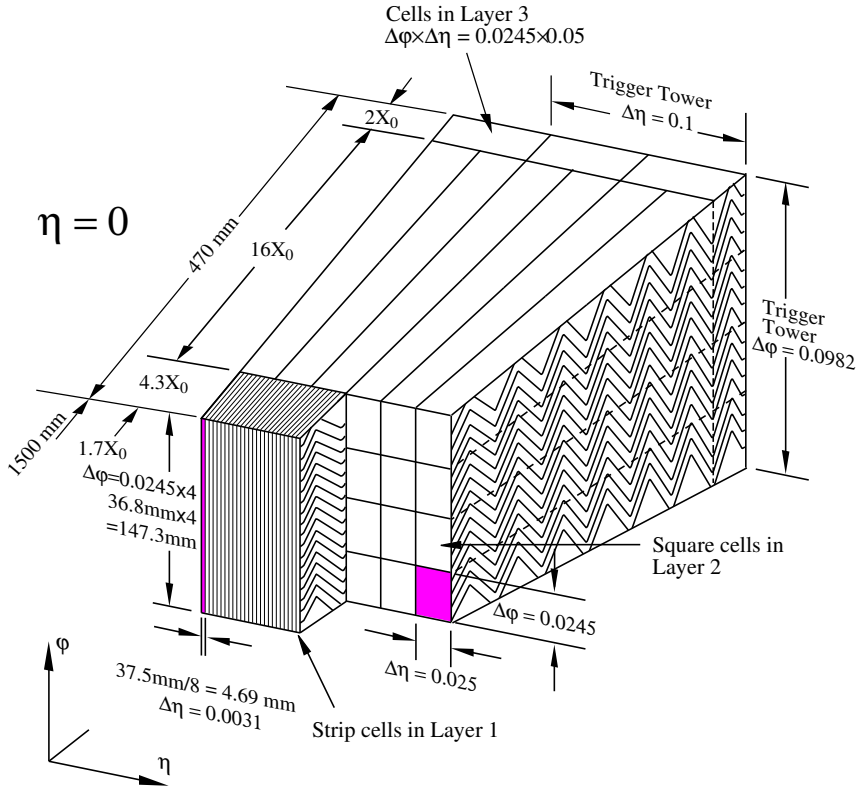



Figure 3.9: Different samplings in the ATLAS Electromagnetic calorimeter [56].

The lead absorption plates within the calorimeter cause incident photons and electrons to shower. Electrons can undergo bremsstrahlung, resulting in a photon which can subsequently undergo pair production, producing an electron-positron pair. Each resulting particle continues to either undergo bremsstrahlung or pair production until photons fall below the pair production threshold and electron energy losses other than from bremsstrahlung dominate (i.e. ionisation losses) [67]. The longitudinal depth of electromagnetic showers is governed by the radiation length $X_0$, whereas the width is governed by multiple scattering. The liquid

argon cells operate in a similar way to the drift tubes in the TRT. Liquid argon was chosen as the active medium due to its intrinsic linear behaviour, stability of response over time and radiation hardness. The sampling term of the energy resolution is approximately 10 $\%/\sqrt{E}$ in the barrel and the global constant term has a design value of 0.7 %. The resolution of the this calorimeter will be discussed further in Chapter 5.

The ECal is complemented by the forward calorimeter (FCal) and a presampling layer. The FCal provides measurements for $3.2 < |\eta| < 4.9$. The presampler is a thin liquid argon layer, situated within the barrel cryostat and in front of the active ECal. It provides an estimate of the energy lost in front of the ECal from interactions in the ID, cryostat wall and solenoid, and extends to $|\eta| = 1.8$.

### 3.6.2 Hadronic calorimeter

The HadCal has a coarser granularity and is used for single-hadron and jet reconstruction. It is also hermetic, such that missing transverse energy measurements can be performed with good precision. Preventing punch through to the muon chambers from jets is important, hence at $\eta = 0$ the calorimeter has a thickness of 11 interaction lengths. The barrel HadCal is situated immediately outside the ECal and provides coverage over the range of $|\eta| < 1.7$. It consists of steel absorbers and scintillating tiles, which are each read out by two wavelength shifting fibres connected to photomultiplier tubes.

In addition, there is the Hadronic Endcap Calorimeter, which shares a cryostat with the endcaps of the ECal. It consists of copper plates interleaved with 8.5 mm LAr gaps, which provide the active medium. The $\eta$ range slightly overlaps with both the barrel HadCal and the FCal, extending from $|\eta| = \pm 1.5$ to $|\eta| = \pm 3.2$ [56]. The FCal is approximately 10 interaction lengths deep. Each endcap consists of three modules; the first layer, consisting of tungsten absorber,performs electromagnetic measurements (as mentioned in ECal section) and the second and third layers, consisting of copper absorber, measure hadronic interactions.

The absorption plates within the HadCal cause hadronic cascades to occur. However, a fraction of the energy of the incident hadron is lost as it is spent breaking up nuclear bonds. Hadrons can also decay into neutrinos and muons in the calorimeter, which result in further energy losses. Since the amount of energy lost varies considerably, hadronic calorimeters have a much lower energy resolution than electromagnetic calorimeters [67]. Particles in the cascade cause the scintillators to release ultraviolet light, which is converted to visual light by wavelength shifting fibres which are coupled to each cell. This is necessary as the scintillator is not completely transparent to its own scintillation light, and hence the wavelength must be converted so that the light can reach the photomultiplier tubes without being absorbed [68]. The wavelength shifting also matches the wavelength to the spectral sensitivity of the photomultipliers.

The energy resolution of the hadronic calorimeter can be parameterised by the following equation.

$$\frac{\sigma}{E} = \left(\frac{A}{\sqrt{E}} + B\right) \oplus \frac{C}{E} \tag{3.5}$$

For jets in the central region of the detector, the stochastic term is approximately 60 $\%/\sqrt{E}$. $C$ is approximately 3%. The noise term $B$ is approximately 2 GeV in the central region and is larger in the endcaps.

## 3.7 Muon system

There are four different types of muon chamber: monitored drift tubes (MDTs), cathode strip chambers (CSCs), resistive plate chambers (RPCs) and thin gap chambers (TGCs). The precision measurement of muon track coordinates is provided by MDTs, and therefore they extend over the full eta range of the MS. The CSCs are used within the innermost plane, over the range of $2.2 < |\eta| < 2.7$ where there is a high rate, and provide precision measurements in this region. RPCs are used for triggering in the barrel ($|\eta| < 1.05$), whereas

TGCs are used for triggering within the endcaps ($1.05 < |\eta| < 2.4$). The layout of the Muon system can be seen in figure 3.10. The muon system is used for muon $p_T$ measurements, in conjunction with the Inner Detector. Measuring muon $p_T$ is one way to measure $m_W$, as discussed in the previous chapter.

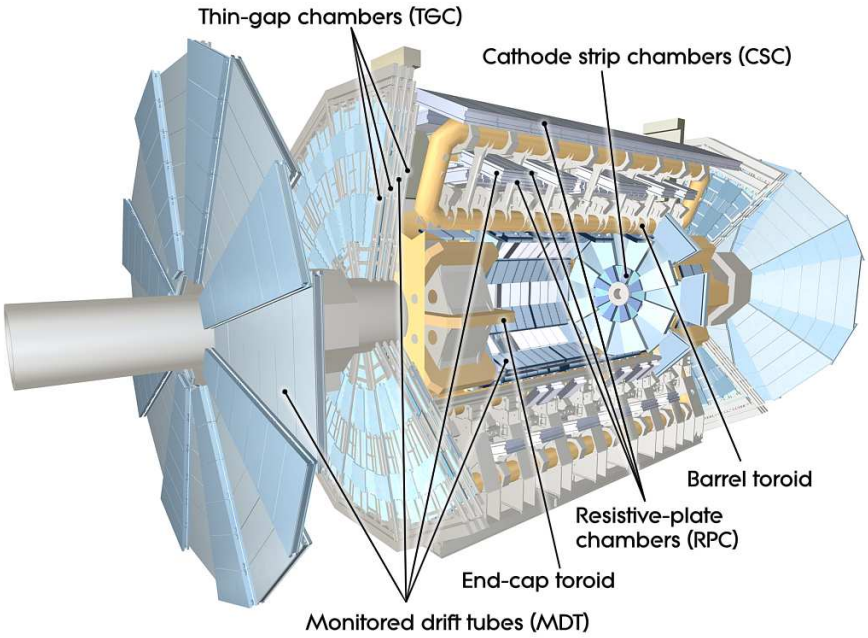



Figure 3.10: Layout of the ATLAS muon chambers [56].

The RPCs consist of two parallel plates made of a very high resistivity plastic material, with gas in between [69]. One plate is positively charged and forms an anode, whereas the other forms a cathode. A muon passing through the gas volume knocks electrons off gas atoms. Each of these electrons can knock further electrons off atoms, causing an avalanche. Electrons pass through the electrodes, to be detected by small external metallic strips. The pattern of hit strips can give a measure of the muon momentum in under a nanosecond, which allows a trigger decision to be made. In ATLAS, the gap between the two plates is ≈2 mm, since they are used for triggering (larger gaps are used in other experiments where RPCs can be used for time-of-flight measurements). The gas mixture used in the RPCs is 97.4% $C_2H_2F_4$, 5% $C_4H_10$ and 0.3% $SF_6$. The signal width of the RPCs at nominal voltage is 5 ns, so that the bunch-crossing can be tagged [70].

The MDTs are pressurised drift tubes with a diameter of 30 mm, filled with 93% Ar and 7% $CO_2$ gas [71]. As in the TRT, each tube consists of a positively charged wire within the gas volume, which attracts the electrons knocked off gas atoms. The drift time is taken to be the time of arrival of the first 15-20 electrons at the wire [72]. This is converted into a radius from the wire, and a track is fitted by combining drift radii measurements from several tubes in an MDT chamber. The MDT chambers are positioned in three layers, to allow a measurement of the curvature of a muon track passing through them. They achieve an average position resolution of 80 $\mu$m per tube, or 35 $\mu$m per chamber.

The CSCs are a type of multiwire proportional chamber [73]. They consist of arrays of positively charged anode wires crossed with negatively charged cathode strips, which reside in a gas volume. Electrons knocked off gas atoms travel to the anodes and the positively charged ions remaining travel to the cathode. This allows a 2D position measurement. The wires are closely spaced, providing a fast measurement that can be used for triggering. The CSCs are arranged in four layers to provide multiple measurements of the same track. The resolution of a CSC is 5 mm in the transverse plane and 40 $\mu$m in the bending plane.

A TGC consists of a plane of closely spaced anode wires sandwiched between two cathode planes, with a gas volume between the planes. The wire-cathode distance of 1.4 mm is less than the wire-wire distance of 1.8 mm. As the wires provide a high electric field, and there is very small spacing between wires, the TGCs have a very good time resolution of 25 ns and are used for triggering in the endcaps [70]. They also provide an azimuthal coordinate, which complements the endcap MDTs measurement in the bending plane.

Muons with momentum of less than 3 GeV do not generally reach the Muon Spectrometer, and muons with momentum of less than 6 GeV do not always reach the outer and middle muon stations. The standalone (i.e. without information from the Inner Detector measurements) momentum resolution for muons with $p_T = 100$ GeV is approximately 3%

over most of the $\eta - \phi$ plane. At $|\eta| = 0.2$, 0.3 and 0.7, where the support structures of the toroidal magnets are located, the momentum resolution is degraded to approximately 5%.

## 3.8 Forward detectors

ATLAS has three detectors, which provide coverage in the very forward region: LUCID, ZDC and ALFA. LUCID is a Cherenkov detector that provides measurements of the luminosity delivered to ATLAS. It is a fast detector with electronics capable of making luminosity measurements separately for each bunch crossing [60]. LUCID surrounds the beam pipe 17m away on each side of the beam crossing (also known as interaction point). The ZDC is used predominantly in heavy ion collisions, to measure the momentum of forward neutrons, and ALFA measures the absolute luminosity of the LHC by measuring the cross-section of elastic scattering at small angles, at a distance of 240 m away from ATLAS [74].

## 3.9 Trigger

The event data recording by ATLAS is limited to approximately 500 Hz in 2011. However, the proton-proton interaction rate at design luminosity is approximately 1 GHz. Therefore, the amount of data must be reduced before it is recorded. The trigger selects interesting collisions and rejects background. It consists of three parts: the L1 trigger, the L2 trigger and the Event Filter. The latter two are often referred to as the High Level Trigger or HLT [56]. A schematic of data flow through the trigger can be seen in Figure 3.11.

### 3.9.1 The L1 trigger

The L1 trigger searches for energy deposits in the ECal or the HadCal (corresponding to the 'L1Calo' Trigger) or the RPCs or the TGCs of the MS ('L1Muon'). All information is

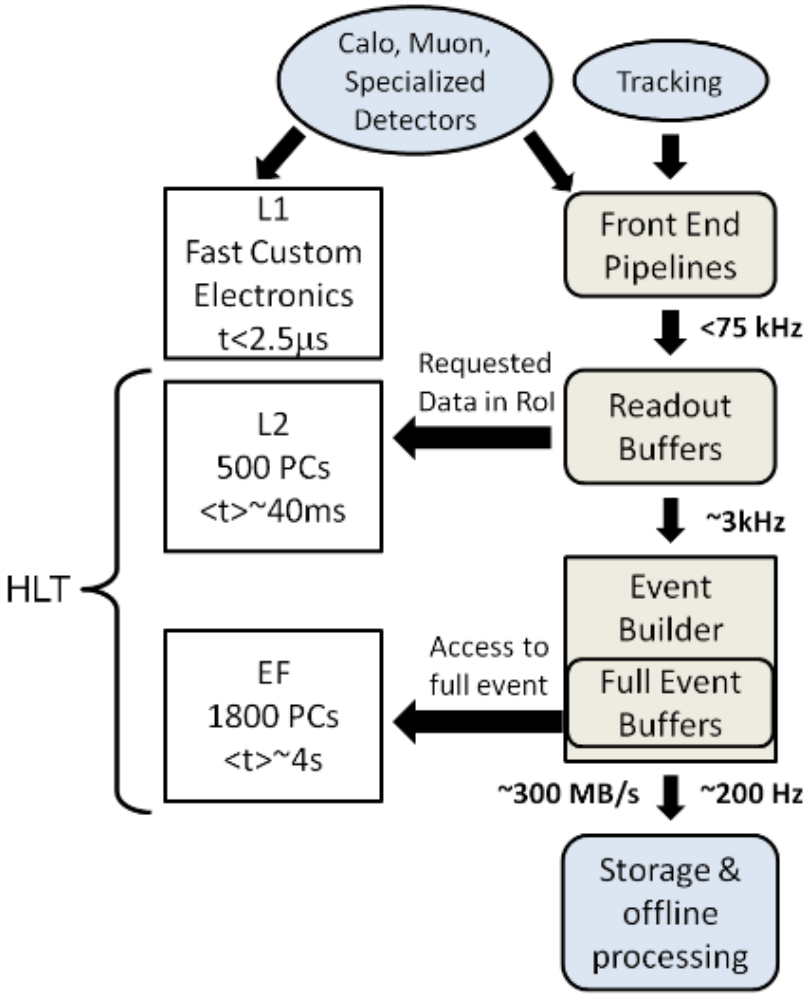



Figure 3.11: Schematic of the ATLAS trigger system [75]. Trigger decision timings are shown for each level.

available at reduced granularity, compared to that available to the later software triggers. The maximum rate the L1 trigger can handle is 75 kHz [56].

L1Calo can detect electrons, photons, jets, $\tau$ leptons decaying into hadrons and events with a large missing energy or a large transverse energy by triggering on large energy deposits in the calorimeters. Isolation can be required for the electron, photon and tau triggers (requiring that there are no other particles recorded by the trigger near to the particle in question). The L1 muon trigger searches for a pattern of hits originating from the interaction point within the RPCs in the barrel and TGCs in the endcap. This trigger has six independently tunable $p_T$ thresholds.

The Central Trigger Processor (or CTP) makes the overall decision whether to accept the event at L1. The trigger menu provided to the CTP consists of an OR of up to 256 different items, each item being a combination of different thresholds of acceptance of input data. The L1 trigger decision rests solely upon the multiplicity and energy of the objects found by it. However, information about the geometry of the event is held by the muon and calorimeter processing systems in order to be passed to the L2 processors as a region of interest or RoI.

At design luminosity, the LHC will have a 25 ns bunch spacing within a train. The MS is sufficiently large that the time of flight of a muon across it exceeds this spacing. Therefore the L1 trigger has pipeline memories (custom electronics placed on or near the detector) that retain the information for all detector channels until it can be processed simultaneously. Pipeline memories must be kept as short as possible to optimise cost and reliability, hence a L1 trigger decision must be made within 2.5 $\mu$s after each bunch crossing.

### 3.9.2 The High Level Trigger

The HLT comprises the Level 2 (L2) trigger and the Event Filter (EF). It consists of farms of processors connected by high-speed networks. The L2 trigger is passed RoIs by the L1 trigger. An RoI is the region around the identified L1 trigger signature, reducing the amount of data to be transferred to the L2 processors and analysed to no more than 6% of the total data volume. Events are held in readout buffers until the L2 decision is available. The L2 trigger must reduce the rate from 75 kHz to below 3.5 kHz.

Finally, the EF reduces the rate to approximately 200 Hz (in 2011), all of which can be recorded. At both L2 and EF, all of the detector systems, including the ID, are available at full granularity. Most of the software used at this level is similar to that used to reconstruct the event offline. The addition of track information, as well as more finely tuned threshold

cuts, improve particle identification and allow background to be rejected [56]. The Event Filter stream recording rates for 2011 and 2012 can be seen in Figures 3.12 and 3.13 (In 2012, the rate of data recorded was increased to approximately 500 Hz). The reconstruction of events from the signals from detector components (referred to as raw data) and the algorithms used by the trigger to select events are covered in chapter 4.

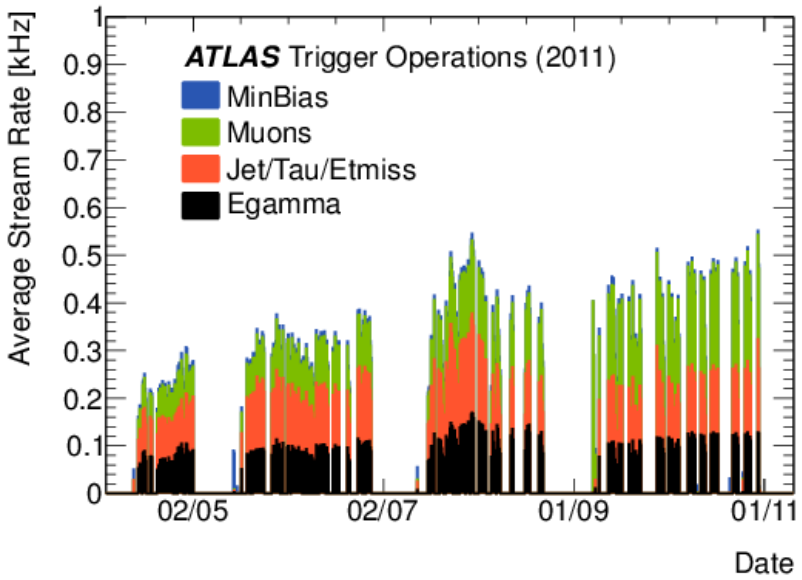



Figure 3.12: Event Filter stream recording rates from 2011 [76].

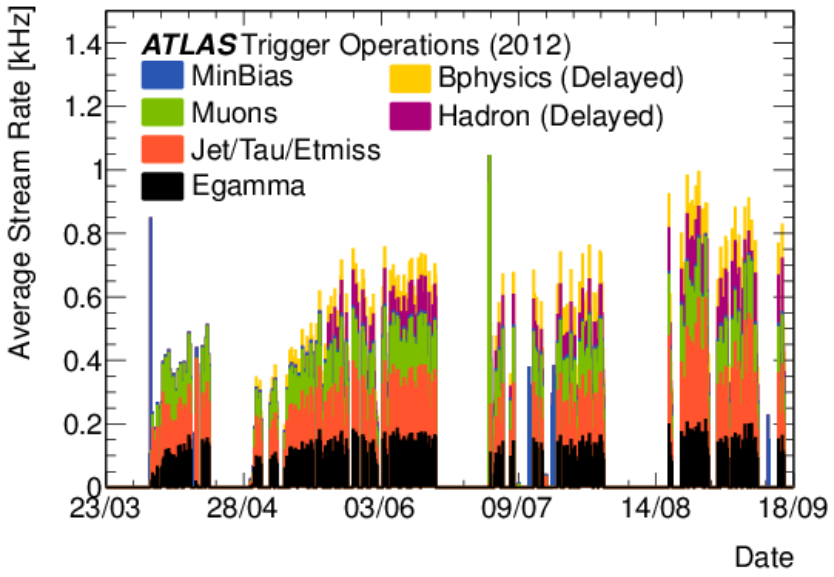



Figure 3.13: Event Filter stream recording rates from 2012 [76].

# Chapter 4

# Simulation and Reconstruction

## 4.1 ATLAS simulation framework

ATLAS has developed a detailed event simulation framework, which takes events from dedicated Monte Carlo generators and processes them using the same algorithms as those applied to the output from the detector [77]. There are three main steps in this process: first, the event generation and immediate decays and hadronisation of those particles performed by the Monte Carlo generators; second, the simulation of the particle interactions with detector material; and finally, the digitisation which converts the deposited energy into signals that can be compared to the readout from the ATLAS detector. The second and final steps rely on an accurate model of the ATLAS detector geometry. The ATLAS software framework that performs these steps is known as Athena, and the model of interactions with the detector in the second and final steps is GEANT4 [78].

## 4.2 Monte Carlo generation

POWHEG and PYTHIA are the Monte Carlo generators used in this work, and therefore only these two will be discussed in detail here. POWHEG performs NLO QCD computations of the hard emissions in an event which can be interfaced to a shower Monte Carlo (SMC)

program [79]. This method allows inclusive quantities to be predicted to NLO accuracy. MC@NLO can also provide NLO matrix element calculations to be interfaced to an SMC program [80].

The SMC typically used with POWHEG is PYTHIA [81] [82]. Another example of a commonly used SMC is HERWIG [83]. PYTHIA takes events from POWHEG, models additional QCD radiation and hadronises the quarks and gluons using phenomenological models. Unstable particles are also decayed by PYTHIA. PYTHIA can also generate events without the need for the interface with POWHEG, but these events will have matrix elements at LO rather than NLO.

Difficulty in interfacing two generators arises when the hard emission has to be matched with the soft emission from the parton shower. The scale for merging energies can be set at any point between the hard and soft processes, hence medium energy gluons or quarks can be included in the hard process or as part of the parton shower. Care must be taken to ensure there is no double counting of particles.

## 4.3 Detector simulation

The ATLAS detector is simulated by interfacing a model of the detector geometry with a software package called GEANT4 [77]. GEANT4 is a Monte Carlo simulation toolkit, designed to model the interaction of particles with different materials. The ATLAS detector geometry is stored in a database that provides an input to GEANT4 . GEANT4 adds to the generated Monte Carlo particles any secondary particles produced during detector simulation if they pass certain criteria.

GEANT4 outputs information as 'HITS', which are hit positions (for tracking detectors) and the position and location of energy losses for calorimeters [84]. In order to simulate pileup

(which in essence is the superposition of events), collections of HITS from different simulated events are added together. In future, real data collected using a minimum bias trigger will be overlaid on Monte Carlo provide a more accurate estimation of pileup, but this has not yet been implemented in ATLAS. All HITS then undergo digitisation, which transforms them into a simulation of the output from the readout electronics of each subdetector. The characteristics of this readout can be changed to model changes in the detector. Noise can also be injected at this stage.

## 4.4 Data processing

A small proportion of all events recorded by the trigger are used to assess data quality. These events, collected in what is known as the express stream, are reconstructed quickly at Tier-0, the Grid computing site at CERN. Information is checked for each subdetector and for each type of reconstructed final-state object, and a data quality flag is set. Generally, most analyses will only use data with all data quality flags set to 'green', meaning that the detector and run conditions were optimal. The data are subdivided into runs, which are characterised by a set of trigger conditions. There can be several runs per stable beam fill at the LHC. There are also runs with special trigger conditions aimed at recording cosmic rays, but these are not considered here. Each run is further subdivided into blocks of luminosity (lumiblocks) – which last approximately 1 minute. Data quality flags are set for each lumiblock in a run.

Data streaming from the detector is in a format known as 'RAW'. All RAW data is stored at Tier-0. Tier-0 streams the data to various Tier-1 processing centres around the world, where the RAW data is backed up at at least one additional site. Each geographical region has a Tier-1 and several Tier-2 Grid sites. Generally, the RAW data is not used for data processing by users, but is instead converted through a chain of processings into a data format known as a D3PD. A D3PD is provided by each analysis group, who choose which

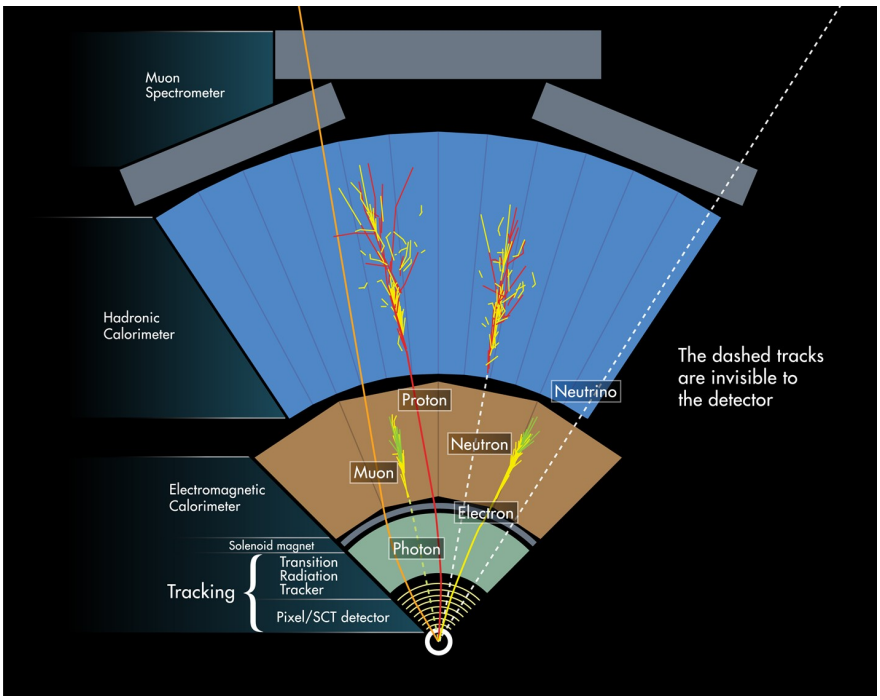



Figure 4.1: A sketch showing how various particles interact with the detector [85]. The grey middle section shows the Inner Detector and the tracks traversing it. The green inner ring shows the Electromagnetic calorimeter, whereas the red outer ring is the Hadronic calorimeter. The yellow squares within the calorimeter represent energy deposits. Finally, the blue and grey segments around the outside are the muon spectrometer.

variables to provide. It is also possible to 'skim' a D3PD, where only events which pass various selection requirements are included. These D3PDs are stored at many Tier-2 Grid sites around the world. A user can submit a job to the Grid, which will select a site with the relevant data and run the job there, before returning the results to the Grid for the user to retrieve.

## 4.5 Particle identification

Particles leave signals in different parts of the detector, depending upon whether they are charged or uncharged and what type of interaction they have with matter. A summary of how different particles interact with the detector can be seen in Figure 4.1. Neutrinos do not interact with the detector at all, and their presence is inferred from the resulting momentum imbalance, or Missing $E_T$.

## 4.6 Track reconstruction

A series of hits in the Pixel detector, SCT and TRT must be grouped together to form a track, so that a particle's motion through the detector can be analysed [86]. The tracking reconstruction use Kalman-filter techniques to account for ionisation energy losses, and Gaussian-sum filters to account for bremsstrahlung [87] [88].

### 4.6.1 Inside-out tracking

The inside-out tracking procedure first searches for hits within the Pixel detector and the SCT. A track 'seed' is formed from a combination of hits in the Pixels and the first layer of the SCT [86]. Hits are searched for along the trajectory of this seed throughout the SCT. Quality cuts are applied to remove outliers from the tracks and to reject fake tracks. Limits are placed on the number of possible tracks with which a hit can be associated. If a track passes through a silicon sensor without leaving a hit, then this is known as a hole. Candidate tracks which contain too many holes are rejected. The tracks are then extended into the TRT, before being refitted with information from all three subdetectors. If the track fit gets worse after being extended to the TRT, the TRT hits remain associated to the track but are defined to be outliers.

### 4.6.2 Outside-in tracking

Particles which are produced within the Pixel detector or SCT from decays of other particles may not be found by the inside-out tracking method. Substantial energy loss of an electron in the outermost part of the SCT can also point the TRT extension of the track in the wrong direction. Hence, it is necessary to have an outside-in tracking algorithm (also referred to as backtracking), which performs the sequence in reverse by starting the pattern recognition in the TRT before extending back into the silicon detectors. The outside-in tracking algorithm runs on hits that have not already been associated to an inside-out track [89].

### 4.6.3 Vertex finding

A dedicated vertex reconstruction algorithm associates groups of tracks to primary collision vertices. Secondary vertices and conversions are then reconstructed from any remaining tracks.

## 4.7 Calorimeter cluster reconstruction

In the electromagnetic calorimeter, cells which contain energy deposits are grouped together to form clusters. The cluster size must be small enough to reduce contributions from electronic noise and pileup, yet large enough to contain the majority of the shower and minimise energy loss from lateral leakage [90]. The optimal cluster size depends on the particle type, energy and pseudorapidity. Electrons have a larger interaction probability than photons in the upstream material and therefore require a larger cluster size. The optimal cluster size in the middle sampling of the calorimeter was found to be $3 \times 5$ (cells in the $\eta$ direction $\times$ cells in the $\phi$ direction) for unconverted photons and $3 \times 7$ for converted photons and electrons. $3 \times 7$ corresponds to an area of approximately $\Delta\eta \times \Delta\phi = 0.075 \times 0.175$. In the endcaps, the cell size in $\eta$ is smaller with respect to the shower size, so a window of $5 \times 5$ is used [84]. In the first sampling, which consists of strips, the cluster size is 1-2 cells in $\phi$ and 5-11 strips in $\eta$ (depending on the pseudorapidity of the particle). The third or back sampling is only used for highly energetic electrons with $E_T > 50$ GeV, in which case $3 \times 2$ cells are used. A sliding window algorithm is used to find the optimal cluster position in each case, by moving the group of cells until the maximum energy deposit possible is contained within the cluster. The search is performed over each region of uniform granularity.

## 4.8 Jet reconstruction

In the hadronic calorimeter, jets are searched for in a similar manner to electrons. A jet cluster candidate is found using a sliding window algorithm with $3 \times 3$ cells searching for any region where there is a local energy maximum. Kinematic variables are calculated using a $9 \times 9$ window centred upon the centre of the jet candidate 'seed' cluster.

### 4.8.1 Theoretical requirements

All jet-finding algorithms must be both 'infrared safe' and 'collinear safe'. A jet-finding algorithm is infrared safe if the presence or absence of soft radiation between two particles does not affect the recombination of those two particles into a jet. This means that any number of soft particles added in the fragmentation of a parton should not affect the number of jets reconstructed in the final state. Collinear safety means that a jet should be reconstructed whether it consists of one particle with a certain amount of transverse momentum or is split into two collinear particles [86].

### 4.8.2 Jet algorithms

There are three popular choices of infrared and collinear safe algorithms: $k_t$, Cambridge-Aachen and anti-$k_t$. Each of the three algorithms utilises the 'distance' and difference of transverse momentum between clusters of energy. The algorithms are defined as follows:

$$d_{ij} = min(k_{ti}^{2p}, k_{tj}^{2p}) \frac{\Delta_{ij}^2}{R^2} \tag{4.1}$$

$$d_{iB} = k_{ti}^{2p} \tag{4.2}$$

$$\Delta_{ij}^2 = (y_i - y_j)^2 + (\phi_i - \phi_j)^2 \tag{4.3}$$

$\Delta_{ij}$ is the distance between two clusters measured in the $\eta - \phi$ plane. $R$ is a parameter used to constrain the size of the jet reconstructed (a typical value of $R$ used by ATLAS is 0.4). $k_{ti}$, $y_i$ and $\phi_i$ are the transverse momentum, rapidity and the azimuthal angle respectively of cluster $i$. $d_{iB}$ represents the weighted 'distance' between the energy cluster and the beam. The variable $p$ is different in each of the three algorithms, and adjusts the importance placed on particle momentum in the equation. The equations are evaluated for all clusters, and the smallest distance found. If $d_{ij}$ is the smallest, clusters $i$ and $j$ are combined to form a larger energy cluster, whereas if $d_{iB}$ is the smallest, $i$ is called a jet and is removed from the rest of the calculation. The process is repeated until all energy clusters have been formed into jets.

For the Cambridge-Aachen algorithm, $p = 0$, and hence the calculation is based on distance alone [91] [92]. The $k_T$ algorithm sets $p = 1$ and as a result clusters particles that are closest in transverse momentum and distance first [93] [94]. Anti-$k_T$ performs the opposite calculation, with $p = -1$, and clusters particles with the largest relative difference in transverse momentum and the closest 'distance' first [95]. This results in the low-momentum particles being clustered around the high-momentum particles at an early point of the calculation, before any low-momentum particles cluster amongst themselves.

### 4.8.3 ATLAS jet reconstruction

ATLAS reconstructs jets using the anti-$k_T$ algorithm. Energy deposits from both the electromagnetic and hadronic calorimeters are used. An example of a reconstructed jet in the ATLAS detector can be seen in Figure 4.2.

## 4.9 Muon reconstruction

High-$p_T$ muons typically pass through three muon precision detectors (MDTs and CSCs), except for $\eta$-$\phi$ regions where there are holes. Three types of muon algorithm exist: Combined,

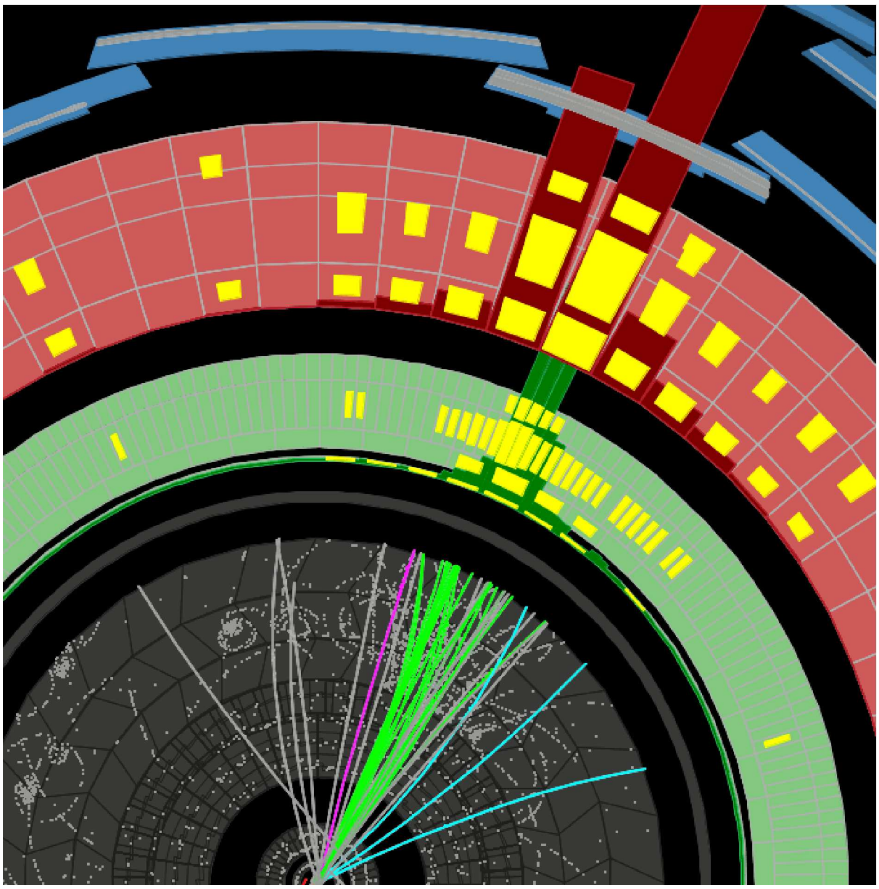


Figure 4.2: A high-$p_T$ jet in the transverse plane of the ATLAS detector. The grey inner circle represents the inner tracker, the green represents the electromagnetic calorimeter, the red the hadronic calorimeter and the blue segments represent the muon spectrometer.

Standalone and Segment Tagged.

### 4.9.1 Combined muon reconstruction

Muon spectrometer tracks are paired with ID tracks to construct combined muons. The quality of the match is measured by the match $\chi^2$, as defined by the following equation.

$$\chi^2_{match} = (T_{MS} - T_{ID})^T (C_{ID} + C_{MS})(T_{MS} - T_{ID}) \tag{4.4}$$

$T$ is a vector of the 5 track parameters (for example, $q/p$ (q=charge, p=momentum), $\phi$, $\theta$, $d_0$ (transverse impact parameter) and $z_0$ (the closest approach to the beam pipe in the $z$-plane), expressed at the closest point to the beam line, and $C$ is its covariance matrix. When the MS track is extrapolated, energy loss and multiple scattering in the calorimeters are both accounted for. The match $\chi^2$ is used to define which pairs of tracks form the best combination. A statistical combination of the inner and outer track vectors is used to obtain a combined track vector. This type of muon reconstruction is used in most physics analyses to find prompt muons, e.g. from $Z$ or $W$ decays.

### 4.9.2 Standalone muon reconstruction

Track segments are reconstructed in each of the three muon stations and the segments are connected to form a track. Standalone algorithms can reconstruct tracks up to $|\eta| = 2.7$, compared to the $|\eta| = 2.5$ limit of the ID. However, there are gaps around $\eta$ of 0.0 and 1.2; the area occupied by the muon system support structures and services. This algorithm has a low efficiency for reconstructing low-$p_T$ muons which do not penetrate to the outer muon station. The algorithm mainly reconstructs muons from $\pi$ and $K$ decays in the calorimeters. These non-prompt muons are a background for most physics analyses.

### 4.9.3 Segment tagged reconstruction

The segment tagged algorithms propagate ID tracks out to the first station of MS and search for nearby track segments. If a segment is sufficiently close, the track is identified as a potential muon.

## 4.10 Electron reconstruction

### 4.10.1 Electron candidates

The calorimeter cluster reconstruction and the track reconstruction have been described in previous subsections. In order to form an electron candidate, seed clusters are matched to reconstructed tracks by extrapolating the last point on the track to the second sampling of the calorimeter [96]. If the extrapolation is within a certain $\eta$ and $\phi$ of the cluster, then the track is matched to the cluster. The window is larger in $\phi$ than $\eta$ in order to account for bremsstrahlung radiation, as the extrapolated track will bend as it traverses the magnetic field in the ID but photons will travel straight through. If there are no silicon hits on the tracks, then only $\phi$ matching is used since the TRT hits do not provide a good $\eta$ measurement (these electron candidates are not used in most analyses). If more than one track is associated to the same seed cluster, then the track with the lowest $\Delta R$ with respect to the cluster is used. However, tracks with silicon hits but a larger $\Delta R$ have priority over tracks with only TRT hits, as the latter tracks are more likely to come from photon conversions.

The energy of the electron is calculated from the energy cluster in the calorimeter. Electron $\eta$ and $\phi$ are taken from the track unless the track has no silicon hits, in which case the cluster $\eta$ is used and the $\phi$ position is taken from the TRT hits.

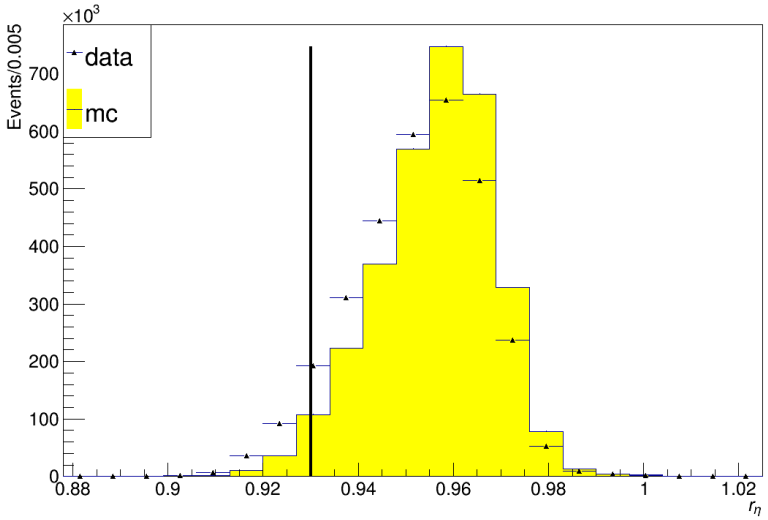



Figure 4.3: $R_\eta$ (the ratio of the cell energies in 3×7 and 7×7 windows) for data and Monte Carlo. The line shows a typical cut value (in this case for $20 < E_T < 30$ GeV and $0.1 < \eta < 0.6$). Electrons with $R_\eta < 0.93$ are rejected.

### 4.10.2 Variables used for electron identification

Table 4.1 shows the variables used for electron identification. For 2011 data, the 'loose' electron selection includes requirements on the calorimeter variables $R_\eta$, $R_{had}$, $R_{had1}$, $\omega_{\eta 2}$, $E_{ratio}$ and $\omega_{stot}$. Electron tracks must also have a minimum of 1 hit in the pixel detector, and 7 hits in the pixel detector and the SCT combined. Finally, there is a very loose cluster-track matching in $\eta$.

The 'medium' electron selection for 2011 data uses the same calorimeter variables as the loose selection, but mostly with more stringent requirements. The cluster-track matching in $\eta$ is tightened and a $d_0$ requirement is added. Track selection is tightened within the $|\eta| < 2.01$ range to require 1 hit in the B-layer of the pixel detector. Finally, a loose requirement is added on the TRT high-threshold hits ratio (the ratio of the number of high-threshold hits in the TRT associated with the track to the total number of hits in the TRT associated with the track). Figures 4.3 to 4.9 show the distributions of the variables used and some typical cut values. All plots within this chapter have been made using all available 2011 data and POWHEG Monte Carlo. Cut values used for each variable vary in $|\eta|$ and $E_T$.

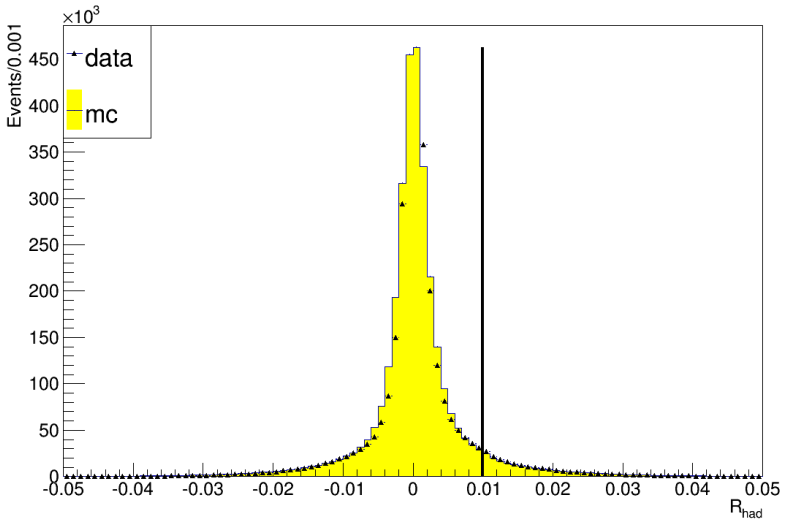



Figure 4.4: $R_{had}$ (the ratio of $E_T$ in all layers of the hadronic calorimeter to $E_T$ of the electron cluster) for data and Monte Carlo. The line shows a typical cut value (in this case for $20 < E_T < 30$ GeV and $0.1 < \eta < 0.6$). Electrons with $R_{had} > 0.01$ are rejected. $R_{had}$ can be negative when cells in the hadronic calorimeter do not exceed the expected energy threshold for noise and pileup and form negative energy clusters.

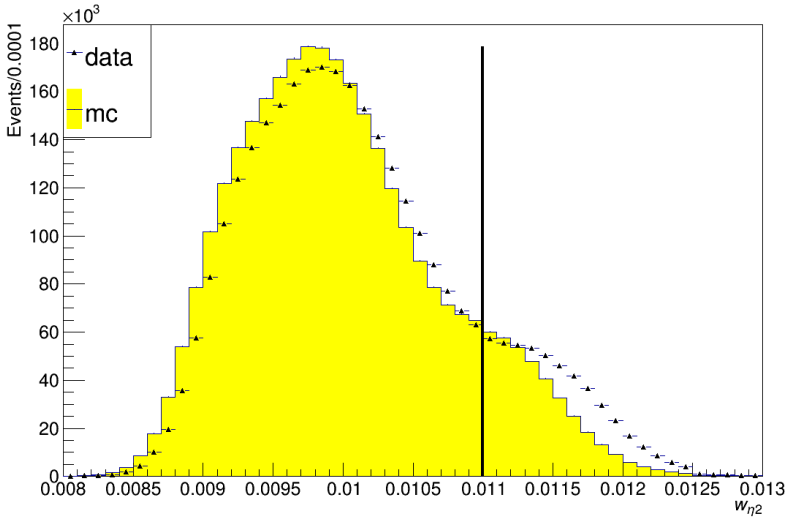



Figure 4.5: $\omega_{\eta 2}$ (Lateral width of the shower in $\eta$ weighted by the energy in the 2nd sampling) for data and Monte Carlo. The line shows a typical cut value (in this case for $20 < E_T < 30$ GeV and $0.1 < \eta < 0.6$). Electrons with $\omega_{\eta 2} > 0.011$ are rejected.

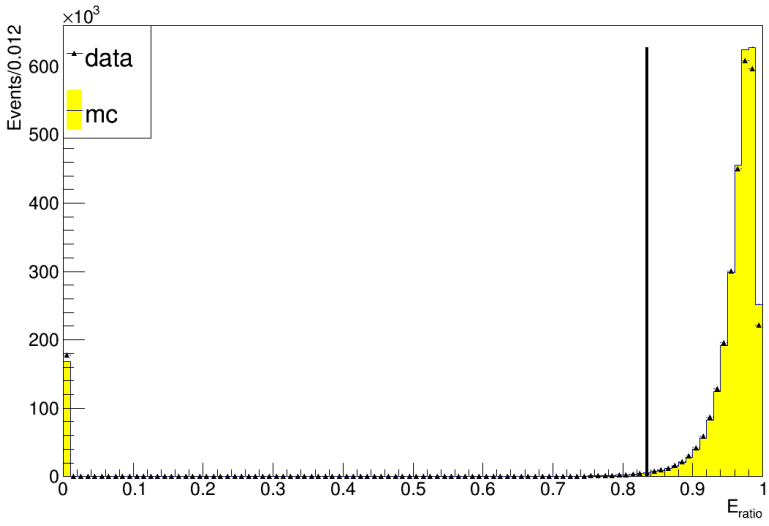



Figure 4.6: $E_{ratio}$ (ratio of the energy difference of the largest and second largest energy deposits in the first sampling of the calorimeter over the sum of those deposits) for data and Monte Carlo. The line shows a typical cut value (in this case for $20 < E_T < 30$ GeV and $0.1 < \eta < 0.6$). Electrons with $E_{ratio} < 0.835$ are rejected. Electrons have $E_{ratio}$ of 0 when peaks in energy could not be found in the 1st sampling of the calorimeter.

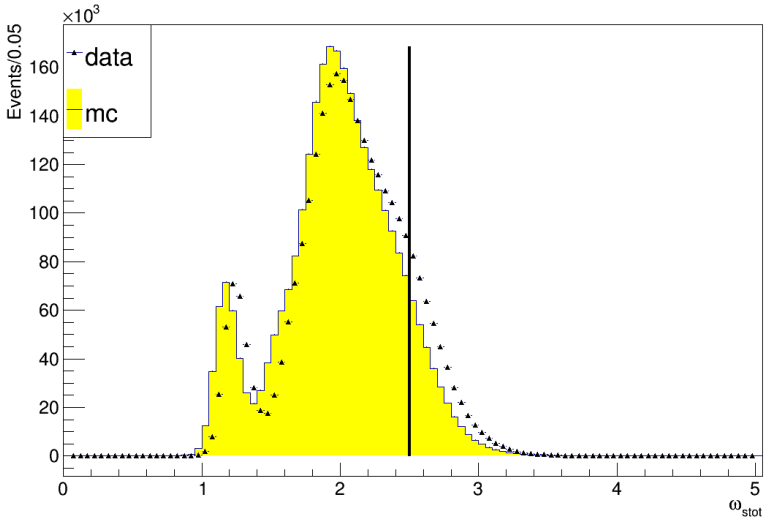



Figure 4.7: $\omega_{stot}$ (lateral width of the shower in strips in the 1st sampling) for data and Monte Carlo. The line shows a typical cut value (in this case for $20 < E_T < 30$ GeV and $0.1 < \eta < 0.6$). Electrons with $\omega_{stot} > 2.50$ are rejected.

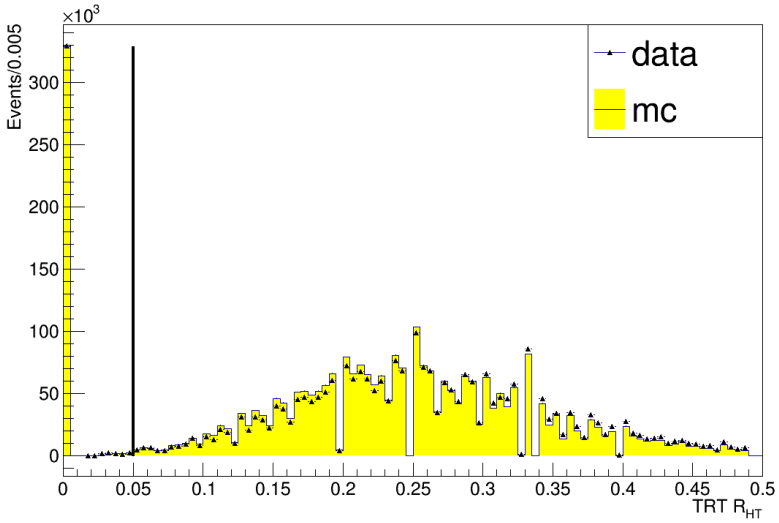



Figure 4.8: TRT High threshold hits ratio (Ratio of High Threshold hits in the TRT to the total number of hits in the TRT) for data and Monte Carlo. The line shows a typical cut value (in this case for $20 < E_T < 30$ GeV and $0.1 < \eta < 0.6$). Electrons with TRT High threshold hits ratio $< 0.05$ are rejected. The large peak at 0 arises from electrons in the outermost $\eta$ bins, which do not have a sufficient number of TRT hits on the track. Therefore, this cut is not applied at $|\eta| > 2$.

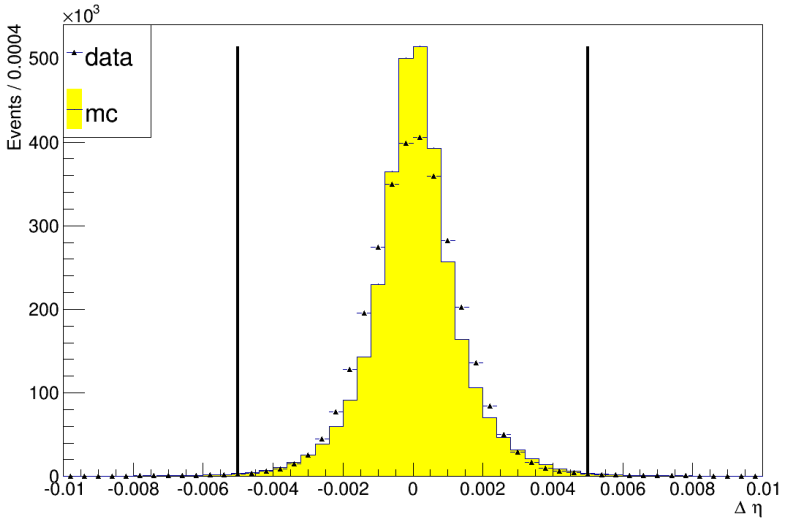



Figure 4.9: $\Delta\eta$ (distance in $\eta$ between the extrapolated track and the cluster) for data and Monte Carlo. The line shows a typical cut value (in this case for $20 < E_T < 30$ GeV and $0.1 < \eta < 0.6$).

| Type | Description | Variable name |
|---|---|---|
| Acceptance of the detector | $\|\eta\| < 2.47$ | |
| Hadronic Leakage | Ratio of $E_T$ in the first layer of the hadronic calorimeter to $E_T$ of the electron cluster (used over the range $\|\eta\| < 0.8$ and $\|\eta\| > 1.37$) | $R_{had1}$ |
| | Ratio of $E_T$ in all layers of the hadronic calorimeter to $E_T$ of the electron cluster (used over the range $\|\eta\| < 0.8$ and $\|\eta\| > 1.37$) | $R_{had}$ |
| Second layer of the EM calorimeter | Ratio of cell energies in 3×7 and 7×7 windows | $R_\eta$ |
| | Lateral width of the shower (variance in $\eta$ weighted by the energy) | $\omega_{\eta 2}$ |
| First layer of the EM calorimeter | Total shower width (in number of strips) | $\omega_{stot}$ |
| | Ratio of the energy difference of the largest and second largest deposits in the window over the sum of those energies | $E_{ratio}$ |
| Track quality | Number of hits in the pixel detector | $N_{pix}$ |
| | Number of hits in the pixels and the SCT | $N_{Si}$ |
| | Transverse impact parameter | $d_0$ |
| Track matching | $\Delta\eta$ between the cluster and the track | $\Delta\eta$ |
| | $\Delta\phi$ between the cluster and the track ($< 0.02$) | $\Delta\phi$ |
| | Ratio of the cluster energy to the track momentum | $E/p$ |
| $b$-layer | Number of hits in the B-layer | $N_B$ |
| TRT | Total number of hits in the TRT | $N_{TRT}$ |
| | Ratio of the number of high-threshold hits in the TRT to total number of hits in the TRT | $R_{HT}$ |
| Conversions | Electron candidates matching to reconstructed photon conversions are rejected | |

Table 4.1: Definition of variables used in electron identification [86].

The 'tight' electron selection has requirements on the same shower shape variables as the medium and loose electron selections, some of which are tightened compared to the medium selection. The cluster-track matching is improved by adding requirements on $E/p$ and $\Delta\phi$. The requirement on $d_0$ is tightened and conversions are removed. The $b$-layer hit requirement is extended to the full $\eta$-range. Typical cuts on each variable for the loose, medium and tight selections can be seen in Table 4.2.

| | **Loose** | **Medium** | **Tight** |
|---|---|---|---|
| $\|R_{had}\| <$ | 0.012 | 0.010 | 0.010 |
| $R_{eta} >$ | 0.910 | 0.930 | 0.930 |
| $\omega_{stot} <$ | 2.90 | 2.50 | 2.50 |
| $\omega_{\eta 2} <$ | 0.013 | 0.011 | 0.011 |
| $E_{ratio} >$ | 0.800 | 0.835 | 0.835 |
| $N_{pix} >=$ | 1 | 1 | 1 |
| $N_{Si} >=$ | 1 | 7 | 7 |
| $\Delta\eta <$ | 0.015 | 0.005 | 0.005 |
| $\Delta\phi$ | - | - | -0.03 to 0.01 |
| $N_B =$ | - | 1 | 1 |
| $\|d_0\| <$ | - | 5 | 1 |
| TRT HT hits ratio > | - | 0.05 | 0.08 |
| $N_{TRT} >=$ | - | - | 32 |

Table 4.2: Typical cuts on each variable for the loose, medium and tight selections for electrons with $25 < E_T < 32$ GeV and $0.1 < |\eta| < 0.6$.

## 4.11 Triggers for the $W$ boson mass measurement

Due to rate considerations, the loose electron trigger was heavily prescaled during 2011. A prescaled trigger records only a fraction of the events that pass its selection. The medium electron trigger was the loosest unprescaled electron trigger. In order to get the largest dataset to minimise the statistical error, the medium trigger was used. Here I assess the suitability of the trigger for the measurement.

At luminosities $< 2 \times 10^{33} cm^{-2} s^{-1}$ , the lowest energy unprescaled electron trigger used in ATLAS was $e20_medium$, meaning that only electrons with greater than 20 GeV were triggered on. Above $2 \times 10^{33} cm^{-2} s^{-1}$, the energy threshold was raised to 22 GeV and hence the lowest energy unprescaled trigger was $e22_medium$. When the luminosity exceeded $2.3 \times 10^{33} cm^{-2} s^{-1}$, an additional hadronic energy veto was added at Level 1 and the trigger was called $e22vh_medium1$. For a representative run from July 2011, at the start of the run the $e20_medium$ trigger rate was approximately 100 Hz, which decreased as luminosity degraded as the run continued. The $e20_loose$ trigger prescaled to approximately 2 Hz. The tight trigger was not run as the medium trigger was unprescaled. The plots below show the combined result for all 2011 data.

Any drop in efficiency across the selected electron $E_T$ range can bias the shape of the electron $E_T$ distribution, impacting the $m_W$ measurement directly [86]. Before ATLAS began taking data, the planned tight electron selection had a reconstruction efficiency drop of 9% over the $E_T$ range from 20 GeV to 40 GeV. It was calculated that assuming flat efficiency across this range would result in a bias on $m_W$, leading to a systematic error of 360 MeV. This number corresponds to a bias of 4 MeV per 0.1% efficiency drop. The resultant systematic uncertainty depends on how well the efficiency is modelled, but should be minimised if the efficiency drop can be minimised.

Scale factors are used to correct for MC mismodelling of inefficiencies in the triggers. The phase space is split into bins of $\eta$ and $E_T$ and Monte Carlo events are reweighted such that the Monte Carlo efficiency matches the data efficiency in each bin. Using this method, the error on the efficiencies after applying the scale factors should be less than 0.1% to keep the electron efficiency systematic on $m_W < 4$ MeV. This constraint could be relaxed if a specialised $m_W$ trigger could be used with a minimal efficiency drop between 20 and 40 GeV. In the following section, I will analyse whether the medium electron selection provides a small enough efficiency drop to be used for the $W$ boson mass selection.

### 4.11.1 Efficiency of medium electron selection

In order to calculate the efficiency of the medium electron selection, the 'tag and probe' technique was be used. The method relies on identifying two leptons from a $Z$ boson decay by applying tight identification requirements to one, known as the 'tag', and looser identification requirements on the other (the 'probe'). The invariant mass of the two leptons must be close to the mass of the $Z$ boson. As the probe has only been loosely identified, the rate at which it passes tighter identification requirements can be used to calculate the relative efficiency of these requirements. A summary of the electron selection cuts used here for both the tag and the probe is shown in Table 4.3.

| Tag and probe electron selection |
|---|
| **Electron cuts for tag and probe** |
| Electron $\|\eta\| < 2.47$ and not in dead $\eta$ region of calorimeter |
| 'Green' Electron Data Quality |
| **Electron cuts for tag only** |
| Electron must pass medium identification cuts |
| **Event cuts** |
| Exactly 2 electrons |
| Electron $E_T > 20$ GeV |
| Opposite charge |
| $66 < M_{ee} < 116$ GeV |

Table 4.3: Tag and probe selection for trigger studies. This selects 1656276 events in data and 6872632 events in Monte Carlo.

Figure 4.10 shows the efficiency of the medium identification criteria used in the trigger. For electrons with $E_T$=40 GeV, the efficiency is 95%, but this drops to 77% at 20 GeV. This efficiency drop of 18% would lead to a systematic error on the $m_W$ measurement of 720 MeV, if a flat efficiency were assumed. The differences in the trigger efficiency drop anticipated in the pre-data taking phase and the actual efficiency drop in the 'medium' trigger used in 2011 arose from incorrectly simulated $R_\eta$ and $\omega_{\eta 2}$ distributions in Monte Carlo used to optimise the trigger before data-taking, resulting in a recalibration of the trigger cut values after data taking had begun. Simulation of these quantities has now been improved using a more detailed description of the calorimeter geometry in GEANT4 − although good agreement between data and Monte Carlo has not been achieved. The previous figures shown use the improved simulation. The distributions of $R_\eta$ and $\omega_{\eta 2}$ before and after the simulation had been improved can be seen in Figures 4.11 and 4.12. It was also necessary to tighten some of the trigger requirements due to the high pileup environment of the LHC in 2011, in order to reduce trigger rates due to bandwidth limitations.

### 4.11.2 Specialised $m_W$ trigger

The purpose of a specialised $m_W$ trigger would be to reduce the efficiency drop between 20 GeV and 40 GeV, reducing the systematic error on $m_W$ (assuming a corresponding decrease in uncertainty on the scale factors). It could only have a small additional rate compared

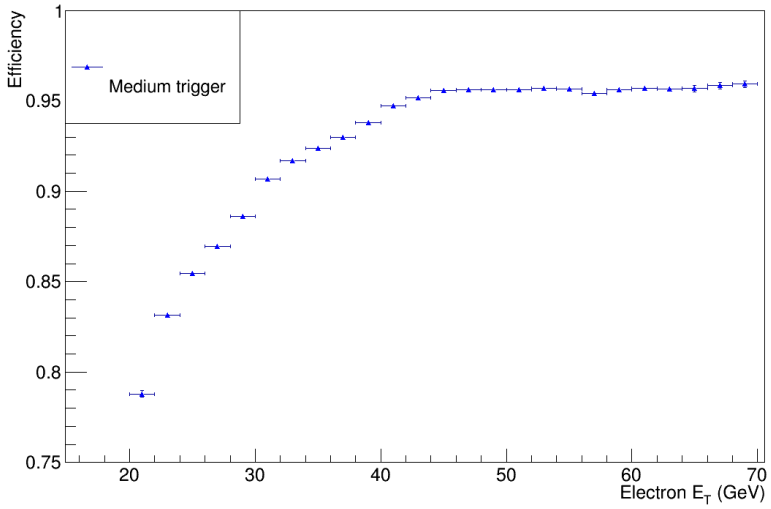



Figure 4.10: Efficiency of reconstruction of electrons for the medium trigger used in 2011.

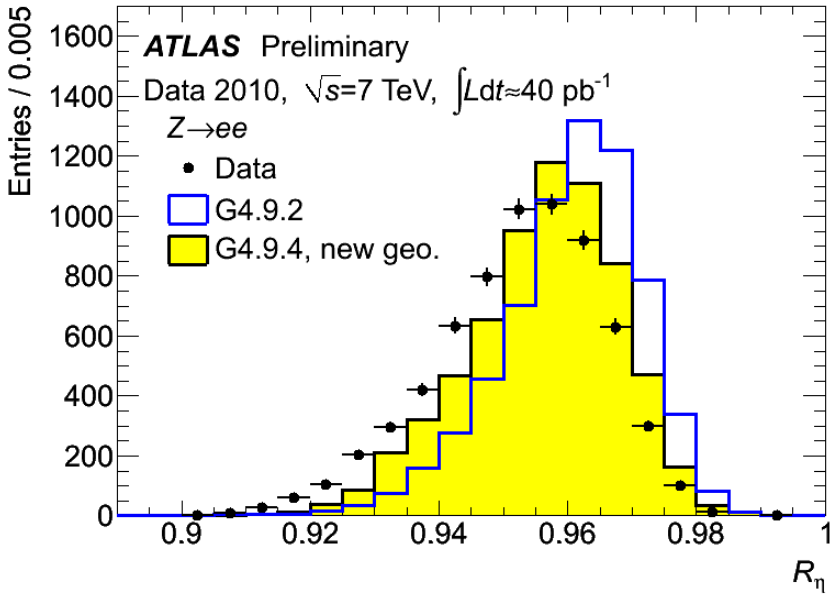



Figure 4.11: $R_\eta$ pre-data taking (G4.9.2) and after the simulation had been optimised (G4.9.4 new. geo.) [97].

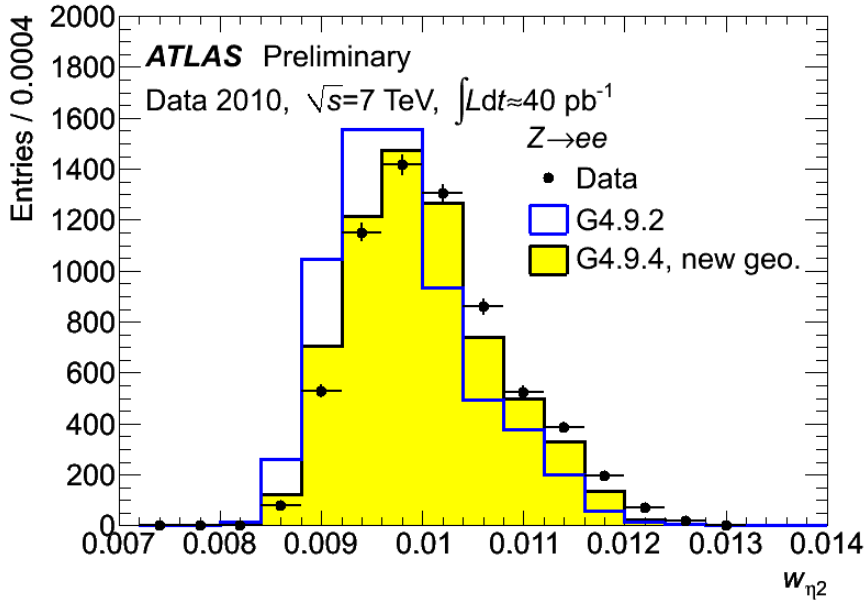



Figure 4.12: $\omega_{\eta 2}$ pre-data taking (G4.9.2) and after the simulation had been optimised (G4.9.4 new. geo.) [97].

to the medium trigger, as there are constraints on the overall bandwidth available. The simplest way to satisfy these constraints is to check which requirements on trigger variables cause the largest efficiency drops and loosen these trigger requirements. Figures 4.13 to 4.17 show the efficiency as a function of $E_T$ for several different trigger variables (all variables were checked in this analysis but not all plots are shown here). The most biased variables were found to be $R_\eta$ and $\omega_{\eta 2}$, as can be seen in Figures 4.15 and 4.16 respectively.

The proposed $m_W$ trigger makes the same requirements as the medium trigger, except for those on $R_\eta$ and $\omega_{\eta 2}$, which are set to the loose cut definitions. The typical cuts used by the $m_W$ trigger are summarised in Table 4.4, alongside the loose, medium and tight selections for comparison. The efficiency of this trigger can be seen in Figure 4.18. The efficiency drop from 40 GeV to 20 GeV has been reduced to 12%, a reduction of 6% compared to the medium efficiency drop. Assuming a flat trigger efficiency, using this trigger would result in a systematic error on the $W$ boson mass of 480 MeV. This is a reduction of a third on the $m_W$ bias from electron inefficiency. Using the 2011 dataset, the measured error on the efficiency ranges from 0.1% to 0.2% across the selected electron $E_T$ range, as shown in Figure 4.19 [98]. At the lowest $E_T$ range, the error on the efficiency of the medium trigger is 0.2%,

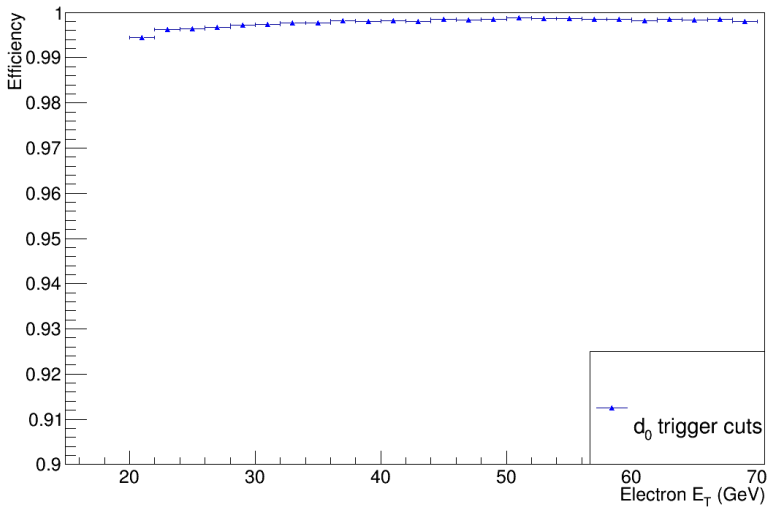



Figure 4.13: Efficiency of reconstruction of electrons as a function of $E_T$ with only the cut on $d_0$ applied.

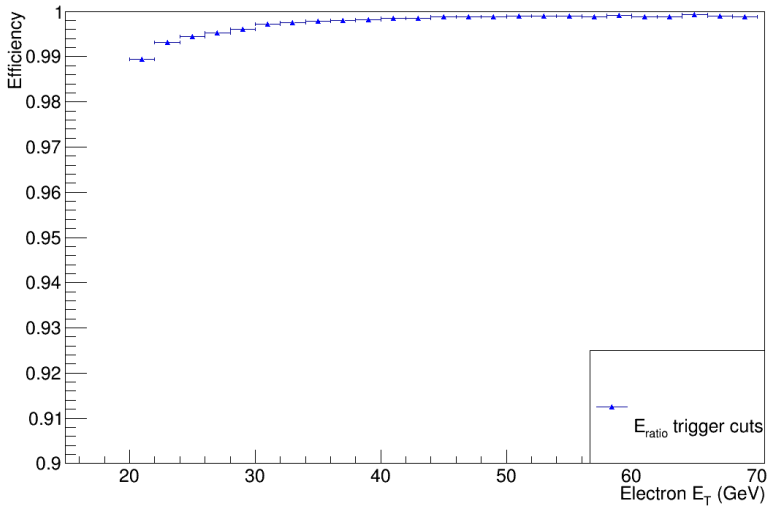



Figure 4.14: Efficiency of reconstruction of electrons as a function of $E_T$ with only the cut on $E_{ratio}$ applied.

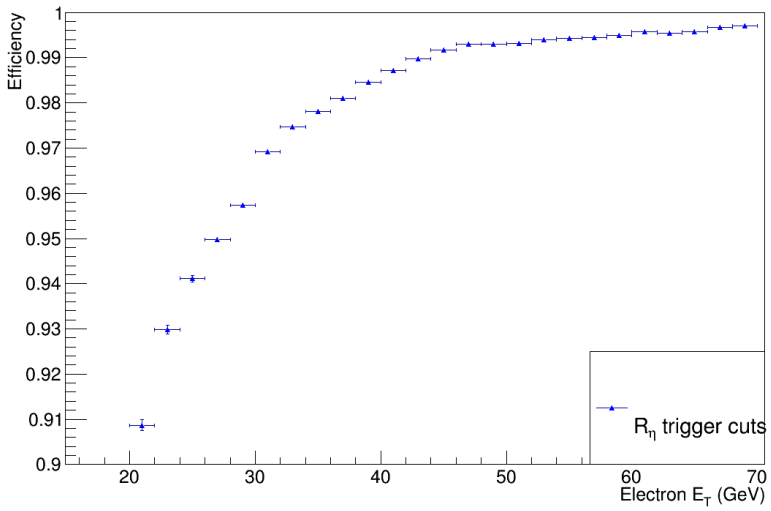



Figure 4.15: Efficiency of reconstruction of electrons as a function of $E_T$ with only the cut on $R_\eta$ applied.

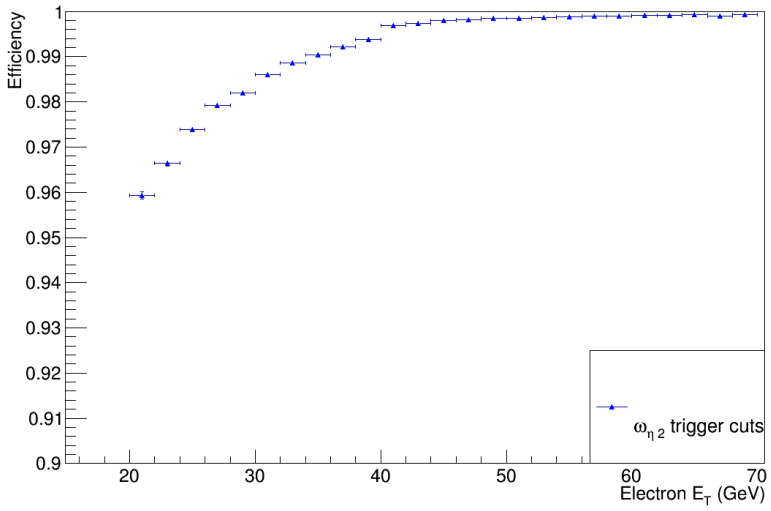



Figure 4.16: Efficiency of reconstruction of electrons as a function of $E_T$ with only the cut on $\omega_{\eta 2}$ applied.

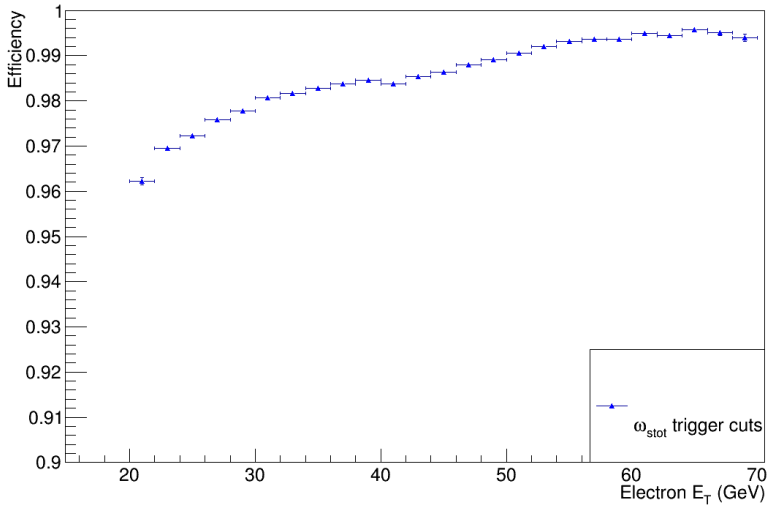



Figure 4.17: Efficiency of reconstruction of electrons as a function of $E_T$ with only the cut on $\omega_{stot}$ applied.

therefore the lowest value within the error bars is 77.844%. At $E_T = 40$ GeV, the error on the efficiency measurement is approximately 0.1%, and the highest efficiency within the error bars is 96.096%. By comparing the maximum possible inefficiency including the extremes of the error bars with the nominal inefficiency, the uncertainty on the inefficiency is calculated to be 1.4%. With a 33% reduction in inefficiency, a relative uncertainty of 0.9% would give the same result. With a smaller inefficiency, the same error on the efficiency measurement will give a smaller error on the $W$ mass measurement.

In addition, the medium trigger has tight requirements on the variables $R_\eta$ and $\omega_{\eta 2}$. As shown in Figures 4.11 and 4.12, these variables are poorly modelled in MC. They are also biased as a function of $E_T$. In the final measurement of $m_W$, care must be taken that this does not bias the calibration of the electron $E_T$.

### 4.11.3 Rates

Loosening the cuts on the medium trigger results in a higher rate as additional hadronic background passes the cuts. The loosening of the $R_\eta$ and $\omega_{\eta 2}$ cuts would result in a rate increase of 160% for the $W$ mass trigger, with respect to the existing medium trigger. An

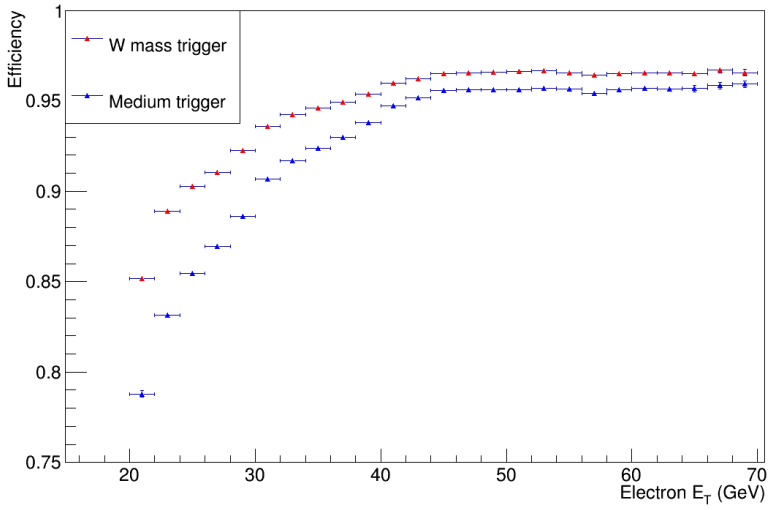



Figure 4.18: Efficiency of reconstruction of electrons of the medium trigger and the proposed $m_W$ trigger.

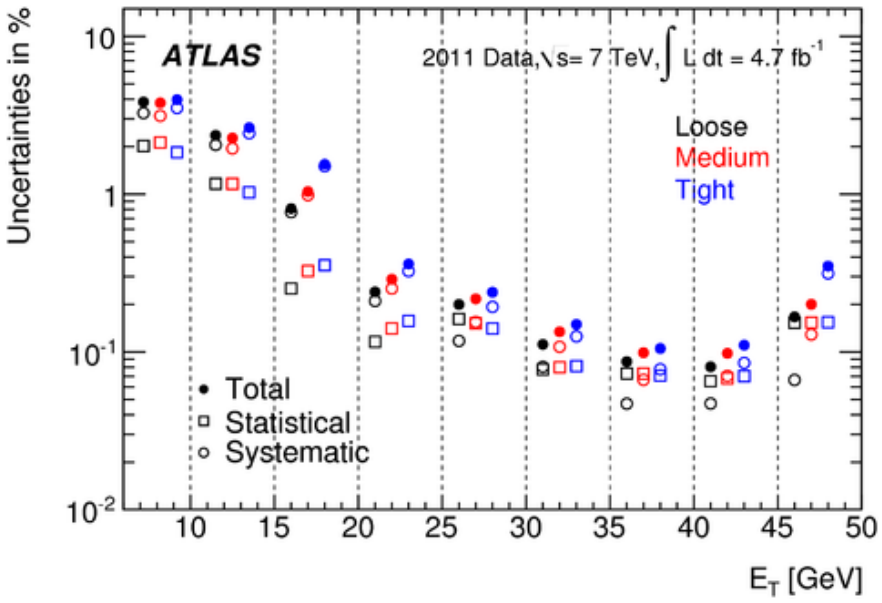



Figure 4.19: The statistical, systematic and total uncertainty on the scale factors as a function of $E_T$. Some points are shifted within the $E_T$ bin horizontally for better visibility [98].

| | **Loose** | **Medium** | **Tight** | **W mass** |
|---|---|---|---|---|
| $\lvert R_{had}\rvert <$ | 0.012 | 0.010 | 0.010 | 0.010 |
| $R_{eta} >$ | 0.910 | 0.930 | 0.930 | 0.910 |
| $\omega_{stot} <$ | 2.90 | 2.50 | 2.50 | 2.50 |
| $\omega_{\eta 2} <$ | 0.013 | 0.011 | 0.011 | 0.013 |
| $E_{ratio} >$ | 0.800 | 0.835 | 0.835 | 0.835 |
| $N_{pix} >=$ | 1 | 1 | 1 | 1 |
| $N_{Si} >=$ | 7 | 7 | 7 | 7 |
| $\Delta\eta <$ | 0.015 | 0.005 | 0.005 | 0.005 |
| $\Delta\phi$ | - | - | -0.03 to 0.01 | - |
| $N_B =$ | - | 1 | 1 | 1 |
| $\lvert d_0\rvert <$ | - | 5 | 1 | 1 |
| TRT HT hits ratio $>$ | - | 0.05 | 0.08 | 0.05 |
| $N_{TRT} >=$ | - | - | 32 | - |

Table 4.4: Typical cuts on each variable for the loose, medium, tight and W mass selections for electrons with $25 < E_T < 32$ GeV and $0.1 < |\eta| < 0.6$.

estimate of the rates of the triggers was performed by running over a sample of minimum bias events that passed the Level 1 triggers (also known as enhanced bias). Insufficient bandwidth was available to use this trigger in 2011. Combining the $W$ mass trigger with an additional cut on missing $E_T > 15$ GeV could reduce this percentage to 41.7% (or 22.7% for missing $E_T > 20$ GeV and 12.8 % for $> 25$ GeV). However, the missing $E_T$ trigger itself had a bias in efficiency as a function of $E_T$ in this region, as can be seen in Figure 4.20.

### 4.11.4 Outcome

Unfortunately, the $m_W$ trigger was not implemented in 2011 or 2012 due to rate considerations. However, this study of electron identification variables can be used to inform trigger design for data taking in the future. The next run of the Large Hadron Collider will have similar rate constraints, but the $m_W$ trigger could be used during low luminosity runs, or for low luminosity bunches. Low luminosity runs will probably be necessary to improve on any measurements of $m_W$ using the existing 2011 data.

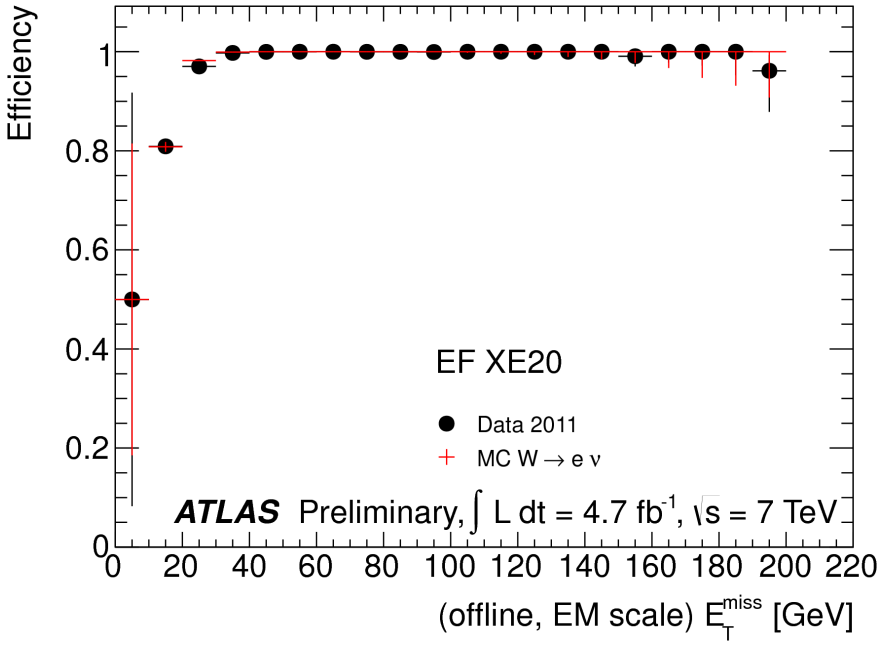



Figure 4.20: Efficiency of the Missing $E_T > 20$ GeV trigger as a function of Missing $E_T$ [99].

# Chapter 5

# Electron energy calibration

## 5.1 Electron calibration overview

$W$ and $Z$ bosons are used to calibrate the electron energy measurements performed with the electromagnetic calorimeter. The $Z$ boson decays to two electrons and has a well known mass, measured with great accuracy by previous experiments. Therefore, a comparison of the invariant mass peak between data and Monte Carlo can be used to calibrate the absolute energy scale of the electromagnetic calorimeter. A testbeam of electrons with energy varying from 10 to 245 GeV was also used to calibrate the calorimeter modules pre-data taking. In this chapter, I will discuss the overall electron energy-scale calibration at ATLAS, followed by an in-depth description of my contributions to this work.

## 5.2 Electron energy calculation

The calibration hits method is used to calculate the electron energy. Starting from the electron energy estimation from the energy measured in the calorimeter layers, this method applies four corrections derived from simulation and test beam data to reach a final estimation [100]. The corrections are as follows: correction for the energy lost in front of the calorimeter, the sampling fraction correction, the out-of-cluster correction and a correction

for longitudinal leakage. For $|\eta| < 1.8$, information from the presampler is available and the particle energy is reconstructed according to the following formula:

$$E_{e,\gamma} = \underbrace{a(E_{tot}^{Acc}, |\eta|) + b(E_{tot}^{Acc}, |\eta|) \times E_{ps}^{raw} + c(E_{tot}^{Acc}, |\eta|) \times (E_{ps}^{raw})^2}_{\text{Energy in front}} + \underbrace{\frac{s_{cl}^{Acc}(X,\eta)}{f_{out}(X,|\eta|)} \times \left(\sum_{i=1,3} E_i^{cl}\right)}_{\text{Energy in the Accordion}} \times \underbrace{(1 + f_{leak}(X,|\eta|))}_{\text{Longitudinal leakage}} \times \underbrace{F(|\eta|,\phi)}_{\text{Energy modulation}} \tag{5.1}$$

The terms in the above equation are defined as follows. $E_{e,\gamma}$ represents the energy of the electron or photon being reconstructed. The $a$, $b$ and $c$ terms are determined using simulation as a function of energy deposited in the accordion (the first, second and third samplings of the ECal). Using the energy deposited in the accordion, $E_{tot}^{Acc}$, the presampler energy, $E_{ps}^{raw}$, is corrected by an offset, $a$, and a slope, $b$. A quadratic coefficient, $c$, is only applied for $1.5 < |\eta| < 1.8$. This first term gives the calibrated presampler energy. $X$ is the longitudinal barycentre of the shower, also known as the shower depth. It is defined by Equation 5.2.

$$X = \frac{\sum_{i=0}^{3} E_i^{clLAr} X_i}{\sum_{i=0}^{3} E_i^{clLAr}} \tag{5.2}$$

$E_i^{clLAr}$ represent the energy deposited in the presampler ($i$=0) and the three sections of the calorimeter - strip, middle and back ($i$ = 1,2,3). $X_i$ is the depth in radiation lengths from the centre of ATLAS to the longitudinal centre of each of these parts of the subdetector. $s_{cl}^{Acc}(X,\eta)$ corrects for the sampling fraction of the calorimeter, which is the fraction of active material in the calorimeter. $f_{out}(X,|\eta|)$ corrects for energy deposited in the calorimeter from an electron or photon that falls outside of our cluster definition, as the shower may not be fully contained in the $\eta$ window chosen for clusters. The longitudinal leakage (i.e. when the shower extends beyond the electromagnetic calorimeter) is corrected for with $f_{leak}(X,|\eta|)$. $F(|\eta|,\phi)$ corrects for energy modulation as a function of the impact point inside a cell, and represents the alternating of lead absorbers and active LAr regions as a function of $\phi$. The variation in $\phi$ arises from the accordion geometry of the calorimeter. Incident particles will cross a varying amount of absorber material in $\phi$, which is adjusted for by this correction.

For the region where there is no presampler ($|\eta| > 1.8$), the energy deposited in front of the calorimeter is estimated using a parameterisation of $X$ (Equation 5.2) (which is calculated using only the main calorimeter).

## 5.3 Data-driven energy calibration

The calibration hits method transforms the reconstructed energy measured in the calorimeter cluster into an estimate of the true energy. However, all the constants have been determined using the simulation. Hence, this method relies upon correct modelling of the passive material in front of the calorimeter, accurate intercalibration of the calorimeter layers and correct estimation of the energy fraction that escapes the calorimeter cluster. The absolute scale of the calorimeter is set using the $Z \rightarrow$ ee resonance in data. The relation between the energy measured in data and the energy measured in Monte Carlo can be represented by Equation 5.3 where $i$ is a range in pseudorapidity, independent of particle type and energy. If one of the above is incorrectly simulated, additional corrective terms will need to be added.

$$E_{correctedMC} = E_{MC}(1 + \alpha_i) \tag{5.3}$$

Both $W$'s and $Z$'s are used in the data-driven energy calibration. $Z$'s tend to be used to set the absolute energy scale and resolution, whereas $W$'s are used to test the uniformity and linearity of the scale. The stability and uniformity of the calorimeter refers to its response with respect to time, level of pileup, $\eta$ and $\phi$. Linearity refers to its response with respect to energy. If the response of the calorimter is non-linear, additional terms would need to be added to Equation 5.3.

## 5.4 Energy resolution

The expected resolution function for the Electromagnetic Calorimeter is shown in Equation 5.4.

$$\sigma_{MC}(E,\eta) = a(\eta) \times \sqrt{E} \oplus b(\eta) \oplus c(\eta) \times E \tag{5.4}$$

The sampling term $a(\eta)$ is assumed to be well modelled by simulation, and depends upon the type of absorber, active material and the thickness of sampling layers of the calorimeter. During pre-data taking calibration runs, the noise term $b(\eta)$ was measured and included in the simulations. Hence, the additional resolution correction is proportional to the energy, as shown in Equation 5.5.

$$\sigma_{corr}(E,\eta) = \sigma_{MC}(E,\eta) \oplus c_{data}(\eta) \times E \tag{5.5}$$

Two complementary methods are used to determine $c_{data}$, in six broad pseudorapidity ranges. The first uses the invariant mass distribution from $Z \rightarrow$ ee events. The distribution is fitted with a Breit-Wigner convoluted with a Crystal-Ball function. A Crystal-Ball function is defined by Equations 5.6− 5.11 [101]. The parameters of the Breit-Wigner are fixed to the world averages from the Particle Data Group [10]. The $\sigma$ of the Crystal-Ball function is the energy resolution. $\overline{x}$, $\alpha$, $\sigma$ and $n$ are all free parameters of the fit.

$$f(x;\alpha,n,\overline{x},\sigma) = N \cdot \begin{cases} \exp(-\frac{(x-\bar{x})^2}{2\sigma^2}), & \text{for } \frac{x-\bar{x}}{\sigma} > -\alpha \\ A \cdot (B - \frac{x-\bar{x}}{\sigma})^{-n}, & \text{for } \frac{x-\bar{x}}{\sigma} \leqslant -\alpha \end{cases} \tag{5.6}$$

$$A = \left(\frac{n}{|\alpha|}\right)^{n} \cdot \exp\left(-\frac{|\alpha|^2}{2}\right) \tag{5.7}$$

$$B = \frac{n}{|\alpha|} - |\alpha| \tag{5.8}$$

$$N = \frac{1}{\sigma(C+D)} \tag{5.9}$$

$$C = \frac{n}{|\alpha|} \cdot \frac{1}{n-1} \cdot \exp\left(-\frac{|\alpha|^2}{2}\right) \tag{5.10}$$

$$D = \sqrt{\frac{\pi}{2}}\left(1 + \mathrm{erf}\left(\frac{|\alpha|}{\sqrt{2}}\right)\right) \tag{5.11}$$

Equation 5.12 is used to extract the constant terms, where $M_Z$ is the $Z$ mass and $\sigma$ is the resolution from the Crystal-Ball function. Electrons from $Z$ decay may be in different bins in $\eta$, which are represented by $i$ and $j$. The fits are performed for each possible value of $i$ and $j$, covering every possible configuration of pairs of electron $\eta$ bins.

$$c^2_{i,j,data} = 2 \times [(\frac{\sigma_M}{M_Z})^2_{i,j,data} - (\frac{\sigma_M}{M_Z})^2_{i,j,MC}] \tag{5.12}$$

The second method is a template method. A series of template histograms are made from Monte Carlo with $c$ varied between 0 and 5%. Templates are produced for each $i$ and $j$. The outcome of $\chi^2$ comparisons between data and each template are plotted against the values of $c$, and the minimum of the resulting parabola is the energy resolution correction.

## 5.5 Absolute energy scale

The mass of a reconstructed $Z \rightarrow$ ee candidate is defined by Equation 5.13, where $E_i$, $\eta_i$ and $\phi_i$ are the energy, pseudorapidity and azimuthal angle, respectively.

$$M = \sqrt{2E_1E_2(\cosh(\eta_1 - \eta_2) - \cos(\phi_1 - \phi_2))} \tag{5.13}$$

As there are two electrons which may be in a different eta range to each other, using Equation 5.3 and neglecting second-order corrections and the uncertainty in the angle of the electrons,

the dielectron invariant mass is:

$$M_{ij}^{correctedMC} \approx M_{ij}^{MC}(1 + \frac{\alpha_i + \alpha_j}{2}) = M_{ij}^{MC}(1 + \beta_{ij}) \tag{5.14}$$

The event sample is split into bins of $(\eta_i, \eta_j)$ and a $\beta_{ij}$ correction is found for each combination of pairs of electrons. Two complementary methods are used to calculate the set of $\beta_{ij}$ : the log likelihood method and the template method. The first involves minimising the unbinned log likelihood, as calculated in Equation 5.15, where $1 < i, j < N_\eta$.

$$-\ln L_{tot} = \sum_{k=1}^{N_{events}} -\ln L_{ij} \frac{M_k}{1 + \beta_{ij}} \tag{5.15}$$

$N_\eta$ is the number of $\eta$ regions being considered and $N_{events}$ is the total number of events in the selection. $L_{ij}$ is the probability density function, which quantifies the compatibility of an event with the expected $Z$ boson line shape at the reconstruction level, with two electrons that fall into the $\eta$ regions $i$ and $j$. $L_{i,j}(M)$ are produced from Monte Carlo simulation for each $i$ and $j$ combination, taking into account theoretical and experimental effects defining the $Z$ mass lineshape. Theoretical effects arise from the relativistic Breit-Wigner shape, interference with and contributions from $\gamma*$, parton density functions, final-state radiation and the shape of the $p_T^Z$ distribution. The experimental effects are described in the previous sections in this chapter. As the histograms from Monte Carlo are not continuous, they are smoothed.

The template method is also used. Over a range of values of the energy scale, a series of template histograms are made from Monte Carlo simulation. Templates are produced for each $i$ and $j$. $\chi^2$ tests are performed between the data and template histograms in each $i, j$ bin. The $\chi^2$ is plotted against the energy scale for each template, and a parabola fitted. The minimum and shape of the parabola give $\beta_{i,j}$ and its uncertainty. Finally, the series of linear equations relating $\beta_{ij}$ to $\alpha_i$ and $\alpha_j$ are solved for $\alpha_i$ and $\alpha_j$.

## 5.6 $E/p$ fits

The energy of electrons is measured both as $E$ in the electromagnetic calorimeter and as $p$ in the inner detector. The $p$ measurement in the inner detector is well calibrated, using $Z$ boson and $J/\Psi$ meson decays to two muons. Muons are a comparitively clean signal, as significantly less QCD background can penetrate to the muon spectrometer. Hence, the invariant mass peaks can be used to calibrate as with electrons, but with less uncertainty on background leading to smaller systematic errors on the inner detector $p$ scale (when compared to the electromagnetic calorimeter $E$ scale). The $E/p$ distribution is used to test the uniformity and linearity of the calorimeter energy measurement. Two complementary methods are used: the convolution method and the template method. I performed tests of linearity and uniformity using the template method, and this shall be described at the end of the chapter.

The convolution method utilises Monte Carlo simulations of electrons and positrons to extract detector response distributions of $E/E_0$, where $E$ is reconstructed energy and $E_0$ is the true energy, as illustrated in Figure 5.1. The distribution was fitted using a Gaussian core convoluted with an exponential tail. The exponential tail arises from the loss of energy by electrons that undergo bremsstrahlung and subsequent photon conversion when traversing material before they reach the calorimeter. Additional terms derived from Crystal-Ball functions were found to improve the description of the tails [101]. A similar distribution was made for $p/p_0$ (Figure 5.2), which was fitted with a Crystal-Ball function.

The two distributions are convoluted to obtain a fit function for the $E/p$ distribution. The correlations between the two were accounted for using Monte Carlo simulation. The result is a mean $\mu_e$ and a width $\sigma_e$ from the fit function, with all other parameters fixed to their Monte Carlo values. The mean $\mu_e$ divided by the mean from the $E/E_0$ fit gives the deviation from the ideal energy scale assumed in the Monte Carlo. This fitting procedure is performed in bins of $E$ and $\eta$.

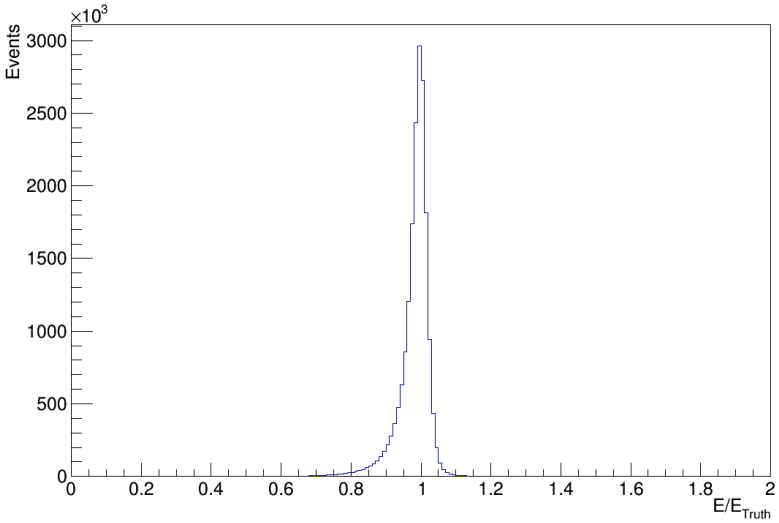



Figure 5.1: The ratio of reconstructed electron energy to the truth level electron energy in Monte Carlo.

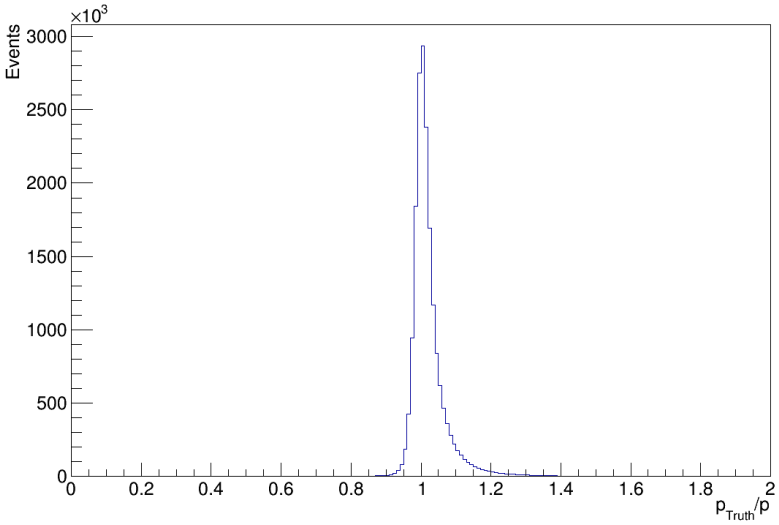



Figure 5.2: The ratio of truth level electron momentum to the reconstructed electron momentum in Monte Carlo.

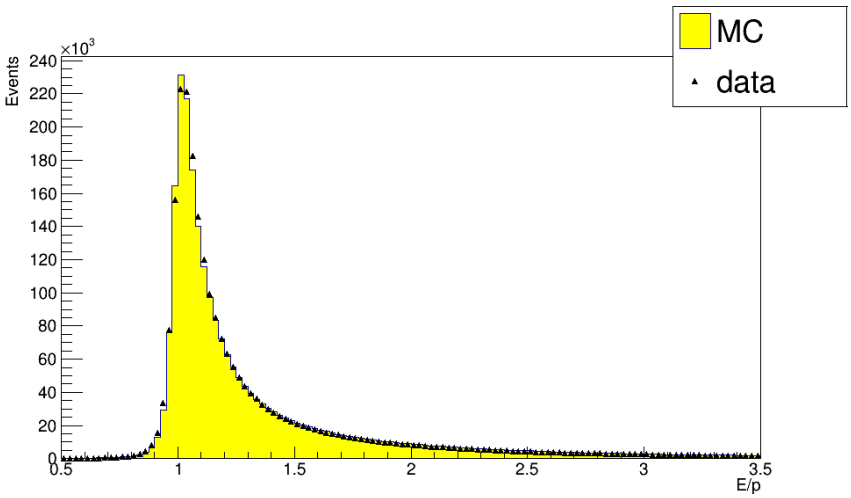



Figure 5.3: $E/p$ distribution showing data and Monte Carlo for both $W$ and $Z$ events. No data-driven calibration corrections have been applied.

## 5.7 Uniformity and linearity: $E/p$ template method

The $E/p$ distribution can be seen in Figure 5.3. The peak of the distribution is approximately at 1, where the electron $E$ (measured in the electromagnetic calorimeter) and $p$ (measured in the inner detector) measurements match exactly. Events in the long tail arise when the electron has undergone bremsstrahlung within the ID. The photon carries away energy, resulting in a lower momentum being measured in the ID. The electromagnetic calorimeter measures electron energy in groups of cells that are longer in the $\phi$ direction than the $\eta$ direction, resulting in the photon forming part of the electromagnetic cluster and contributing to the $E$ measurement. Events with $E/p$ of slightly less than 1 occur when the electron energy has been mismeasured in the electromagnetic calorimeter or has penetrated through to the hadronic calorimeter.

The $E/p$ distribution can be used to calibrate the scale of the electromagnetic calorimeter and also to constrain (or validate) the amount of material in the inner detector. The peak is used to compare the scales of the calorimeter and the well calibrated inner detector, whereas the tail provides a measure of the rate of bremsstrahlung occuring in the inner detector. This rate is directly proportional to the amount of material in the inner detector. Hence, if the level of material in the inner detector is mismodelled in the Monte Carlo, a comparison between data and Monte Carlo of the tails can quantify the level of this disagreement.

| $Z \to ee$ **event selection** |
|---|
| **Electron cuts** |
| Electron $\|\eta\| < 2.47$ and not in dead $\eta$ region of calorimeter |
| 'Green' electron data quality |
| Medium electron identification cuts |
| **Event cuts** |
| Exactly 2 electrons |
| Electron $E_T > 25$ GeV |
| Opposite charge |
| $66 < M_{ee} < 116$ GeV |

Table 5.1: $Z \to ee$ event selection for $E/p$ studies. This selects 1263204 events in data and 5349182 events in Monte Carlo.

| $W \to e\nu$ **event selection** |
|---|
| **Electron cuts** |
| Electron $\|\eta\| < 2.47$ and not in dead $\eta$ region of calorimeter |
| 'Green' electron data quality |
| Tight electron identification cuts |
| **Event Cuts** |
| Exactly 1 electron |
| Electron $E_T > 30$ GeV |
| Missing $E_T > 30$ GeV |
| Transverse Mass $> 60$ GeV |

Table 5.2: $W \to e\nu$ event selection for $E/p$ studies. This selects 2194083 events in data and 7943111 events in Monte Carlo.

### 5.7.1 Event selection

A standard $Z \to ee$ and $W \to e\nu$ event selection is used, as summarised in Tables 5.1 and 5.2 respectively. The Monte Carlo events are reweighted such that the $p_T$ of the $Z$ distribution matches the data.

### 5.7.2 Method

The $E/p$ distribution is used to measure the uniformity and linearity of the calorimeter energy response. In order to measure the linearity, the distribution is plotted in bins of $E_T$. Four bins are used for 25 GeV $< E_T <$ 100 GeV. As there is significant variation in the amount of material in front of the calorimeter at each $\eta$, the linearity must be measured as a function of $\eta$. Twenty five bins in $\eta$ are used, so there are 100 $(\eta, E_T)$ bins altogether.

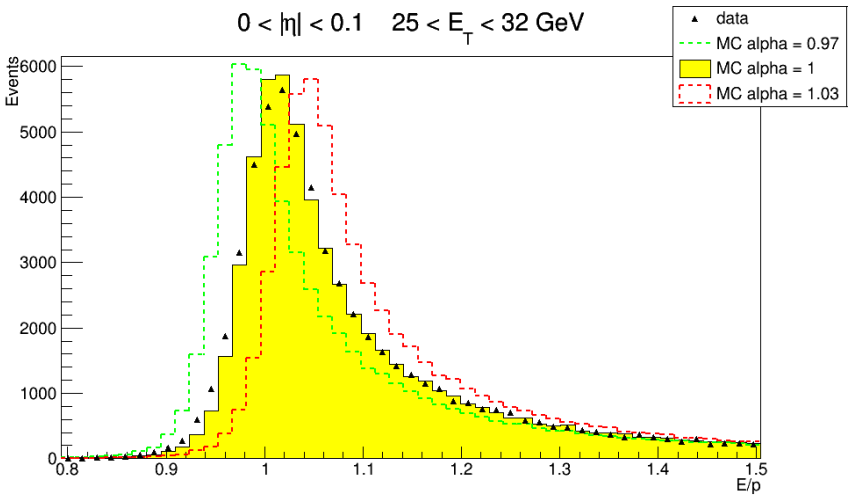



Figure 5.4: $E/p$ distribution showing data and Monte Carlo. Monte Carlo shown with nominal scaling (histogram with yellow fill), and with $\alpha$ of 0.97 (green dotted line) and 1.03 (red dotted line).

Within each bin, 100 different templates are generated from Monte Carlo. In each template, the $E$ of the distribution is scaled by a different $\alpha$, whereas the $p_T$ of the distribution is left unscaled. 60 templates are used with $\alpha$ ranging from 0.97 to 1.03. Examples of an $E/p$ distribution with nominal scaling, $\alpha = 0.97$ and $\alpha = 1.03$ are shown in Figure 5.4.

For each template within each bin, a $\chi^2$ test is performed between the data and the Monte Carlo template. The $\chi^2$ of each template is plotted as a function of the $\alpha$ of that template; an example is shown in Figure 5.5. The resulting graph is fitted with a parabola. The best fitting parabola or cubic is used to provide the minimum ($b$) of the distribution and the error on that minimum ($c$). The cubic term can assist in providing a better fit when the fit range extends far beyond the minima and the points no longer describes a parabola.

Systematics were generated by varying the range of the $E/p$ distribution used in the $\chi^2$ test and by varying the range used in fitting the parabola to the $\chi^2$ vs $\alpha$ distributions. The different ranges of $E/p$ used were as follows: 0.8−2.2, 0.8−2.0, 0.8−1.8, 0.8−1.6, 0.8−1.4, 0.8−1.2, 0.85−2.2 and 0.95−2.2. The different fit ranges used when fitting the parabola were 0.97-1.03, 0.975-1.025, 0.98-1.02 and 0.975-1.015. Any difference in the resulting minimal $\alpha$ is taken as the systematic. The variations in $E/p$ range used are shown in Figures 5.6 and 5.7, and fit range in Figure 5.8. The variations in the $E/p$ range above the peak are a measure of the systematic error arising from the passive material in front of the calorimeter. Using a

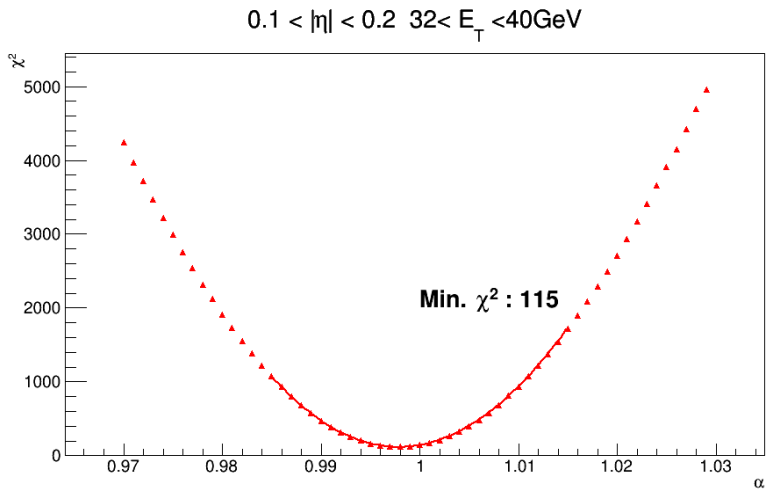



Figure 5.5: $\chi^2$ for each $\alpha$ for $0.1 < \eta < 0.2$ and 40 GeV $< E_T <$ 50 GeV. Minimum of the fit shows the best fit $\alpha$ between data and MC. The range used to fit the parabola was 0.975-1.015

different amount of the $E/p$ tail, the region most strongly affected by bremsstrahlung due to passive material, tests the bias due to differences in the material description in Monte Carlo compared to the actual material in the detector. Varying the $E/p$ range sampled below the peak ensures that modelling of any leakage into the hadronic calorimeter does not bias the result.

The width of the $E/p$ distributions in data is actually larger than in Monte Carlo. Therefore, it must be checked whether this leads to a systematic bias of the scale. Such a check is performed by smearing momentum scale in the ID by a correction derived from fits to the $Z \to \mu\mu$ invariant mass peak [102]. The $1/p$ distribution was smeared with a gaussian with a width of 0.009 to correct for a small ID misalignment. By performing all fits with and without this smearing, the systematic error arising from this small misalignment can be estimated. This check is also a measure of the sensitivity of the analysis to the resolution of the $E/p$ distribution. The fit of the $\chi^2$ tests as a function of $\alpha$ can be seen in Figure 5.9 and the $E/p$ distributions with the optimal $\alpha$ found from the $\chi^2$ fit for both the smeared and the nominal $E/p$ distribution can be seen in Figure 5.10 for one $\eta$, $E_T$ bin. An example of the linearity plot for both smeared and nominal results can be seen in Figure 5.11. The systematic uncertainty is taken to be the maximum deviation up or down from the nominal for all different ranges of E/p, fit ranges of the parabola and the smearing.

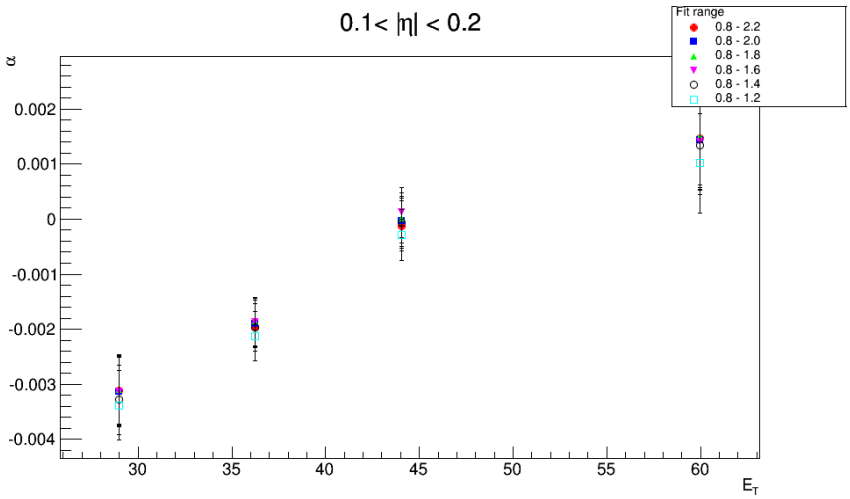



Figure 5.6: Change in $\alpha$ with different upper bands on the fit range of the $E/p$ distribution for $0.1 < |\eta| < 0.2$.

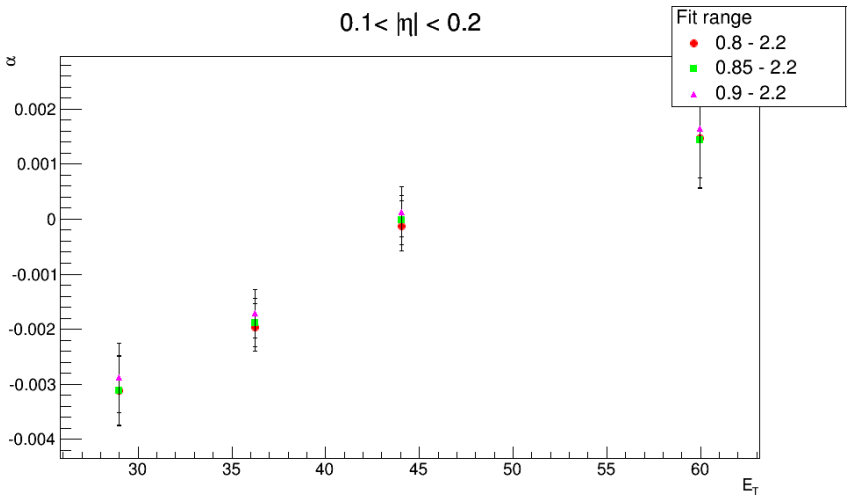



Figure 5.7: Change in $\alpha$ with different lower bands on the fit range of the $E/p$ distribution for for $0.1 < |\eta| < 0.2$.

Table 5.3 shows the energy scale in bins of $E_T$ and $\eta$, with the relevant systematic errors (as generated by taking the most extreme result from varying the fit, ranges and added smearing to the momentum). Figure 5.12 shows the energy scale in bins of $\eta$ with each of the four different $E_T$ bins overlaid. The fits to $E/p$ are also used to test the uniformity of the calorimeter response modelling. The energy scale is calculated using the template method in bins of $|\eta|$ and bins of $\phi$. The electrons are not subdivided into bins of $E_T$ for this test, all electrons passing the selection are used. Figures 5.13 and 5.14 show the uniformity of the calorimeter response modelling. The discrepancy at $|\eta|$=0.8 arises from the increase of material at this $|\eta|$ from the services to the detector. The discrepancies at $1.37 < |\eta| <$

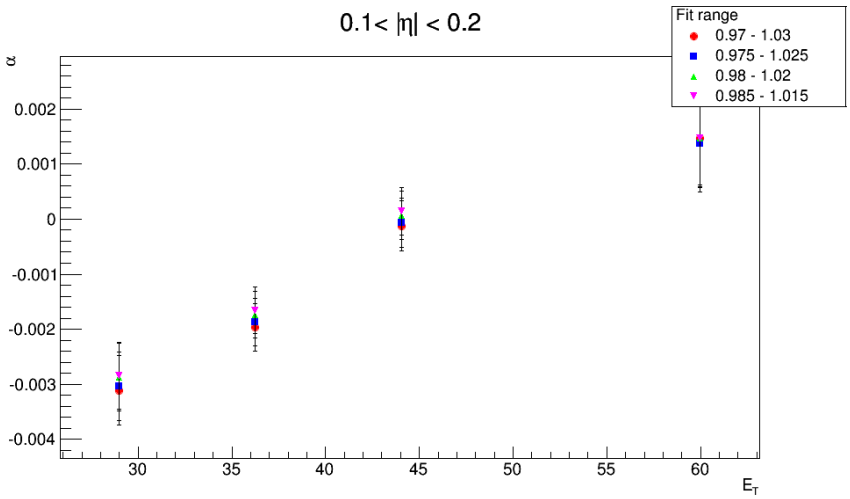



Figure 5.8: Change in $\alpha$ with change in range of $\alpha$ used in the polynomial fit to find the $\chi^2$ minimum for $0.1 < |\eta| < 0.2$.

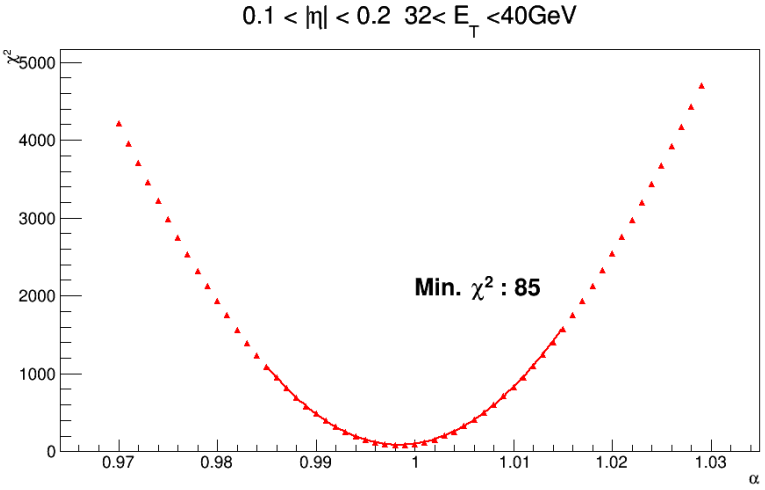



Figure 5.9: $\chi^2$ for each $\alpha$ for $0.1 < \eta < 0.2$ and 40 GeV $< E_T <$ 50 GeV, with the momentum scale smearing applied to the $E/p$ distribution. Minimum of the fit shows the best fit $\alpha$ between data and MC. The range used to fit the parabola was 0.975-1.015. The fit is shown by the red line.

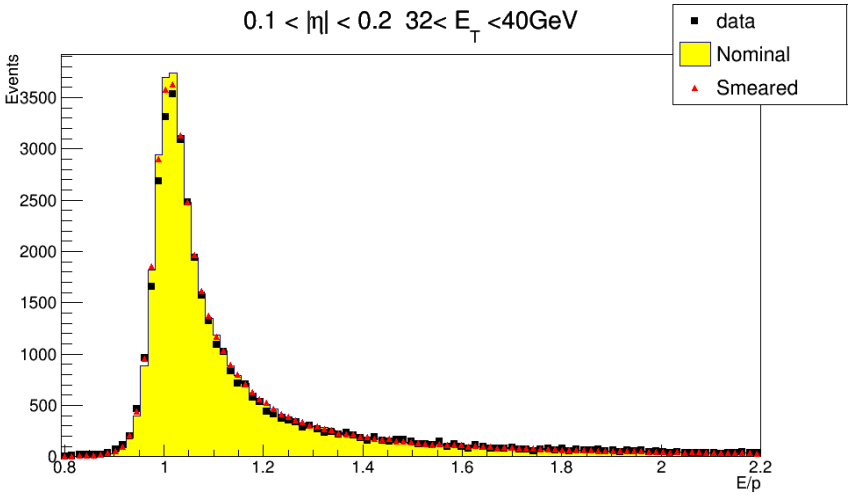



Figure 5.10: Smeared and nominal $E/p$ distribution for the optimal $\alpha$ correction found using the $\chi^2$ fits above for $0.1 < \eta < 0.2$ and 40 GeV $< E_T <$ 50 GeV.

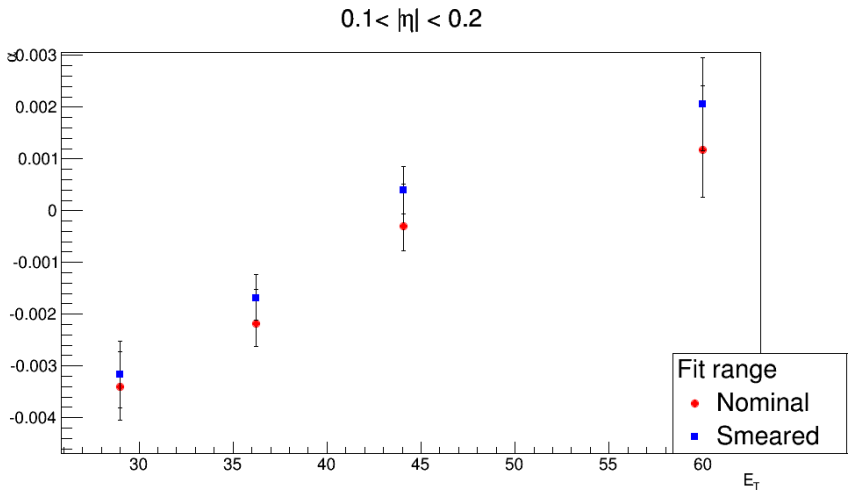



Figure 5.11: Change in $\alpha$ for nominal and smeared $E/p$ distributions for $0.1 < |\eta| < 0.2$.

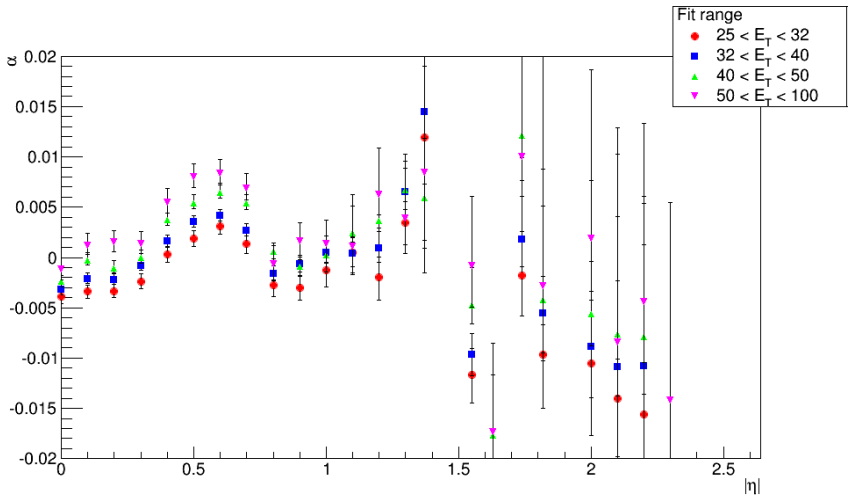



Figure 5.12: $\alpha$ for each $\eta$ and $E_T$ bin overlaid.

| | $25 < E_T < 32$ GeV | $32 < E_T < 40$ GeV | $40 < E_T < 50$ GeV | $50 < E_T < 100$ |
|---|---|---|---|---|
| $0 < \|\eta\| < 0.1$ | $-0.0039\ ^{+0.0007}_{-0.0007}$ | $-0.0032\ ^{+0.0006}_{-0.0005}$ | $-0.0024\ ^{+0.0007}_{-0.0005}$ | $-0.0012\ ^{+0.0011}_{-0.0010}$ |
| $0.1 < \|\eta\| < 0.2$ | $-0.0034\ ^{+0.0007}_{-0.0006}$ | $-0.0022\ ^{+0.0007}_{-0.0004}$ | $-0.0003\ ^{+0.0008}_{-0.0005}$ | $0.0012\ ^{+0.0012}_{-0.0009}$ |
| $0.2 < \|\eta\| < 0.3$ | $-0.0033\ ^{+0.0007}_{-0.0006}$ | $-0.0022\ ^{+0.0006}_{-0.0005}$ | $-0.0011\ ^{+0.0008}_{-0.0005}$ | $0.0015\ ^{+0.0012}_{-0.0009}$ |
| $0.3 < \|\eta\| < 0.4$ | $-0.0024\ ^{+0.0007}_{-0.0007}$ | $-0.0009\ ^{+0.0006}_{-0.0005}$ | $-0.0001\ ^{+0.0008}_{-0.0005}$ | $0.0013\ ^{+0.0013}_{-0.0009}$ |
| $0.4 < \|\eta\| < 0.5$ | $0.0003\ ^{+0.0007}_{-0.0007}$ | $0.0016\ ^{+0.0006}_{-0.0005}$ | $0.0037\ ^{+0.0008}_{-0.0005}$ | $0.0054\ ^{+0.0014}_{-0.0010}$ |
| $0.5 < \|\eta\| < 0.6$ | $0.0019\ ^{+0.0008}_{-0.0008}$ | $0.0035\ ^{+0.0006}_{-0.0005}$ | $0.0054\ ^{+0.0008}_{-0.0005}$ | $0.0080\ ^{+0.0014}_{-0.0011}$ |
| $0.6 < \|\eta\| < 0.7$ | $0.0031\ ^{+0.0009}_{-0.0008}$ | $0.0041\ ^{+0.0007}_{-0.0005}$ | $0.0064\ ^{+0.0009}_{-0.0006}$ | $0.0083\ ^{+0.0014}_{-0.0011}$ |
| $0.7 < \|\eta\| < 0.8$ | $0.0014\ ^{+0.0010}_{-0.0010}$ | $0.0027\ ^{+0.0007}_{-0.0006}$ | $0.0054\ ^{+0.0009}_{-0.0006}$ | $0.0069\ ^{+0.0015}_{-0.0012}$ |
| $0.8 < \|\eta\| < 0.9$ | $-0.0028\ ^{+0.0012}_{-0.0011}$ | $-0.0016\ ^{+0.0008}_{-0.0007}$ | $0.0006\ ^{+0.0009}_{-0.0007}$ | $-0.0007\ ^{+0.0019}_{-0.0016}$ |
| $0.9 < \|\eta\| < 1$ | $-0.0030\ ^{+0.0011}_{-0.0012}$ | $-0.0007\ ^{+0.0009}_{-0.0008}$ | $-0.0010\ ^{+0.0010}_{-0.0008}$ | $0.0016\ ^{+0.0018}_{-0.0018}$ |
| $1 < \|\eta\| < 1.1$ | $-0.0012\ ^{+0.0013}_{-0.0017}$ | $0.0005\ ^{+0.0012}_{-0.0010}$ | $0.0002\ ^{+0.0019}_{-0.0008}$ | $0.0014\ ^{+0.0024}_{-0.0028}$ |
| $1.1 < \|\eta\| < 1.2$ | $0.0005\ ^{+0.0015}_{-0.0020}$ | $0.0004\ ^{+0.0016}_{-0.0013}$ | $0.0024\ ^{+0.0027}_{-0.0009}$ | $0.0011\ ^{+0.0052}_{-0.0028}$ |
| $1.2 < \|\eta\| < 1.3$ | $-0.0020\ ^{+0.0021}_{-0.0023}$ | $0.0009\ ^{+0.0020}_{-0.0013}$ | $0.0036\ ^{+0.0027}_{-0.0010}$ | $0.0063\ ^{+0.0047}_{-0.0020}$ |
| $1.3 < \|\eta\| < 1.37$ | $0.0034\ ^{+0.0021}_{-0.0030}$ | $0.0065\ ^{+0.0024}_{-0.0025}$ | $0.0067\ ^{+0.0036}_{-0.0019}$ | $0.0039\ ^{+0.0057}_{-0.0026}$ |
| $1.37 < \|\eta\| < 1.47$ | $0.0119\ ^{+0.0099}_{-0.0110}$ | $0.0145\ ^{+0.0079}_{-0.0072}$ | $0.0059\ ^{+0.0060}_{-0.0042}$ | $0.0084\ ^{+0.0106}_{-0.0099}$ |
| $1.47 < \|\eta\| < 1.55$ | $-0.0275\ ^{+0.0167}_{-0.0088}$ | $-0.0327\ ^{+0.0068}_{-0.0256}$ | $-0.0302\ ^{+0.0119}_{-0.0074}$ | $-0.0209\ ^{+0.0117}_{-0.0118}$ |
| $1.55 < \|\eta\| < 1.63$ | $-0.0117\ ^{+0.0027}_{-0.0028}$ | $-0.0097\ ^{+0.0021}_{-0.0021}$ | $-0.0048\ ^{+0.0038}_{-0.0018}$ | $-0.0008\ ^{+0.0069}_{-0.0041}$ |
| $1.63 < \|\eta\| < 1.74$ | $-0.0375\ ^{+0.0067}_{-0.0054}$ | $-0.0317\ ^{+0.0044}_{-0.0077}$ | $-0.0177\ ^{+0.0060}_{-0.0022}$ | $-0.0173\ ^{+0.0088}_{-0.0031}$ |
| $1.74 < \|\eta\| < 1.82$ | $-0.0018\ ^{+0.0043}_{-0.0041}$ | $0.0018\ ^{+0.0058}_{-0.0027}$ | $0.0121\ ^{+0.0123}_{-0.0022}$ | $0.0100\ ^{+0.0184}_{-0.0040}$ |
| $1.82 < \|\eta\| < 2$ | $-0.0097\ ^{+0.0078}_{-0.0053}$ | $-0.0055\ ^{+0.0106}_{-0.0040}$ | $-0.0042\ ^{+0.0130}_{-0.0024}$ | $-0.0028\ ^{+0.0250}_{-0.0075}$ |
| $2 < \|\eta\| < 2.1$ | $-0.0105\ ^{+0.0063}_{-0.0072}$ | $-0.0088\ ^{+0.0084}_{-0.0051}$ | $-0.0056\ ^{+0.0133}_{-0.0032}$ | $0.0019\ ^{+0.0168}_{-0.0052}$ |
| $2.1 < \|\eta\| < 2.2$ | $-0.0141\ ^{+0.0118}_{-0.0057}$ | $-0.0109\ ^{+0.0150}_{-0.0028}$ | $-0.0076\ ^{+0.0179}_{-0.0024}$ | $-0.0085\ ^{+0.0214}_{-0.0116}$ |
| $2.2 < \|\eta\| < 2.3$ | $-0.0156\ ^{+0.0169}_{-0.0043}$ | $-0.0108\ ^{+0.0168}_{-0.0028}$ | $-0.0079\ ^{+0.0133}_{-0.0025}$ | $-0.0044\ ^{+0.0177}_{-0.0957}$ |
| $2.3 < \|\eta\| < 2.4$ | $-0.0282\ ^{+0.0077}_{-0.0173}$ | $-0.0270\ ^{+0.0108}_{-0.0026}$ | $-0.0242\ ^{+0.0127}_{-0.0037}$ | $-0.0142\ ^{+0.0196}_{-0.0105}$ |
| $2.4 < \|\eta\| < 2.47$ | $-0.1000\ ^{+0.0057}_{-0.0057}$ | $-0.1000\ ^{+0.0586}_{-0.0059}$ | $-0.0928\ ^{+0.0580}_{-0.0123}$ | $-0.0260\ ^{+0.0148}_{-0.0741}$ |

Table 5.3: $\alpha$ for each $E_T$ (in GeV) and $|\eta|$ bin. Errors stated here are calculated by adding the systematic and statistical errors in quadrature. The typical size of the statistical errors in the central $|\eta|$ bins is approximately 0.0005.

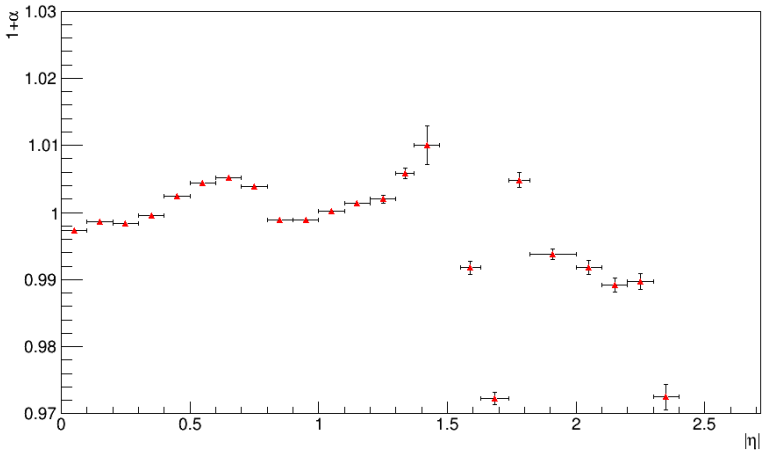



Figure 5.13: Uniformity of the calorimeter response modelling: Energy scale $\alpha$ for each $\eta$ bin for all electrons passing the selection.

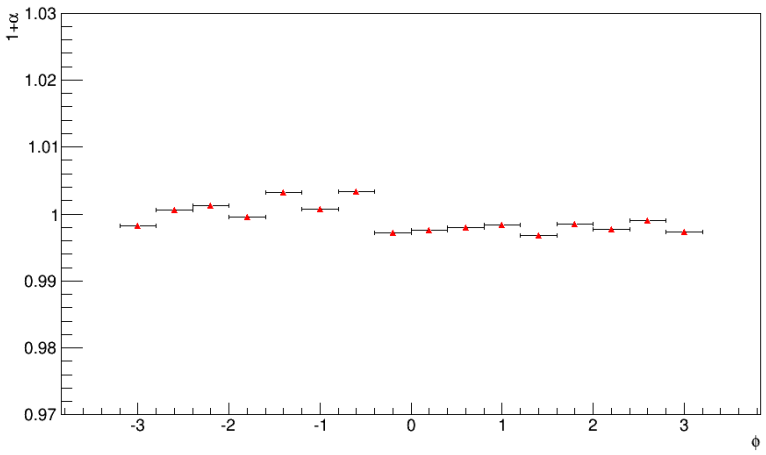



Figure 5.14: Uniformity of the calorimeter response modelling: Energy scale $\alpha$ for each $\phi$ bin for all electrons passing the selection.

1.52 are due to the crack region of the calorimeter.

### 5.7.3 Comparison with the convolution method

Both methods use exactly the same variables when calculating $E/p$ (taking the cluster energy from the calorimeter, and converting track $p_T$ to $p$ using the track $\eta$). Error bars are larger for the template method than the convolution method, as systematic and statistical errors are included for the template method, yet the convolution method has only statistical errors. The convolution method needs sufficient statistics for the fits to converge, and above $|\eta| =$

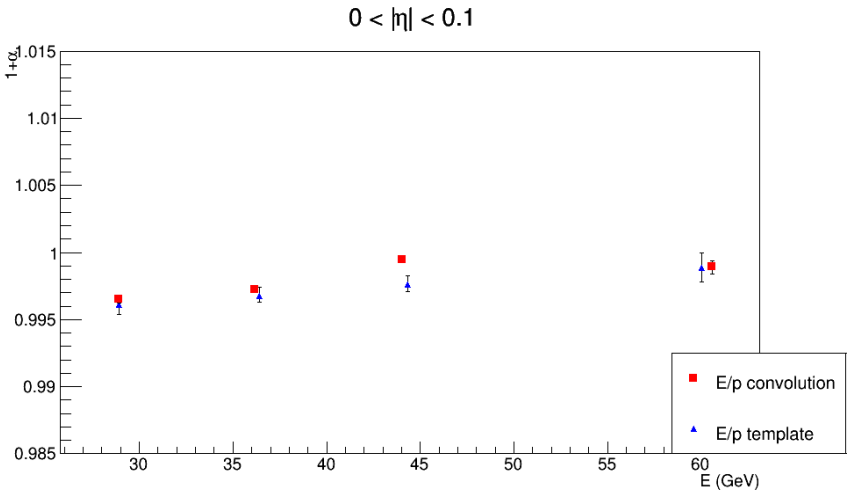



Figure 5.15: Linearity plots from the template method and the convolution method overlaid for $0 < |\eta| < 0.1$. The mean $E$ for that $E_T$ bin is used as the $x$-coordinate.

1.82, some points are not available due to non-converging fits and some of the data points that are available do not fit in with the overall trends shown by the other data points and the template method. Nevertheless, for many of the data points, the template method and the convolution method show relatively good agreement within error bars. For the highest $E$ bins at high $\eta$ the convolution method and the template method show different mean $E$ within the $E_T$ bin - possibly due to the range of the $E$ distribution used to find the mean for the convolution method. Figures 5.15 to 5.22 show linearity plots for a selection of $\eta$ bins. At $0.4 < |\eta| < 0.6$, the convolution method has higher $\alpha$'s than the template method, although shows the same trend in linearity. The discrepancies in the endcap $\eta$ bins are likely due to low statistics and large variation in the amount of material in the Inner Detector in this section of the detector.

### 5.7.4 Comparison with log likelihood method

As a cross check of the 3 methods, the energy scale was measured in bins of $E_T$ using the same log likelihood method used to set the absolute energy scale (see Section 5.5). As this method only uses $Z \rightarrow ee$ events, larger $\eta$ bins are used to ensure there are sufficient statistics. Comparisons of the results of the three methods can be seen in Figures 5.23 – 5.27. The template method is in good agreement with the log likelihood method within the

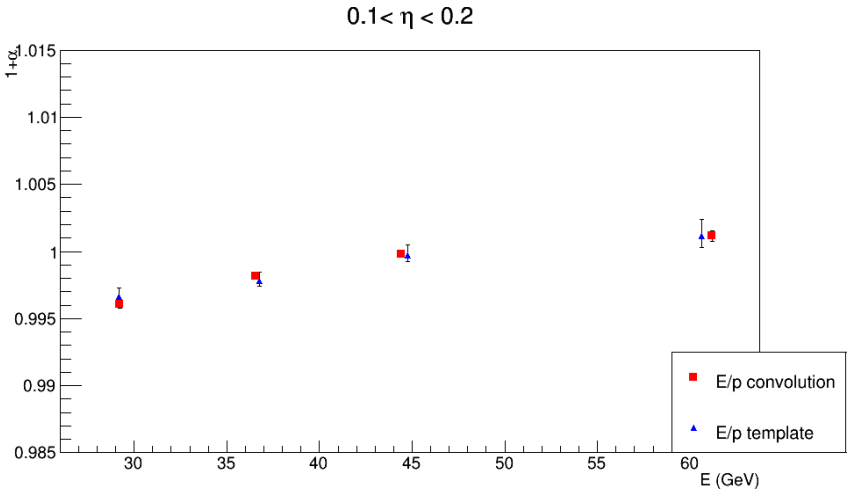



Figure 5.16: Linearity plots from the template method and the convolution method overlaid for $0.1 < |\eta| < 0.2$. The mean $E$ for that $E_T$ bin is used as the $x$-coordinate.

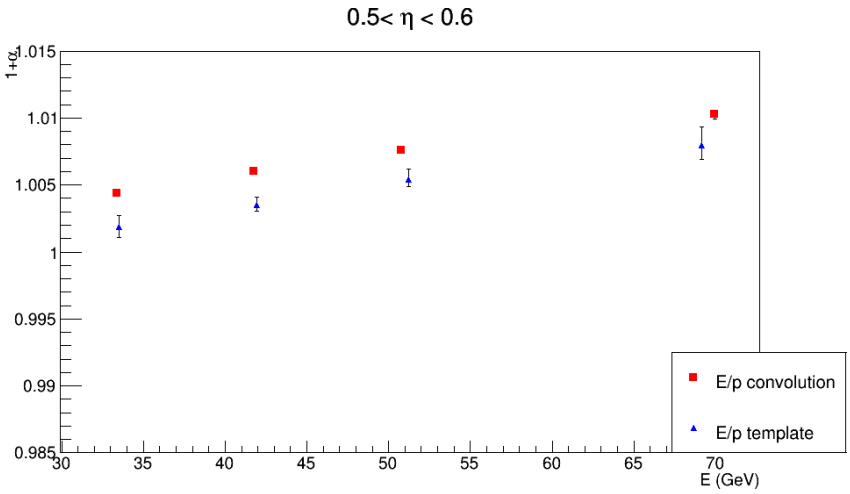



Figure 5.17: Linearity plots from the template method and the convolution method overlaid for $0.5 < |\eta| < 0.6$. The mean $E$ for that $E_T$ bin is used as the $x$-coordinate.

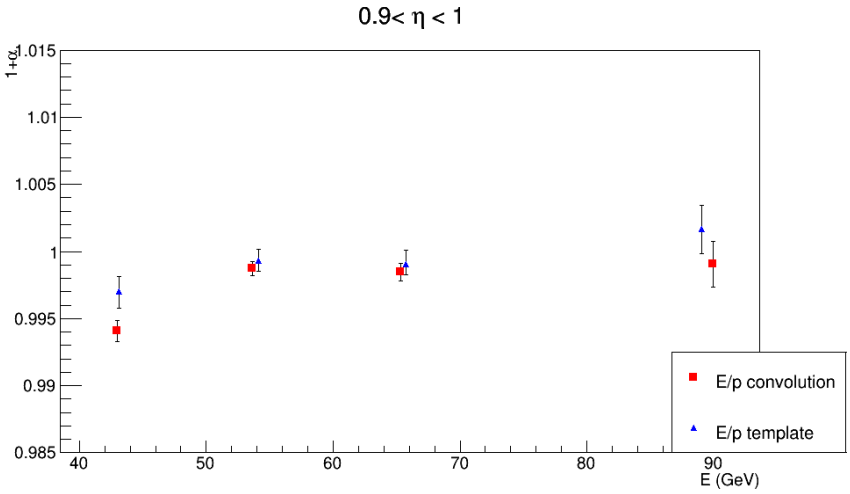



Figure 5.18: Linearity plots from the template method and the convolution method overlaid for $0.9 < |\eta| < 1$. The mean $E$ for that $E_T$ bin is used as the $x$-coordinate.

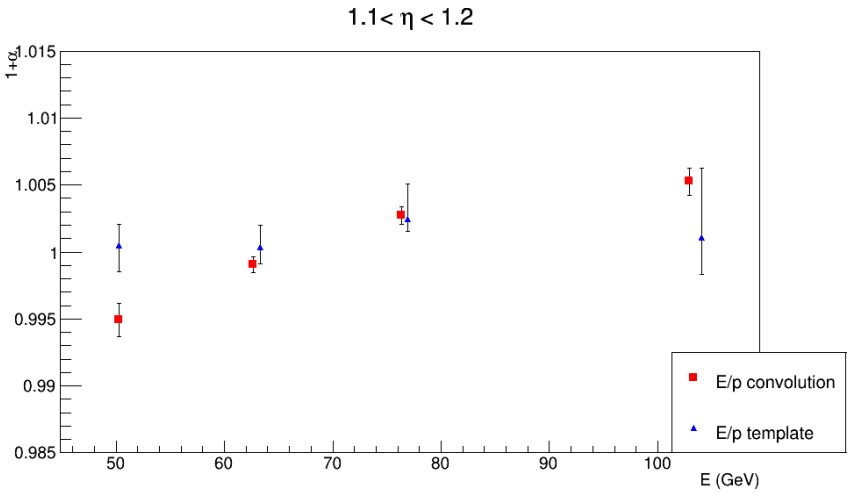



Figure 5.19: Linearity plots from the template method and the convolution method overlaid for $1.1 < |\eta| < 1.2$. The mean $E$ for that $E_T$ bin is used as the $x$-coordinate.

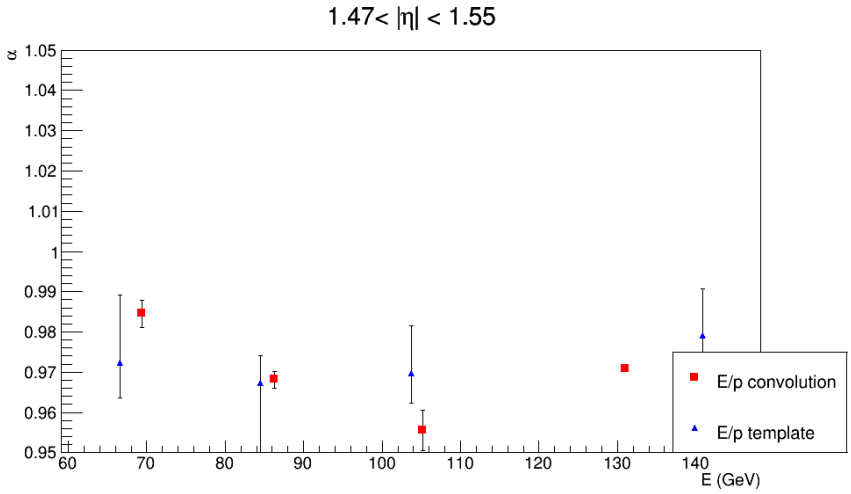



Figure 5.20: Linearity plots from the template method and the convolution method overlaid for $1.47 < |\eta| < 1.55$. The mean $E$ for that $E_T$ bin is used as the $x$-coordinate.

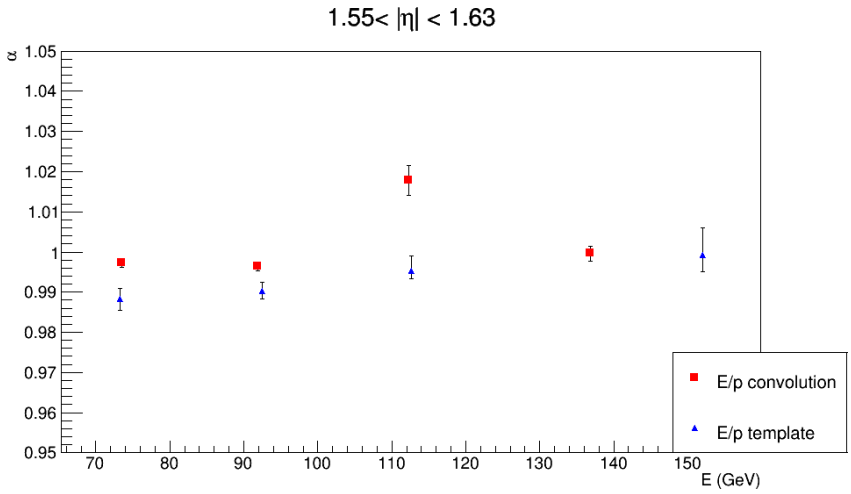



Figure 5.21: Linearity plots from the template method and the convolution method overlaid for $1.55 < |\eta| < 1.63$. The mean $E$ for that $E_T$ bin is used as the $x$-coordinate.

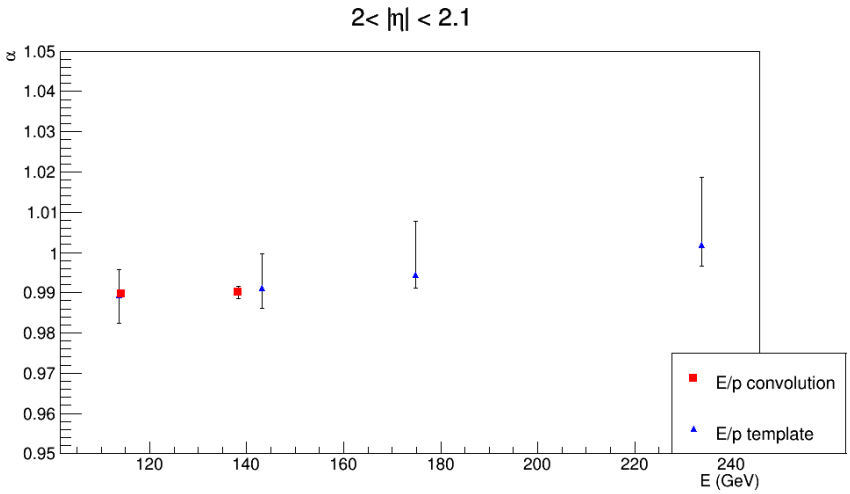



Figure 5.22: Linearity plots from the template method and the convolution method overlaid for $2 < |\eta| < 2.1$. The mean $E$ for that $E_T$ bin is used as the $x$-coordinate.

error bars. As before, some of the fits from the convolution method have not converged and hence some points are missing.

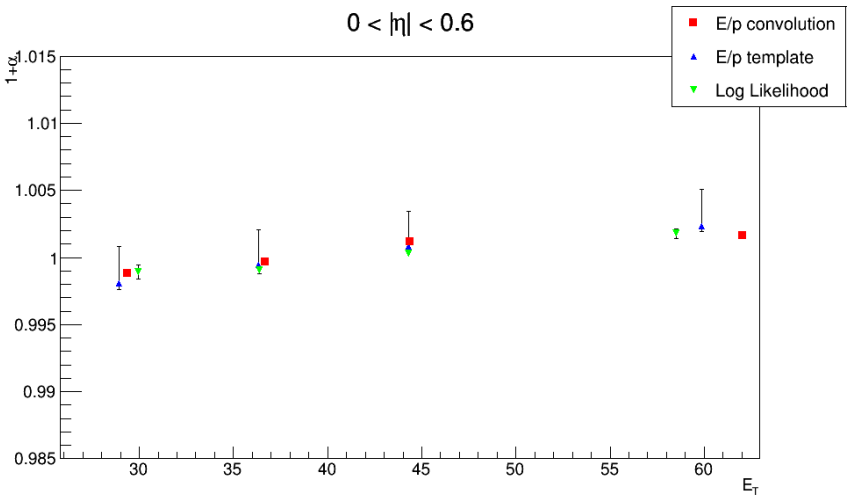



Figure 5.23: Linearity plots from the template method, the convolution method and the log likelihood method overlaid for $0 < |\eta| < 0.6$. The mean $E_T$ for that $E_T$ bin is used as the $x$-coordinate.

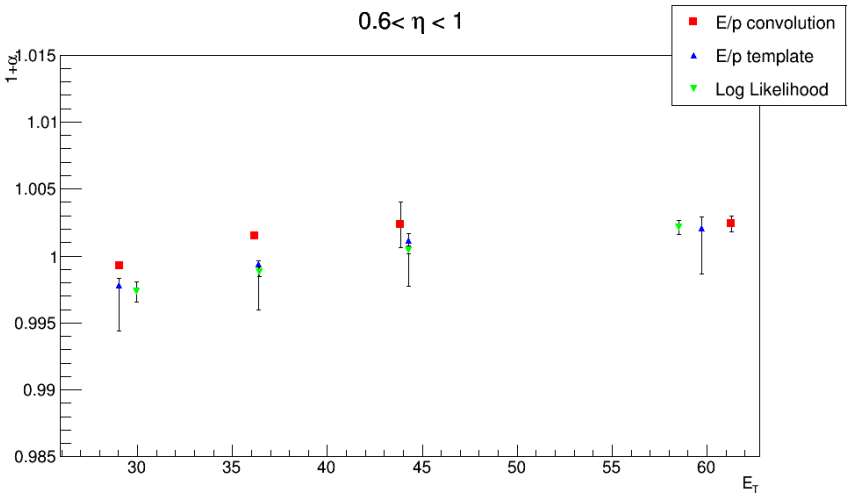



Figure 5.24: Linearity plots from the template method, the convolution method and the log likelihood method overlaid for $0.6 < |\eta| < 1$. The mean $E_T$ for that $E_T$ bin is used as the $x$-coordinate.

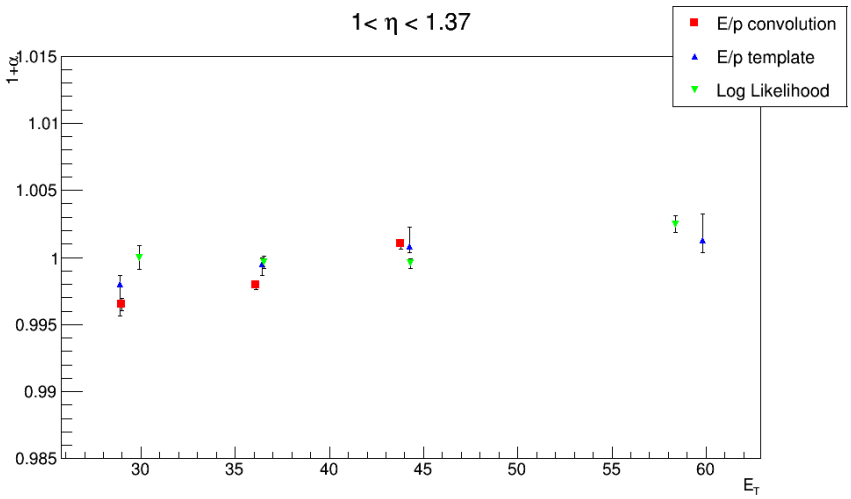



Figure 5.25: Linearity plots from the template method, the convolution method and the log likelihood method overlaid for $1 < |\eta| < 1.37$. The mean $E_T$ for that $E_T$ bin is used as the $x$-coordinate.

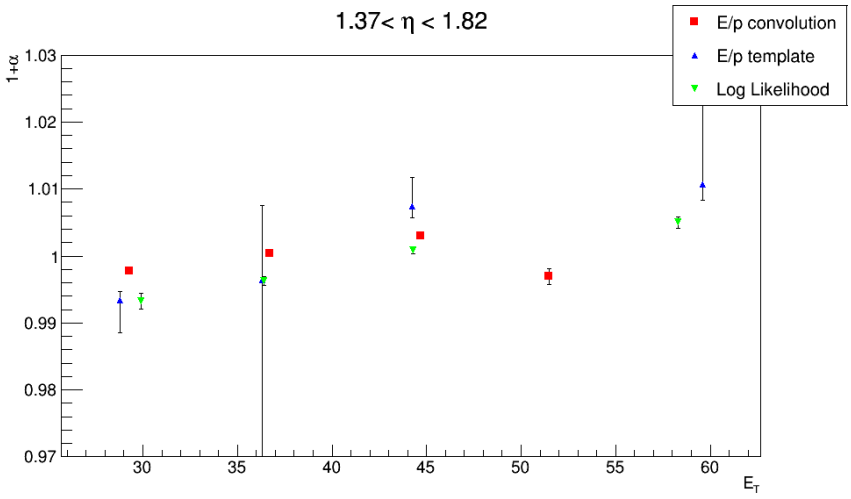



Figure 5.26: Linearity plots from the template method, the convolution method and the log likelihood method overlaid for $1.37 < |\eta| < 1.82$. The mean $E_T$ for that $E_T$ bin is used as the $x$-coordinate.

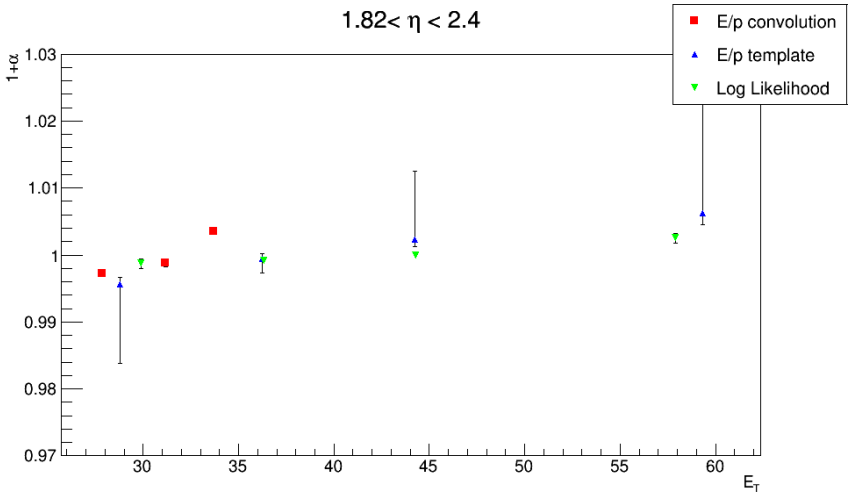



Figure 5.27: Linearity plots from the template method, the convolution method and the log likelihood method overlaid for $1.82 < |\eta| < 2.4$. The mean $E_T$ for that $E_T$ bin is used as the $x$-coordinate.

# Chapter 6

# Hadronic recoil for $W$ mass

## 6.1 Recoil overview

The two decay channels of the $W$ boson studied here are $W \to e\nu$ and $W \to \mu\nu$ . It is not possible to detect neutrinos using the ATLAS detector; their presence must be inferred from the momentum imbalance. The two key observables for the measurement of the $W$ boson mass are therefore the lepton from $W$ boson decay and the hadronic recoil, which originates from the initial-state parton shower. The recoil consists of jets and other soft particles not clustered into jets. By summing the hadronic recoil and the lepton momentum vectorially, the neutrino transverse momentum can be inferred from the measured $\not{E}_T$ . A diagram of the showing the electron, neutrino and recoil in $W$ events can be seen in Figure 6.1.

A simple hadronic recoil calculation can be performed by summing the calorimeter clusters vectorially. However, charged leptons from $W$ boson decay deposit energy in the calorimeter and therefore must be removed from the calculation. The recoil algorithm used here excludes a cone around the lepton(s) of $\Delta R < 0.2$. The small bias in excluding this cone is corrected for by adding an estimated amount of underlying event energy in the cone to the overall calculation. The amount of underlying event energy is estimated by taking another cone, which does not overlap with lepton exclusion cone, at the $\eta$ of the lepton

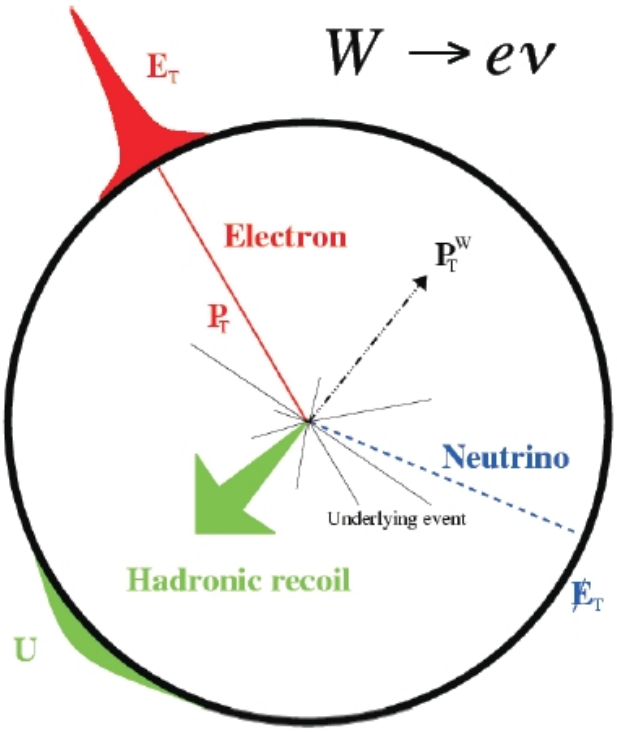



Figure 6.1: Diagram showing electron, neutrino and recoil in $W$ events [103].

but at a random angle in phi. Aside from any recoiling jets, the rest of the event mainly contains soft hadronic activity, resulting from additional soft proton-proton interactions and the underlying event.

It is preferable to use the hadronic recoil for the $W$ boson mass measurement, as opposed to the standard missing $E_T$ algorithms for several reasons. The default inputs to the missing $E_T$ algorithms include objects (like $\tau$ candidates) that are not present in selected $W$ events. Lepton-induced calorimetric energy deposits are included in the standard missing $E_T$ algorithms, but there is no consideration whether the lepton originates from the $W$ or $Z$ boson decay or from the hadronic recoil. Therefore, it is desirable to use the hadronic recoil algorithms corrected for leptons from $W$ or $Z$ decay only.

## 6.2 Algorithm

The uncorrected hadronic recoil can be defined in Equation 6.1, where $\Delta R$ is the distance between the cluster and the closest selected lepton, and $\Delta R_{min}$ is chosen to be 0.2.

$$\vec{R}_{uncorr} = \sum_{\Delta R > \Delta R_{min}} \vec{P}_{T,clus} \tag{6.1}$$

The sum is over the transverse momentum of each cluster. When choosing $\Delta R_{min}$, a sufficiently large cone size must be used such that all energy deposits from the lepton are within the cone. However, in addition to the lepton deposits, the cone also contains deposits from the underlying event. Even though this can be corrected for, as discussed in the following paragraph, removal of too large a cone will result in the loss of too much information from the underlying event and the recoil resolution overall will be degraded.

A sample cone of typical energy arising from the underlying event is taken by rotating the cone around the transverse plane and selecting a random point in $\phi$. As the transverse plane is used, the cone will be at the same point in $\eta$, which will reduce any dependence on detector layout. The sample cone must be sufficiently removed from any leptons in the event to avoid lepton contamination, hence the azimuth of the cone is required to be $\Delta\phi > 2\Delta R$ away from a lepton from $W$ or $Z$ boson decay. The hadronic recoil will be predominantly in the direction opposite to the $W$ boson, where the parton shower has recoiled against the boson. This area would not provide a good underlying event estimate, and the sample cone is therefore required to be $\Delta\phi > \frac{\pi}{3}$ away from the uncorrected recoil vector. The sum of clusters in the cone is taken, and then the resulting vector is rotated around the beam axis to where the lepton cone was removed. The sample cone is used to fill in the lepton cone and the total recoil is taken as the sum of the filled in lepton cone and the uncorrected recoil calculation as in the equation above.

In this study, $Z$ bosons will be used to calibrate the recoil, which have two leptons

| $Z \to ee$ **event selection** |
|---|
| **Electron cuts** |
| Electron $\|\eta\| < 2.47$ and not in dead $\eta$ region of calorimeter |
| 'Green' electron data quality |
| Medium electron identification cuts |
| **Event cuts** |
| Exactly 2 electrons |
| Electron $E_T > 20$ GeV |
| Opposite charge |
| $66 < M_{ee} < 116$ GeV |

Table 6.1: $Z \to ee$ event selection for recoil studies. This selects 1262457 events in data and 5131973 events in Monte Carlo. The number of events are slightly different in this selection to that used in the $E/p$ chapter, as different calibrations have been applied to the data before the cuts are made.

| $Z \to \mu\mu$ **event selection** |
|---|
| **Muon cuts** |
| Muon $\|\eta\| < 2.47$ and not in dead $\eta$ region of calorimeter |
| 'Green' muon data quality |
| Combined muon. (recorded in both ID and MS) |
| Isolated track (tracks in cone ($\Delta R < 0.2$) surrounding muon in inner detector have less than 10% of muon $p_T$) |
| **Event cuts** |
| Exactly 2 muons |
| Muon $p_T > 20$ GeV |
| Opposite charge |
| $66 < M_{ee} < 116$ GeV |

Table 6.2: $Z \to \mu\mu$ event selection for recoil studies. This selects 1673358 events in data and 7003525 events in Monte Carlo.

compared to the $W$ boson's one. Therefore, filling in the removed cones accurately is essential to reduce the bias between the two samples. It is possible make a pseudo-$W$ event sample from data by removing the second lepton in $Z$ events and treating the resulting momentum imbalance as missing $E_T$. Unfortunately, due to the way the clusters from electrons are stored in ATLAS, it would be difficult to completely remove the lepton shower, which could add extra bias. Therefore, for the first calibration of the model presented here, both leptons are used and no replacement procedure is performed. Figure 6.2 shows the corrected recoil from $Z \to ee$ events for both data and POWHEG Monte Carlo. The $Z \to ee$ and $Z \to \mu\mu$ event selections are summarised in Table 6.1 and 6.2. The $M_Z$ distributions after all cuts can be seen in Figures 6.3 and 6.4.

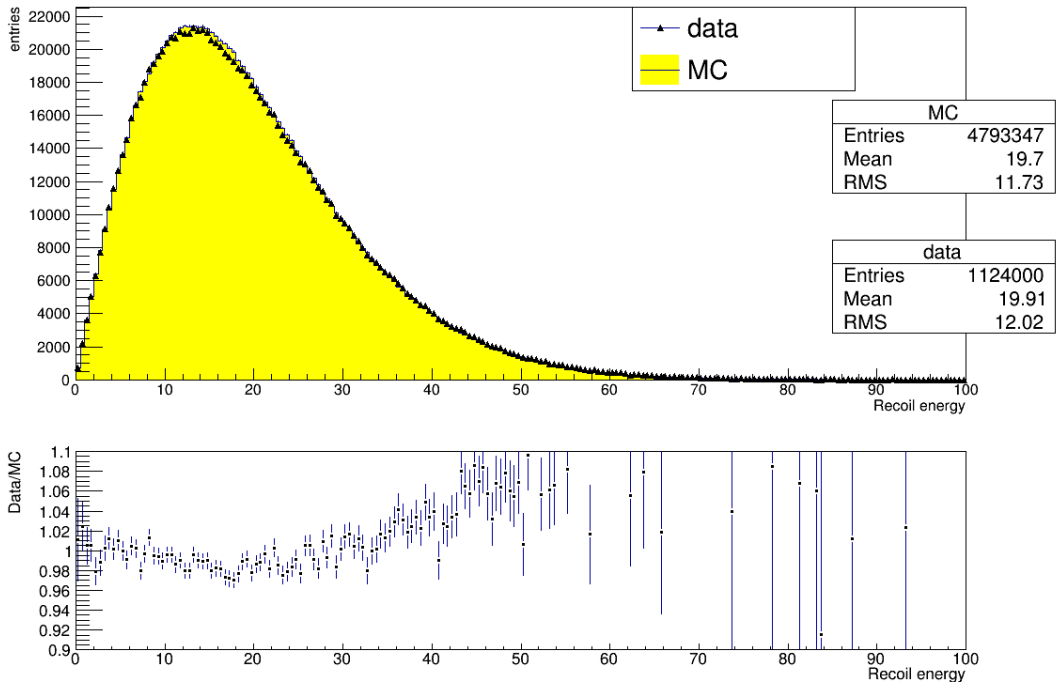



Figure 6.2: Recoil from $Z \to ee$ events for data and POWHEG Monte Carlo. The number of events in Monte Carlo has been normalised to the number of events in data.

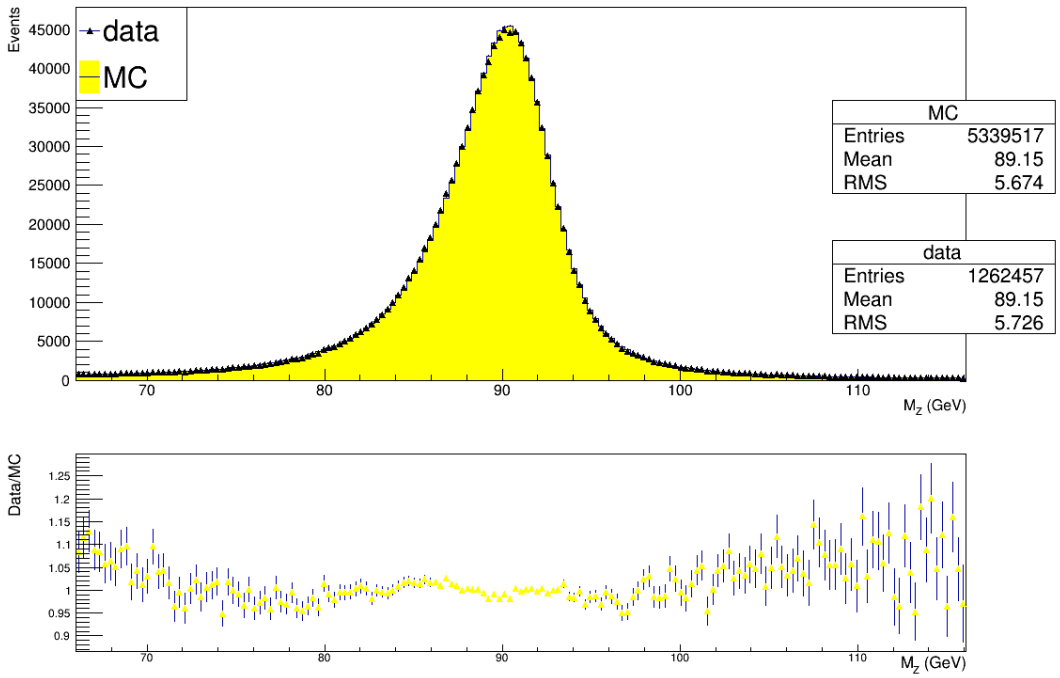



Figure 6.3: $M_Z$ from $Z \to ee$ events for data and POWHEG Monte Carlo. The number of events in Monte Carlo has been normalised to the number of events in data.

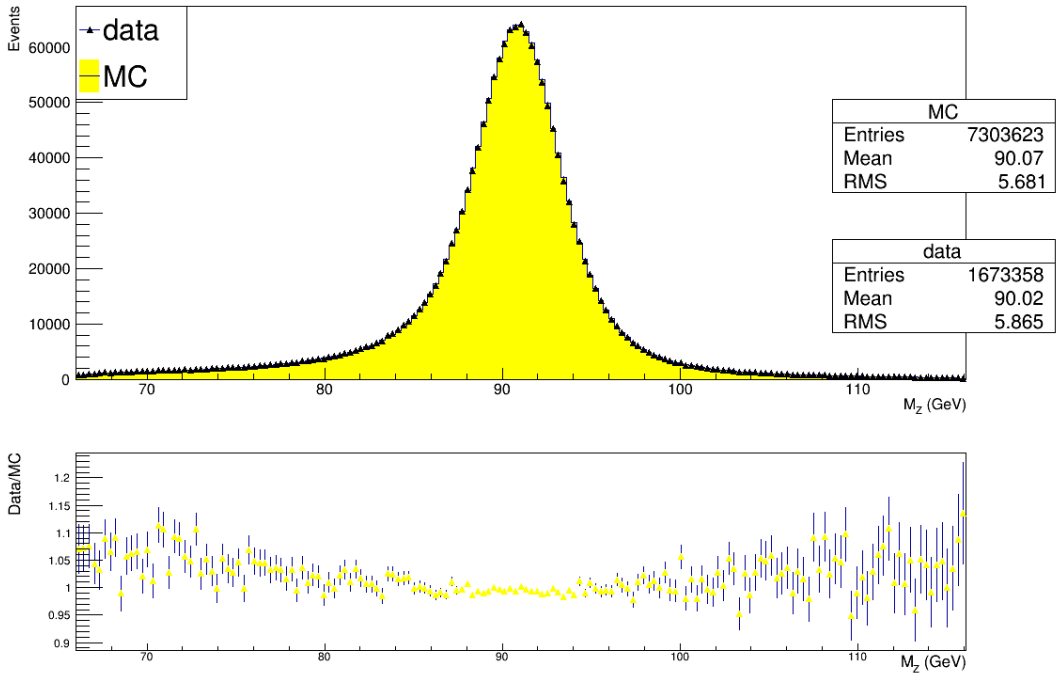



Figure 6.4: $M_Z$ from $Z \to \mu\mu$ events for data and POWHEG Monte Carlo. The number of events in Monte Carlo has been normalised to the number of events in data.

## 6.3 Recoil algorithm limitations

The algorithm implicitly assumes that the $W$ or $Z$ boson recoils against a single jet. The cone replacement procedure avoids a region containing a jet by sampling $\Delta\phi > \frac{\pi}{3}$ away from the recoil vector. When an event contains more than one jet, the recoil vector will not indicate the location of jets in the event and the method could use energy from a jet in its replacement cone.

Similarly, the recoil algorithm assumes that the leptons are isolated from other high-$p_T$ particles and that the lepton cone contains only the lepton energy and soft hadronic activity. If the leptons are not isolated, the cone would also contain energy deposits from other particles, and this small amount of hadronic activity would be insufficient as a correction. This effect will be averaged out over all events, but will have an effect on an event-by-event basis. The recoil algorithm could be modified to calculated the recoil component parallel to the lepton cone removal and select a replacement cone that has a similar parallel recoil

component, but this could lead to complicated biases and will not be used for the first $m_W$ measurement being performed now.

## 6.4 Algorithm efficiency

The 'Tag and probe' method is used with $Z$ boson decays to find the efficiency of both the electron and muon selections. Projecting the recoil along the lepton (in this case, the probe lepton) forms the variable $u_{parallel}$. Large positive $u_{parallel}$ indicates that the recoiling partons are in the same direction as the lepton, i.e. the lepton is within the location of a soft jet. The reconstruction efficiency of electrons and muons will be lower when this occurs. It is important to ensure that data and Monte Carlo have the same behaviour in this configuration.

The 'Tag and probe' selection differs from the event selections used in the rest of the chapter described in the tables above. For electrons, the tag is defined as an electron passing the medium selection, whereas the probe need only pass the loose selection. Both electrons must have $E_T > 20$ GeV. A tight lepton pair mass window is used of 81 GeV $< M_{ee} <$ 101 GeV.

For muons, the tag must both be a combined muon (i.e. recorded in both the ID and the MS). It must pass an isolation requirement that the tracks in the cone (of $\Delta R = 0.2$) surrounding the muon in the ID have less than 10 % of the $p_T$ of the muon. There is no isolation requirement or quality requirement on the probe, although it must have passed one of the muon triggers. Both muons must have a $p_T > 15$ GeV and pass standard ID tracking cuts. As in the case of electrons, an invariant mass window of 81 GeV $< M_{\mu\mu} <$ 101 GeV is required. The two leptons must also have opposite charge. Fig. 6.5 shows the $u_{parallel}$ distribution for leptons that pass the tag selection and for all electrons for $Z \to ee$ events.

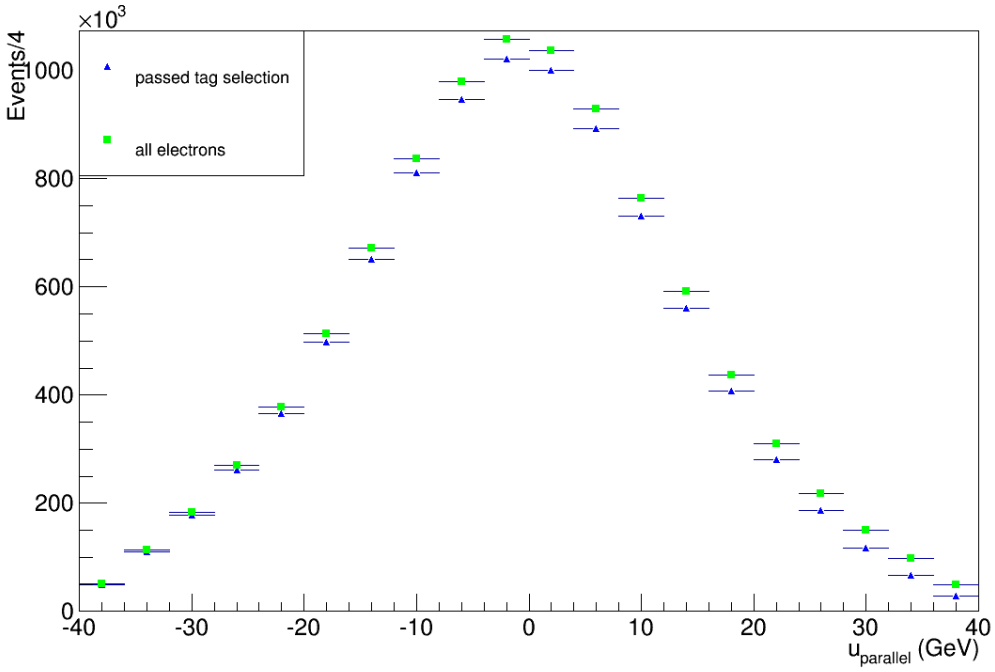



Figure 6.5: $u_{parallel}$ distribution for all electrons (including those that only pass the probe selection) and only electrons that pass the tag selection for $Z \rightarrow ee$ events.

$W$ bosons produced in association with jets where one of the jets is misidentified as an electron or muon will be the principal background in this sample. A simple way to estimate the background is to require that the leptons have the same sign. There will be an approximately equal number of background events with same-charge leptons and with opposite-charge leptons; therefore, the same charge leptons can be subtracted from the opposite charge sample, effectively subtracting the $W$+jets events and leaving $Z$ boson events remaining. The proportion of leptons that are the same charge and are therefore subtracted from the sample can be seen in Fig. 6.6.

The efficiency for a given lepton is calculated by dividing the sample that passes the tag selection by the sample containing all leptons of that type. The results for electrons can be seen in Fig. 6.7. Data and Monte Carlo show different inefficiencies as a function of $u_{parallel}$, therefore a correction must be made in the electron sample. $\epsilon_{data}$ (data efficiency) is divided by $\epsilon_{MonteCarlo}$ (Monte Carlo efficiency) in Fig. 6.8. This plot is parameterised with piecewise

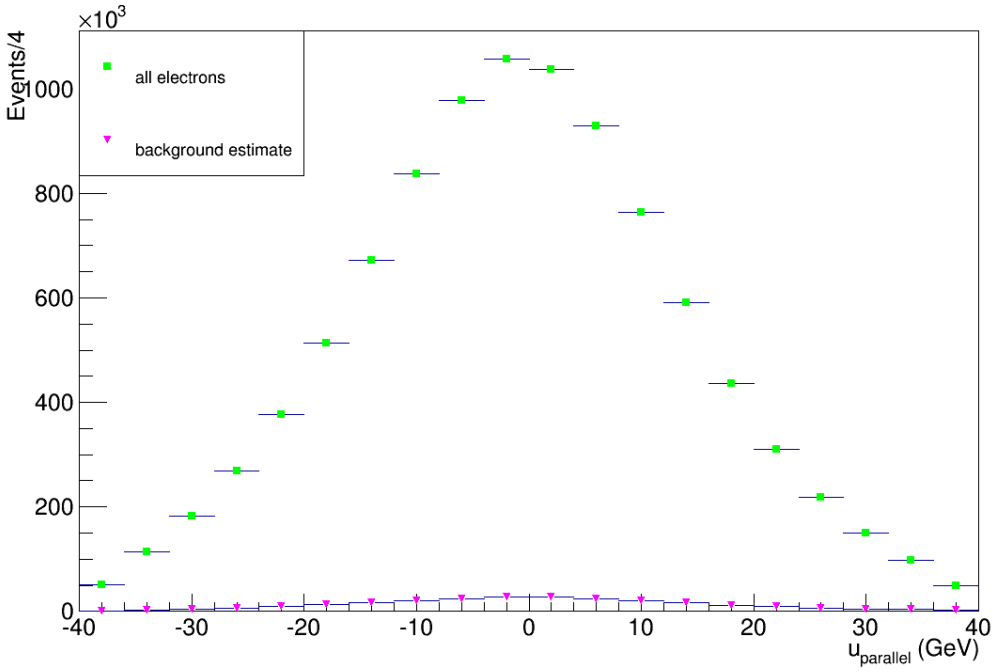



Figure 6.6: $u_{parallel}$ distribution for electrons passing the background estimate selection and electrons passing the probe selection for $Z \to ee$ events.

linear fits for simplicity, with results shown in Equations 6.2, 6.3 and 6.4.

$$\frac{\epsilon_{data}}{\epsilon_{MC}} = 1.63 \times 10^{-5} u_{parallel} + 0.997 \quad \text{for} \quad u_{parallel} < 0\,\text{GeV} \tag{6.2}$$

$$\frac{\epsilon_{data}}{\epsilon_{MC}} = -4.50 \times 10^{-4} u_{parallel} + 0.997 \quad \text{for} \quad 0 < u_{para} < 17\,\text{GeV} \tag{6.3}$$

$$\frac{\epsilon_{data}}{\epsilon_{MC}} = -4.08 \times 10^{-3} u_{parallel} + 1.059 \quad \text{for} \quad u_{para} > 17\text{GeV} \tag{6.4}$$

The events are weighted using the above parameterisations. To test the procedure, weights are also determined for those failing the selection.

$$SF_{passed} = \frac{\epsilon_{data}}{\epsilon_{MC}} \tag{6.5}$$

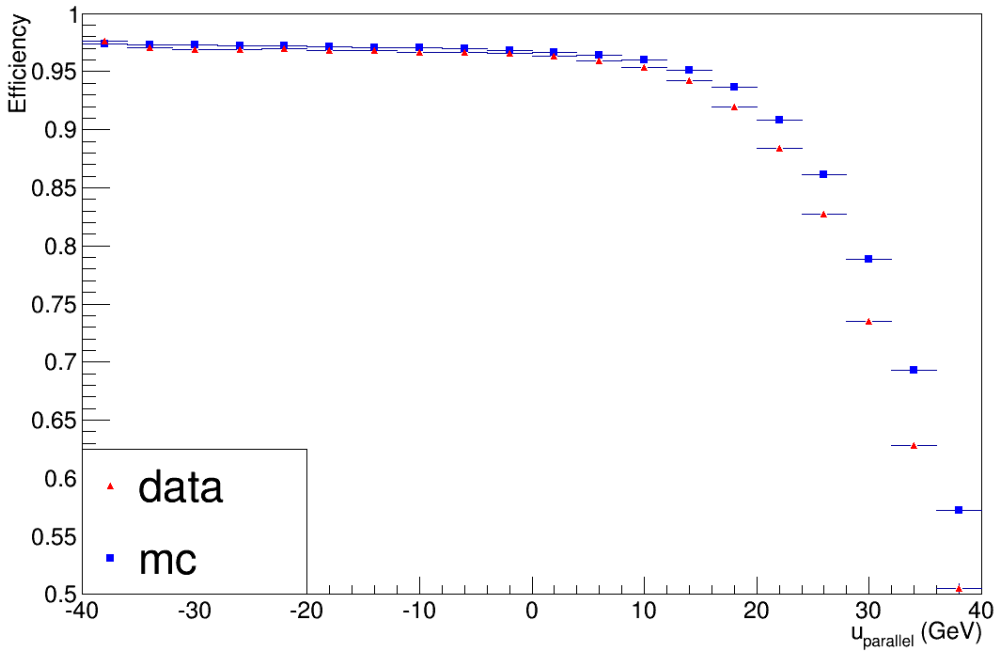



Figure 6.7: Efficiency vs $u_{parallel}$ for data and Monte Carlo for $Z \rightarrow ee$ events.

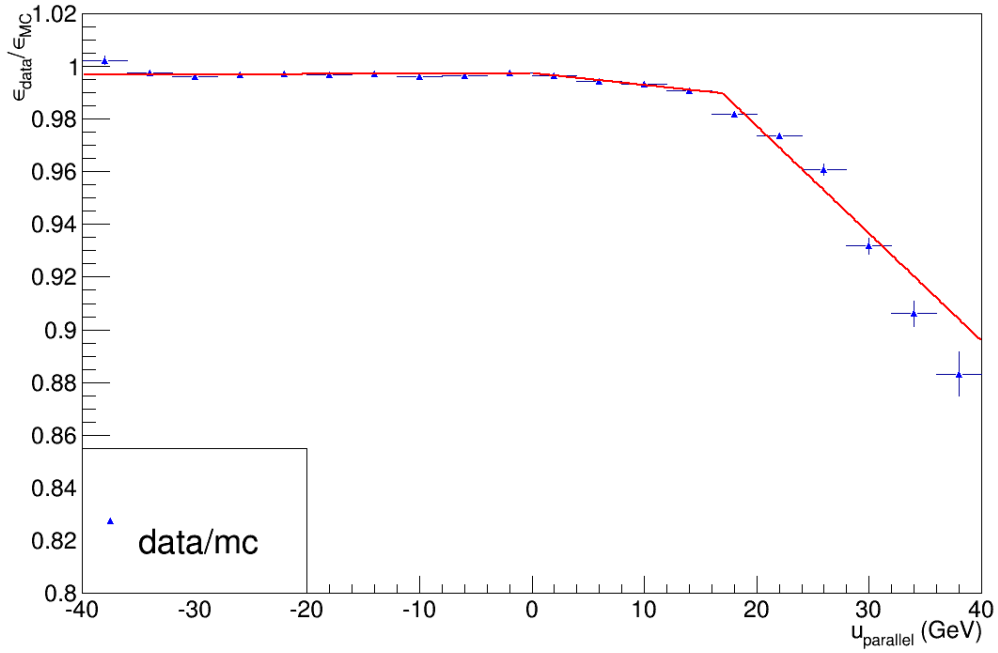



Figure 6.8: Data efficiency divided by Monte Carlo efficiency fitted with a piecewise linear parameterisation for $Z \rightarrow ee$ events.

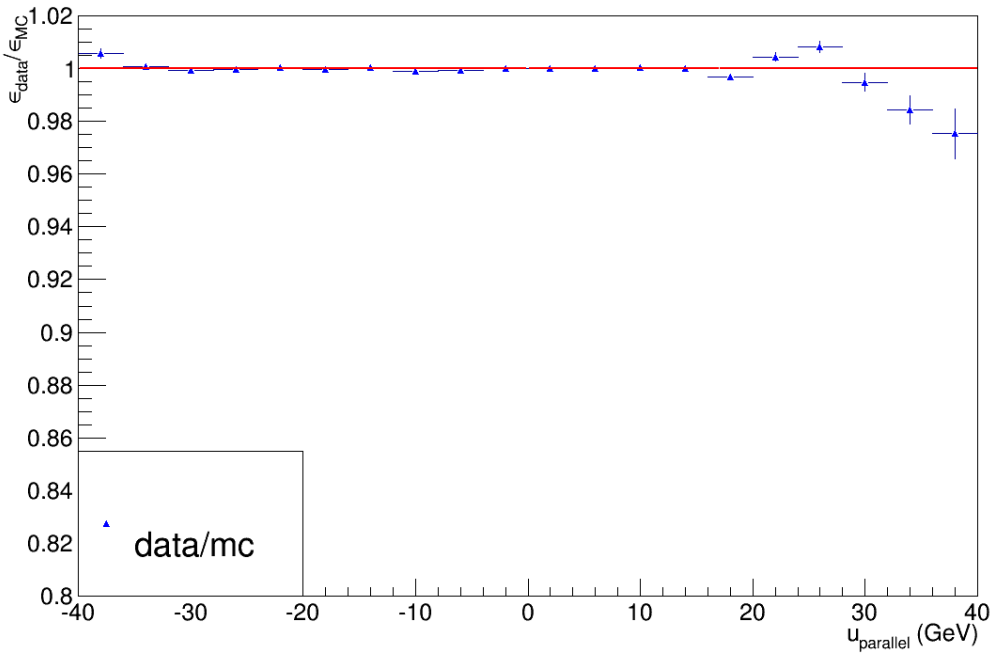



Figure 6.9: Data efficiency divided by Monte Carlo efficiency after the reweighting for $Z \to ee$ events.

$$SF_{failed} = \frac{1 - \epsilon_{data}}{1 - \epsilon_{MC}} \tag{6.6}$$

$$SF_{failed} = \frac{\frac{1}{\epsilon_{MC}} - SF_{passed}}{\frac{1}{\epsilon_{MC}} - 1} \tag{6.7}$$

Figure 6.9 shows the data efficiency divided by the MC efficiency after reweighting events that pass the tag selection and those that fail. The straight line shows that the reweighting has succeeded in removing the bias.

The procedure is repeated for $Z \to \mu\mu$ events. Whilst there is a small decrease in efficiency at positive $u_{parallel}$, as shown in Figure 6.10, Figure 6.11 shows that the efficiency drop is the same in data and Monte Carlo and hence no correction is necessary.

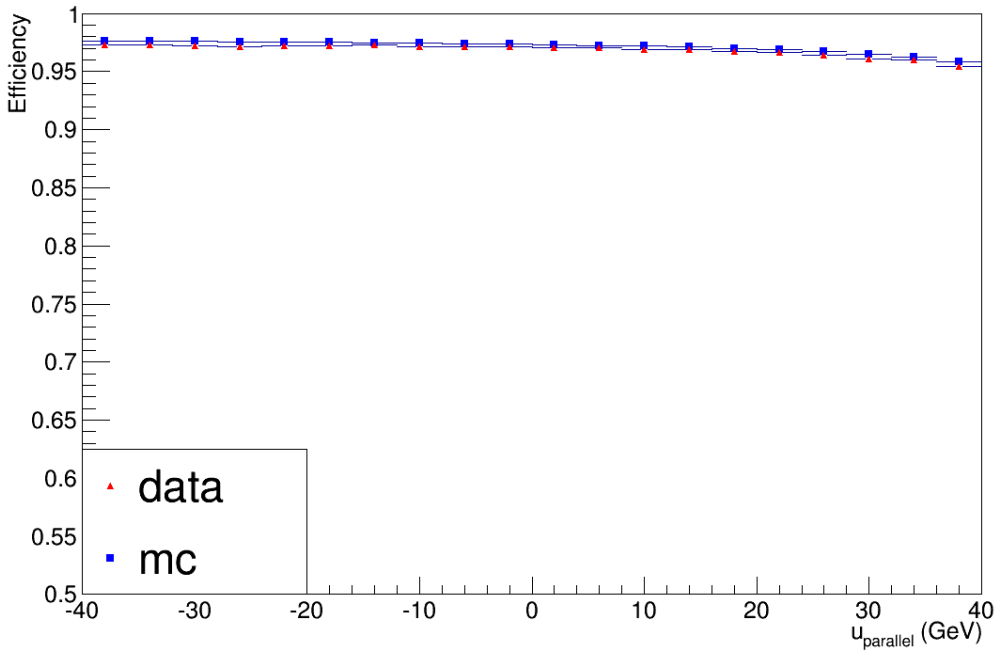



Figure 6.10: Data and Monte Carlo efficiency vs $u_{parallel}$ for $Z \rightarrow \mu\mu$ events.

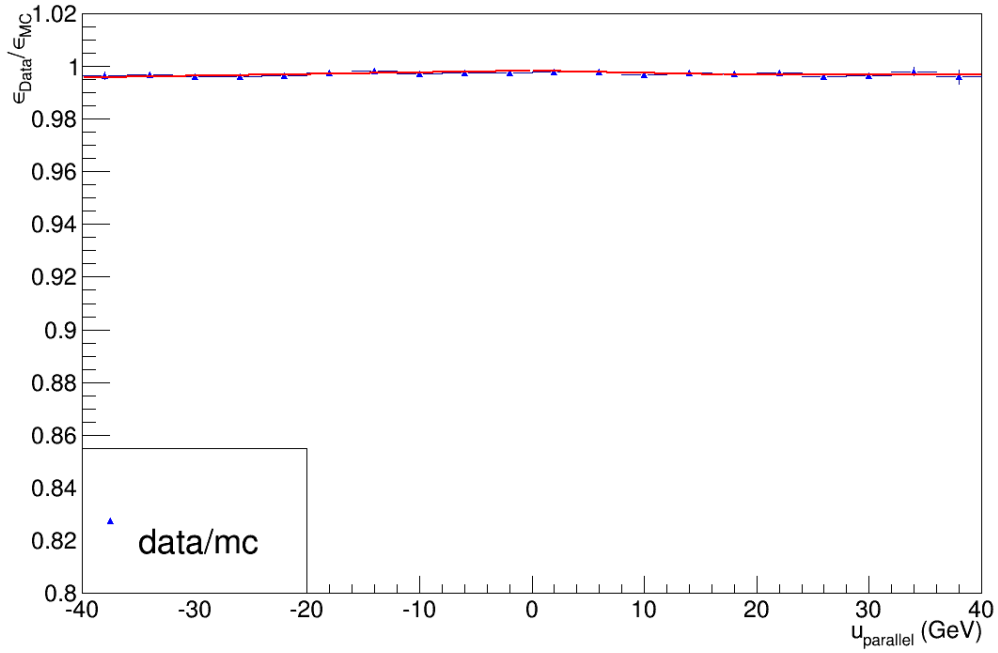



Figure 6.11: Data efficiency divided by Monte Carlo efficiency vs $u_{parallel}$ for $Z \rightarrow \mu\mu$ events. The efficiency ratio is consistent with a constant (also shown).

## 6.5 Performance

The performance of this algorithm can be characterised by studying the mean and the resolution of the components of the recoil perpendicular and parallel to the $p_T$ of a $Z$ boson. In this instance, the resolution is taken to be the root mean square of the distribution. The behaviour of the parallel and perpendicular components can be quite different. At production level, the parallel component should be equal and opposite to the $Z$ boson $p_T$, whereas the perpendicular component should be equal to zero. We can tune the measurement of the recoil using the $Z$ boson events, as we can measure the $Z$ boson $p_T$ precisely by measuring the momentum of the two well-measured leptons from the $Z$ decay. If the detector response to the recoil and the hadronic activity is the same in $W$ and $Z$ events, we can transfer our calibration from the $Z$ events, to $W$ events.

The $Z \to ee$ and $Z \to \mu\mu$ selections used in the rest of this chapter are summarised in Tables 6.1 and 6.2. An additional cut of $Z$ $p_T < 40$ GeV was made as the $m_W$ selection will include a cut on recoil $< 30$ GeV to remove events with large recoil (which are too biasing). The $Z$ $p_T$ distribution is shown in Figures 6.12 and 6.13. Figures 6.14 to 6.17 show plots of the parallel and perpendicular components of recoil, which will be referred to as $u_\gamma$ and $u_\epsilon$ respectively, for $Z \to ee$ and $Z \to \mu\mu$ events. As the parallel component is approximately equal and opposite to the $Z$ boson $p_T$, the mean is not 0. To suppress dependence on $Z_{p_T}$, the net $p_T$ imbalance in the event should be plotted instead. As not all of the parallel component will be detected by the calorimeters, the $Z$ $p_T$ is scaled down before adding the two variables. The scaling is calculated by dividing the parallel component by the $Z$ $p_T$, known as the response. Figure 6.19 shows the response for $Z \to \mu\mu$ events. As can be seen, approximately 70% of the $Z$ $p_T$ is measured as recoil and hence the $Z$ $p_T$ in the balance calculation is multiplied by 0.7. Figure 6.20 shows the balance after correcting the $Z$ $p_T$.

From here onwards, the balance shall be referred to as $u_\alpha$, and the perpendicular com-

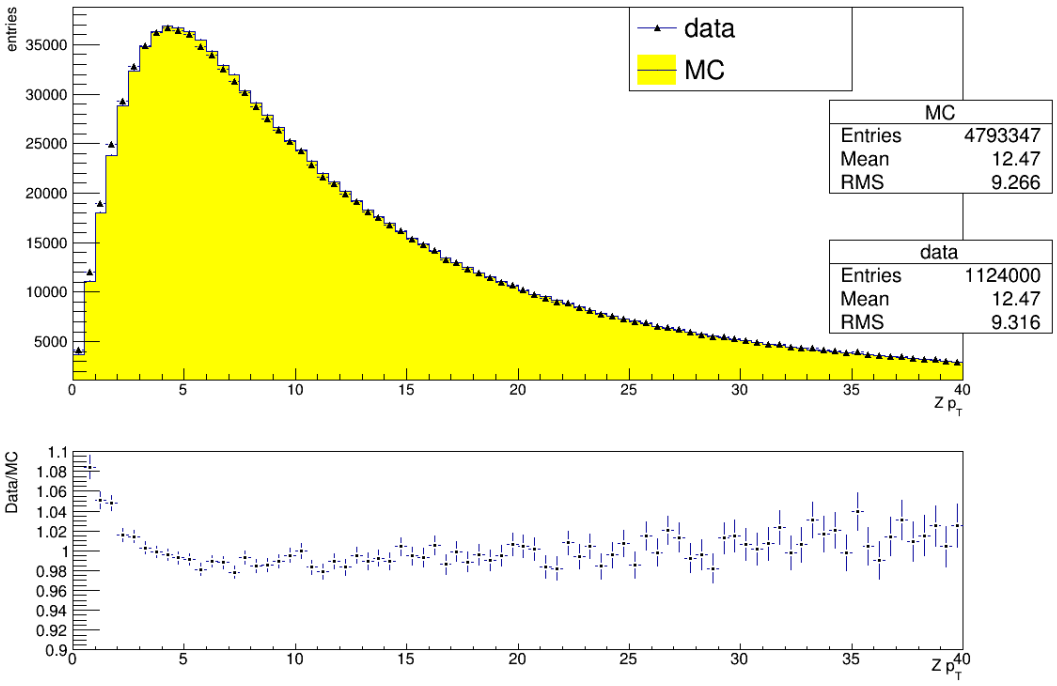



Figure 6.12: $Z$ boson $p_T$ distribution for $Z \to ee$ events for data and POWHEG Monte Carlo.

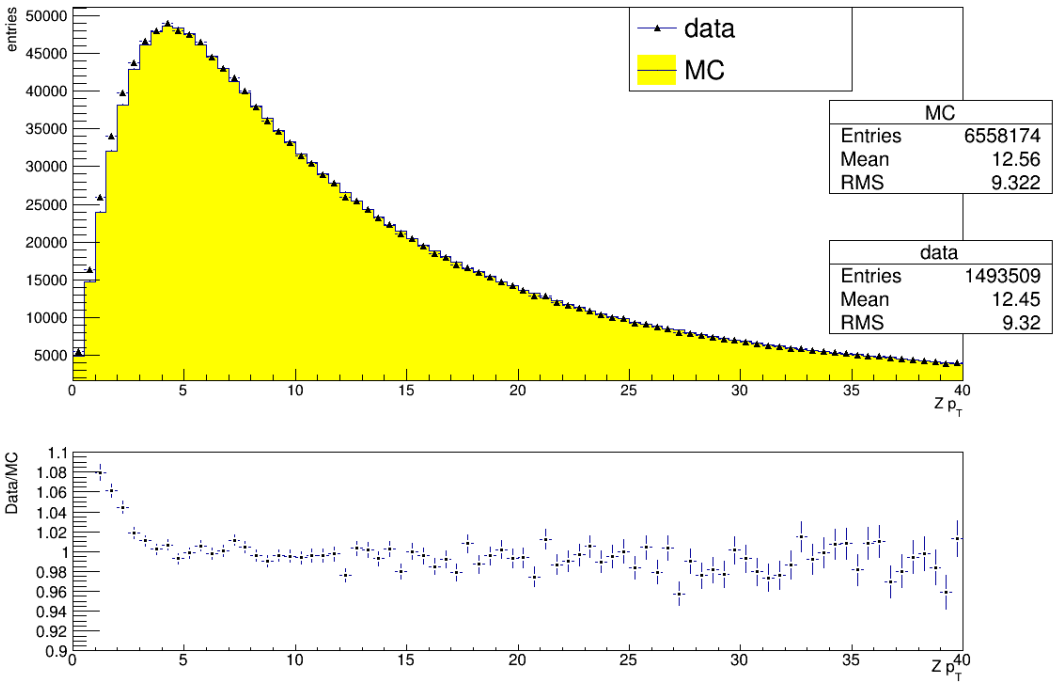



Figure 6.13: $Z$ boson $p_T$ distribution for $Z \to \mu\mu$ events for data and POWHEG Monte Carlo.

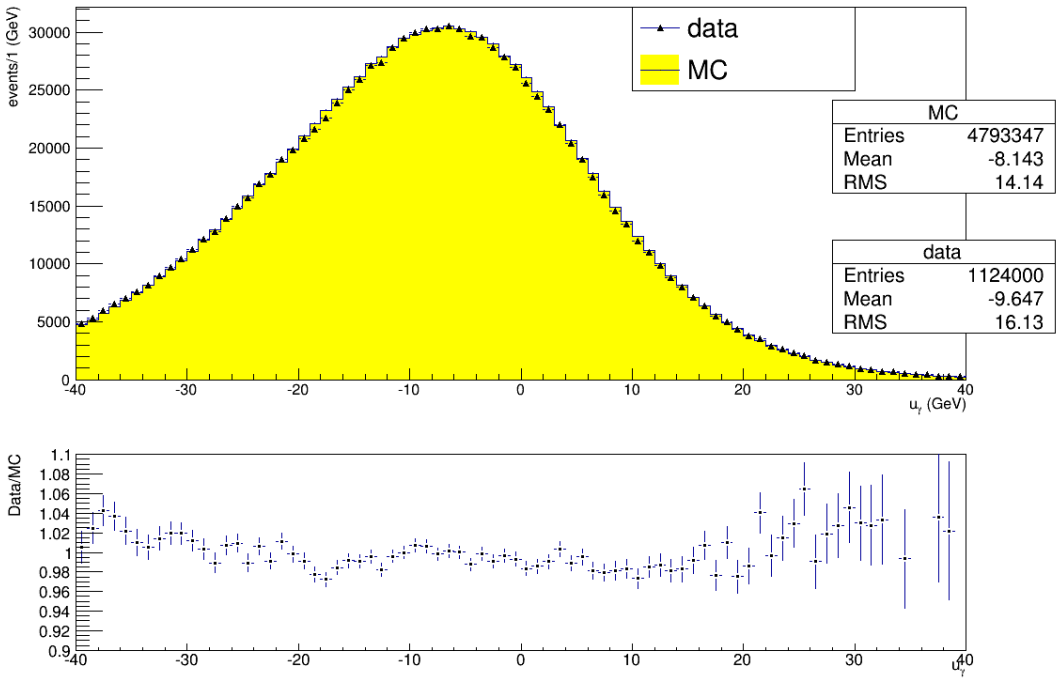



Figure 6.14: Component of recoil parallel to the $Z$ boson $p_T$ for $Z \to ee$ events for data and POWHEG Monte Carlo.

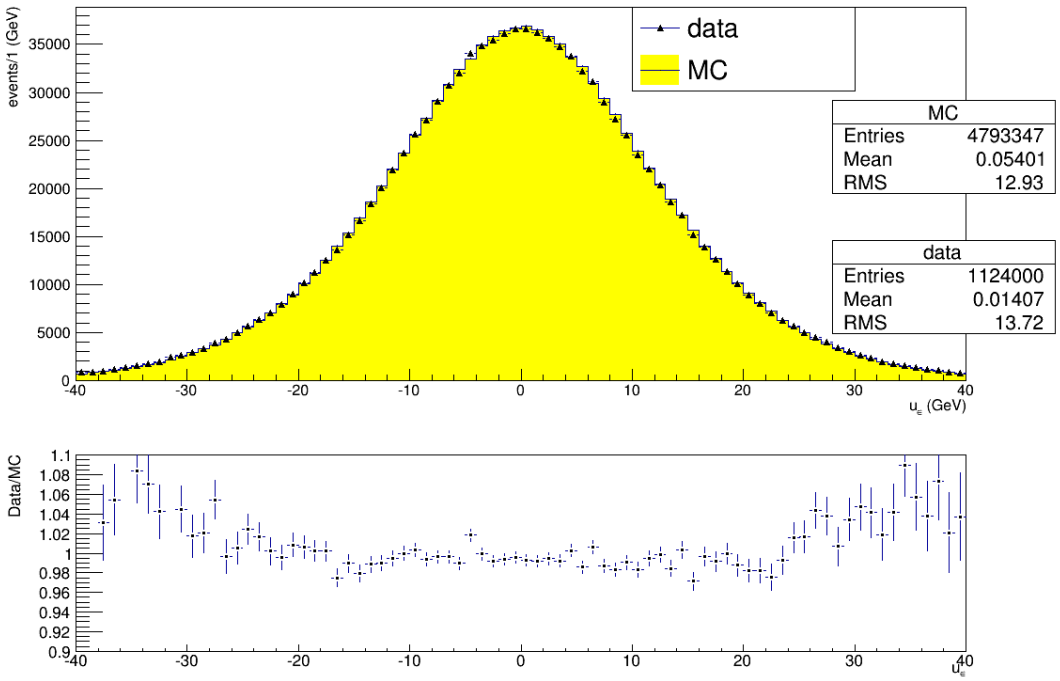



Figure 6.15: Component of recoil perpendicular to the $Z$ boson $p_T$ for $Z \to ee$ events for data and POWHEG Monte Carlo.

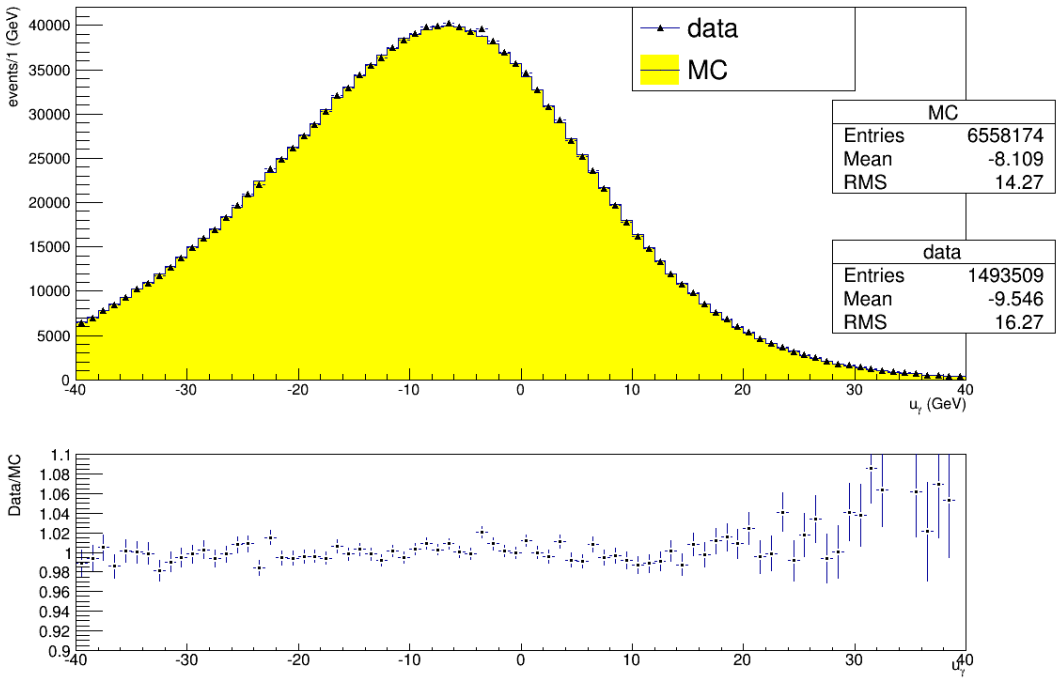



Figure 6.16: Component of recoil parallel to the $Z$ boson $p_T$ for $Z \to \mu\mu$ events for data and POWHEG Monte Carlo.

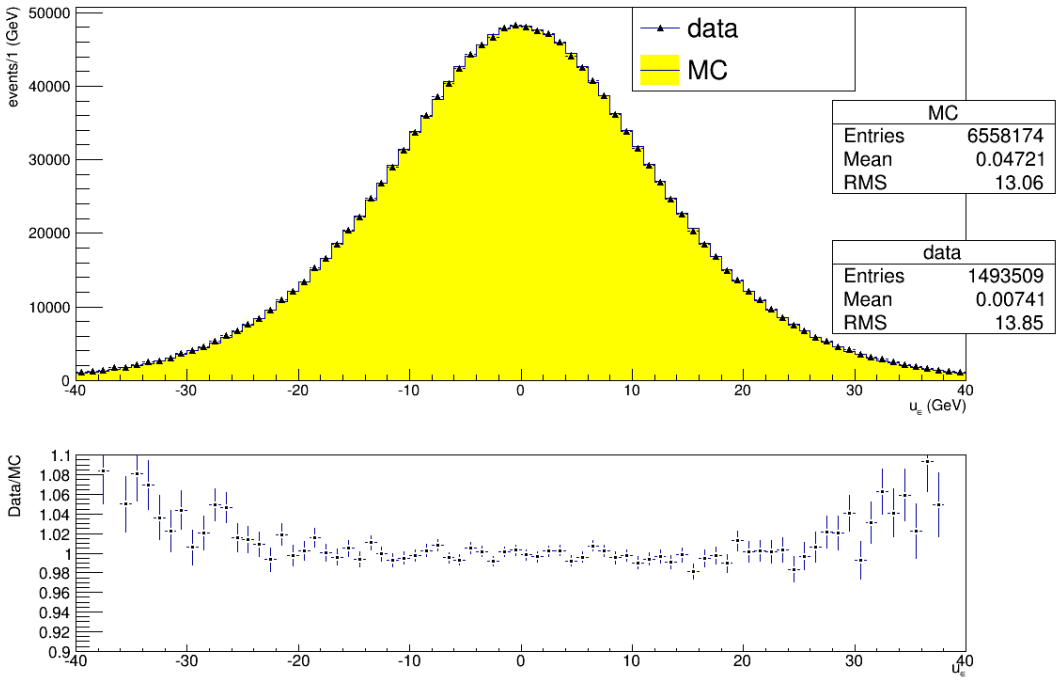



Figure 6.17: Component of recoil perpendicular to the $Z$ boson $p_T$ for $Z \to \mu\mu$ events for data and POWHEG Monte Carlo.

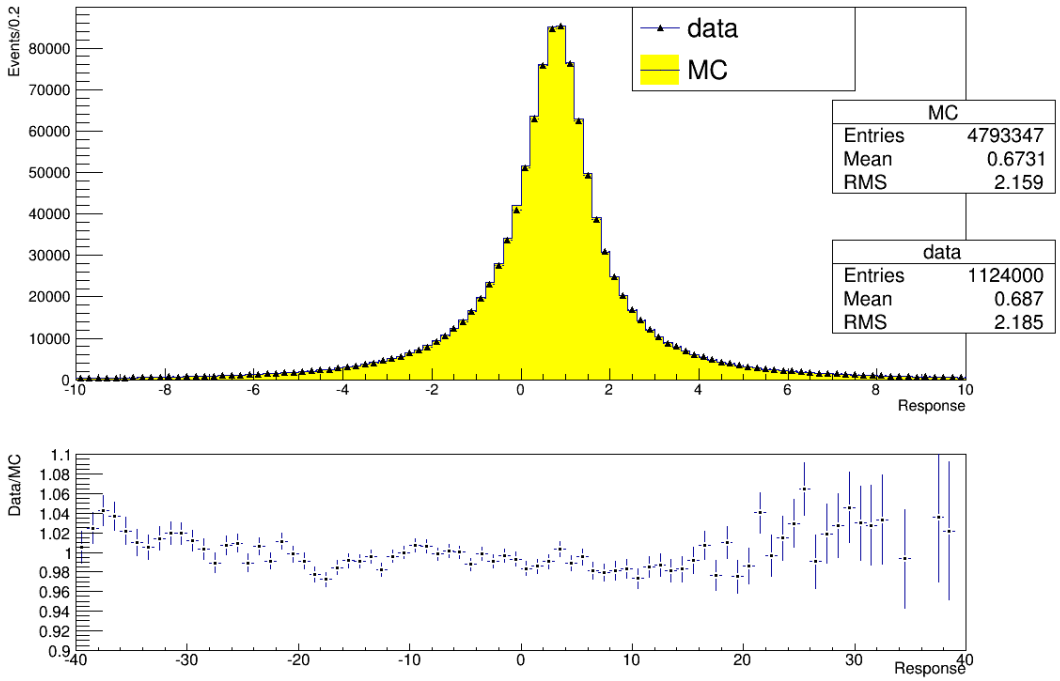



Figure 6.18: Recoil response ($Z$ $p_T$ / -component of recoil parallel to the $Z$ boson) in $Z \to ee$ events for data and POWHEG Monte Carlo.

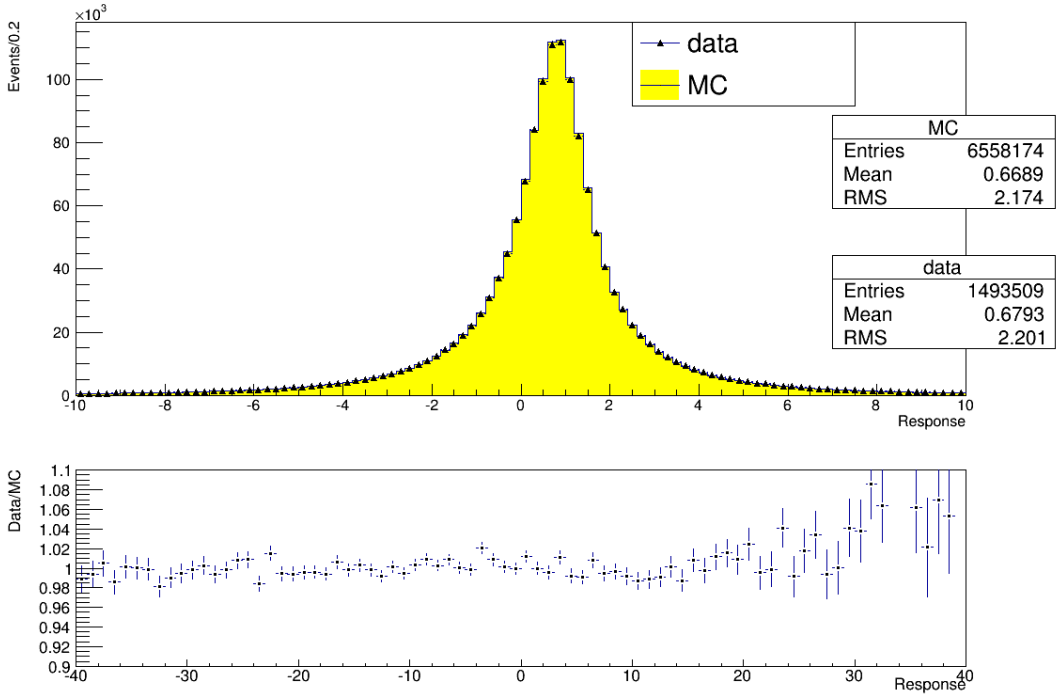



Figure 6.19: Recoil response ($Z$ $p_T$ / -component of recoil parallel to the $Z$ boson) in $Z \to \mu\mu$ events for data and POWHEG Monte Carlo.

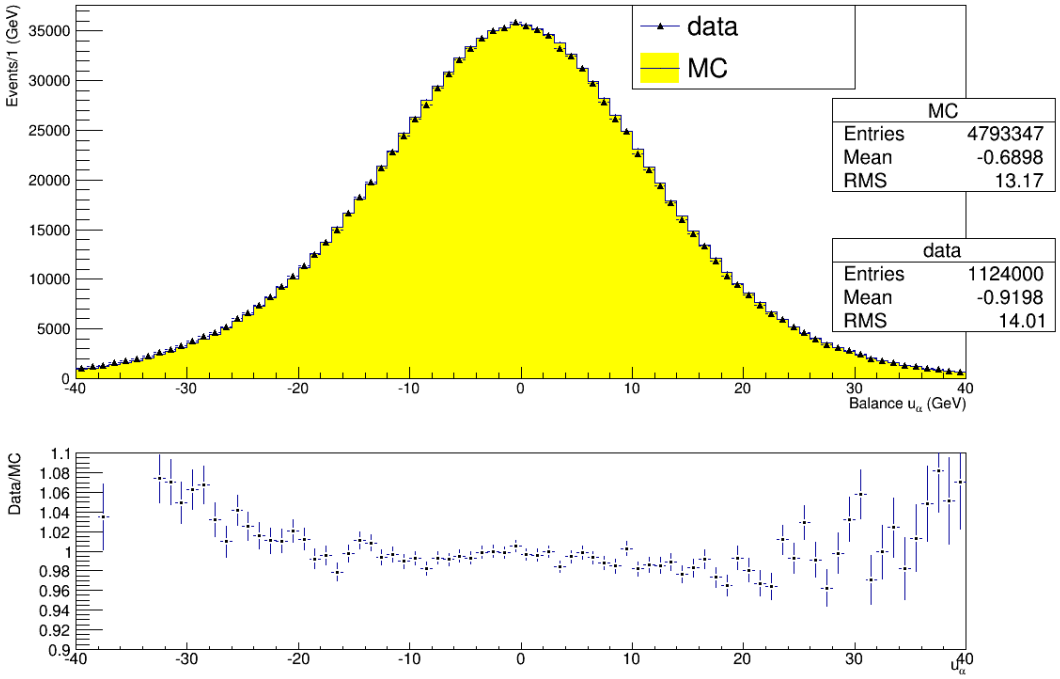



Figure 6.20: Balance distribution (the component of the recoil parallel to the $Z$ $p_T$ added to the $Z$ $p_T$ after scaling the $Z$ $p_T$ for imperfect calorimeter response) for $Z \to ee$ events for data and POWHEG Monte Carlo.

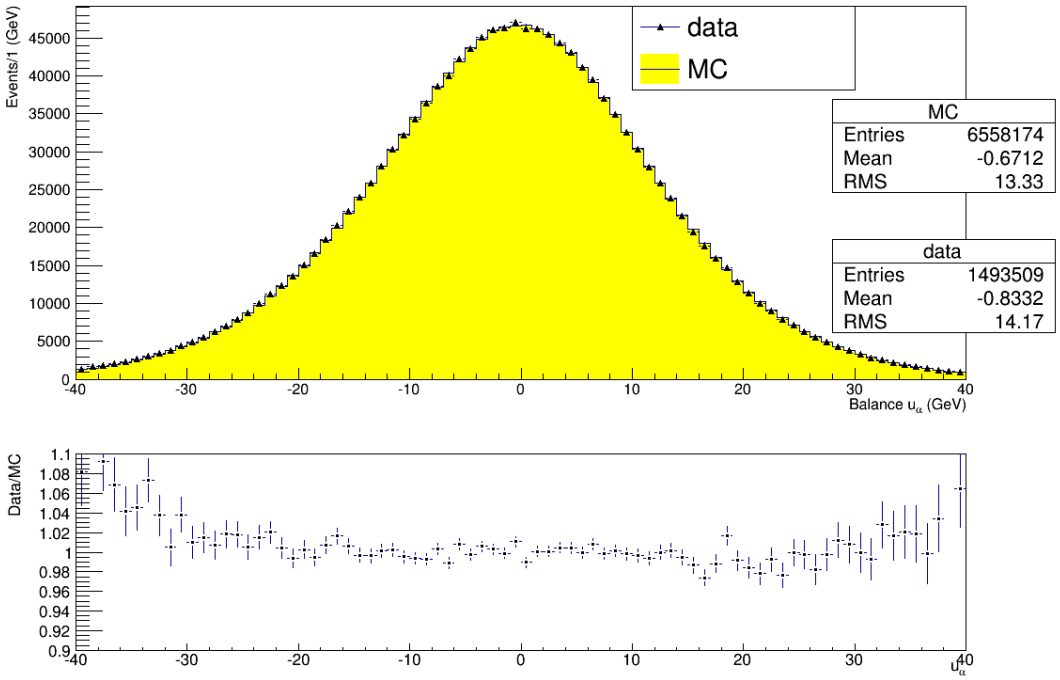



Figure 6.21: Balance distribution (the component of the recoil parallel to the $Z$ $p_T$ added to the $Z$ $p_T$ after scaling the $Z$ $p_T$ for imperfect calorimeter response) for $Z \to \mu\mu$ events for data and POWHEG Monte Carlo.

ponent, $u_\epsilon$. $u_\alpha$ is defined as follows:

$$u_\alpha = -0.7 p_T^Z + u_\gamma \tag{6.8}$$

The mean of the response plots shown above (6.18 and 6.19) to 1 decimal place is 0.7 and hence this is the number used in the above equation to quantify the proportion of recoil energy detected by the calorimeter. This correction will be tuned further in a later section. $u_\epsilon$ is only affected by resolution effects, which include the underlying event, the additional proton-proton interactions in each bunch crossing, the jet energy resolution and the jet angular resolution. A method for tuning the recoil resolution will be presented for each of these parameters. In order to separate the corrections, $u_\alpha$ and $u_\epsilon$ are split into bins of $Z$ $p_T$ and the mean and resolution are plotted for each. Figures 6.22 to 6.29 show the mean and resolution for $u_\alpha$ and $u_\epsilon$ for $Z \to ee$ and $Z \to \mu\mu$ events before tuning. These plots show that the resolutions of $u_\alpha$ and $u_\epsilon$ have the largest discrepancy between data and Monte Carlo, hence these plots are tuned first. There are some discrepancies in the means as well, but this is a relatively small effect.

## 6.6 Pileup and underlying event correction

The scalar sum of all the clusters that enter the recoil calculation (i.e. excluding the removed lepton and including the correction) is known as the hadronic activity or the $\Sigma$ $E_T$. For each additional proton-proton, or pileup, collision that accompanies the hard interaction, there will be additional energy clusters in the calorimeters, resulting in a larger $\Sigma$ $E_T$. To ensure that there is sufficient $\Sigma$ $E_T$ added to the simulation per extra pileup collision, the mean $\Sigma$ $E_T$ is plotted in bins of $\mu$, as shown in Figure 6.30. $\mu$ is the average number of interactions per bunch crossing, as estimated from luminosity measurements. As it is an average, $\mu$ is a continuous variable in data, but is discrete in Monte Carlo due to constraints in the way Monte Carlo is simulated.$\mu$ is used here instead of the number of vertices measured due to inefficiencies in the vertex detection, which would add an extra systematic error. Figure 6.31

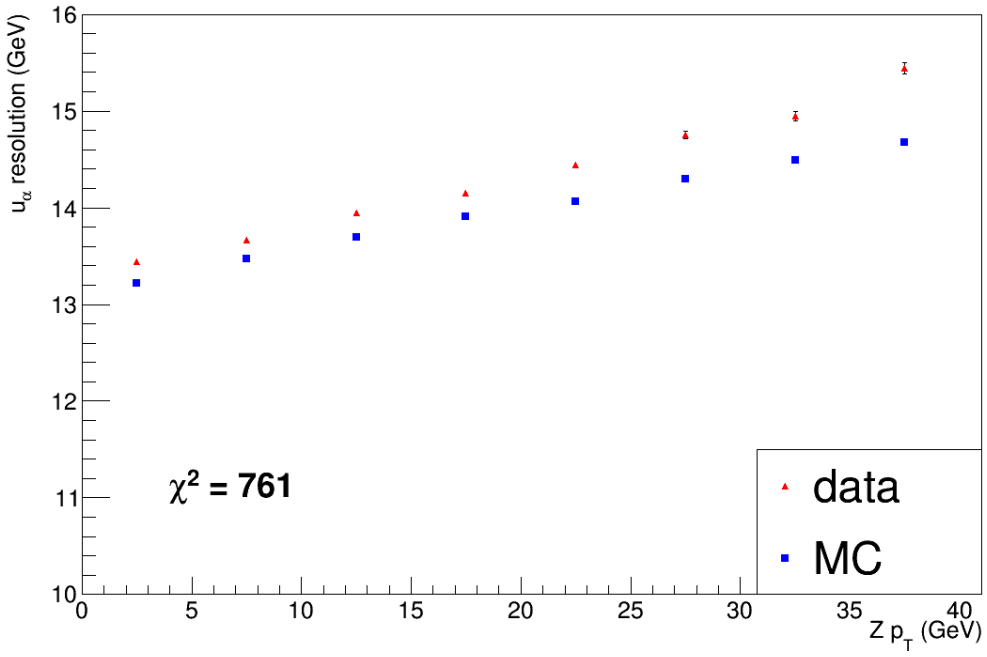



Figure 6.22: Resolution of $u_\alpha$ in bins of $Z$ $p_T$ for $Z \to ee$ events for data and POWHEG Monte Carlo. In this case, the resolution is the root mean square of the $u_\alpha$ distributions for $Z \to ee$ events split into bins of $Zp_T$. The $\chi^2$ shown here is a measure of the goodness of fit of the Monte Carlo resolution to the data resolution and hence there are 8 degrees of freedom.

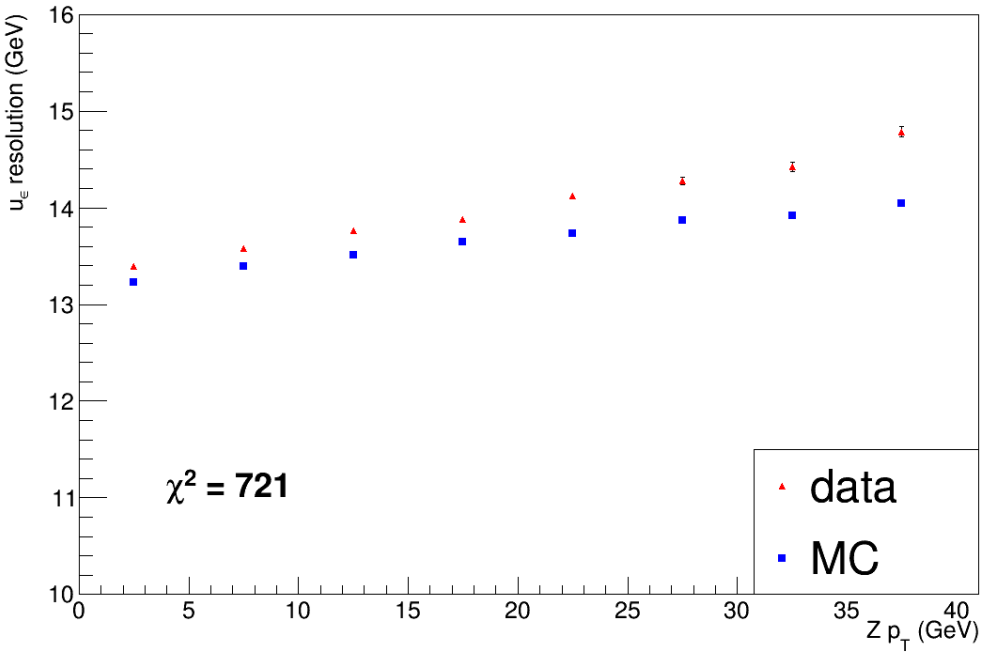



Figure 6.23: Resolution of $u_\epsilon$ in bins of $Z$ $p_T$ for $Z \to ee$ events for data and POWHEG Monte Carlo. In this case, the resolution is the root mean square of the $u_\epsilon$ distributions for $Z \to ee$ events split into bins of $Zp_T$. The $\chi^2$ shown here is a measure of the goodness of fit of the Monte Carlo resolution to the data resolution and hence there are 8 degrees of freedom.

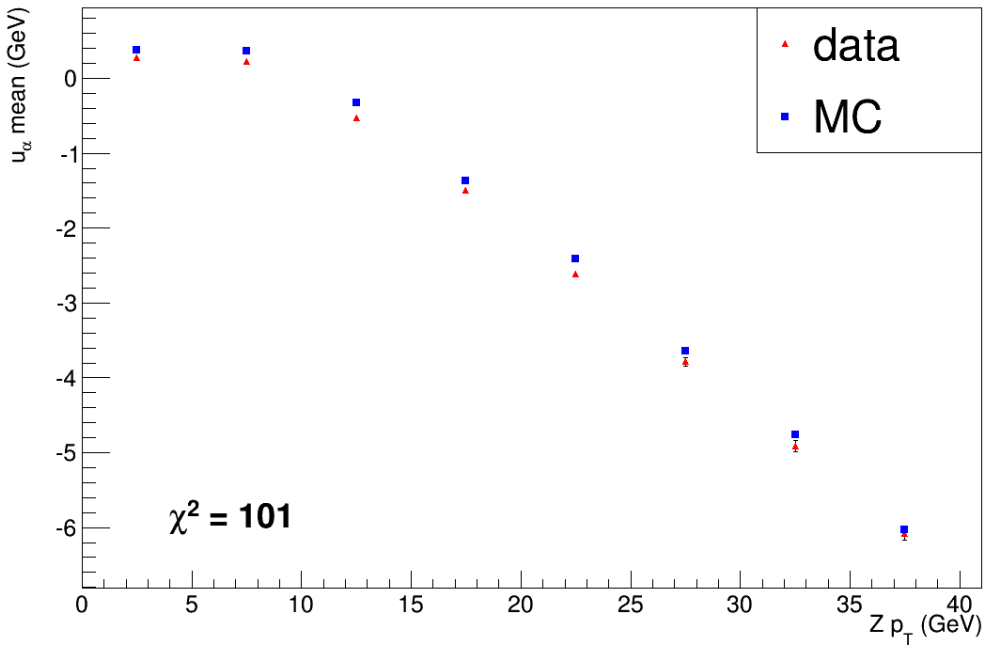



Figure 6.24: Mean of $u_\alpha$ in bins of $Z$ $p_T$ for $Z \to ee$ events for data and POWHEG Monte Carlo. In this case, this plot shows the mean of the $u_\alpha$ distributions for $Z \to ee$ events split into bins of $Zp_T$. The $\chi^2$ shown here is a measure of the goodness of fit of the Monte Carlo mean to the data mean and hence there are 8 degrees of freedom. There are small discrepancies in the means but this is a relatively small effect, that can be tuned in the later stages of building a recoil model.

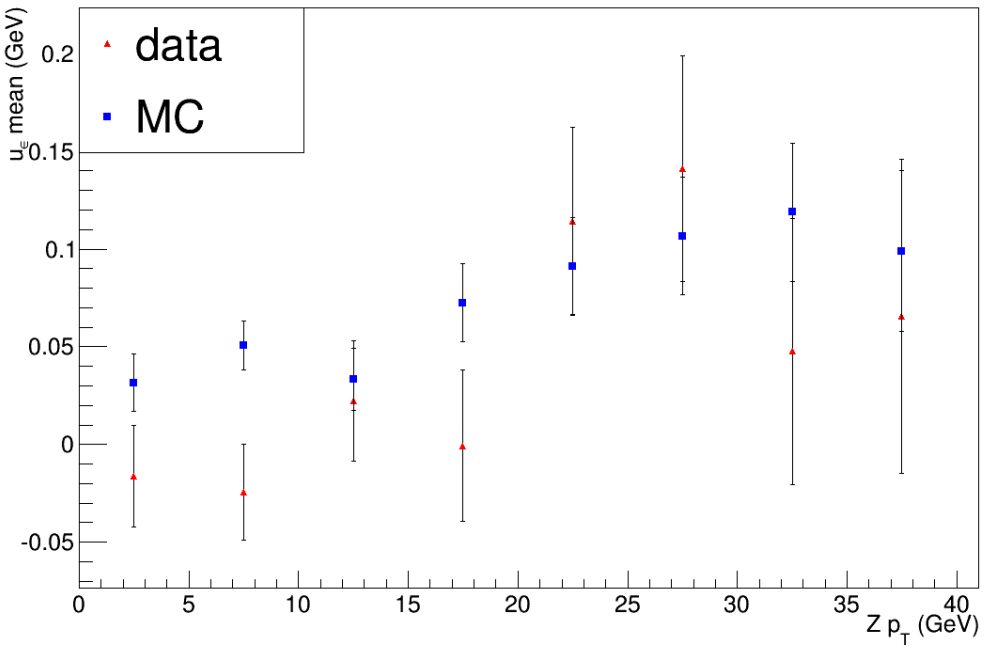



Figure 6.25: Mean of $u_\epsilon$ in bins of $Z$ $p_T$ for $Z \to ee$ events for data and POWHEG Monte Carlo. In this case, this plot shows the mean of the $u_\epsilon$ distributions for $Z \to ee$ events split into bins of $Zp_T$. The $\chi^2$ shown here is a measure of the goodness of fit of the Monte Carlo mean to the data mean and hence there are 8 degrees of freedom. There are small discrepancies in the means but this is a relatively small effect, that can be tuned in the later stages of building a recoil model.

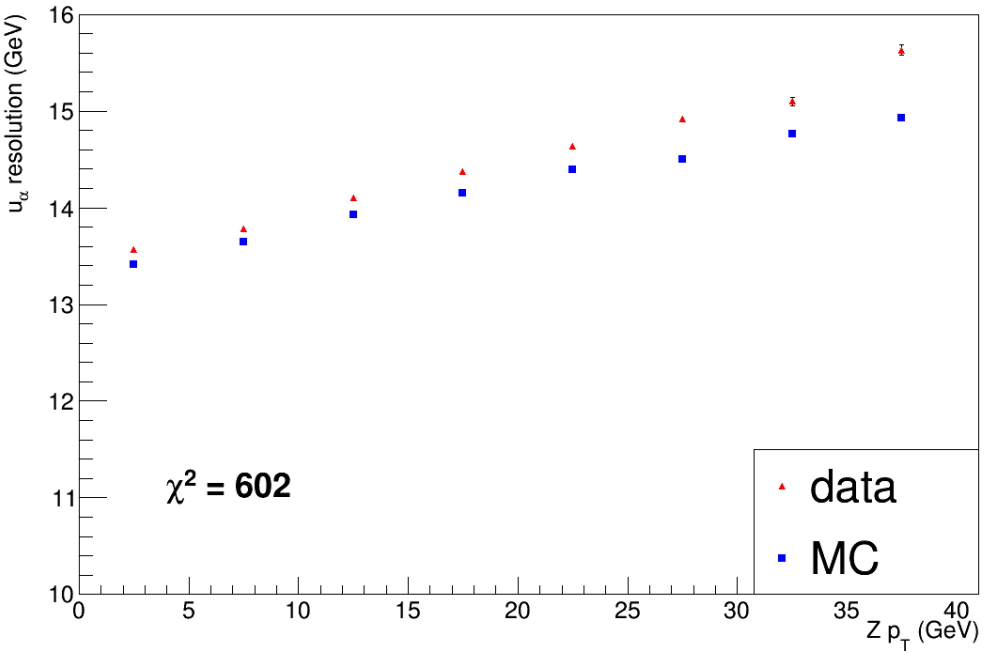



Figure 6.26: Resolution of $u_\alpha$ in bins of $Z$ $p_T$ for $Z \to \mu\mu$ events for data and POWHEG Monte Carlo. In this case, the resolution is the root mean square of the $u_\alpha$ distributions for $Z \to \mu\mu$ events split into bins of $Zp_T$. The $\chi^2$ shown here is a measure of the goodness of fit of the Monte Carlo resolution to the data resolution and hence there are 8 degrees of freedom.

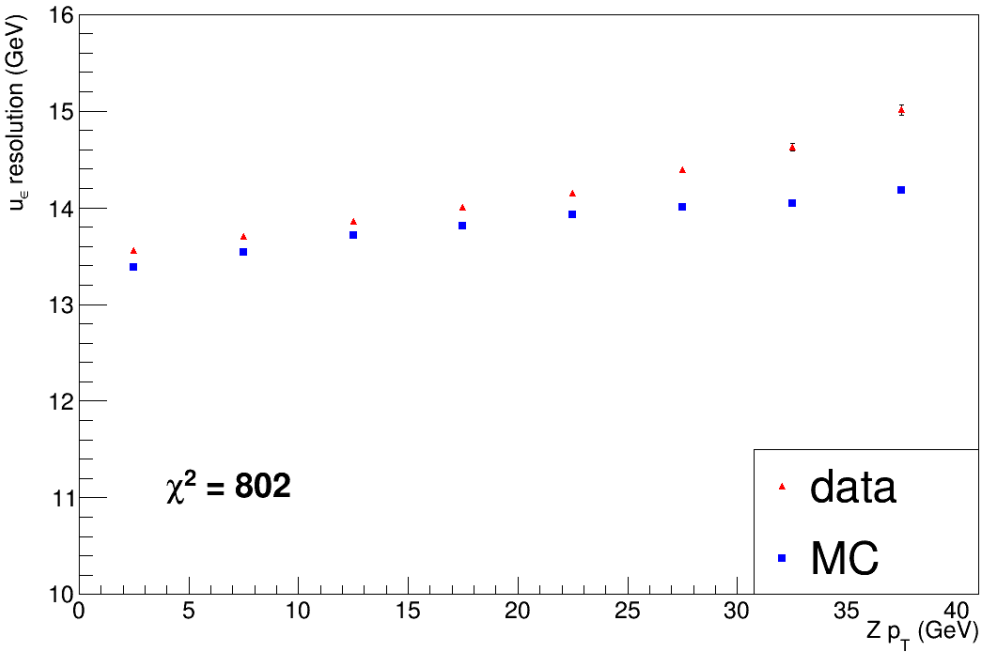



Figure 6.27: Resolution of $u_\epsilon$ in bins of $Z$ $p_T$ for $Z \to \mu\mu$ events for data and POWHEG Monte Carlo. In this case, the resolution is the root mean square of the $u_\epsilon$ distributions for $Z \to \mu\mu$ events split into bins of $Zp_T$. The $\chi^2$ shown here is a measure of the goodness of fit of the Monte Carlo resolution to the data resolution and hence there are 8 degrees of freedom.

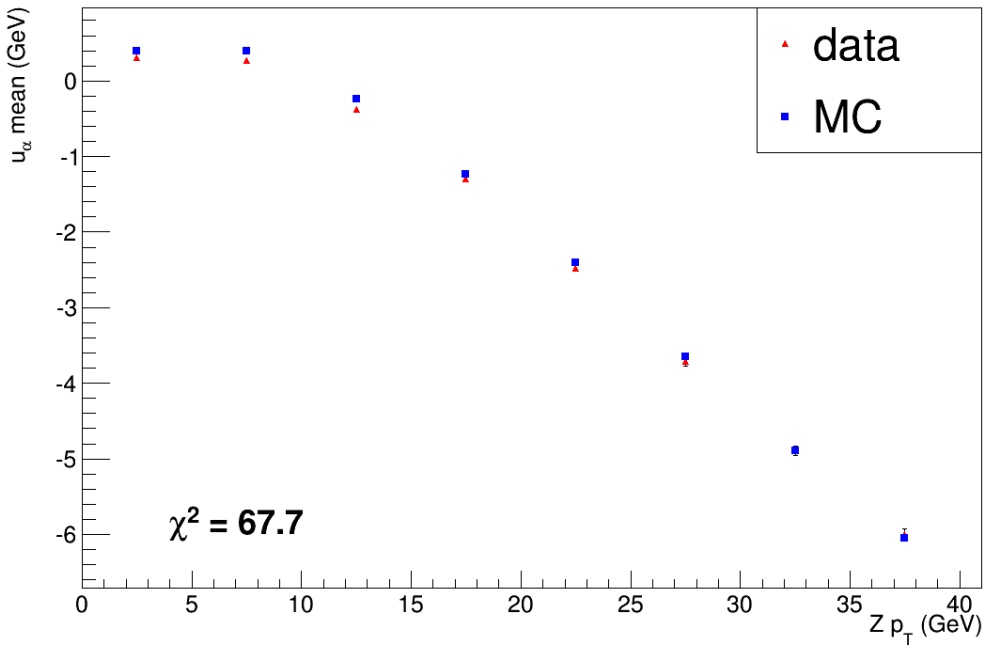



Figure 6.28: Mean of $u_\alpha$ in bins of $Z$ $p_T$ for $Z \to \mu\mu$ events for data and POWHEG Monte Carlo. In this case, this plot shows the mean of the $u_\alpha$ distributions for $Z \to \mu\mu$ events split into bins of $Zp_T$. The $\chi^2$ shown here is a measure of the goodness of fit of the Monte Carlo mean to the data mean and hence there are 8 degrees of freedom. There are small discrepancies in the means but this is a relatively small effect, that can be tuned in the later stages of building a recoil model.

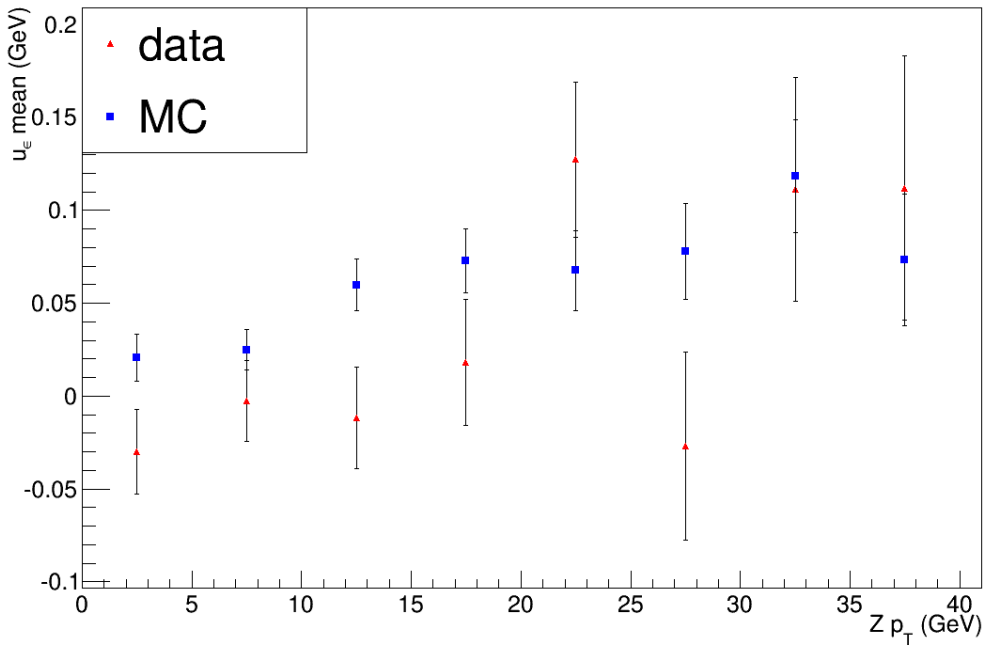



Figure 6.29: Mean of $u_\epsilon$ in bins of $Z$ $p_T$ for $Z \to \mu\mu$ events for data and POWHEG Monte Carlo. In this case, this plot shows the mean of the $u_\epsilon$ distributions for $Z \to \mu\mu$ events split into bins of $Zp_T$. The $\chi^2$ shown here is a measure of the goodness of fit of the Monte Carlo mean to the data mean and hence there are 8 degrees of freedom. There are small discrepancies in the means but this is a relatively small effect, that can be tuned in the later stages of building a recoil model.

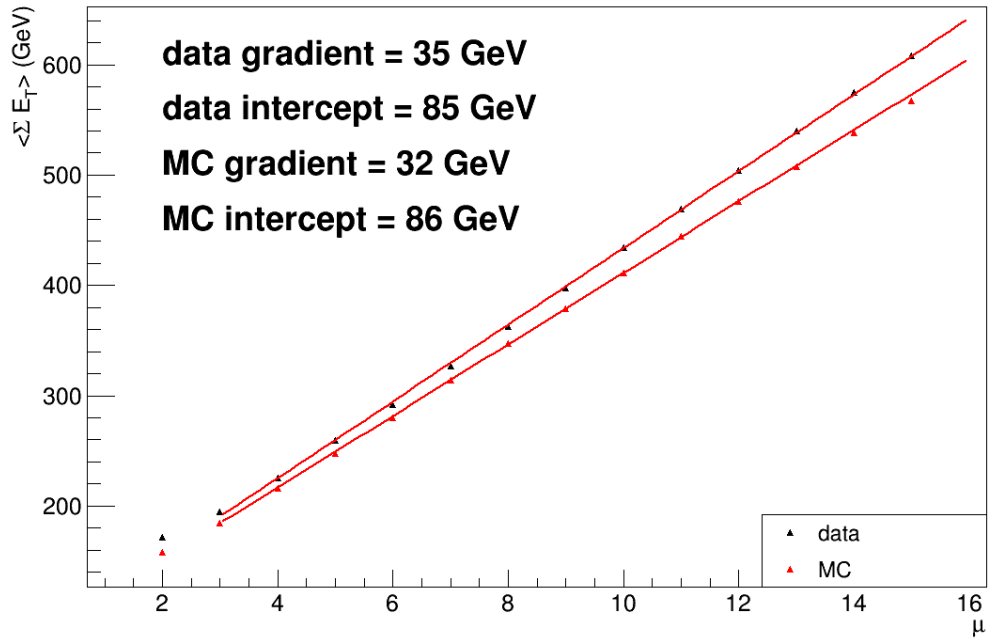



Figure 6.30: Mean $\Sigma E_T$ as a function of $\mu$ for data and POWHEG Monte Carlo for $Z \to ee$ and $Z \to \mu\mu$ events combined.

confirms that the same effect can be seen if the number of vertices is used instead of $\mu$. The additional $\Sigma E_T$ will bias $Z \to ee$ and $Z \to \mu\mu$ events equally, so we study the effect using the combined samples. The difference in gradient between data and Monte Carlo shows that the Monte Carlo has insufficient hadronic activity in each additional proton interaction.

As Monte Carlo events were generated before the end of the LHC Run in 2011, the $\mu$ distribution in Monte Carlo does not match the distribution in data. An ATLAS-wide correction is applied to the Monte Carlo, reweighting each event so that the $\mu$ distribution is the same as that of data. To correct the Monte Carlo for the difference in mean $\Sigma E_T$ as a function of $\mu$, we add an extra step to the reweighting procedure. A scale factor is applied to the $\mu$ distribution of the data. The Monte Carlo is then reweighted to match the scaled data distribution. The scale is chosen to increase the weight of the Monte Carlo events with a large number of pileup interactions, thereby increasing the weight of events with a large $\Sigma$ $E_T$. To calculate this scale factor, we subtract the mean $\Sigma$ $E_T$ in Monte Carlo from the mean $\Sigma$ $E_T$ in data and then divide by the gradient of the Monte Carlo found in Figure 6.30, for each bin of

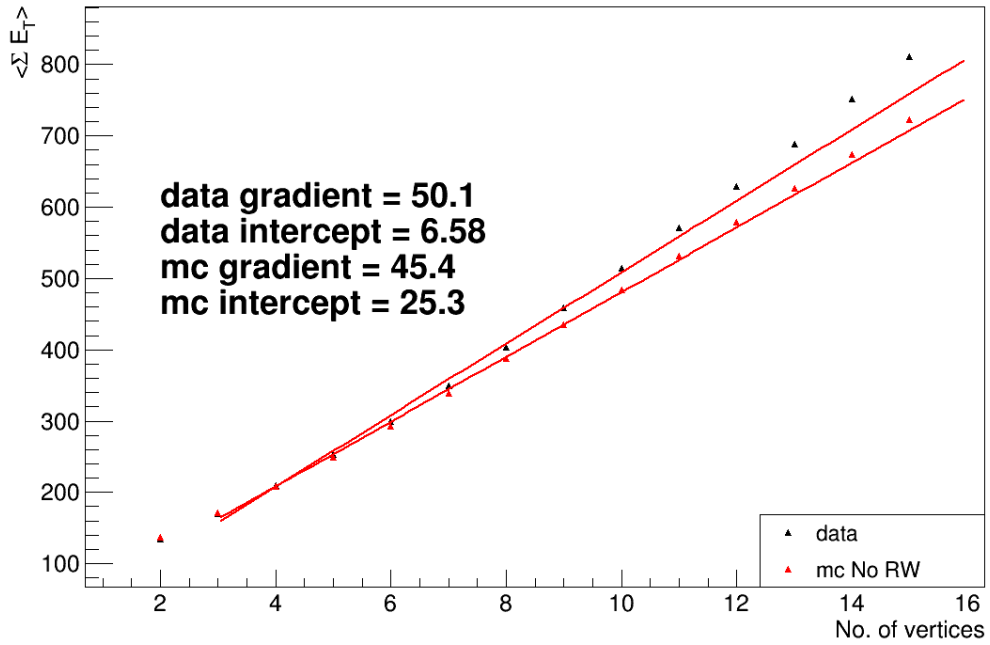



Figure 6.31: Mean $\Sigma E_T$ as a function of the number of vertices for data and POWHEG Monte Carlo for $Z \to ee$ and $Z \to \mu\mu$ events combined.

$\mu$. The result is shown in Figure 6.32 for both decay channels combined. Two straight lines proved to be the best fit to the graph, so depending on the value of $\mu$ a different scale factor is applied to the Monte Carlo. Events with $\mu = 4$ to 8 have the gradient of the first line applied as a scale factor, whereas events with $\mu$= 8 to 16 have the gradient of the second line applied.

The intercept of this graph (the line of the first fit to the lower $\mu$ bins extrapolated to 0) also has a physical interpretation: it captures any mismodelling of the hard-interaction underlying event. To account for the underlying event mismodelling, we add a constant equal to the intercept of the graph to the $\mu$ of each event in MC. The two lines are forced to meet, so with the gradients fixed, the intercept of the second graph can be recalculated each time the intercept of the first graph (also known as the intercept tune constant) is changed. Again, depending on whether the event has high or low $\mu$ (i.e. less than or greater than 8), a different underlying event correction or intercept tune is applied.

The Monte Carlo $\mu$ distribution is not continuous, and therefore it is not appropriate to

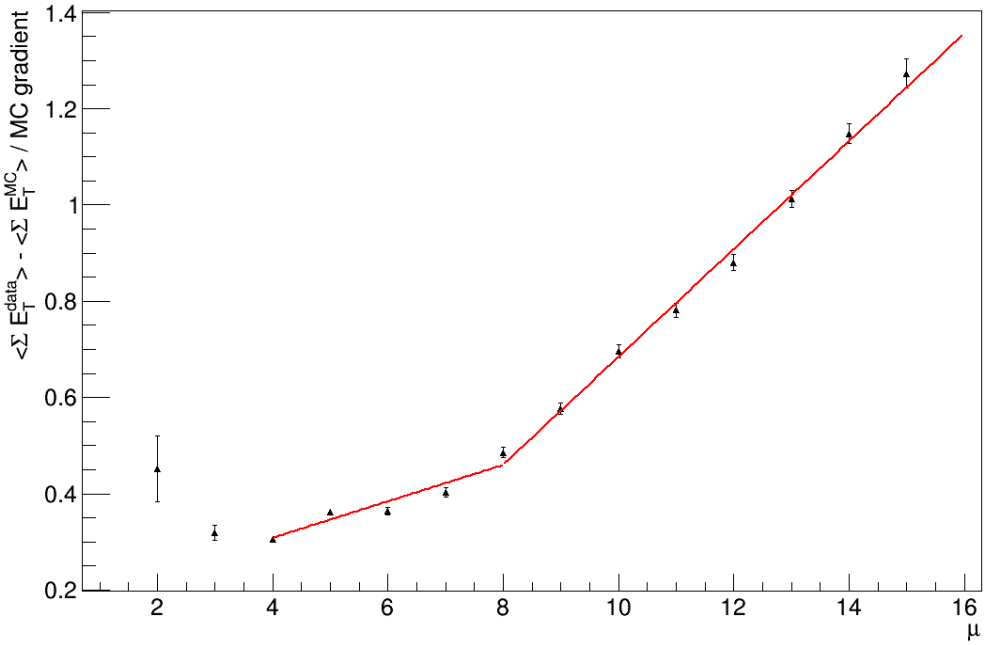



Figure 6.32: Difference between Mean $\Sigma E_T$ as a function of $\mu$ for data and POWHEG Monte Carlo divided by the Monte Carlo gradient for both $Z \to ee$ and $Z \to \mu\mu$ events combined.

simply scale and shift the $\mu$ distribution itself. Instead, we use a scaled and shifted copy of the data distribution (which is continuous) and reweight the Monte Carlo to this. It is important to note that no corrections are actually applied to the data $\mu$ distribution, the scaling is purely to facilitate the MC reweighting. The overall effect is that the bins of the Monte Carlo distribution are reweighted with respect to each other. Within one $\mu$ bin, the events are all reweighted by the same amount. To test the reweighting, one must compare the mean $\Sigma E_T$ as a function of $\mu$ of the shifted data distribution to the existing Monte Carlo distribution. Figures 6.33 and 6.34 show the reweighting for $Z \to ee$ and $Z \to \mu\mu$ events respectively.

The 'intercept', which dominantly corrects the underlying event modelling can also be used to incorporate corrections of the detector response to the recoil. Adding $\Sigma E_T$ to each event will increase the resolution of $u_\alpha$ and $u_\epsilon$ and can be used to tune the intrinsic resolution of the detector. To that end, we plot the $u_\alpha$ and $u_\epsilon$ resolution in bins of $Z$ $p_T$ for both data and Monte Carlo in both the electron and muon channels, shown in Figures 6.35 – 6.38.

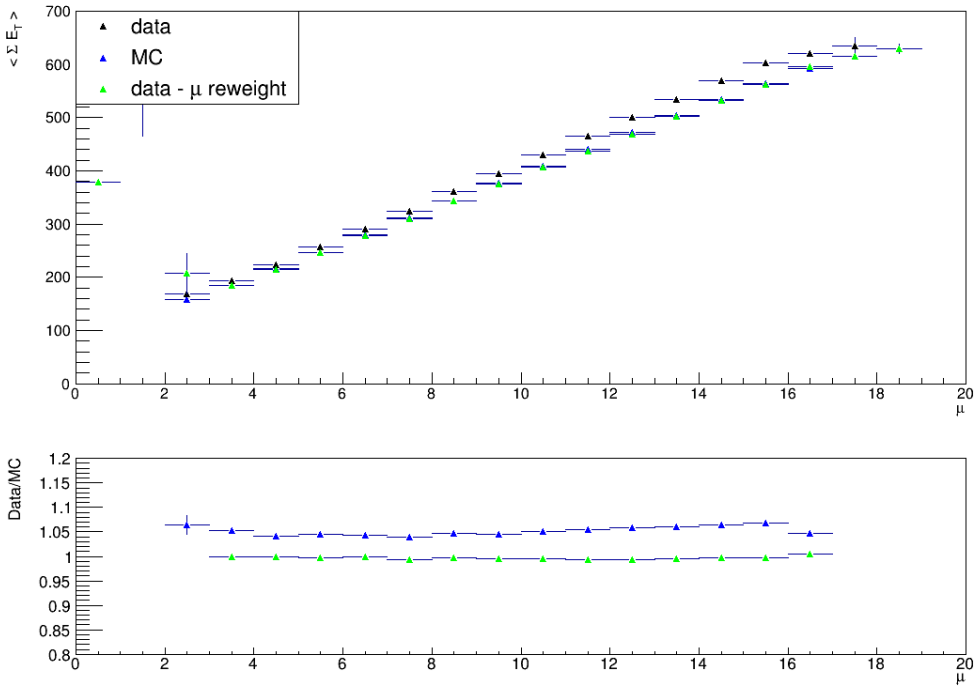



Figure 6.33: Mean $\Sigma E_T$ as a function of $\mu$ for data, shifted data (to which the Monte Carlo is reweighted) and Monte Carlo for $Z \to ee$ events. There are very few events for $\mu < 4$.

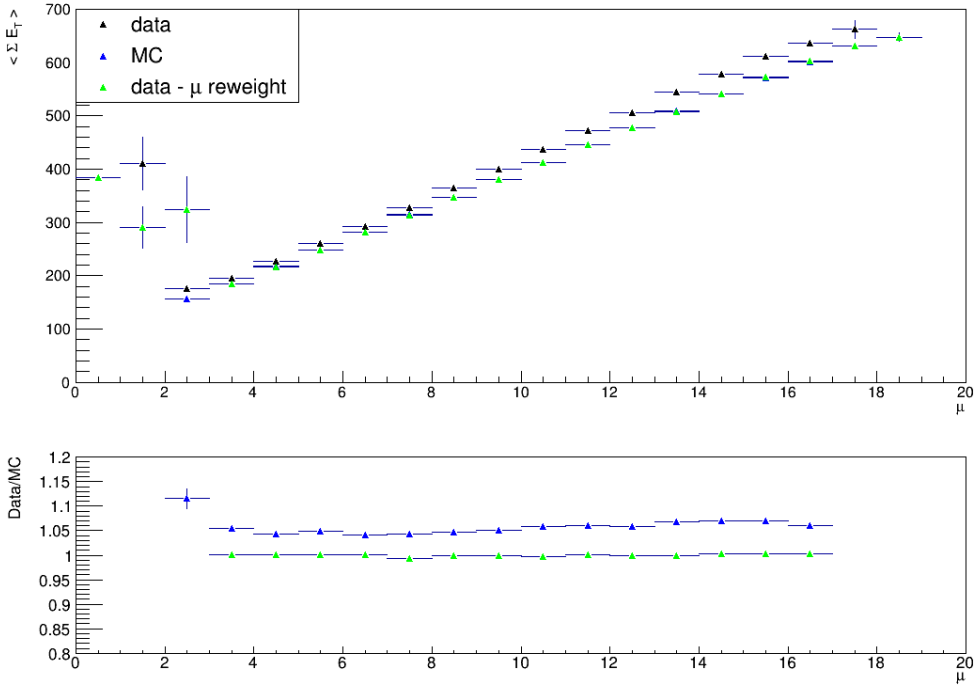



Figure 6.34: Mean $\Sigma E_T$ as a function of $\mu$ for data, shifted data (to which Monte Carlo is reweighted) and Monte Carlo for $Z \to \mu\mu$ events. There are very few events for $\mu < 4$.

| | Intercept tune constant | Minimum $\chi^2$ | $+1\sigma$ | $-1\sigma$ |
|---|---|---|---|---|
| Combined | 0.483 | 577 | 0.473 | 0.494 |
| Electron | 0.530 | 218 | | |
| Muon | 0.443 | 324 | | |

Table 6.3: Best-fit values for the intercept tune constant with no other corrections applied. The $\chi^2$ has 32 degrees of freedom for the combined tune and 16 degrees of freedom for the electron and muon tunes.

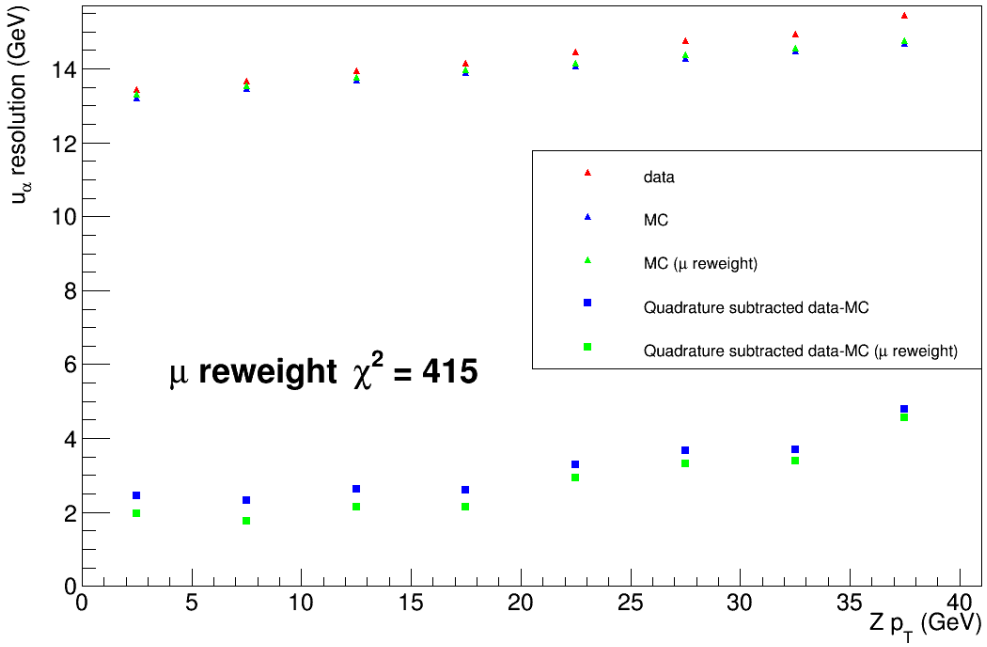



Figure 6.35: Resolution of $u_\alpha$ for data and Monte Carlo before and after the $\mu$ reweighting is applied for $Z \to ee$ events. Square points show the quadrature subtraction of data and MC. These points are used to study the residual dependence of the recoil resolution (see 6.40). The $\chi^2$ shown is a measure of the goodness of fit between the Monte Carlo with the $\mu$ reweighting applied and the data resolutions, and therefore has 8 degrees of freedom.

The $\mu$ reweighting has increased the agreement of the resolutions for data and Monte Carlo, but it is clear that further corrections are necessary. The intercept correction is varied, and $\chi^2$ is calculated between data and Monte Carlo for the resolution versus $p_T$ in the four distributions ($u_\alpha$ and $u_\epsilon$ for both electrons and muons). In Figure 6.39, several mismodelling corrections have been plotted versus the sum of the $\chi^2$ values from the four distributions. A parabola is fitted to this graph, the minimum of which gives the best-fit correction. The best-fit corrections for electrons, muons and the combined fit are shown in Table 6.3.

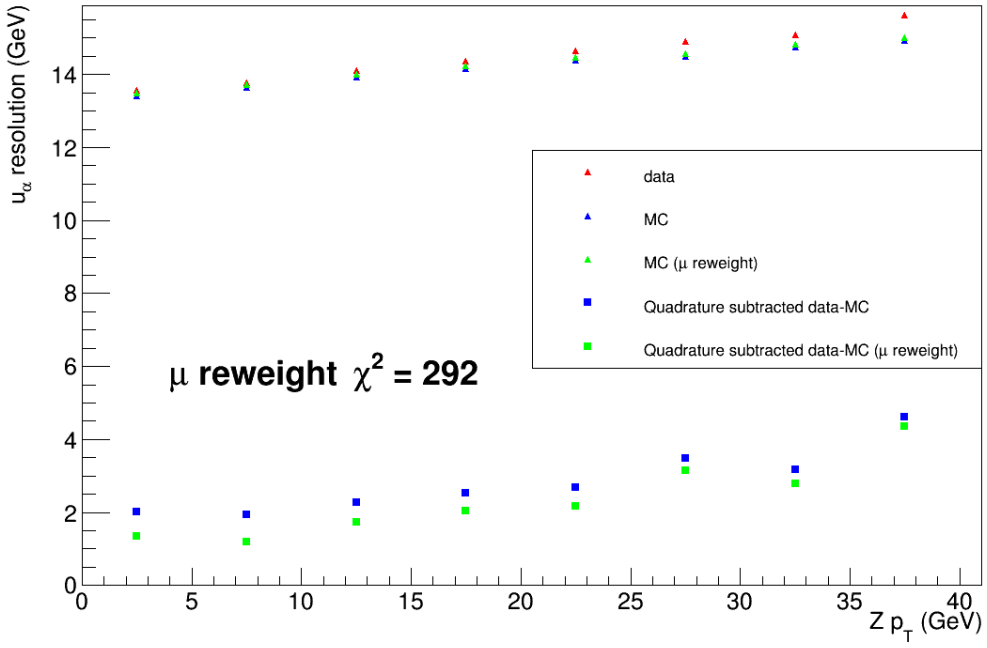



Figure 6.36: Resolution of $u_\alpha$ for data and Monte Carlo before and after the $\mu$ reweighting is applied for $Z \to \mu\mu$ events. Square points show the quadrature subtraction of data and MC. These points are used to study the residual dependence of the recoil resolution (see 6.41). The $\chi^2$ shown is a measure of the goodness of fit between the Monte Carlo with the $\mu$ reweighting applied and the data resolutions, and therefore has 8 degrees of freedom.

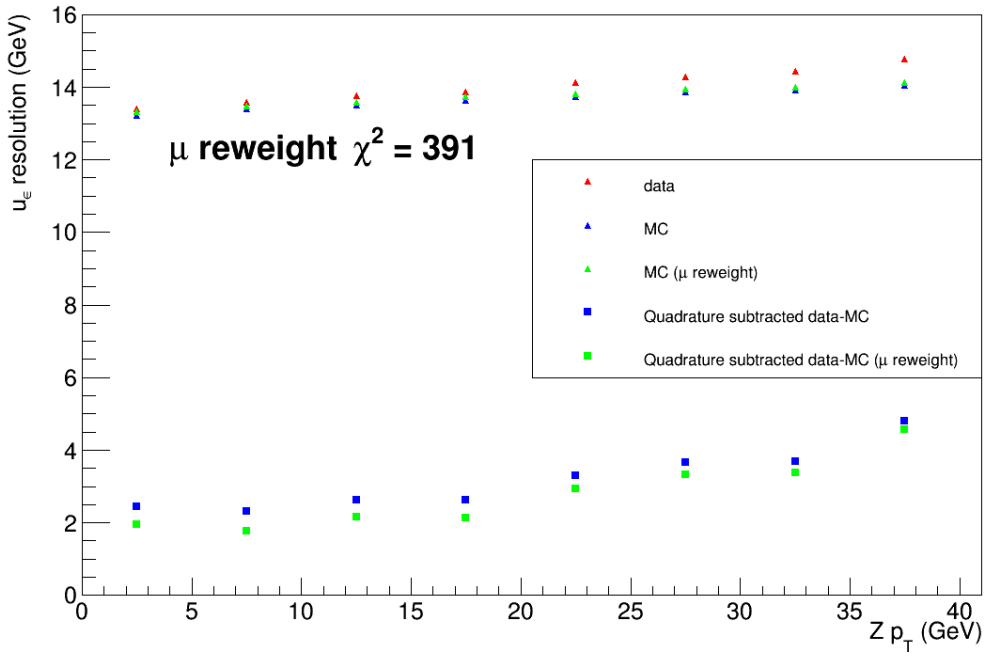



Figure 6.37: Resolution of $u_\epsilon$ for data and Monte Carlo before and after the $\mu$ reweighting is applied for $Z \to ee$ events. The $\chi^2$ shown is a measure of the goodness of fit between the Monte Carlo with the $\mu$ reweighting applied and the data resolutions, and therefore has 8 degrees of freedom.

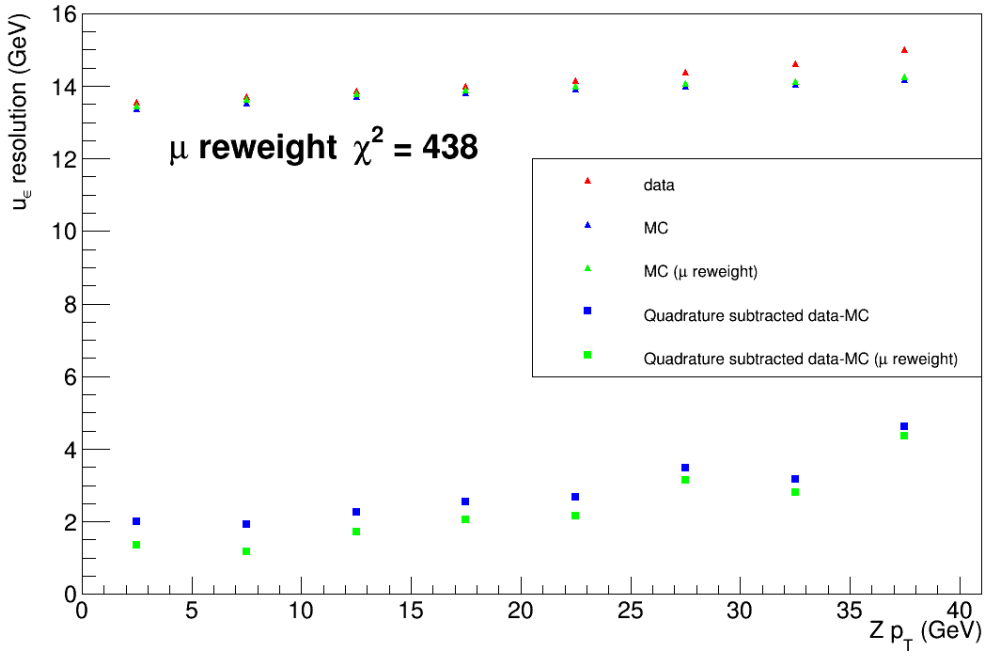



Figure 6.38: Resolution of $u_\epsilon$ for data and Monte Carlo before and after the $\mu$ reweighting is applied for $Z \to \mu\mu$ events. The $\chi^2$ shown is a measure of the goodness of fit between the Monte Carlo with the $\mu$ reweighting applied and the data resolutions, and therefore has 8 degrees of freedom.

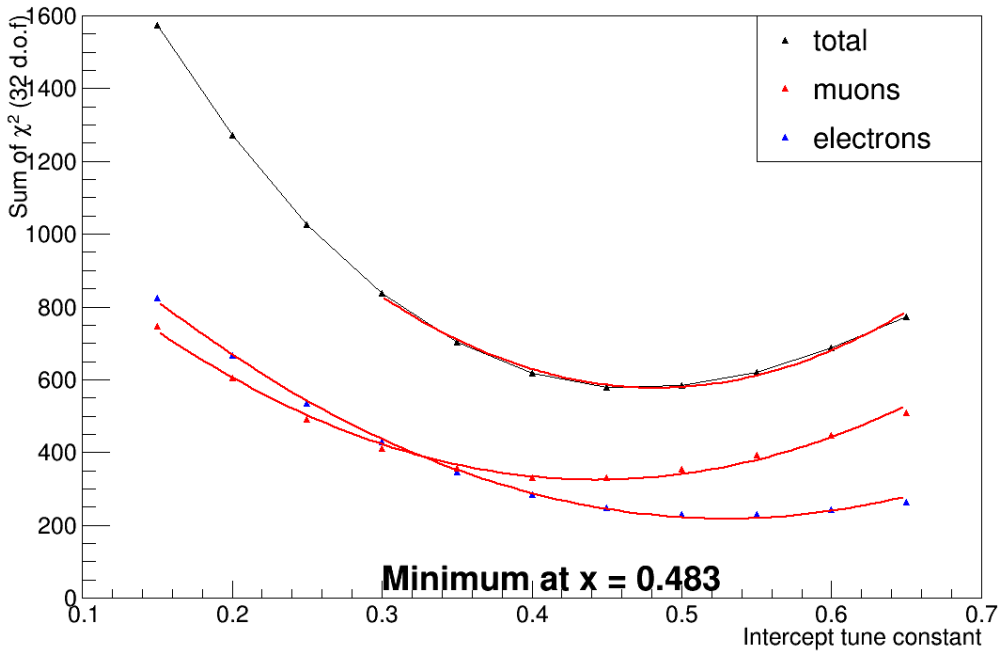



Figure 6.39: Sum of $\chi^2$ values from $Z \to ee$ and $Z \to \mu\mu$ $u_\alpha$ and $u_\epsilon$ plots vs the underlying event correction used. The $\chi^2$'s have 32 degrees of freedom in the combined tune and 16 degrees in the individual electron and muon tunes. The fit function is a parabola.

## 6.7 Jet energy resolution correction

The sampling resolution of the calorimeter will limit the accuracy of the recoil energy measurement at large values of recoil. As the majority of the recoil is in the direction parallel to the $Z$ boson, the resolution of $u_\alpha$ is the most sensitive observable to this sampling resolution. In section 6.6, the resolution of $u_\alpha$ is plotted in bins of $Z$ $p_T$ for data and Monte Carlo and for both the muon channel and the electron channel in Figures 6.35 and 6.36. The Monte Carlo points are also subtracted from the data points in quadrature. When plotted against the square root of $Z$ $p_T$ a linear distribution is obtained (as shown in Figures 6.40 and 6.41). The linear dependence indicates that additional resolution proportional to the square root of the $Z$ $p_T$ is required in the Monte Carlo.

To correct the recoil energy resolution a $Z$ $p_T$ smearing is added to Monte Carlo along the recoil direction at production, proportional to the square root of $Z$ $p_T$. This is done on

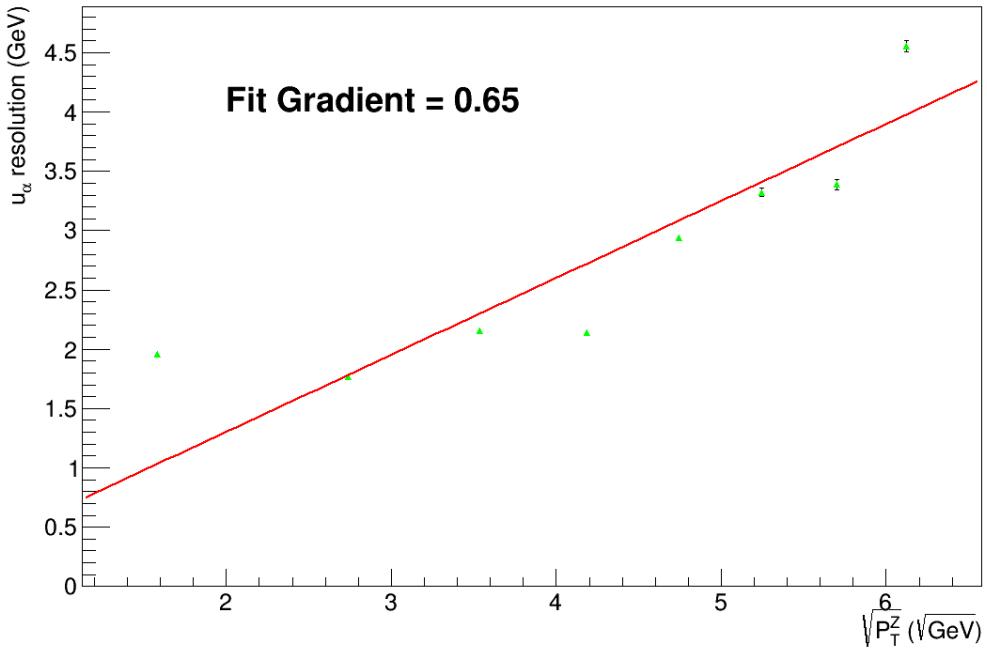



Figure 6.40: Quadrature difference of data and MC $u_\alpha$ resolution as a function of the square root of $Z$ $p_T$ for $Z \to ee$ events.

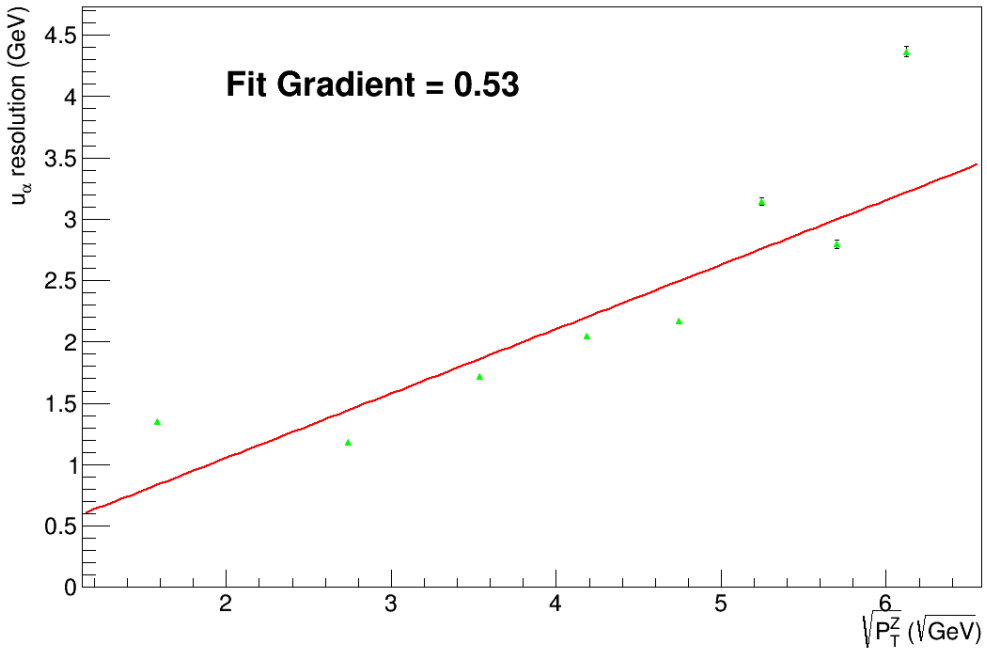



Figure 6.41: Quadrature difference of data and MC $u_\alpha$ resolution as a function of the square root of $Z$ $p_T$ for $Z \to \mu\mu$ events.

| | Recoil magnitude smearing constant | Minimum $\chi^2$ | $+1\sigma$ | $-1\sigma$ |
|---|---|---|---|---|
| Combined | 0.312 | 182 | 0.333 | 0.291 |
| Electron | 0.381 | 47 | | |
| Muon | 0.260 | 121 | | |

Table 6.4: Best-fit values for the recoil magnitude constant with only the initial intercept tune applied. As only the $u_\alpha$ resolution graphs are used to tune this value, the combined tune has 16 degrees of freedom and the electron and muon tunes each have 8.

an event by event basis: in each event a Gaussian is randomly sampled and the resulting number added to the recoil energy measurement, along the direction of the produced recoil. The width of the Gaussian (henceforth referred to as the recoil-magnitude smearing constant) by varying the constant and finding the closest match between data and Monte Carlo resolutions using a $\chi^2$ test. Since the recoil-magnitude smearing has the largest impact on $u_\alpha$ resolution, only the $u_\alpha$ graphs are used in the fit (as seen in Figures 6.35 and 6.36). As before, the sum of both the muon and the electron channels is used. The resulting graph can be seen in Figure 6.42. Table 6.4 summarises the minima of the electron, muon and combined fits.

## 6.8 Jet angular resolution correction

As discussed in section 6.7, the majority of the recoil is in the direction antiparallel to the $Z$ boson $p_T$. The magnitude of the recoil in the perpendicular direction is relatively small. However, the resolution on the angle of the recoil can result in a significant component in the perpendicular direction. To model and correct this angular resolution, we plot the $\Delta\phi$ between $-p_T^Z$ and the recoil vector for both data and Monte Carlo for $Z \to ee$ and $Z \to \mu\mu$ events, as shown in Figures 6.43 and 6.44.

The recoil $\phi$ is smeared using a box function with bounds $-1$ and $+1$ multiplied by a recoil-$\phi$-smearing constant. A box function is used instead of a gaussian as the $\Delta\phi$ distribution does not have the long tails of the other distributions. As before, we must tune this

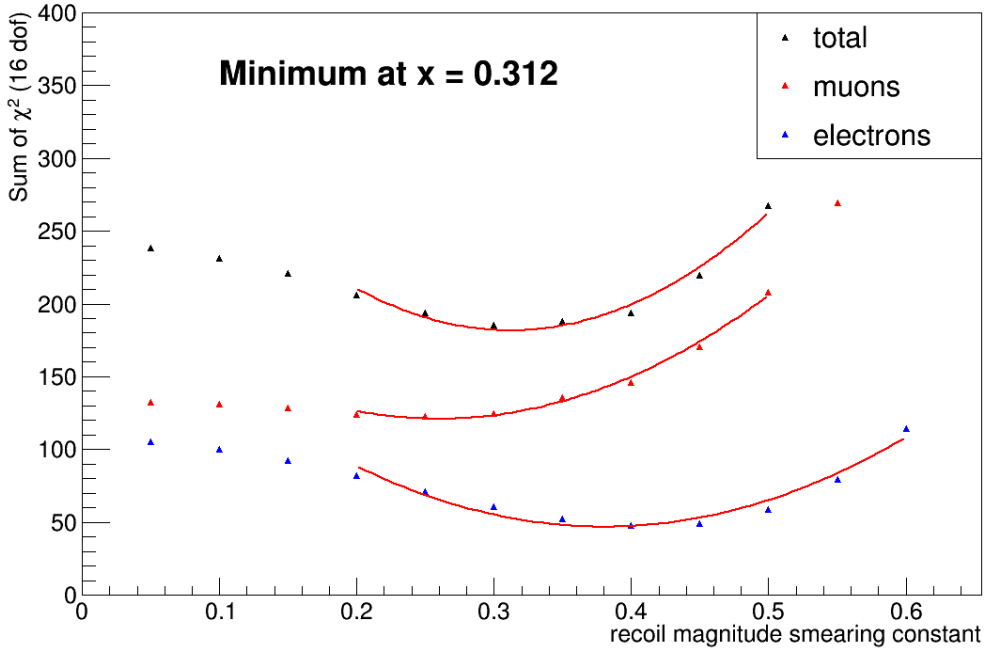



Figure 6.42: Sum of $\chi^2$ values from $Z \to ee$ and $Z \to \mu\mu$ $u_\alpha$ plots as a function of the recoil magnitude correction used. As only the $u_{alpha}$ resolution graphs are used, the combined tune has 16 degrees of freedom and the electron and muon tunes each have 8. The fit function is a parabola.

constant. In this case, we use the sum of the $\chi^2$ from the $u_\epsilon$ resolution graphs for electrons and muons (whereas for the recoil-magnitude smearing we used $u_\alpha$ graphs). Figure 6.45 shows the result. Table 6.5 summarises the best-fit corrections for electrons, muons and the combined fit.

| | Recoil $\phi$ smearing constant | Minimum $\chi^2$ | $+1\sigma$ | $-1\sigma$ |
|---|---|---|---|---|
| Combined | 0.0173 | 88 | 0.0179 | 0.0167 |
| Electron | 0.0170 | 23 | | |
| Muon | 0.0175 | 65 | | |

Table 6.5: Best-fit values for the recoil $\phi$ smearing constant with the first tunes for the intercept and recoil magnitude smearing constant applied. As only the $u_{epsilon}$ resolution graphs are used to tune this constant, the combined tune has 16 degrees of freedom whereas the electron and muon individual tunes have 8.

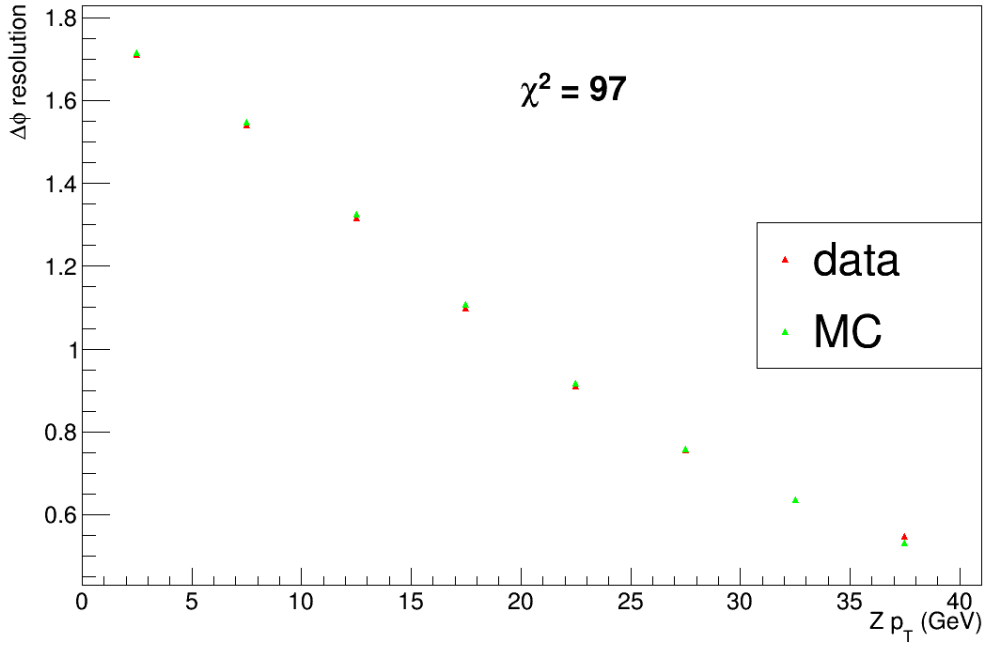



Figure 6.43: $\Delta\phi$ between $-p_T^Z$ and the recoil vector for data and Monte Carlo for $Z \to ee$ events. The MC has been corrected using the best-fit tune of the pileup, underlying event and recoil magnitude smearing. The $\chi^2$ shown here is a measure of the goodness of fit for the resolution of $\Delta\phi$ between data and Monte Carlo on the above plot and therefore has 8 degrees of freedom.

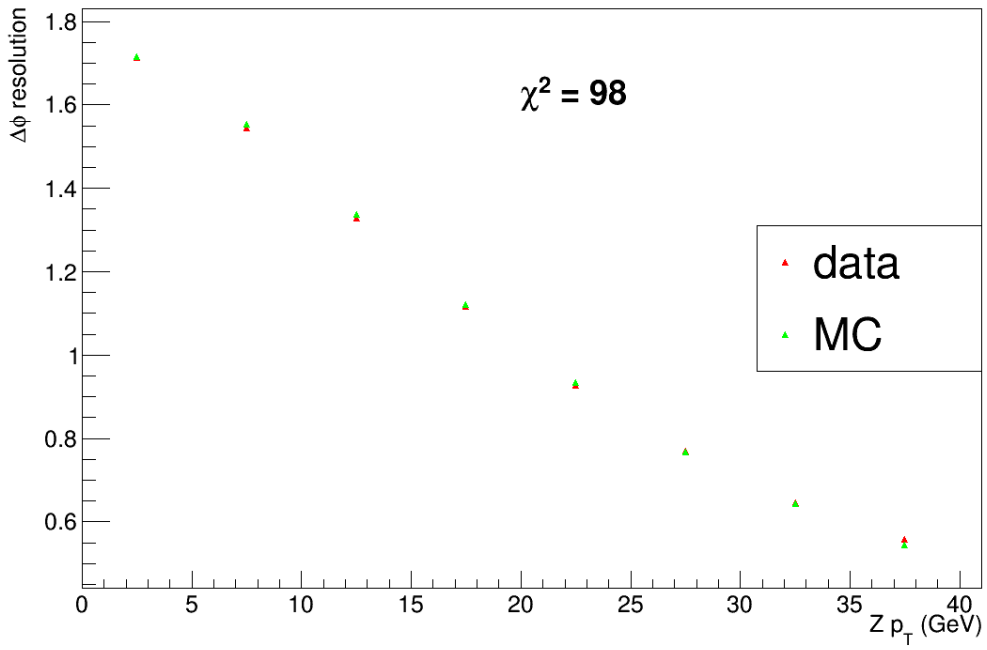



Figure 6.44: $\Delta\phi$ between $-p_T^Z$ and the recoil vector for data and Monte Carlo for $Z \to \mu\mu$ events. The MC has been corrected using the best-fit tune of the pileup, underlying event and recoil magnitude smearing. The $\chi^2$ shown here is a measure of the goodness of fit for the resolution of $\Delta\phi$ between data and Monte Carlo on the above plot and therefore has 8 degrees of freedom.

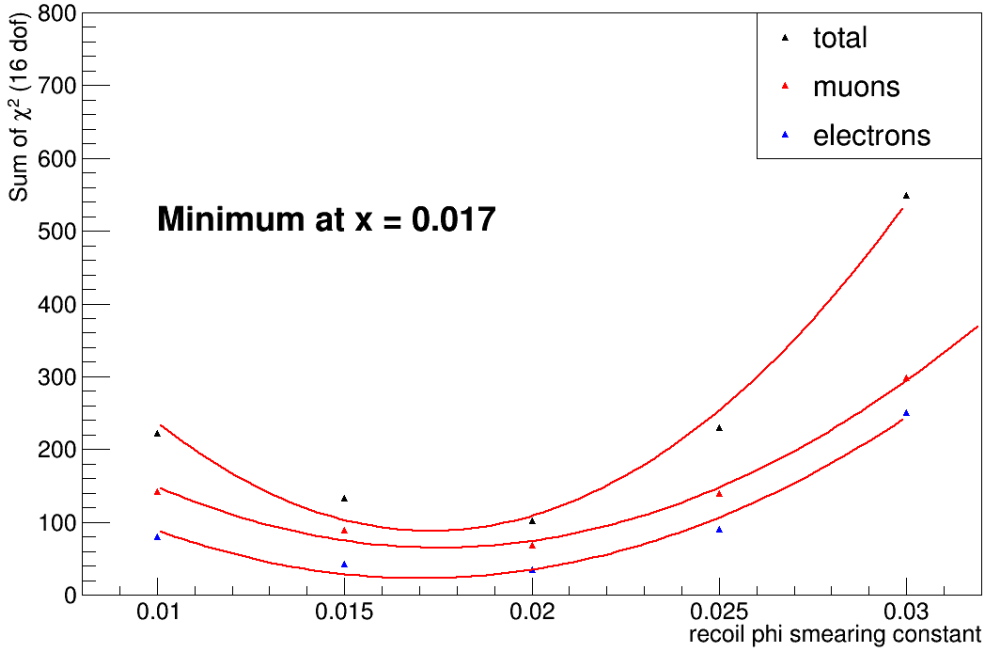



Figure 6.45: Sum of $\chi^2$ values from $Z \to ee$ and $Z \to \mu\mu$ $u_\epsilon$ plots vs the recoil phi correction used. The fit function is a parabola. The combined tune has 16 degrees of freedom, whereas the electron and muon individual tunes each have 8.

| | Intercept tune constant | Minimum $\chi^2$ | $+1\sigma$ | $-1\sigma$ |
|---|---|---|---|---|
| Combined | 0.298 | 133 | 0.307 | 0.287 |
| Electron | 0.347 | 50 | | |
| Muon | 0.255 | 63 | | |

Table 6.6: Best-fit values for the intercept tune constant with the best-fit values for the recoil magnitude and recoil $\phi$ smearing applied. $u_{alpha}$ and $u_{epsilon}$ graphs are used to tune this value, so there are 32 degrees of freedom in the combined tune and 16 degrees of freedom in the individual electron and muon channels. The errors are included for the combined tune only, as they will be used later in the chapter to measure correlations between the different corrections.

| | Recoil magnitude smearing constant | Minimum $\chi^2$ | $+1\sigma$ | $-1\sigma$ |
|---|---|---|---|---|
| Combined | 0.491 | 101 | 0.511 | 0.480 |
| Electron | 0.556 | 29 | | |
| Muon | 0.451 | 60 | | |

Table 6.7: Best-fit values for the recoil magnitude smearing constant with the best-fit values for the intercept and recoil $\phi$ smearing applied. Only $u_{alpha}$ graphs are used to tune this constant, so there are 16 degrees of freedom in the combined tune and 8 in the electron and muon tunes. The errors are included for the combined tune only, as they will be used later in the chapter to measure correlations between the different corrections.

## 6.9 Iterating

These corrections are somewhat dependent on each other. Therefore, to find the minimal $\chi^2$ overall, we vary each with the others set to their tuned values found independently. These variations can be seen in Figures 6.46, 6.47 and 6.48. This can result in a lower $\chi^2$ overall. The minimum $\chi^2$ values found for the combined samples and for electrons and muons separately are shown in Tables 6.6, 6.7 and 6.8.

The resolutions of $u_\alpha$ and $u_\epsilon$ as a function of $Z$ $p_T$ for $Z \to ee$ and $Z \to \mu\mu$ events can

| | Recoil $\phi$ constant | Minimum $\chi^2$ | $+1\sigma$ | $-1\sigma$ |
|---|---|---|---|---|
| Combined | 0.0215 | 32 | 0.0220 | 0.0209 |
| Electron | 0.0212 | 23 | | |
| Muon | 0.0217 | 8 | | |

Table 6.8: Best-fit values for the recoil $\phi$ smearing constant with the best-fit values for the intercept tune and recoil magnitude smearing applied. Only $u_{epsilon}$ graphs are used to tune this constant, so there are 16 degrees of freedom in the combined tune and 8 in the electron and muon individual tunes. The errors are included for the combined tune only, as they will be used later in the chapter to measure the correlations between the different corrections.

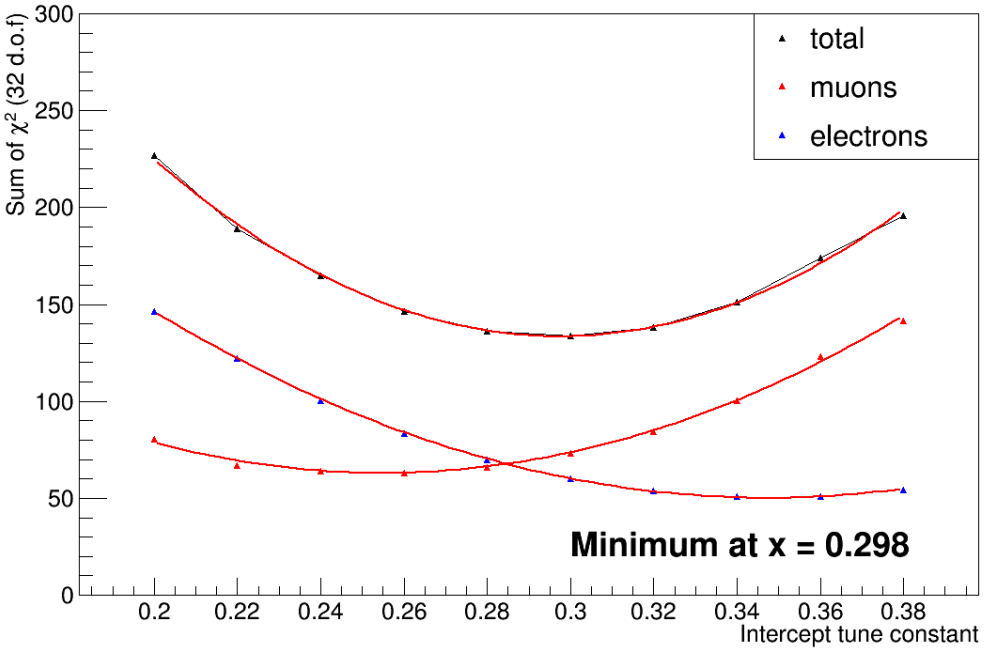



Figure 6.46: Sum of $\chi^2$ values from $Z \to ee$ and $Z \to \mu\mu$ $u_\alpha$ and $u_\epsilon$ resolution plots vs the underlying event correction used, resulting in 32 degrees of freedom in the combined tune and 16 in the electron and muon individual tunes. The fit function is a parabola. In this graph, the recoil magnitude smearing constant has been set to 0.49 and the recoil $\phi$ smearing constant to 0.021. The minimum is shifted somewhat relative to 6.39.

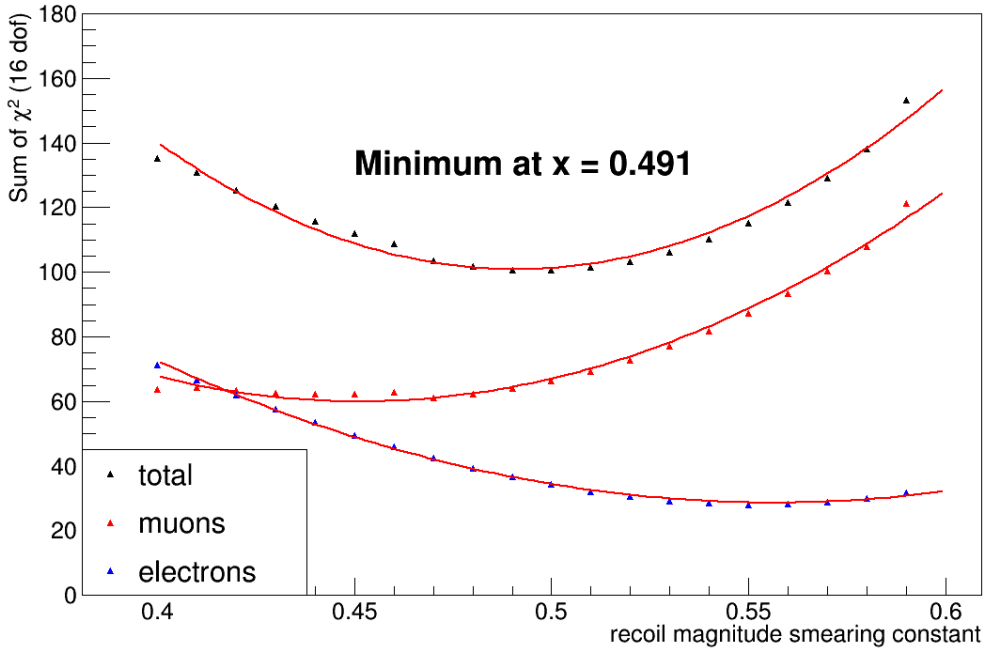



Figure 6.47: Sum of $\chi^2$ values from $Z \to ee$ and $Z \to \mu\mu$ $u_\alpha$ resolution plots vs the recoil magnitude correction used, resulting in 16 degrees of freedom in the combined tune and 8 in the individual electron and muon tunes. The fit function is a parabola. In this graph, the underlying event modelling correction has been set to 0.3 and the recoil $\phi$ smearing constant to 0.021. The minimum is shifted somewhat relative to 6.42

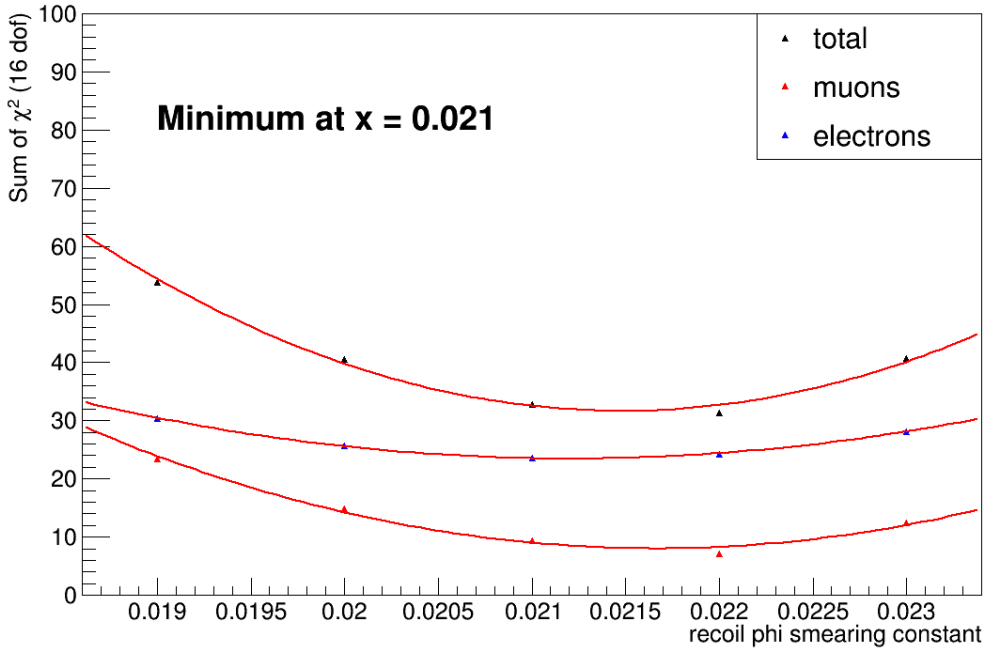



Figure 6.48: Sum of $\chi^2$ values from $Z \to ee$ and $Z \to \mu\mu$ $u_\epsilon$ resolution plots vs the recoil phi correction used, resulting in 16 degrees of freedom in the combined tune and 8 in the electron and muon tunes. The fit function is a parabola. In this graph, the underlying event modelling correction has been set to 0.3 and the recoil magnitude smearing constant to 0.49. The minimum is shifted somewhat relative to 6.45.

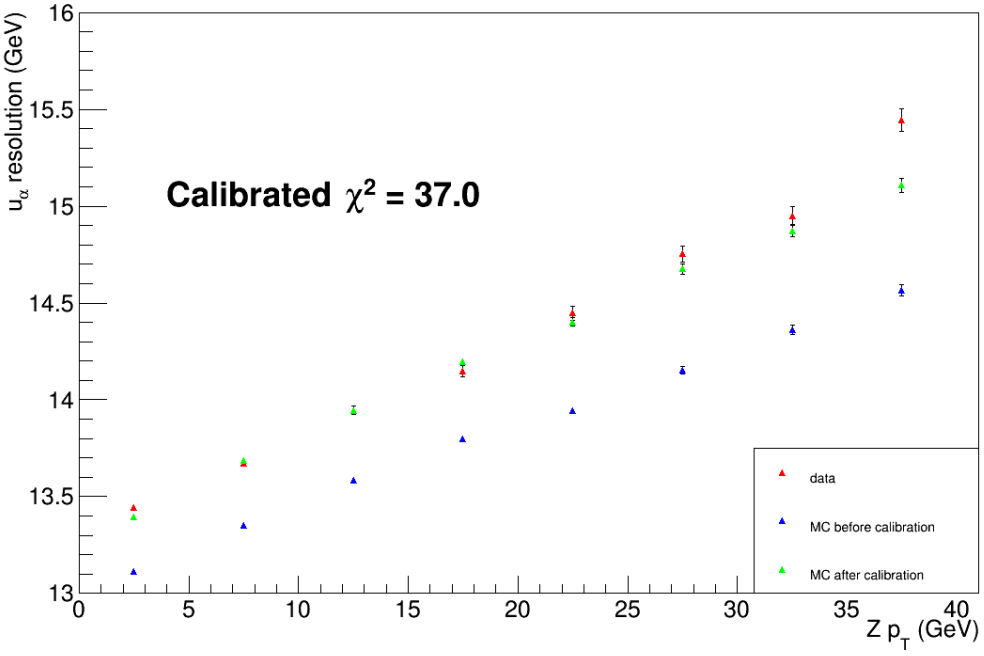



Figure 6.49: Resolution of $u_\alpha$ in $Z \to ee$ events as a function of $Z$ $p_T$ after the corrections for pileup and underlying event, recoil magnitude smearing and recoil $\phi$ smearing. The $\chi^2$ shown here indicates the goodness of fit for the resolutions between Monte Carlo and the data and has 8 degrees of freedom.

be seen in Figures 6.49 to 6.52. The recoil model has significantly improved the agreement of the resolutions of $u_\alpha$ and $u_\epsilon$ between data and Monte Carlo at a first-order level.

## 6.10 Response correction

As shown in Chapter 5, the calorimeter energy scale may have a $E_T$ dependence. Those studies were for electrons in the ECal, but the response of the calorimeters to the hadronic recoil may also be non-linear. The mean of the $u_\alpha$ and $u_\epsilon$ plots depends upon the response of the calorimeter, which may not be modelled correctly in Monte Carlo. The response (the component of the recoil parallel to the $Z$ $p_T$ divided by the $Z$ $p_T$) is plotted as a function of $Z$ $p_T$, as shown in Figures 6.53 and 6.54. The ratio of the data and Monte Carlo produced is fit to a constant. This magnitude of the produced recoil is tuned using the $\chi^2$ of plots of the mean of $u_\alpha$ as a function of $Z$ $p_T$ for both electrons and muons, as seen in Figure 6.55. A summary of the best-fit values for the recoil response tune can be seen in Table 6.9. In

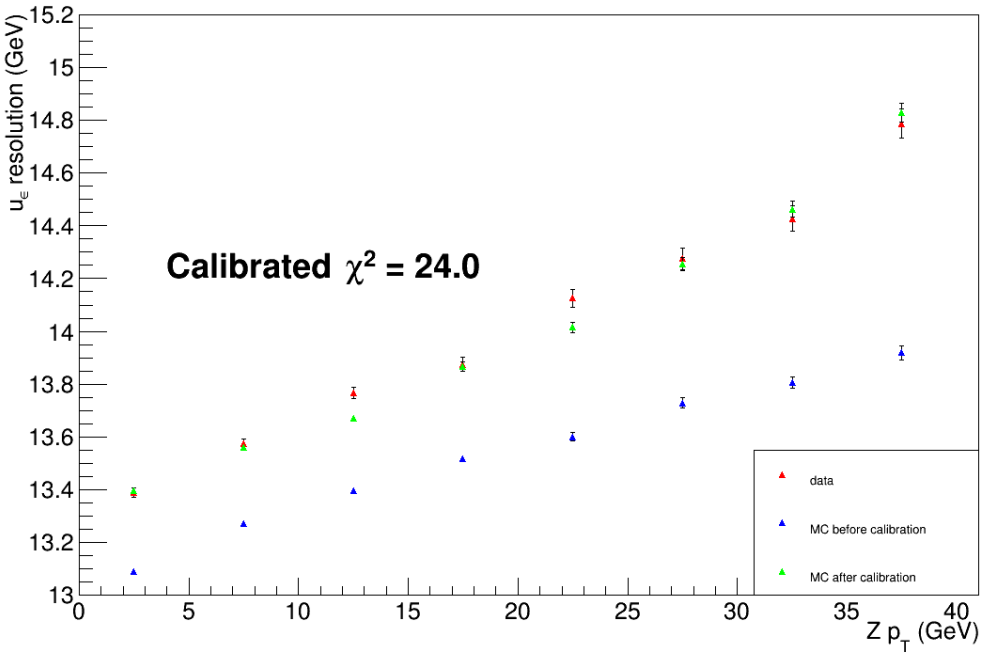



Figure 6.50: Resolution of $u_\epsilon$ in $Z \to ee$ events as a function of $Z$ $p_T$ after the corrections for pileup and underlying event, recoil magnitude smearing and recoil $\phi$ smearing corrections. The $\chi^2$ shown here indicates the goodness of fit for the resolutions between Monte Carlo and the data and has 8 degrees of freedom.

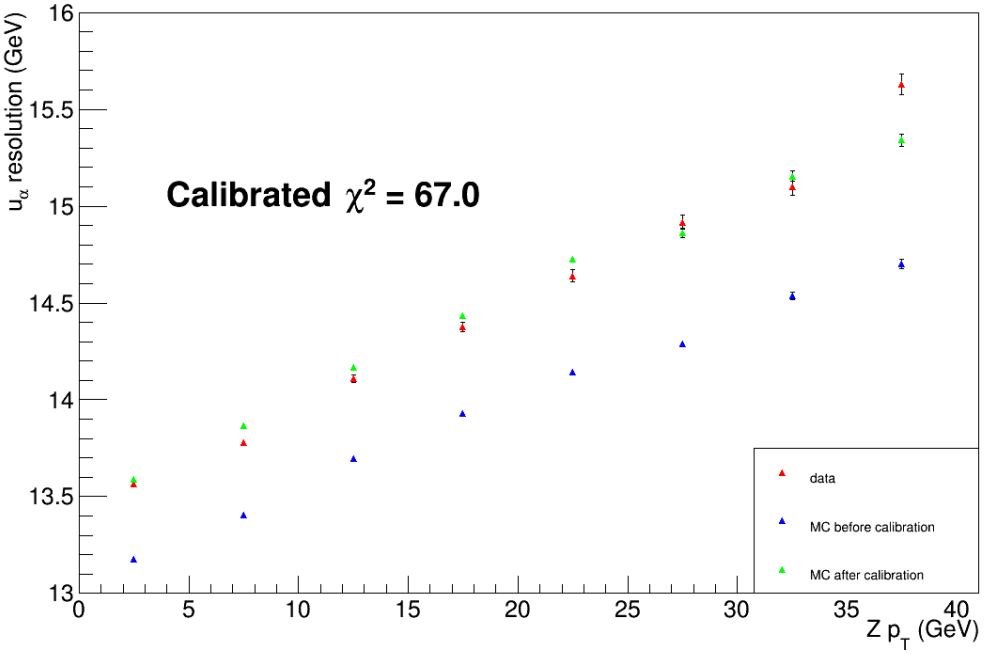



Figure 6.51: Resolution of $u_\alpha$ in $Z \to \mu\mu$ events as a function of $Z$ $p_T$ after the corrections for pileup and underlying event, recoil magnitude smearing and recoil $\phi$ smearing. The $\chi^2$ shown here indicates the goodness of fit for the resolutions between Monte Carlo and the data and has 8 degrees of freedom.

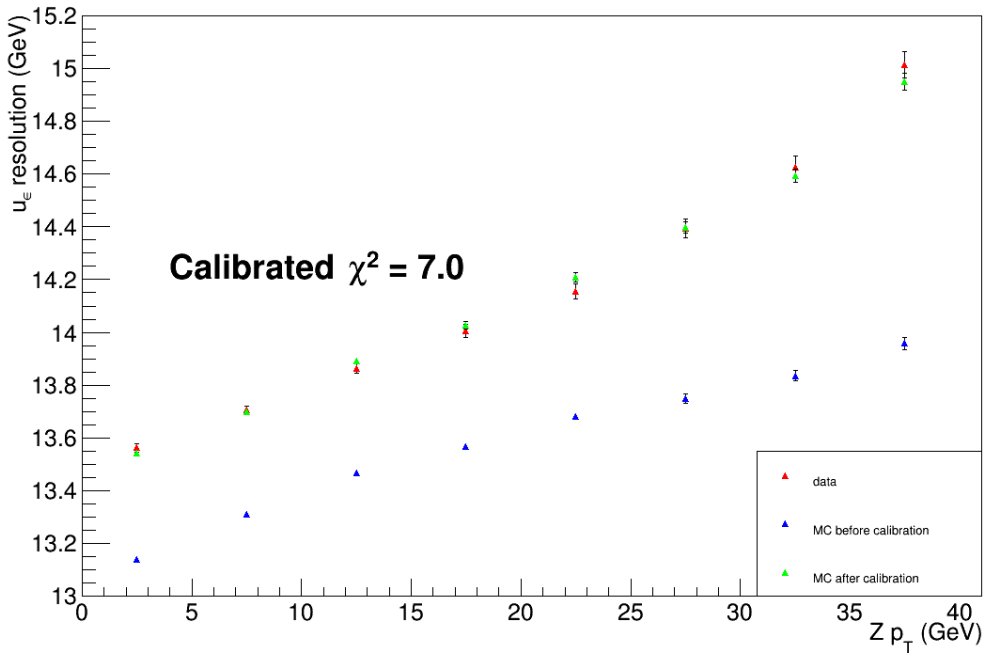



Figure 6.52: Resolution of $u_\epsilon$ in $Z \to \mu\mu$ events as a function of $Z$ $p_T$ after the corrections for pileup and underlying event, recoil magnitude smearing and recoil $\phi$ smearing corrections. The $\chi^2$ shown here indicates the goodness of fit for the resolutions between Monte Carlo and the data and has 8 degrees of freedom.

| | Recoil response tune | Minimum $\chi^2$ |
|---|---|---|
| Combined | 0.0129 | 102 |
| Electron | 0.0160 | 47 |
| Muon | 0.0102 | 47 |

Table 6.9: Best-fit values for the recoil response tune. This constant is optimised using the mean of the $u_\alpha$ distributions only, therefore there are 16 degrees of freedom in the combined tune and 8 degrees of freedom in the electron and muon tune.

order to correct for this discrepancy in response between data and Monte Carlo, the recoil response tune constant is applied as a scale factor to the recoil magnitude in Monte Carlo.

Inclusive $u_\alpha$ and $u_\epsilon$ distributions for $Z \to ee$ and $Z \to \mu\mu$ events after all corrections are shown in Figures 6.56 – 6.59. As can be seen, applying the corrections causes a discrepancy between the data and Monte Carlo in the peak, although the resolution of the distribution has been successfully calibrated. Much of this discrepancy arises from applying the pileup and underlying event corrections. This is likely due to an underlying discrepancy in the shape of the $\Sigma E_T$ distribution, which will require tuning in order to further reduce the $\chi^2$ of

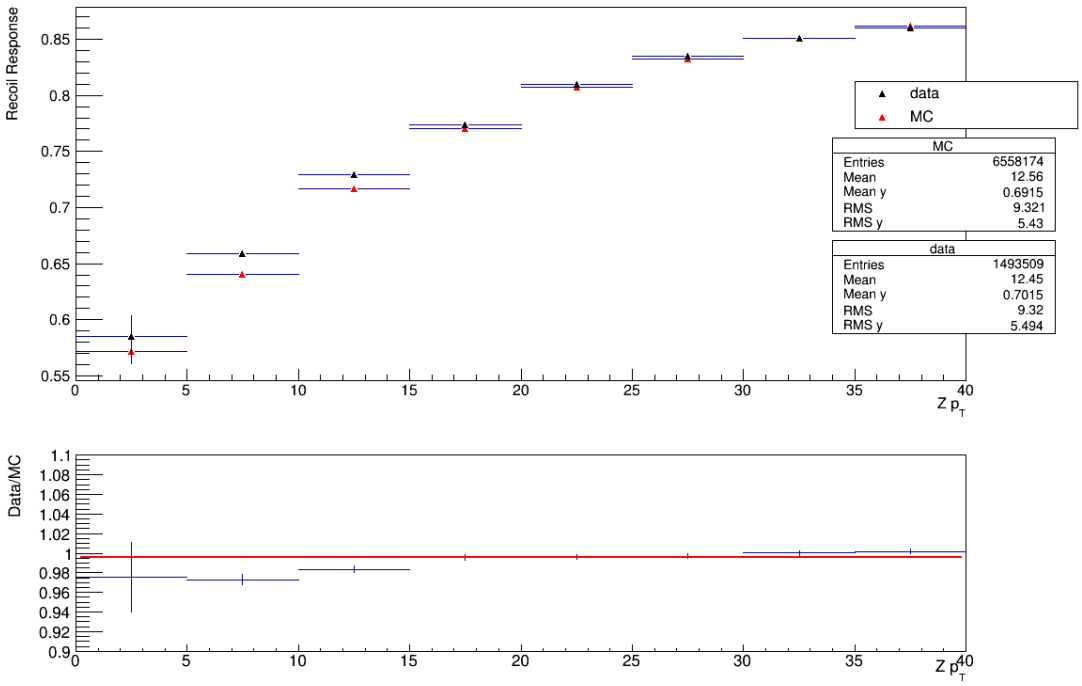



Figure 6.53: Recoil response ($Z$ $p_T$/-component of recoil parallel to the $Z$ boson) in $Z \to \mu\mu$ events for data and POWHEG Monte Carlo. The resolution corrections have been applied to the MC.

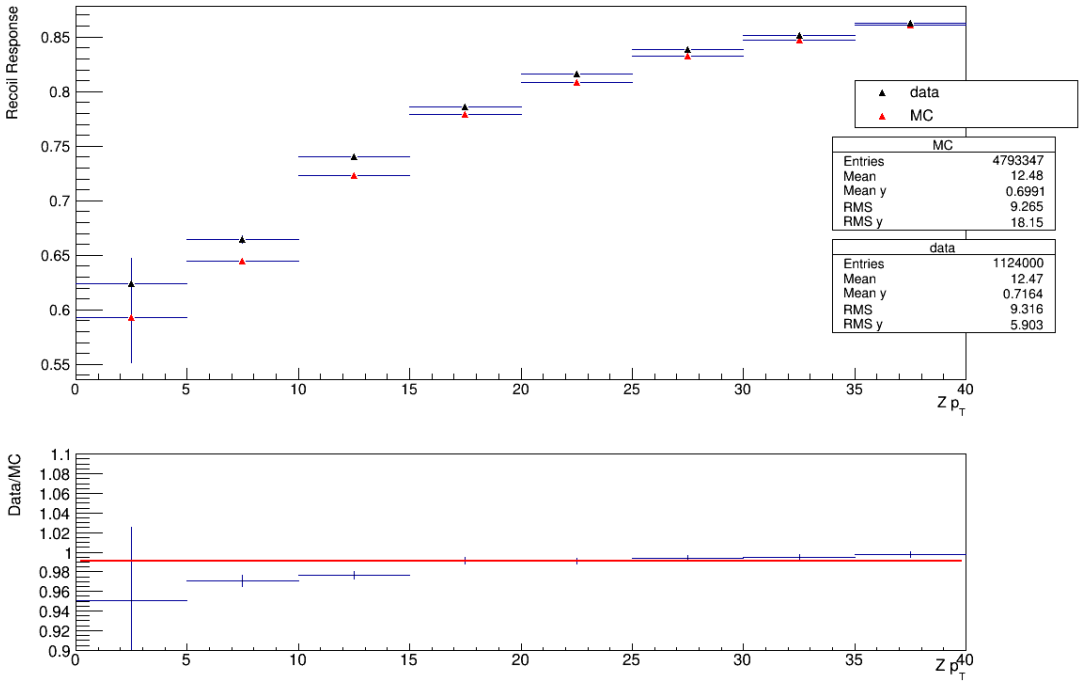



Figure 6.54: Recoil response ($Z$ $p_T$/-component of recoil parallel to the $Z$ boson) in $Z \to ee$ events for data and POWHEG Monte Carlo. The resolution corrections have been applied to the MC.

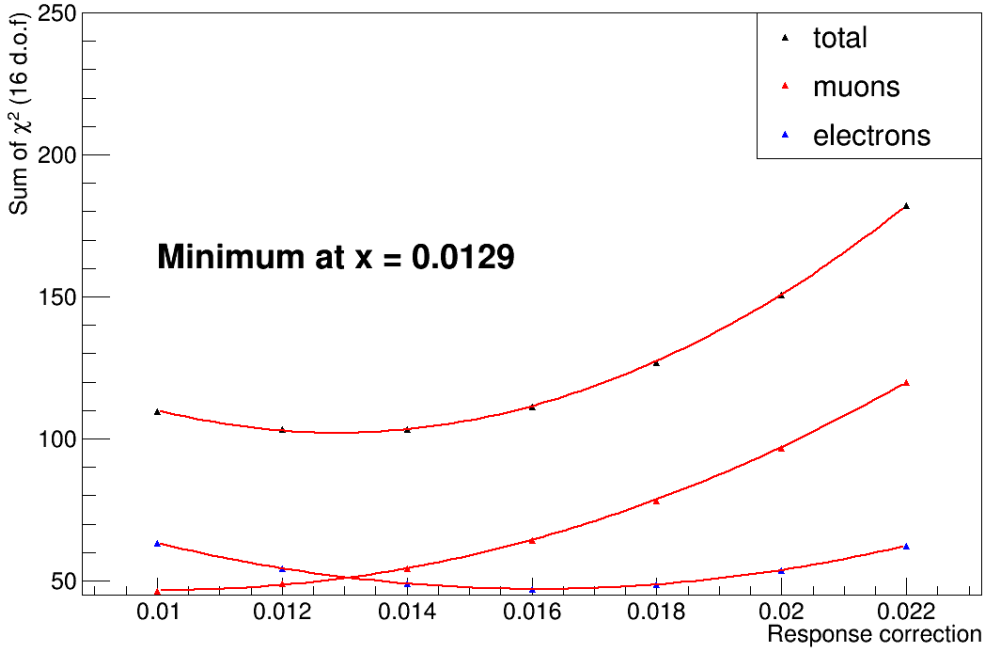



Figure 6.55: Sum of the $\chi^2$ of plots of the mean of $u_\alpha$. The $\chi^2$ test was performed between the mean of $u_\alpha$ in bins of $Zp_T$ for data and POWHEG Monte Carlo, resulting in 16 degrees of freedom in the combined tune and 8 degrees of freedom in electron and muon tunes.

the tuning distributions.

## 6.11 $\Sigma E_T$ reweighting

The shape of the $\Sigma E_T$ distribution of the underlying event is difficult to understand using the whole dataset as the pileup interactions significantly affect the shape. Therefore, the $\Sigma E_T$ distribution is studied for data and Monte Carlo for events with $\mu < 6$ (see Figures 6.60 and 6.61).

By reweighting the $\Sigma E_T$ of the underlying event, we attempt to improve the modelling of the peak of the recoil resolution distribution. The reweighting is tuned to $Z$ boson events by applying weights as a function of the produced $\Sigma E_T$. The weights can then be transferred directly to $W$ events. The relation between the produced $\Sigma E_T$ and reconstructed $\Sigma E_T$ is shown in Figure 6.62. The produced $\Sigma E_T$ is calculated by summing the transverse energies of all produced particles in Monte Carlo events, excluding the leptons from the $Z$ boson

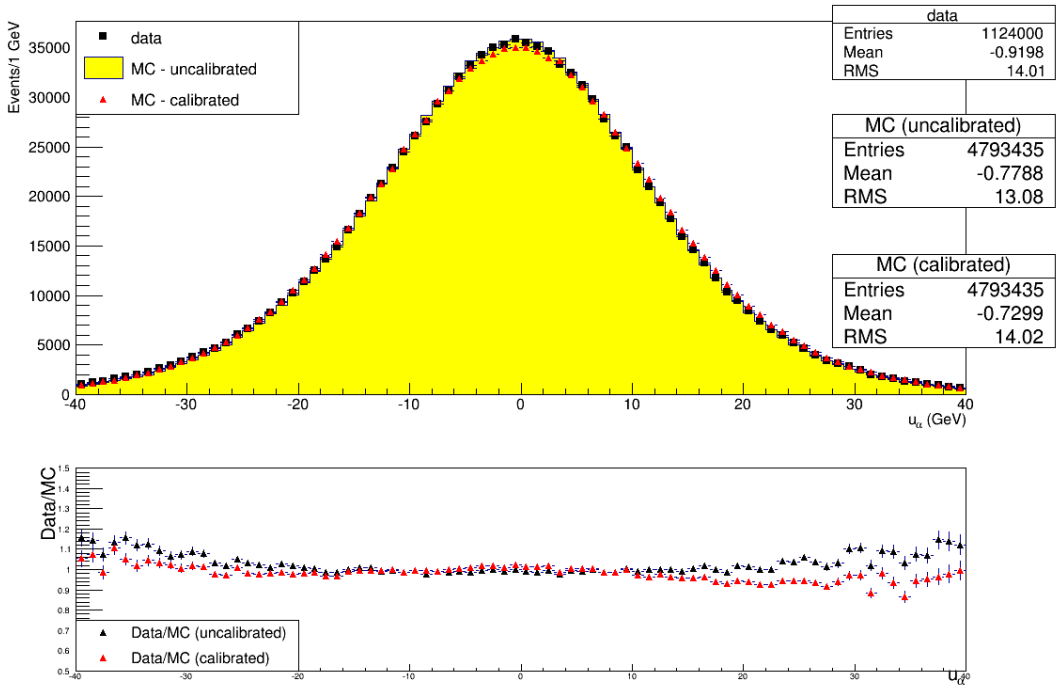



Figure 6.56: $u_\alpha$ distribution for data, uncorrected Monte Carlo (or no RW) and calibrated Monte Carlo (new RW) for $Z \to ee$ events. The resolution of the MC distribution has been fully corrected to match the data, as can be seen from the RMS. There is some discrepancy in the peak between the corrected Monte Carlo and the uncorrected Monte Carlo.

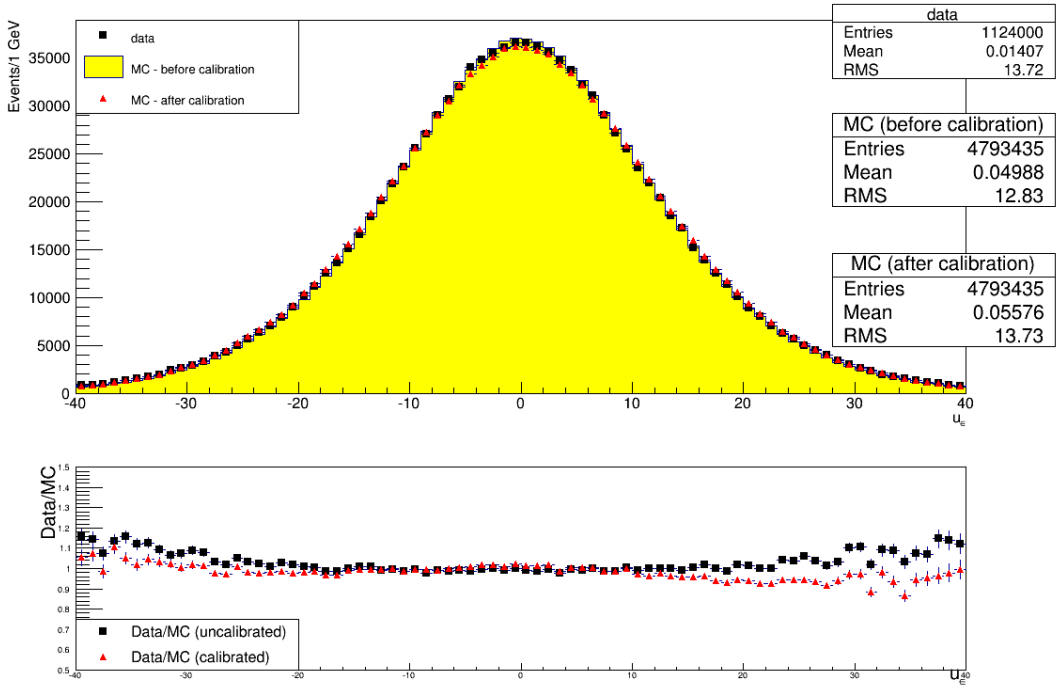



Figure 6.57: $u_\epsilon$ distribution for data, uncorrected Monte Carlo (or no RW) and calibrated Monte Carlo (new RW) for $Z \to ee$ events. The resolution of the MC distribution has been fully corrected to match the data, as can be seen from the RMS. There is some discrepancy in the peak between the corrected Monte Carlo and the uncorrected Monte Carlo.

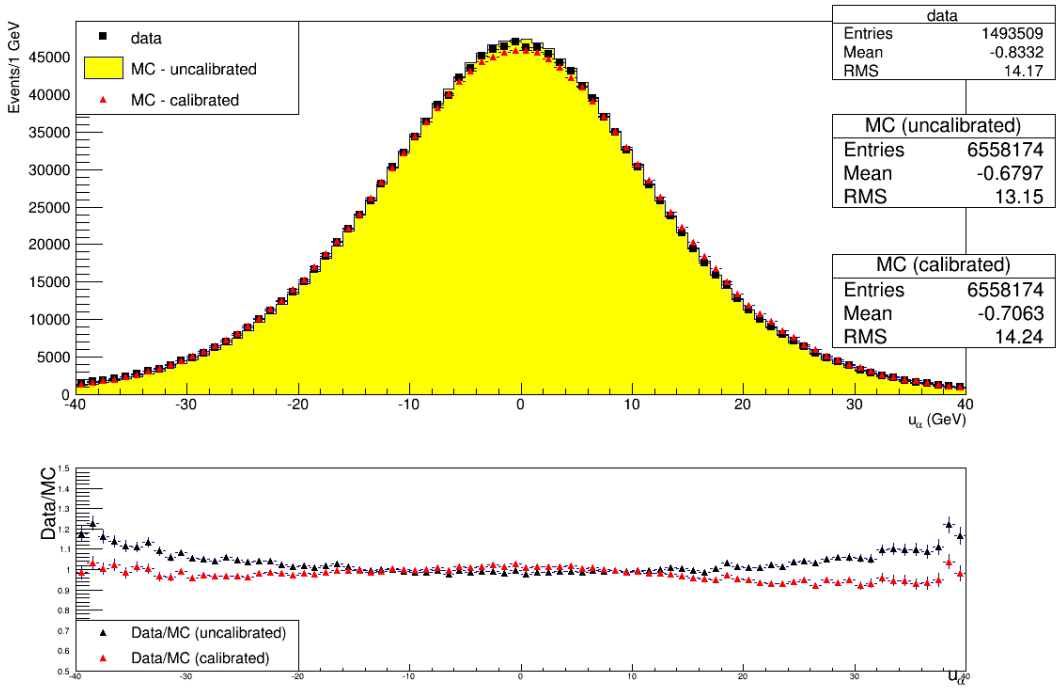



Figure 6.58: $u_\alpha$ distribution for data, uncorrected Monte Carlo (or no RW) and calibrated Monte Carlo (new RW) for $Z \to \mu\mu$ events. The resolution of the MC distribution has been fully corrected to match the data, as can be seen from the RMS. There is some discrepancy in the peak between the corrected Monte Carlo and the uncorrected Monte Carlo.

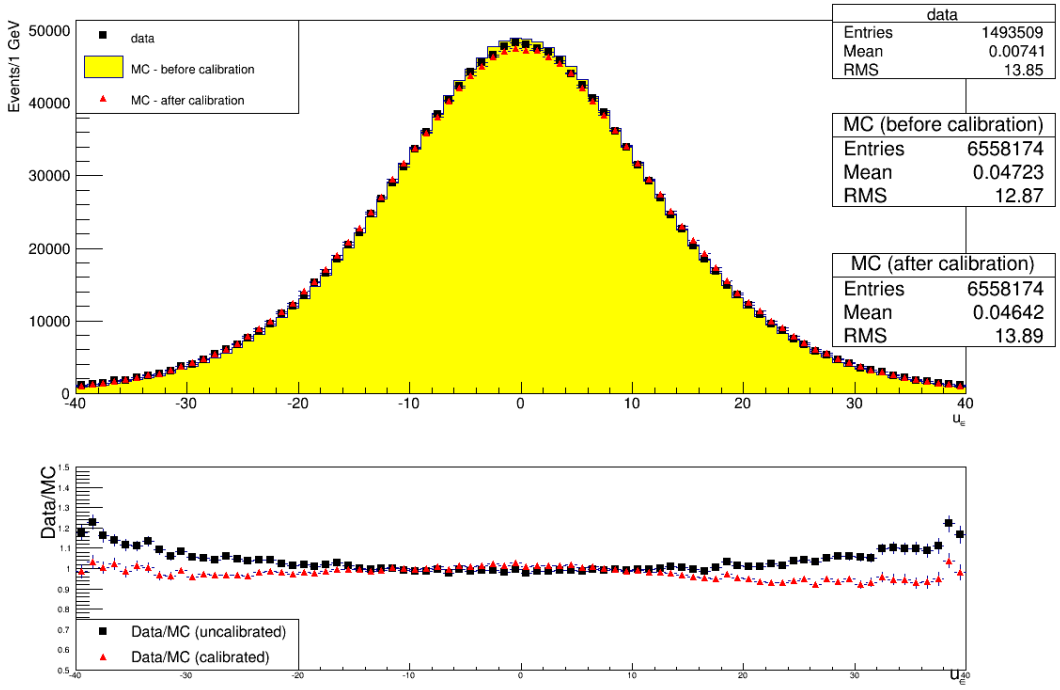



Figure 6.59: $u_\epsilon$ distribution for data, uncorrected Monte Carlo (or no RW) and calibrated Monte Carlo (new RW) for $Z \to \mu\mu$ events. The resolution of the MC distribution has been fully corrected to match the data, as can be seen from the RMS. There is some discrepancy in the peak between the corrected Monte Carlo and the uncorrected Monte Carlo.

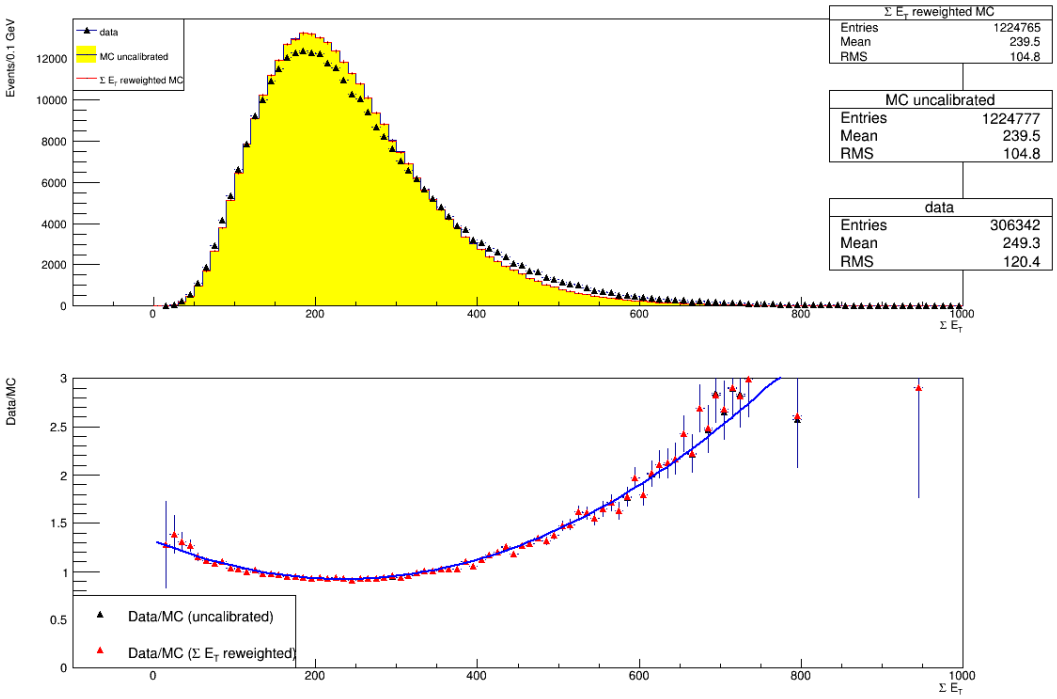



Figure 6.60: $\Sigma E_T$ for $Z \to ee$ events with $\mu < 6$ for data, Monte Carlo and Monte Carlo with the underlying event and pileup tune applied. The line shows a parabolic fit to Data/Uncalibrated Monte Carlo.

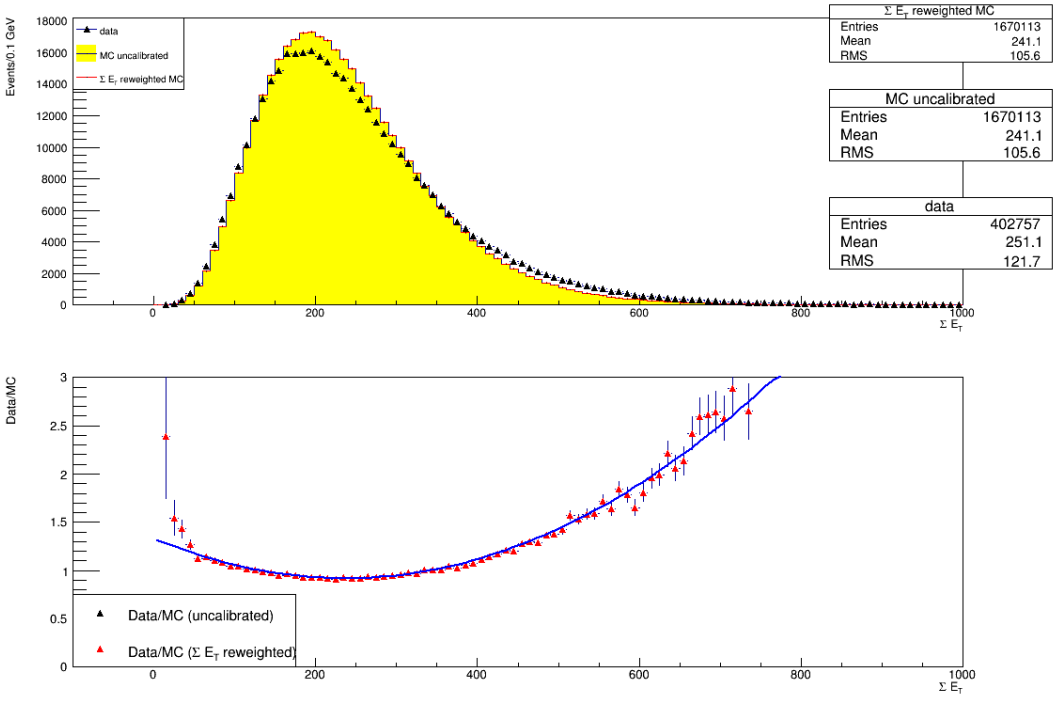



Figure 6.61: $\Sigma E_T$ for $Z \to \mu\mu$ events with $\mu < 6$ for data, Monte Carlo and Monte Carlo with the underlying event and pileup tune applied. The line shows a parabolic fir to Data/Uncalibrated Monte Carlo.

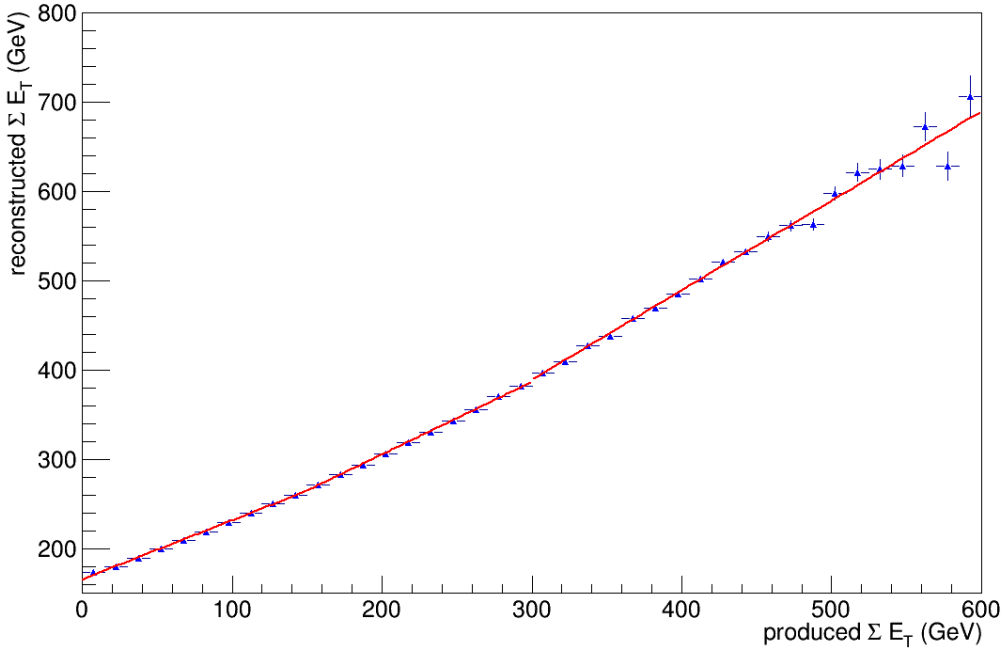



Figure 6.62: A profile of the Reconstructed $\Sigma E_T$ as a function of the truth level $\Sigma E_T$ for $Z \to ee$ and $Z \to \mu\mu$ Monte Carlo events with $\mu$ <6. The profile has been fitted with 3 straight lines.

decay. This distribution is fitted with three straight lines.

Using this fit and the fit to Data/MC reconstructed $\Sigma E_T$ in Figures 6.60 and 6.61, we derive a weight to apply to the produced $E_T$. Figures 6.63 and 6.64 show how this procedure corrects the $\Sigma E_T$ distribution for $\mu < 6$. The correction does not correct the shape of the $\Sigma E_T$ distribution sufficiently. The $\Sigma E_T$ reweighting is not applied in the following sections as it complicates the procedure without improving data-MC agreement, as shown in Figures 6.65 to 6.68.

## 6.12 Correlations between corrections

In order to calculate systematic errors, it is necessary to understand the correlations between the corrections that are applied to the recoil. If they are minimally correlated, the errors can be added together in quadrature. The recoil response correction is assumed to be minimally

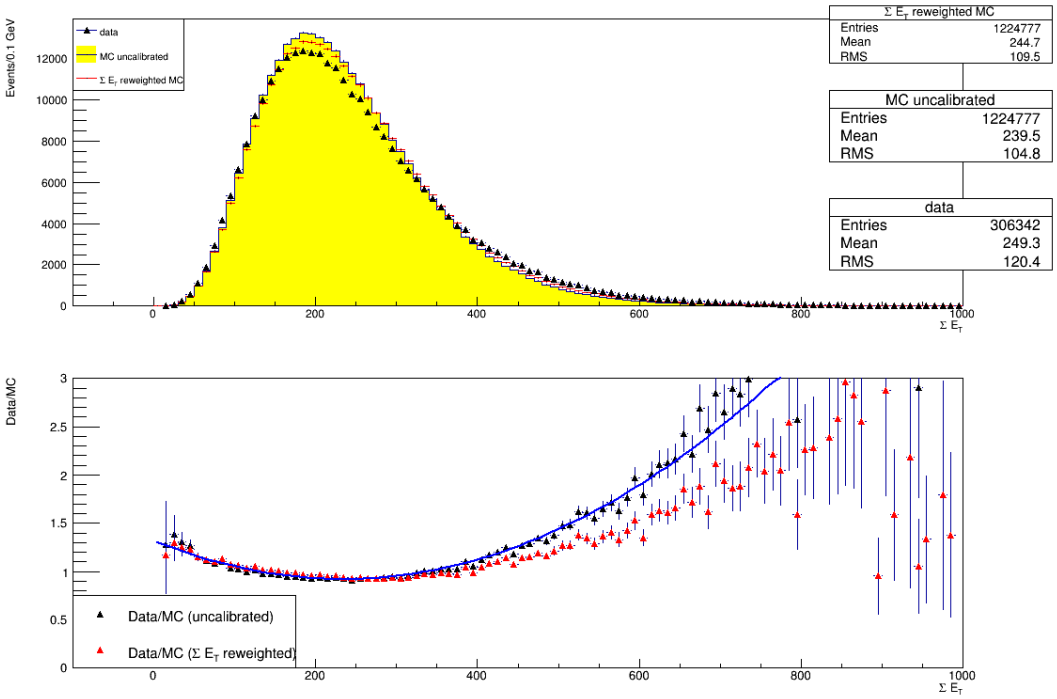



Figure 6.63: $\Sigma E_T$ for $Z \to ee$ events with $\mu < 6$ for data, Monte Carlo and Monte Carlo with the $\Sigma E_T$ reweighting applied. The line shows a parabolic fit to Data/Uncalibrated Monte Carlo.

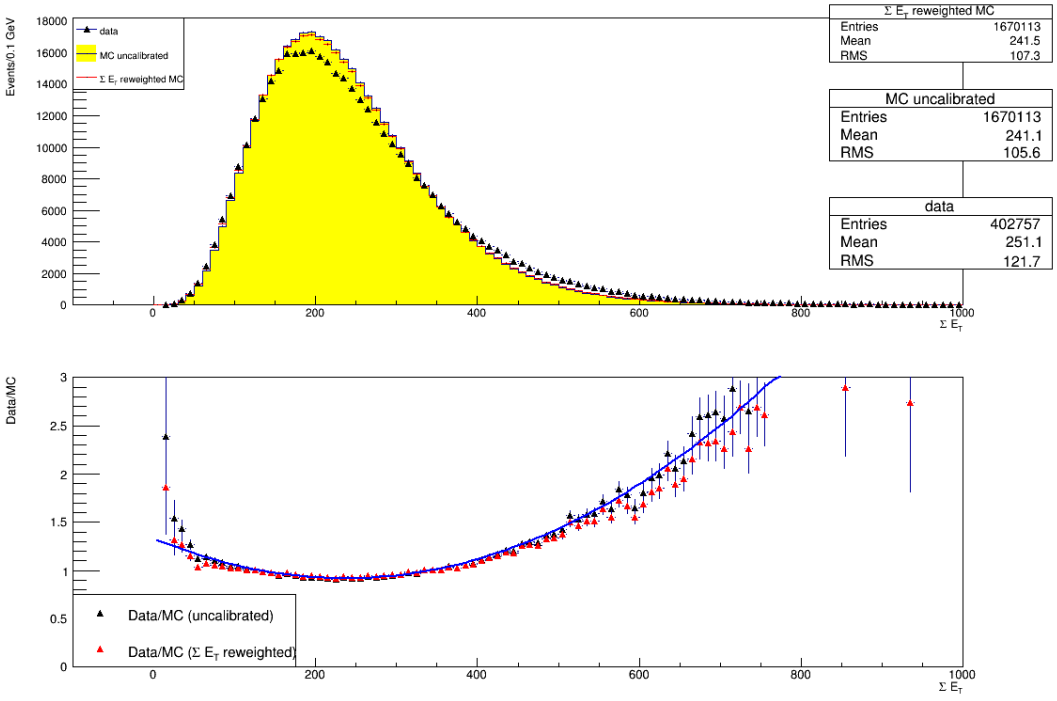



Figure 6.64: $\Sigma E_T$ for $Z \to \mu\mu$ events with $\mu < 6$ for data, Monte Carlo and Monte Carlo with the $\Sigma E_T$ reweighting applied. The line shows a parabolic fit to Data/Uncalibrated Monte Carlo.

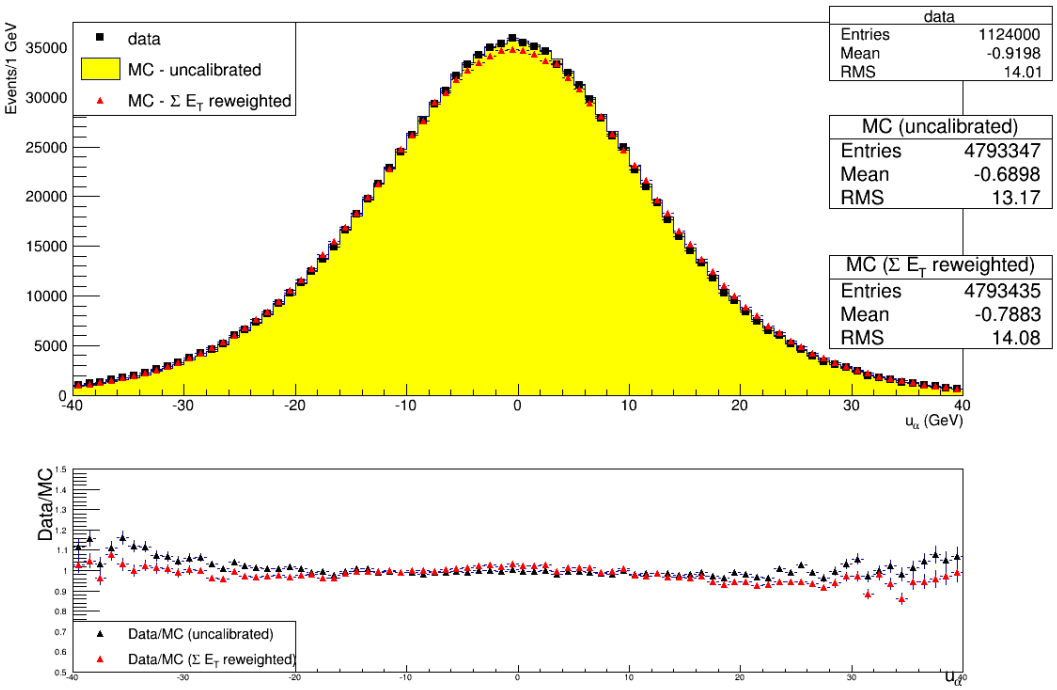



Figure 6.65: $u_\alpha$ distribution for data, calibrated Monte Carlo and calibrated Monte Carlo with $\Sigma E_T$ reweighting for $Z \rightarrow ee$ events. The $\Sigma E_T$ reweighting has not corrected the discrepancy in the peak.

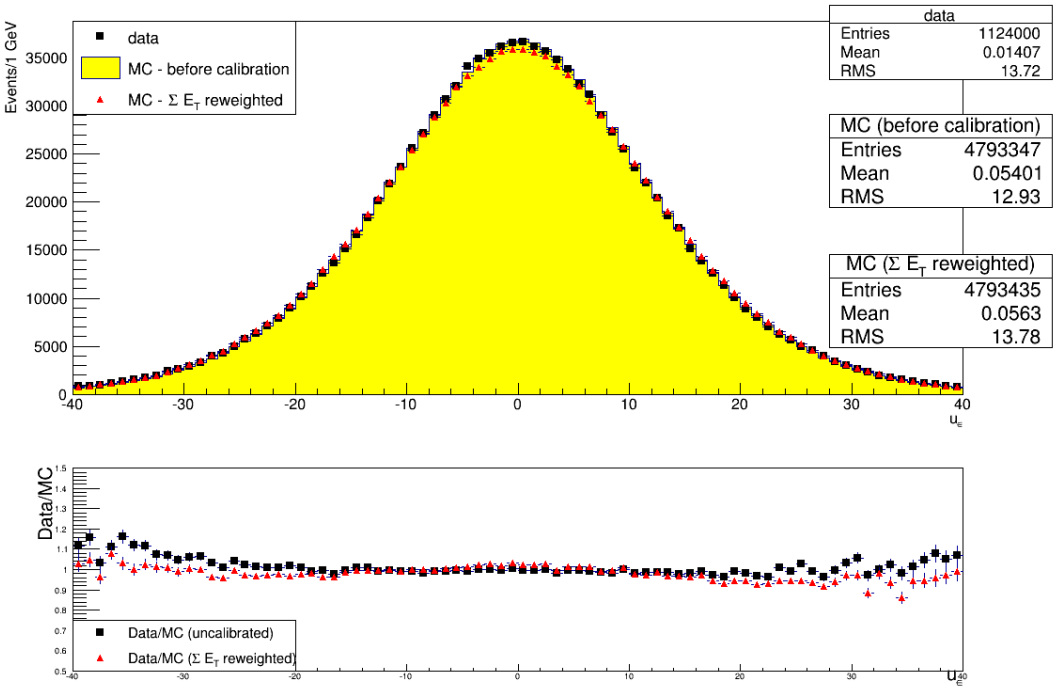



Figure 6.66: $u_\epsilon$ distribution for data, calibrated Monte Carlo and calibrated Monte Carlo with $\Sigma E_T$ reweighting for $Z \rightarrow ee$ events. The $\Sigma E_T$ reweighting has not corrected the discrepancy in the peak.

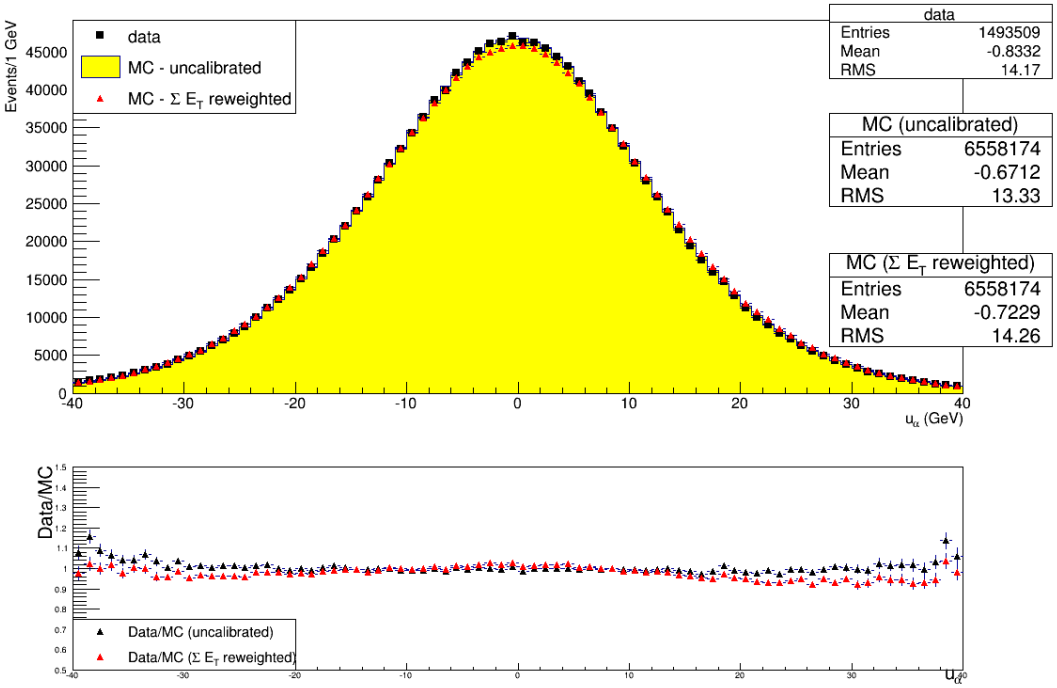



Figure 6.67: $u_\alpha$ distribution for data, calibrated Monte Carlo and calibrated Monte Carlo with $\Sigma E_T$ reweighting for $Z \to \mu\mu$ events. The $\Sigma E_T$ reweighting has not corrected the discrepancy in the peak.

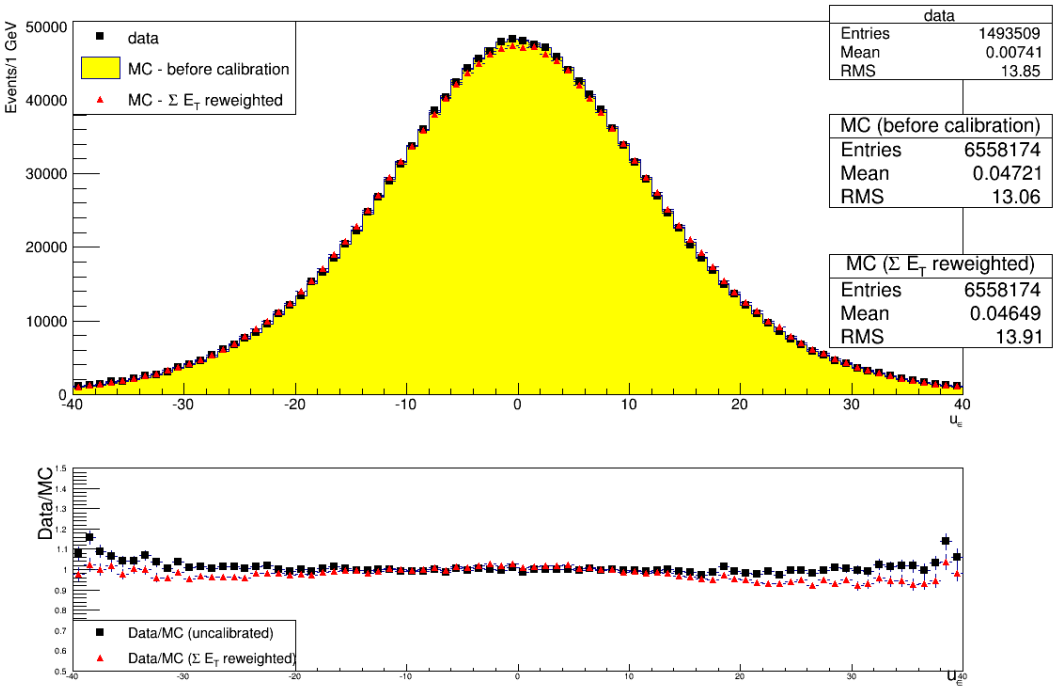



Figure 6.68: $u_\epsilon$ distribution for data, calibrated Monte Carlo and calibrated Monte Carlo with $\Sigma E_T$ reweighting for $Z \to \mu\mu$ events. The $\Sigma E_T$ reweighting has not corrected the discrepancy in the peak.

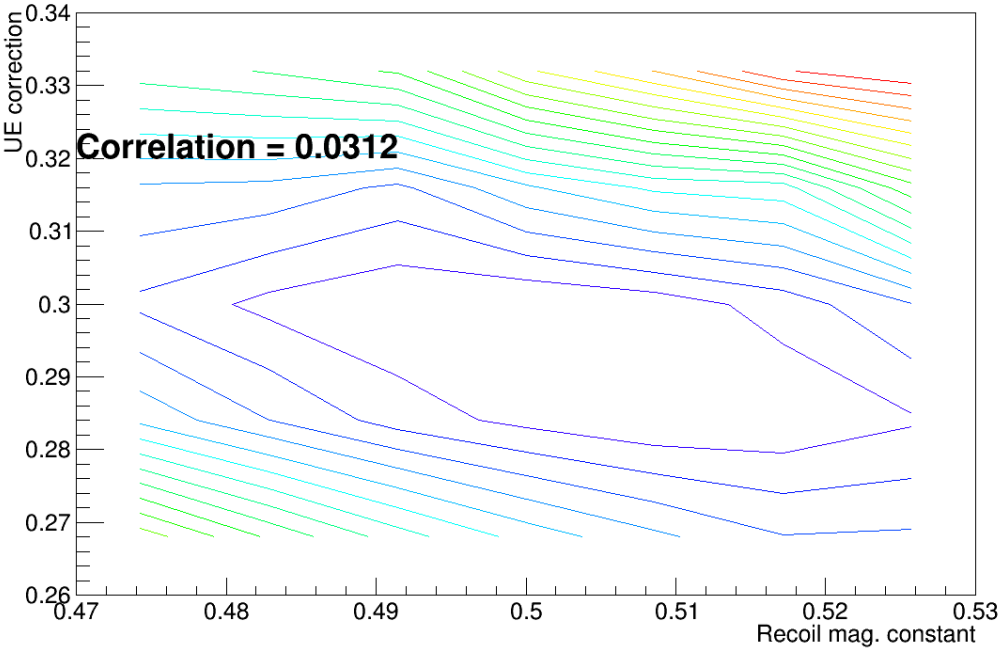



Figure 6.69: $\chi^2$ as the constants used in the recoil magnitude smearing and the underlying event correction are varied. The correlation factor is the covariance divided by the product of the RMS values on the two axes. The optimal constants for each corrections are varied up and down by 1 $\sigma$.

correlated with the other corrections as it varies the mean whereas the other three corrections correct the resolution of the recoil. In order to calculate correlations, two-dimensional plots are made of the $\chi^2$ with both corrections varied at once. The corrections are varied between the optimal constant $-1\sigma$ and the optimal constant $+1\sigma$, with the values given in the tables above. These can be seen in Figures 6.69 to 6.71.

The correlation factors shown are the covariance divided by the product of the RMS values on the two axes. The largest correlation is between the underlying event correction and the recoil $\phi$ smearing, and is 3 %. This is small enough to be ignored, and therefore the uncertainty on each correction can be calculated separately and added in quadrature to find the total uncertainty on the recoil calibration.

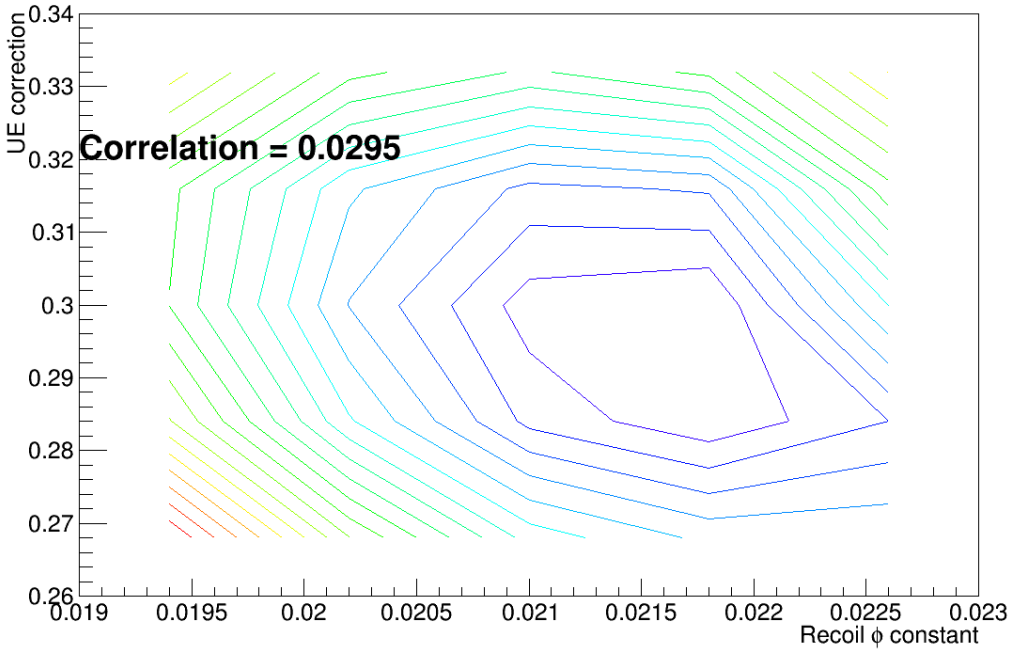



Figure 6.70: $\chi^2$ as the constants used in the recoil $\phi$ smearing and the underlying event correction are varied. The correlation factor is the covariance divided by the product of the RMS values on the two axes. The optimal constants for each corrections are varied up and down by 1 $\sigma$.

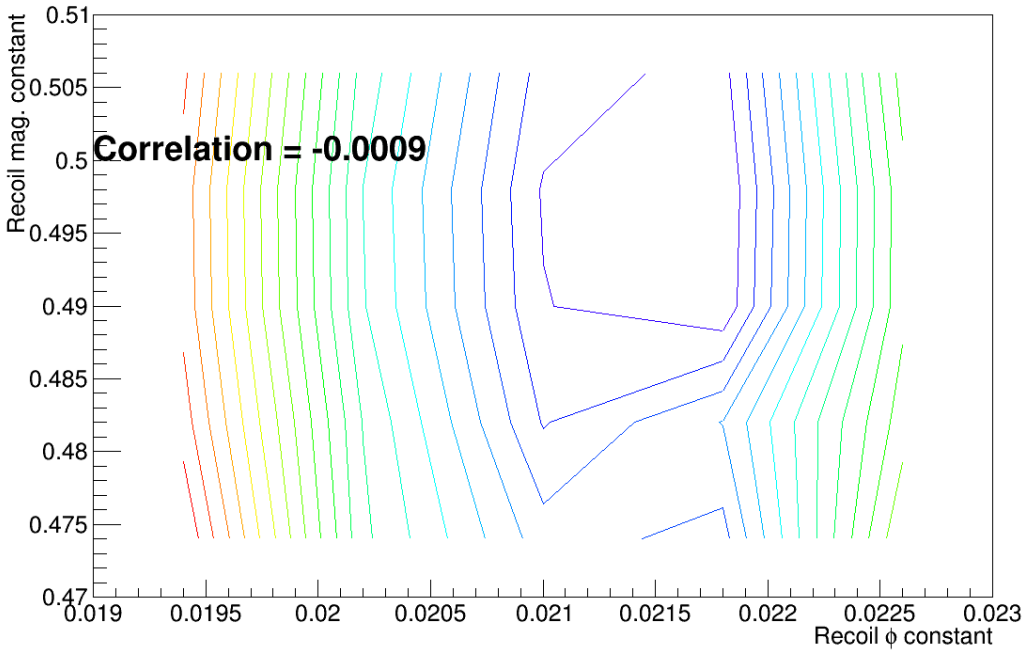



Figure 6.71: $\chi^2$ as the constants used in the recoil $\phi$ smearing and the recoil magnitude smearing correction are varied. The correlation factor is the covariance divided by the product of the RMS values on the two axes. The optimal constants for each corrections are varied up and down by 1 $\sigma$.

## 6.13 Impact on the $m_W$ measurement

In order to estimate the impact of the recoil calibration on the $m_W$ measurement, the recoil calibration determined using $Z$ boson events is applied to $W$ boson events. The calibrations derived from $Z$ events are applied directly to the $W$ Monte Carlo, along the direction of the $W$ boson $p_T$. The variables $u_{parallel}$ (the component of the recoil parallel to the charged lepton) and $u_{perp}$ (the component of the recoil perpendicular to the charged lepton) are calculated once these corrections have been applied (these variables were also used to find the scale factors used to correct the efficiency in Section 6.4) in order to measure the impact of the recoil model on $m_W$. $u_{parallel}$ is sensitive to the lepton efficiency as a function of $u_{parallel}$, the removal of the cone in the recoil algorithm, the boson $p_T$ and $\phi$ and the recoil response and resolutions. As the lepton $p_T$ is much greater than $u_{perpendicular}$ for this event selection, the equation for missing $E_T$ can be simplified to Equation 6.9.

$$\not{E}_T \approx |p_T + u_{parallel}| \tag{6.9}$$

As a result, the transverse mass equation for the $W$ boson can be rewritten as Equation 6.10.

$$m_T \approx 2p_T\sqrt{1 + \frac{u_{parallel}}{p_T}} \approx 2p_T + u_{parallel} \tag{6.10}$$

Therefore, any bias in $u_{parallel}$ can be approximated to be a bias in the $m_T$ fit.

Figures 6.72 to 6.75 show distributions of $u_{parallel}$ and $u_{perpendicular}$ for the MC with no correction, the MC with the nominal correction and with the correction plus or minus 1 standard deviation and for data. The change in $u_{parallel}$ is used to calculate the uncertainty on $m_W$. For $W \to e\nu$ events, there is a 1.9 MeV shift on the mean of the $W \to e\nu$ distribution by varying the UE correction up by 1 $\sigma$ and a 1.7 MeV shift by varying it down by 1 $\sigma$. For the recoil magnitude correction, the mean of the $u_{parallel}$ distribution varies by $\pm^{0.9}_{1.0}$ MeV and for the recoil $\phi$ correction, the mean also varies by $\pm^{1.0}_{0.9}$ MeV. This results in an uncertainty on $m_W$ from the recoil resolution corrections of $\pm^{2.3}_{2.2}$ MeV. Varying the response

correction up and down by 1 $\sigma$ results in a shift in the mean of $\pm^{3.2}_{3.3}$ MeV, and therefore this is the uncertainty on $m_W$ from the recoil response. Combining these two uncertainties results in a total uncertainty on $m_W$ from recoil calibration statistics of $\pm^{3.9}_{4.0}$ MeV in the electron channel. For $W \to \mu\nu$ events, the UE correction has an associated uncertainty of $\pm^{2.0}_{1.8}$ MeV, the recoil magnitude correction has an uncertainty of $\pm^{0.5}_{1.0}$ MeV and the recoil phi correction $\pm^{0.2}_{0.5}$ MeV. The response correction has an uncertainty of $\pm^{3.2}_{3.1}$ MeV. This corresponds to a total uncertainty of $\pm^{3.8}_{3.8}$ MeV. The $Z \to ee$ and $Z \to \mu\mu$ samples were combined when deriving the corrections, so these uncertainties are fully correlated.

The recoil calibration does not correct all the observed systematic effects, most notably those due to the $\Sigma$ $E_T$ mismodelling. There is an additional undetermined systematic uncertainty on $m_W$ due to the residual mismodelling. Future improvements to the generator modelling of the $\Sigma E_T$ distribution, or additional data-based corrections, will be required to reduce this residual uncertainty. The recoil calibration will need additional work to remove residual systematic effects producing imperfect $\chi^2$ fits between the data and MC when performing the tuning, and the small discrepancy in the peak of the inclusive distributions of $u_\alpha$ and $u_\epsilon$.

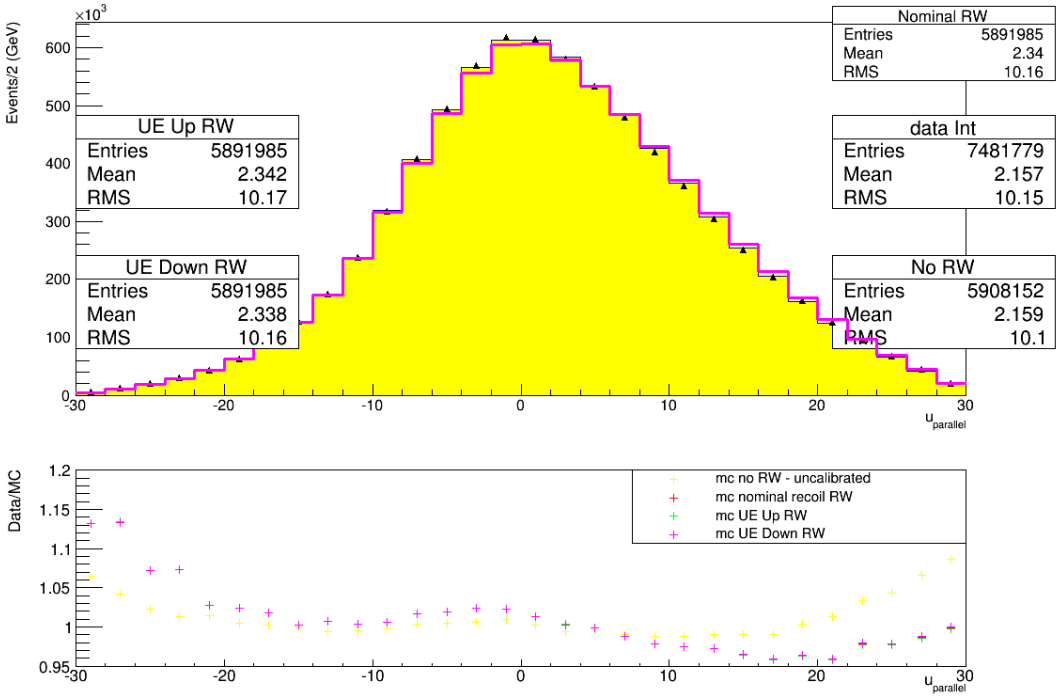



Figure 6.72: $u_{parallel}$ for uncorrected MC, corrected MC with the nominal UE correction and with the correction ±1 standard deviation (described here as Up and Down) and data for $W \to e\nu$ events. The lines for the nominal, up and down corrections closely overlay each other.

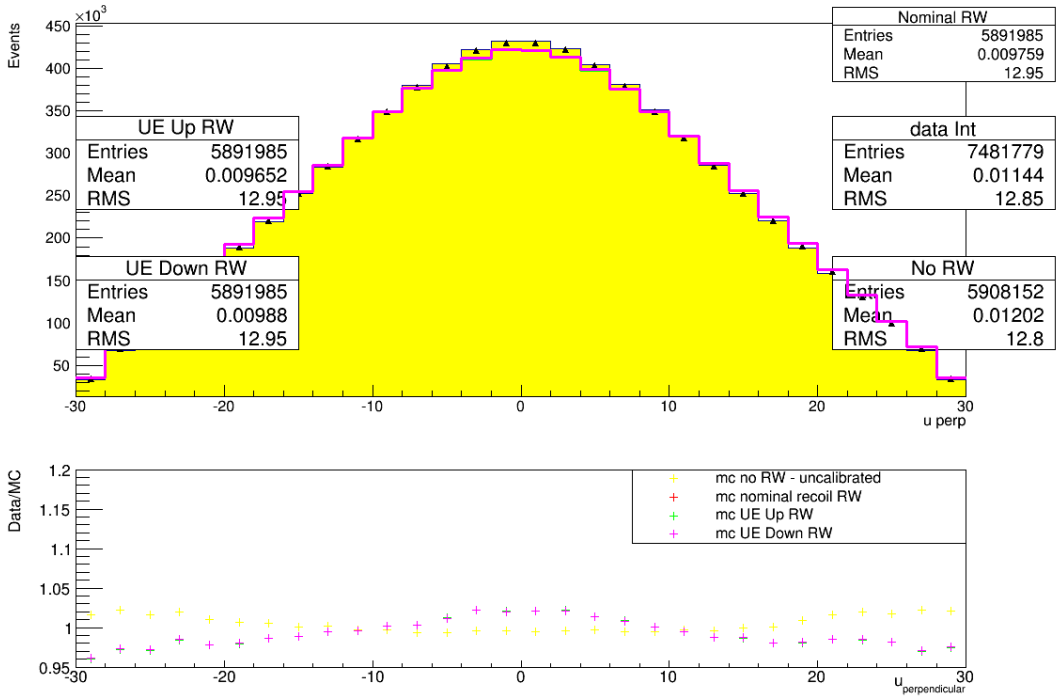



Figure 6.73: $u_{perpendicular}$ for uncorrected MC, corrected MC with the nominal UE correction and with the correction ±1 standard deviation (described here as Up and Down) and data for $W \to e\nu$ events. The lines for the nominal, up and down corrections closely overlay each other.

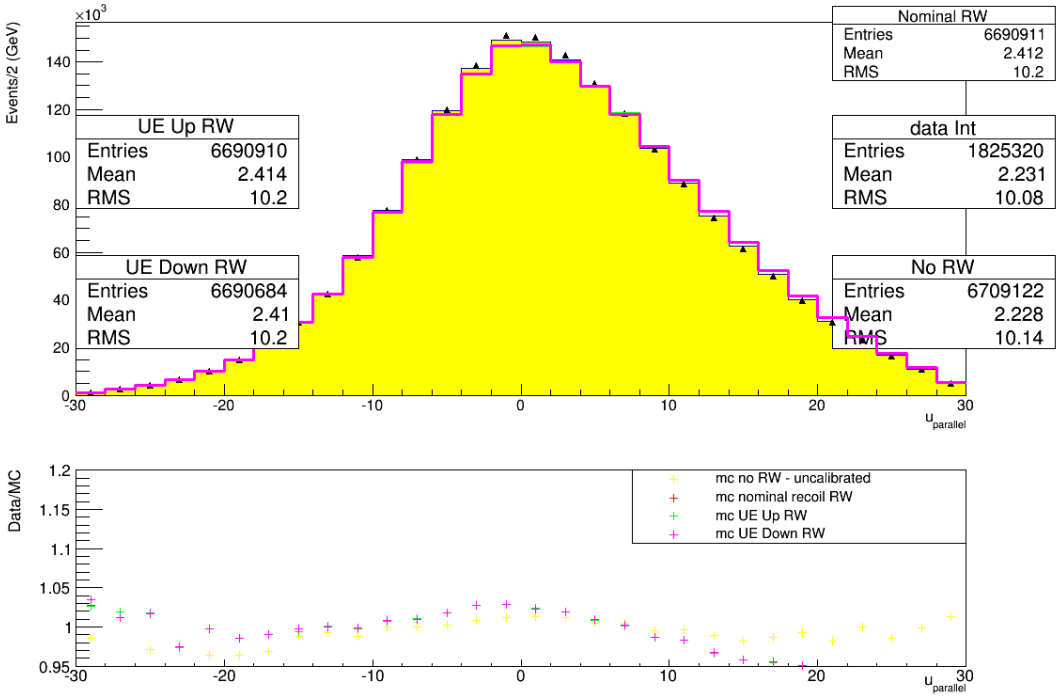



Figure 6.74: $u_{parallel}$ for uncorrected MC, corrected MC with the nominal UE correction and with the correction ±1 standard deviation (described here as Up and Down) and data for $W \to \mu\nu$ events. The lines for the nominal, up and down corrections closely overlay each other.

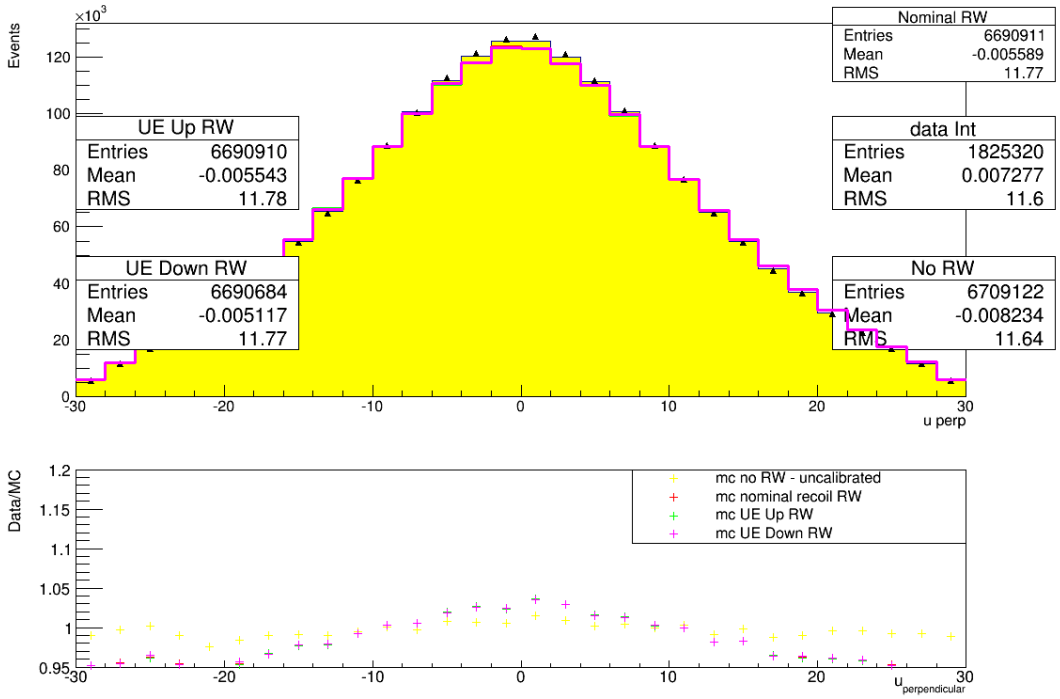



Figure 6.75: $u_{perpendicular}$ for uncorrected MC, corrected MC with the nominal UE correction and with the correction ±1 standard deviation (described here as Up and Down) and data for $W \to \mu\nu$ events. The lines for the nominal, up and down corrections closely overlay each other.

# Chapter 7

# Conclusions

Data collected by the ATLAS experiment in 2011 were used to perform calibrations for the forthcoming measurement of the mass of the $W$ boson. The world average measurement for the mass of the $W$ boson is $m_W = 80.385 \pm 0.015$ GeV from a combination of measurements from LEP experiments (ALEPH, DELPHI, OPAL and L3) and from Tevatron experiments (CDF and D0) [10]. The CDF measurement has the lowest total uncertainty on $m_W$ of 0.019 GeV. The largest experimental uncertainties on the CDF measurement are from the lepton scale and recoil calibration (in addition to errors arising from uncertainty in the parton distribution functions). Therefore, these uncertainties are likely to be significant for the ATLAS measurement and this thesis describes my contributions to this effort.

The electron energy scale calibration was performed using $Z$ and $W$ boson events, using the $Z \to ee$ mass peak and the $E/p$ distribution. The absolute electron energy scale was calibrated using the $Z \to ee$ mass peak. Both a log-likelihood method and a template method were used to find the absolute energy scale for pairs of $\eta$ bins (as the pair of electrons in the invariant mass peak may not be in the same $\eta$ bin). The series of linear equations was solved to give the absolute energy scale for each $\eta$ bin. The $E/p$ distribution was used to calculate the linearity and uniformity of the detector, using both a template and a convolution method. The linearity results from these two methods were also compared to results

from the log-likelihood method used to calculate the absolute energy scale but in bins of $E_T$. The results were largely consistent with each other.

The recoil energy scale was calibrated using $Z \to ee$ and $Z \to \mu\mu$ events. Corrections were applied to account for mismodelling of pileup, the underlying event, recoil energy and angular resolution and the recoil response. The mismodelling of pileup and the underlying event were calibrated by reweighting the underlying $\mu$ distribution. An additional reweighting of the produced $\Sigma E_T$ distribution was investigated but not found to be an improvement. The recoil magnitude and recoil $\phi$ were smeared using a Gaussian distribution and a box function respectively. The recoil response was corrected using a scale factor. The various corrections were found to be uncorrelated. Applying them to $W$ boson events with $\pm$ 1 $\sigma$ statistical variations in the corrections led to changes in $u_{parallel}$ (the recoil component parallel to the lepton in the $W$ event) corresponding to approximate systematic uncertainties on $m_W$ of 3.9 MeV for both $W \to e\nu$ and $W \to \mu\nu$ events. The $Z \to ee$ and $Z \to \mu\mu$ samples were combined when determining the corrections so the errors are fully correlated.

The trigger used for the $m_W$ measurement was also studied. The efficiency of the lowest unprescaled electron trigger was found to be dependent on $E_T$ over a range relevant for the $m_W$ measurement (20 to 40 GeV). This trigger used a 'medium' identification, which included cuts on the shape of the shower of the electron in the electromagnetic calorimeter. These shower-shape variables were found to cause the inefficiency of the trigger. The drop in efficiency over this range would cause a bias of 360 MeV on $m_W$ if a flat efficiency were to be assumed. Scale factors are used to mitigate this effect, which have an uncertainty across the $E_T$ range of 0.1-0.2 %. An uncertainty of 0.1% on the scale factors corresponds to a systematic uncertainty on $m_W$ of $\approx$ 4 MeV [86]. Therefore, a specialised $m_W$ trigger was designed, which reduced the efficiency drop of the medium trigger by a third by loosening the biasing cuts on the shower shapes. However, due to rate considerations, the $m_W$ trigger could not be used during data taking in 2011. However, this trigger could be used in low

luminosity fills or bunches in Run II of the Large Hadron Collider. These low luminosity fills or bunches are likely to be necessary to make an $m_W$ measurement during Run II in any case, as the extremely high pileup environment of the next run is likely to lead to large uncertainties on $m_W$.

# References


[1] LEP Higgs Working Group for Higgs boson searches, OPAL Collaboration, ALEPH Collaboration, DELPHI Collaboration, L3 Collaboration Collaboration, *Search for the standard model Higgs boson at LEP*, PoS **HEP2001** (2001) 128, arXiv:hep-ex/0107029 [hep-ex].

[2] CDF Collaboration, D0 Collaboration, T. T. Group, *Combined CDF and D0 Upper Limits on Standard Model Higgs-Boson Production with up to 6.7 $fb^{-1}$ of Data*, arXiv:1007.4587 [hep-ex].

[3] ATLAS Collaboration, G. Aad et al., *Combined search for the Standard Model Higgs boson using up to 4.9 $fb^{-1}$ of pp collision data at $\sqrt{s} = 7$ TeV with the ATLAS detector at the LHC*, Phys.Lett. **B710** (2012) 49–66, arXiv:1202.1408 [hep-ex].

[4] CMS Collaboration, S. Chatrchyan et al., *Combined results of searches for the standard model Higgs boson in pp collisions at $\sqrt{s} = 7$ TeV*, Phys.Lett. **B710** (2012) 26–48, arXiv:1202.1488 [hep-ex].

[5] ATLAS Collaboration, G. Aad et al., *Observation of a new particle in the search for the Standard Model Higgs boson with the ATLAS detector at the LHC*, Phys.Lett. **B716** (2012) 1–29, arXiv:1207.7214 [hep-ex].

[6] CMS Collaboration, S. Chatrchyan et al., *Observation of a new boson at a mass of 125 GeV with the CMS experiment at the LHC*, Phys.Lett. **B716** (2012) 30–61, arXiv:1207.7235 [hep-ex].

[7] ATLAS Collaboration, *Updated coupling measurements of the Higgs boson with the ATLAS detector using up to 25 $fb^{-1}$ of proton-proton collision data*, Tech. Rep. ATLAS-CONF-2014-009, CERN, Geneva, Mar, 2014.

[8] S. P. Martin, *A Supersymmetry primer*, arXiv:hep-ph/9709356 [hep-ph].

[9] R. Kaul and P. Majumdar, *Cancellation of quadratically divergent mass corrections in globally supersymmetric spontaneously broken gauge theories*, Nucl. Phys. **B199** (1982) 36.

[10] Particle Data Group Collaboration, J. Beringer and et al., *Review of Particle Physics*, Phys. Rev. D **86** (2012) 010001. http://link.aps.org/doi/10.1103/PhysRevD.86.010001.

[11] CDF Collaboration, T. Aaltonen et al., *Precise measurement of the W-boson mass with the CDF II detector*, Phys.Rev.Lett. **108** (2012) 151803, arXiv:1203.0275 [hep-ex].

[12] ATLAS Collaboration, N. Besson, M. Boonekamp, E. Klinkby, S. Mehlhase, and T. Petersen, *Re-evaluation of the LHC potential for the measurement of Mw*, Eur.Phys.J. **C57** (2008) 627–651, arXiv:0805.2093 [hep-ex].

[13] C. Quigg, *Unanswered Questions in the Electroweak Theory*, Ann.Rev.Nucl.Part.Sci. **59** (2009) 505–555, arXiv:0905.3187 [hep-ph].

[14] S. Dittmaier and M. Schumacher, *The Higgs Boson in the Standard ModelFrom LEP to LHC: Expectations, Searches, and Discovery of a Candidate*, Progress in Particle and Nuclear Physics **70** no. 0, (2013) 1 – 54. http://www.sciencedirect.com/science/article/pii/S0146641013000033.

[15] G. Altarelli, *Standard Model of Particle Physics*, pp. , 32 – 38. Academic Press, Oxford, 2006. http://www.sciencedirect.com/science/article/pii/B0125126662000596.

[16] J. L. Rosner, *The Standard Model in 2001*, arXiv:hep-ph/0108195 [hep-ph].

[17] M. Gell-Mann, *The interpretation of the new particles as displaced charge multiplets*, Il Nuovo Cimento **4** no. 2, (1956) 848–866. http://dx.doi.org/10.1007/BF02748000.

[18] K. Nishijima, *Charge Independence Theory of V Particles*, Progress of Theoretical Physics **13** (1955) 285–304.

[19] T. Nakano and K. Nishijima, *Charge Independence for V-particles*, Progress of Theoretical Physics **10** (1953) 581–582.

[20] P. A. M. Dirac, *The Principles of Quantum Mechanics (International Series of Monographs on Physics)*. Oxford University Press, USA, 4 ed., Feb., 1982.

[21] P. W. Higgs, *Broken Symmetries and the Masses of Gauge Bosons*, Physical Review Letters **13** (1964) 508–509.

[22] R. Brout and F. Englert, *Spontaneous symmetry breaking in gauge theories: A Historical survey*, arXiv:hep-th/9802142 [hep-th].

[23] F. Englert and R. Brout, *Broken Symmetry and the Mass of Gauge Vector Mesons*, Physical Review Letters **13** (1964) 321–323.

[24] M. Kobayashi and T. Maskawa, *CP-Violation in the Renormalizable Theory of Weak Interaction*, Progress of Theoretical Physics **49** (1973) 652–657.

[25] N. Cabibbo, *Unitary Symmetry and Leptonic Decays*, Physical Review Letters **10** (1963) 531–533.

[26] J. R. Ellis, *Limits of the Standard Model*, arXiv:hep-ph/0211168 [hep-ph].

[27] G. Bellini, L. Ludhova, G. Ranucci, and F. Villante, *Neutrino oscillations*, Advances in High Energy Physics (191960) 2013, arXiv:1310.7858 [hep-ph].

[28] SNO Collaboration Collaboration, Q. Ahmad et al., *Measurement of the rate of $\nu_e + d \to p + p + e^-$ interactions produced by $^8B$ solar neutrinos at the Sudbury Neutrino Observatory*, Phys.Rev.Lett. **87** (2001) 071301, arXiv:nucl-ex/0106015 [nucl-ex].

[29] Super-Kamiokande Collaboration Collaboration, Y. Fukuda et al., *Evidence for oscillation of atmospheric neutrinos*, Phys.Rev.Lett. **81** (1998) 1562–1567, arXiv:hep-ex/9807003 [hep-ex].

[30] W. de Boer, *Grand unified theories and supersymmetry in particle physics and cosmology*, Prog.Part.Nucl.Phys. **33** (1994) 201–302, arXiv:hep-ph/9402266 [hep-ph].

[31] C. Giunti, C. W. Kim, and U. Lee, *Running coupling constants and grand unification models*, Mod. Phys. Lett. **A6** (1991) 1745–1755.

[32] M. Holthausen, K. S. Lim, and M. Lindner, *Planck scale Boundary Conditions and the Higgs Mass*, JHEP **1202** (2012) 037, arXiv:1112.2415 [hep-ph].

[33] J. M. Campbell, J. Huston, and W. Stirling, *Hard Interactions of Quarks and Gluons: A Primer for LHC Physics*, Rept.Prog.Phys. **70** (2007) 89, arXiv:hep-ph/0611148 [hep-ph].

[34] A. Buckley, J. Butterworth, S. Gieseke, D. Grellscheid, S. Hoche, et al., *General-purpose event generators for LHC physics*, Phys.Rept. **504** (2011) 145–233, arXiv:1101.2599 [hep-ph].

[35] D. E. Soper, *Partons and Their Transverse Momenta in Quantum Chromodynamics*, Phys. Rev. Lett. **43** (1979) 1847–1851. http://link.aps.org/doi/10.1103/PhysRevLett.43.1847.

[36] P. M. Nadolsky, H.-L. Lai, Q.-H. Cao, J. Huston, J. Pumplin, et al., *Implications of CTEQ global analysis for collider observables*, Phys.Rev. **D78** (2008) 013004, arXiv:0802.0007 [hep-ph].

[37] A. Martin, W. Stirling, R. Thorne, and G. Watt, *Uncertainties on alpha(S) in global PDF analyses and implications for predicted hadronic cross sections*, Eur.Phys.J. **C64** (2009) 653–680, arXiv:0905.3531 [hep-ph].

[38] R. D. Ball, V. Bertone, S. Carrazza, C. S. Deans, L. Del Debbio, et al., *Parton distributions with LHC data*, Nucl.Phys. **B867** (2013) 244–289, arXiv:1207.1303 [hep-ph].

[39] A. D. Martin, R. Roberts, W. J. Stirling, and R. Thorne, *Parton distributions and the LHC: W and Z production*, Eur.Phys.J. **C14** (2000) 133–145, arXiv:hep-ph/9907231 [hep-ph].

[40] ATLAS Collaboration, G. Aad et al., *Measurement of the inclusive $W^{\pm}$ and Z/gamma cross sections in the electron and muon decay channels in pp collisions at $\sqrt{s} = 7$ TeV with the ATLAS detector*, Phys.Rev. **D85** (2012) 072004, arXiv:1109.5141 [hep-ex].

[41] S. Frixione, P. Nason, and B. R. Webber, *Matching NLO QCD and parton showers in heavy flavor production*, JHEP **0308** (2003) 007, arXiv:hep-ph/0305252 [hep-ph].

[42] ATLAS Collaboration Collaboration, G. Aad et al., *Measurement of the $W \to \ell\nu$ and $Z/\gamma^* \to \ell\ell$ production cross sections in proton-proton collisions at $\sqrt{s} = 7$ TeV with the ATLAS detector*, JHEP **1012** (2010) 060, arXiv:1010.2130 [hep-ex].

[43] M. Awramik, M. Czakon, A. Freitas, and G. Weiglein, *Precise prediction for the W boson mass in the Standard Model*, Phys.Rev. **D69** (2004) 053006, arXiv:hep-ph/0311148 [hep-ph].

[44] S. Heinemeyer, W. Hollik, D. Stockinger, A. Weber, and G. Weiglein, *Precise prediction for M(W) in the MSSM*, JHEP **0608** (2006) 052, arXiv:hep-ph/0604147 [hep-ph].

[45] D. Kennedy and B. Lynn, *Electroweak radiative corrections with an effective Lagrangian: Four-fermions processes*, Nuclear Physics B **322** no. 1, (1989) 1 – 54. http://www.sciencedirect.com/science/article/pii/0550321389904835.

[46] S. Heinemeyer, W. Hollik, G. Weiglein, and L. Zeune, *Implications of LHC search results on the W boson mass prediction in the MSSM*, JHEP **1312** (2013) 084, arXiv:1311.1663 [hep-ph].

[47] M. Baak and R. Kogler, *The global electroweak Standard Model fit after the Higgs discovery*, arXiv:1306.0571 [hep-ph].

[48] CDF Collaboration, D0 Collaboration, T. E. W. Group, *2012 Update of the Combination of CDF and D0 Results for the Mass of the W Boson*, arXiv:1204.0042 [hep-ex].

[49] D0 Collaboration, V. M. Abazov et al., *Measurement of the W boson Mass with the D0 Detector*, Phys.Rev.Lett. **108** (2012) 151804, arXiv:1203.0293 [hep-ex].

[50] ALEPH Collaboration, DELPHI Collaboration, L3 Collaboration, OPAL Collaboration, LEP Electroweak Working Group Collaboration, J. Alcaraz et al., *A Combination of preliminary Electroweak measurements and constraints on the Standard Model*, arXiv:hep-ex/0612034 [hep-ex].

[51] Particle Data Group, *Review of particle physics*, J. Phys. G **33** (2006) 1.

[52] P. Golonka and Z. Was, *PHOTOS Monte Carlo: A Precision tool for QED corrections in Z and W decays*, Eur.Phys.J. **C45** (2006) 97–107, arXiv:hep-ph/0506026 [hep-ph].

[53] ATLAS Collaboration, G. Aad et al., *Measurement of the Muon Charge Asymmetry from W Bosons Produced in pp Collisions at $\sqrt{s} = 7$ TeV with the ATLAS detector*, Phys.Lett. **B701** (2011) 31–49, arXiv:1103.2929 [hep-ex].

[54] ATLAS Collaboration, G. Aad et al., *Measurement of the production of a W boson in association with a charm quark in pp collisions at $\sqrt{(s)}$=7 TeV with the ATLAS detector*, arXiv:1402.6263 [hep-ex].

[55] ATLAS Collaboration, G. Aad et al., *Measurement of the Transverse Momentum Distribution of W Bosons in pp Collisions at $\sqrt{s} = 7$ TeV with the ATLAS Detector*, Phys.Rev. **D85** (2012) 012005, arXiv:1108.6308 [hep-ex].

[56] ATLAS Collaboration, G. Aad et al., *The ATLAS Experiment at the CERN Large Hadron Collider*, Journal of Instrumentation **3** no. 08, (2008) S08003. http://stacks.iop.org/1748-0221/3/i=08/a=S08003.

[57] V. Frigo, "LHC map in 3D. Schema du LHC en 3D." AC Collection. Legacy of AC. Pictures from 1992 to 2002., Mar, 1997.

[58] O. S. Bruning, P. Collier, P. Lebrun, S. Myers, R. Ostojic, J. Poole, and P. Proudlock, *LHC Design Report*. CERN, Geneva, 2004.

[59] E. Keil, *The Large Hadron Collider LHC*, eConf **C960625** (1996) OPS010.

[60] ATLAS Collaboration, G. Aad et al., *Improved luminosity determination in pp collisions at $\sqrt{s}$ = 7 TeV using the ATLAS detector at the LHC*, Eur.Phys.J. **C73** (2013) 2518, arXiv:1302.4393 [hep-ex].

[61] ATLAS Collaboration, *Luminosity working group public results*, 2012. https://twiki.cern.ch/twiki/bin/view/AtlasPublic/LuminosityPublicResults.

[62] ATLAS Collaboration, G. Aad et al., *The ATLAS Inner Detector commissioning and calibration*, Eur. Phys. J. C **70** no. arXiv:1004.5293. CERN-PH-EP-2010-043, (2010) 787–821. 34 p. Comments: 34 pages, 25 figures.

[63] F. Hugging, *The ATLAS Pixel Detector*, IEEE Transactions on Nuclear Science **53** (2006) 1732–1736, physics/0412138.

[64] R. Klingenberg, *The ATLAS pixel detector*, Nuclear Instruments and Methods in Physics Research Section A: Accelerators, Spectrometers, Detectors and Associated Equipment **579** no. 2, (2007) 664 – 668. http://www.sciencedirect.com/science/article/pii/S0168900207011588. Proceedings of the 6th Hiroshima Symposium on the Development and Application of Semiconductor Detectors.

[65] ATLAS SCT Collaboration Collaboration, Y. Unno, *ATLAS silicon microstrip semiconductor tracker (SCT)*, Nucl.Instrum.Meth. **A453** (2000) 109–120.

[66] ATLAS TRT Collaboration Collaboration, V. A. Mitsou, *The ATLAS transition radiation tracker*, arXiv:hep-ex/0311058 [hep-ex].

[67] C. Grupen, *Physics of particle detection*, in *American Institute of Physics Conference Series*, pp. , 3–34. Sept., 2000. physics/9906063.

[68] G. Aad, B. Abbott, J. Abdallah, A. A. Abdelalim, A. Abdesselam, O. Abdinov, B. Abi, M. Abolins, H. Abramowicz, H. Abreu, and et al., *Readiness of the ATLAS Tile Calorimeter for LHC collisions*, European Physical Journal C **70** (2010) 1193–1236, arXiv:1007.5423 [physics.ins-det].

[69] ATLAS Muon Collaboration, G. Cattani, *Performance of the ATLAS resistive plate chambers*, Nucl.Instrum.Meth. **A661** (2012) S6–S9.

[70] A. Belloni and for the ATLAS collaboration, *Integration and commissioning of the ATLAS Muon spectrometer*, ArXiv e-prints (2008), arXiv:0810.2869 [physics.ins-det].

[71] Y. Arai, B. Ball, M. Beretta, H. Boterenbrood, G. Brandenburg, et al., *ATLAS muon drift tube electronics*, JINST **3** (2008) P09001.

[72] D. S. Levin, N. Amram, R. Ball, M. ben Moshe, Y. Benhammou, et al., *Drift time spectrum and gas monitoring in the ATLAS Muon Spectrometer precision chambers*, Nucl.Instrum.Meth. **A588** (2008) 347–358.

[73] T. Argyropoulos, K. A. Assamagan, B. H. Benedict, V. Chernyatin, E. Cheu, et al., *Cathode strip chambers in ATLAS: Installation, commissioning and in situ performance*, IEEE Trans.Nucl.Sci. **56** (2009) 1568–1574.

[74] A. Mapelli, F. Anghinolfi, S. Ask, P. Barrillon, G. Blanchot, S. Blin, A. Braem, C. Cheiklali, C. de La Taille, B. Di Girolamo, I. Efthymiopoulos, J. Faustino, D. Fournier, S. Franz, P. Grafstrm, L. Gurriana, M. Haguenauer, V. Hedberg, M. Heller, S. Hoffmann, W. Iwanski, C. Joram, A. Kocnar, B. Lavigne, B. Lundberg, A. Maio, M. J. P. Maneira, C. Marques, U. Mjrnmark, P. Conde-Muo, P. Puzo, M. Rijssenbeeck, J. P. Santos, J. G. Saraiva, N. Seguin-Moreau, S. Soares, H. Stenzel, M. Thioye, E. Valladolid-Gallego, and V. Vorobel, *Development of a detector (ALFA) to measure the absolute LHC luminosity at ATLAS*, Tech. Rep. ATL-LUM-PUB-2007-006. ATL-COM-LUM-2007-008, CERN, Geneva, Oct, 2007.

[75] ATLAS Collaboration, G. Aad et al., *Performance of the ATLAS Trigger System in 2010*, Eur.Phys.J. **C72** (2012) 1849, arXiv:1110.1530 [hep-ex].

[76] ATLAS Collaboration, *Trigger working group public results*, 2012. https://twiki.cern.ch/twiki/bin/view/AtlasPublic/TriggerOperationPublicResults.

[77] G. Aad, B. Abbott, J. Abdallah, A. A. Abdelalim, A. Abdesselam, O. Abdinov, B. Abi, M. Abolins, H. Abramowicz, H. Abreu, and et al., *The ATLAS Simulation Infrastructure*, European Physical Journal C **70** (2010) 823–874, arXiv:1005.4568 [physics.ins-det].

[78] GEANT4 Collaboration, S. Agostinelli et al., *GEANT4: A Simulation toolkit*, Nucl.Instrum.Meth. **A506** (2003) 250–303.

[79] S. Alioli, P. Nason, C. Oleari, and E. Re, *NLO vector-boson production matched with shower in POWHEG*, JHEP **0807** (2008) 060, arXiv:0805.4802 [hep-ph].

[80] S. Frixione and B. R. Webber, *Matching NLO QCD computations and parton shower simulations*, JHEP **0206** (2002) 029, arXiv:hep-ph/0204244 [hep-ph].

[81] T. Sjostrand, S. Mrenna, and P. Z. Skands, *PYTHIA 6.4 Physics and Manual*, JHEP **0605** (2006) 026, arXiv:hep-ph/0603175 [hep-ph].

[82] T. Sjostrand, S. Mrenna, and P. Z. Skands, *A Brief Introduction to PYTHIA 8.1*, Comput.Phys.Commun. **178** (2008) 852–867, arXiv:0710.3820 [hep-ph].

[83] M. Bahr, S. Gieseke, M. Gigg, D. Grellscheid, K. Hamilton, et al., *Herwig++ Physics and Manual*, Eur.Phys.J. **C58** (2008) 639–707, arXiv:0803.0883 [hep-ph].

[84] *ATLAS: Detector and physics performance technical design report. Volume 1*,. CERN-LHCC-99-14.

[85] ATLAS Collaboration, *ATLAS Photo Gallery*, 2014. http://www.atlas.ch/photos/index.html.

[86] The ATLAS Collaboration, *Expected Performance of the ATLAS Experiment, Detector, Trigger and Physics*, vol. CERN-OPEN-2008-020. CERN, Geneva, 2009. Pages 368-396.

[87] R. Fruhwirth, *Application of Kalman filtering to track and vertex fitting*, Nuclear Instruments and Methods in Physics Research Section A: Accelerators, Spectrometers, Detectors and Associated Equipment **262** no. 23, (1987) 444 – 450. http://www.sciencedirect.com/science/article/pii/0168900287908874.

[88] R. Fruhwirth and A. Strandlie, *Application of adaptive filters to track finding*, Nucl.Instrum.Meth. **A559** (2006) 162–166.

[89] ATLAS Collaboration, *Tracking Results and Comparison to Monte Carlo simulation at* $\sqrt{s} = 900$ *GeV*, Tech. Rep. ATLAS-CONF-2010-011, CERN, Geneva, Jul, 2010.

[90] ATLAS Collaboration, A. Airapetian et al., *ATLAS calorimeter performance Technical Design Report*,.

[91] Y. L. Dokshitzer, G. Leder, S. Moretti, and B. Webber, *Better jet clustering algorithms*, JHEP **9708** (1997) 001, arXiv:hep-ph/9707323 [hep-ph].

[92] M. Wobisch and T. Wengler, *Hadronization corrections to jet cross-sections in deep inelastic scattering*, arXiv:hep-ph/9907280 [hep-ph].

[93] S. D. Ellis and D. E. Soper, *Successive combination jet algorithm for hadron collisions*, Phys.Rev. **D48** (1993) 3160–3166, arXiv:hep-ph/9305266 [hep-ph].

[94] S. Catani, Y. Dokshitzer, M. Seymour, and B. Webber, *Longitudinally-invariant k-clustering algorithms for hadron-hadron collisions*, Nuclear Physics B **406** no. 12, (1993) 187 – 224. http://www.sciencedirect.com/science/article/pii/055032139390166M.

[95] M. Cacciari, G. P. Salam, and G. Soyez, *The Anti-k(t) jet clustering algorithm*, JHEP **0804** (2008) 063, arXiv:0802.1189 [hep-ph].

[96] *Expected electron performance in the ATLAS experiment*, Tech. Rep. ATL-PHYS-PUB-2011-006, CERN, Geneva, Apr, 2011.

[97] M. Vincter, J. Kretzschmar, and E. Schmidt, *Update of electron shower shapes in EM calorimeter*, Tech. Rep. ATL-COM-PHYS-2011-1299, CERN, Geneva, Sep, 2011.

[98] ATLAS Collaboration, G. Aad et al., *Electron reconstruction and identification efficiency measurements with the ATLAS detector using the 2011 LHC proton-proton collision data*, arXiv:1404.2240 [hep-ex].

[99] *The ATLAS transverse-momentum trigger performance at the LHC in 2011*, Tech. Rep. ATLAS-CONF-2014-002, CERN, Geneva, Feb, 2014.

[100] D. Banfi, L. Carminati, and L. Mandelli, *Calibration of the ATLAS electromagnetic calorimeter using calibration hits*, Tech. Rep. ATL-LARG-PUB-2007-012. ATL-COM-LARG-2007-007, CERN, Geneva, Jul, 2007.

[101] J. Gaiser, *Charmonium spectroscopy from radiative decays of the J/psi and psi'*. PhD thesis, Calif. Univ. Stanford, Stanford, CA, 1982. Presented on Aug 1982.

[102] ATLAS Collaboration, *Inner Detector Tracking Performance results*, 2011. https://twiki.cern.ch/twiki/bin/view/AtlasPublic/InDetTrackingPerformanceApprovedPlots.

[103] CDF Collaboration, D0 Collaboration, T. Dorigo, *New Tevatron measurements of the W boson mass*,.